

Turbulent boundary layers over surfaces with streamwise-preferential permeability

Experimental investigation into the drag and flow mechanics

F. H. (Friso) Hartog

Delft University of Technology

This page has been intentionally left blank.

Turbulent boundary layers over surfaces with streamwise-preferential permeability

Experimental investigation into
the drag and flow mechanics

Master of Science Thesis

by

F. H. (Friso) Hartog

in partial fulfilment of the requirements for the degree of

**Master of Science
in Aerospace Engineering**

at the Delft University of Technology

To be defended on Thursday September 9, 2021 at 10:00

Student number:	4359461	
Thesis committee:	Prof. dr. ir. L. L. M. (Leo) Veldhuis	Delft University of Technology
	Dr. ir. B. W. (Bas) van Oudheusden	Delft University of Technology
	Dr. ir. F. F. J. (Ferry) Schrijer	Delft University of Technology
	Dr. K. (Kunal) Masania	Delft University of Technology
	Ir. M. (Michiel) van Nesselrooij	Dimple Aerospace B.V.

This thesis is confidential and cannot be made public until September 9, 2023.
At which point, an electronic version will be available at <http://repository.tudelft.nl/>.



Copyright © 2021 by F. H. (Friso) Hartog

All rights reserved. No part of this publication may be reproduced, distributed, or transmitted in any form or by any means, including photocopying, recording, or other electronic or mechanical methods, without the prior written permission of the publisher, except in the case of brief quotations embodied in critical reviews and certain other noncommercial uses permitted by copyright law.

Delft University of Technology

Faculty of Aerospace Engineering
Department of Aerodynamics, Wind Energy, Flight Performance and Propulsion

The undersigned hereby certify that they have read and recommend to the Faculty of Aerospace Engineering for acceptance the thesis entitled **Turbulent boundary layers over surfaces with streamwise-preferential permeability** by **F. H. (Friso) Hartog** in partial fulfilment of the requirements for the degree of **Master of Science in Aerospace Engineering**.

Dated: September 9, 2021

Chair of supervisory committee:

Prof. dr. ir. L. L. M. (Leo) Veldhuis

Supervisors:

Dr. ir. B. W. (Bas) van Oudheusden

Dr. ir. F. F. J. (Ferry) Schrijer

Ir. M. (Michiel) van Nesselrooij

Reader:

Dr. K. (Kunal) Masania

This page has been intentionally left blank.

Preface

This thesis marks the end of a year of research at the Aerodynamics Group at Delft University of Technology. It has been a joyful time during which I have learnt a lot, and it was made possible by the support of many people.

First of all, I would like to thank Michiel van Nesselrooij and Olaf van Campenhout from Dimple Aerospace. Michiel has been a great supervisor. His approachability and attention to detail were indispensable for the quality of this research. Olaf his enthusiasm sparked energy at any moment of the day. The trip to the Pieterburen Seal Centre with both was memorable and marked the start of an exciting year.

I would also like to express my gratitude towards Dr. Ferry Schrijer, Dr. Bas van Oudheusden, Dr. Kunal Masania and Prof. Leo Veldhuis. Their doors were always open, which I greatly appreciated. Ferry his experimental aptitude and hands-on approach have been instrumental to the success of the measurement campaigns. It was good fun to build the PIV setup together. Bas his thorough understanding of aerodynamics and ability to explain tough concepts were highly valuable for me to gain a better judgment of the content of this research and more knowledge on turbulent boundary layers in general. Also, the consistent involvement of Ferry and Bas have kept this research on the right track, especially during challenging periods. Kunal his easygoing attitude gave me the freedom to play around in his Shaping Matter Lab. His expertise in additive manufacturing pushed me and the Prusa SL1 to the limits of our capabilities. Lastly, Leo reserved ample time for discussing potential thesis topics prior to the start of this project, and was always delighted to discuss the contents of this research during our encounters at the lab or faculty.

I owe a lot of thanks to the staff that supported me during the preparation and execution of the experiments. Peter Duyndam, Ir. Frits Donker Duyvis, Nico van Beek and Dennis Bruikman in the High Speed Laboratory; Ir. Stefan Bernardy and Emiel Langedijk in the Low Speed Laboratory; and Victor Horbowiec in the Delft Aerospace Structures and Materials Laboratory. Also, I would want to thank those not directly involved in this research, but who were nevertheless very willing to help: Dr. Woutijn Baars in discussing turbulent boundary layers and relevant analysis methods, Dr. Daniele Ragni in the execution of PIV experiments, Dr. Andrea Sciacchitano in experimental uncertainty quantification and Dr. Alejandro Rubio Carpio & Alberto Rius Vidales in the permeability measurements. It has been a unique opportunity to learn from experts in so many different and simultaneously related fields of research.

This research has also been made possible by two external parties. I want to recognise the efforts by Ana Rubio García and Byron Martina from the Pieterburen Seal Centre, who were so kind to provide two large seal fur specimens; and by Gertjan Vancoillie from Centexbel, who arranged and prepared the filament winding manufacturing process required for fabricating one of my wind tunnel test plates.

A great deal of pleasure came from working with and alongside fellow thesis students involved in similar topics. I especially want to thank Christopher Lai, who was the first in many aspects and whose learnings paved the way for many improvements in this research. Also, conducting the wind tunnel experiments and subsequently digging into the data together with Oriol Solergibert Travé made those weeks enjoyable and brought this work to a higher level.

Lastly, I would like to express my warmest gratitude towards my friends and family. They have been very supportive over the past year and made me realise that, regardless of its importance, there is more to life than the quest for turbulent drag reduction.

*Friso Hartog
Delft, 24th of August 2021*

This page has been intentionally left blank.

Abstract

Surfaces with streamwise-preferential permeability have shown potential for significant reduction in turbulent friction in studies based on direct numerical simulations (DNS). Recently, a theoretical framework has been proposed by Gómez-de-Segura and García-Mayoral (2019), modelling the hypothesised working mechanism - an offset in virtual origins of the mean flow and quasi-streamwise (QS-)vortices - and relating substrate permeability to predicted drag reduction. To date, little experimental data has been published on the topic. This work aims to experimentally explore the potential of this concept in air. It is the first experimental study in which the permeability requirements are met and the framework assumptions and hypotheses on drag reduction and flow modulation are extensively assessed and tested.

Three different physical realisations of streamwise-preferential permeable substrates were investigated: two seal furs, a substrate with unidirectional fibres, and a 3D-printed structure using masked stereolithography (MSLA). Permeability was experimentally characterised for the latter using a pressure drop - flow rate setup. Direct force measurements were performed to obtain drag characteristics. Planar (2D-2C) particle image velocimetry (PIV) measurements revealed the flow behaviour above the permeable surface. Both measurements were performed against a reference smooth wall. Correlating the results from these two measurement methods yielded insights on the nature of the drag sources and validity of the theoretical framework.

The direct force measurements show an increase in drag for all test specimens. For the 3D-printed surface, $0\% < \Delta C_D < 8\%$. PIV experiments yield a u_r -based friction estimate of $-2.5\% < \Delta C_f < 4\%$. The discrepancy between the measurements suggests that other sources than surface friction are non-negligible and contribute to the measured drag. One-point turbulent statistics show an overall increase in turbulence, mainly wall-normal velocity fluctuations enabled by the wall-normal permeability, which results in higher Reynolds stresses. No significant flow modulation in terms of turbulent events or change in coherent structures is observed.

The measurements and results are a first of its kind and none of the theoretical framework predictions on drag reduction or flow modulation are found. The tested surface does not physically allow for a lower friction contribution of QS-vortices. Based on analytical derivations, pores of a given size are expected to always lead to permeabilities that yield virtual origins between one and three orders of magnitude smaller than the pore size. The theoretical framework does not consider this physical relationship between pore size and permeability. As such, there is an inherent mismatch between the pore size assumption and the virtual origin model. All things considered, it is deemed unlikely that turbulent drag reduction by means of streamwise-preferential permeable surfaces is feasible in experimental settings. Nevertheless, given the relatively small increase in drag, streamwise-preferential permeable surfaces might be interesting for other (flow control) purposes involving turbulent boundary layers.

This page has been intentionally left blank.

Table of Contents

List of Figures	xi
List of Tables	xv
Nomenclature	xvii
I Introduction and theoretical background	1
1 Introduction	3
1.1 Relevance of drag reduction.	3
1.2 Introduction to flow control.	3
1.3 From seal fur to anisotropic permeable substrates	4
1.4 Research scope and objectives	5
1.5 Report overview.	6
2 Wall-bounded turbulence	7
2.1 Skin friction and boundary layer fundamentals	7
2.2 Coherent structures	11
2.3 Analysis methods	13
3 Anisotropic permeable substrates for turbulent friction reduction	17
3.1 Flow modelling through porous media	17
3.2 Historical overview	19
3.3 Drag reduction working mechanism	23
3.4 Concluding remarks	28
II Design, production, and assessment of anisotropic permeable substrates	31
4 General considerations for test plate production	33
4.1 Experimental circumstances and test specimens	33
4.2 Characterisation of permeability design space	35
5 Seal fur	39
5.1 Scaling from prior experiments	39
5.2 Manufacturing process	42
5.3 Test plate assessment	43
6 Continuous fibres	45
6.1 Test plate design	45
6.2 Manufacturing process	47
6.3 Test plate assessment	49
7 3D-printed structures	51
7.1 Design and design process	51
7.2 Printing methodology	54
7.3 Topography characterisation	56
7.4 Permeability characterisation	60
7.5 Test plate assessment	66
8 Concluding remarks on manufacturing of anisotropic permeable substrates	69

III	Wind tunnel experiments with streamwise-preferential permeable surfaces	71
9	Direct force measurements - Methodology	73
9.1	Measurement plan	73
9.2	Experimental setup	74
9.3	Data processing.	76
10	Direct force measurements - Results and discussion	77
10.1	Seal fur	77
10.2	Continuous fibre substrates.	78
10.3	3D-printed surfaces.	78
10.4	Discussion	82
11	Particle image velocimetry - Methodology	87
11.1	Measurement plan	87
11.2	Experimental setup	88
11.3	Data processing.	90
12	Particle image velocimetry - Results and discussion	93
12.1	Data quality assessment and uncertainty quantification	93
12.2	Boundary layer development	99
12.3	Boundary layer profiles: mean velocity and turbulent statistics.	104
12.4	Quadrant analysis.	108
12.5	Turbulent flow structures	113
12.6	Discussion	114
IV	Discussion, conclusions, and recommendations	119
13	Discussion	121
13.1	Correlation of experimental results	121
13.2	Theoretical framework discussed	125
14	Conclusions and recommendations for further research	129
14.1	Conclusions.	129
14.2	Recommendations for further research	131
V	Appendices	141
A	Statistical methods	143
B	Permeability of fibrous substrates	145
C	3D-printing prototyping phase	149
D	Permeability characterisation	155
E	Taylor-Couette flow measurements with seal fur	161
F	Pressure probe measurements	165
G	PIV cross-correlation benchmark test	169
H	PIV data processing routine	171
I	PIV results	181

List of Figures

1.1	Roadmap on reduction of CO2 emissions in aviation	4
2.1	Regions within the boundary layer	9
2.2	Visualisation of an instance of the near-wall cycle through the formation of hairpin vortices	11
2.3	Hairpin vortex formation	12
2.4	Schematic of QS-vortices above riblets of different sizes	12
2.5	Identification of spanwise coherent rollers	13
2.6	Example of boundary layer profiles	13
2.7	Example of quadrant analysis	14
2.8	Premultiplied two-dimensional cospectra of the Reynolds shear stress above riblet tips	15
3.1	Highly and poorly connected streamwise-preferential materials	21
3.2	Mean velocity profile for an anisotropic permeable substrate	23
3.3	Dependence of drag reduction on Reynolds number for constant ΔU^+	24
3.4	Schematic representation of streamwise and spanwise slip lengths	25
3.5	Maximum amplification versus permeability length scale for different permeable substrates	26
3.6	Comparison of flow structures above anisotropic permeable substrate to smooth flat plate	27
4.1	Theoretical values for a zero-pressure-gradient turbulent boundary layer over a smooth plate in the Hill in the M-tunnel	34
4.2	Theoretical development of a zero-pressure-gradient turbulent boundary layer over a smooth flat plate at $U_\infty = 35$ m/s	35
4.3	Dependence of theoretical DR predictions on flow conditions	36
4.4	Dependence of theoretical DR predictions on permeability parameters	36
4.5	Demarcating the permeability design space including the wall-normal permeability	37
5.1	Spanwise distribution of local skin friction coefficient on smooth and seal fur surfaces at $Re_m = 7,000$ for the glycerol-water mixture	40
5.2	Friction factor versus Reynolds number on the seal fur surface	40
5.3	Re_τ for different seal circumstances	41
5.4	Seal furs after treatment	42
5.5	Seal fur test plate manufacturing process steps	43
5.6	Seal fur test plates	43
5.7	SEM images of the harbour seal fur	44
6.1	Conceptual design of continuous fibre test plate	45
6.2	Filament winding around an open frame	46
6.3	Schematic exploded view of continuous fibre test plate aluminium mould	46
6.4	Conceptual design of continuous fibre winding frame for filament winding process	47
6.5	Schematic exploded view of continuous fibre frame assembly for filament winding process	47
6.6	Filament winding and cutting procedure	48
6.7	Bottom of fibre frame	49
6.8	Continuous fibre plate finishing with moulding clay	49
6.9	Continuous fibre plate imperfections	50
6.10	DR predictions for different continuous fibre substrate configurations	50
7.1	3D-printed plate unit cell design	52
7.2	Design process steps	52
7.3	Example of permeability sample	53
7.4	Example of wind tunnel test plate part	53

7.5	Working principle of MSLA printing	54
7.6	Apparatus used in printing process	55
7.7	Examples of scanned images for topography characterisation of 3D-printed samples	56
7.8	Dimensions of wall-normal pores	57
7.9	Statistics on dimensions of wall-normal pores	58
7.10	Example of roughness profile and determination of roughness metrics	59
7.11	Statistics on wind tunnel test plate part roughness	60
7.12	Setup for permeability characterisation	61
7.13	Technical drawings of permeability setup test section	62
7.14	Examples of pressure drop - flow rate experimental results and fitted models for permeability characterisation	64
7.15	Wind tunnel test plate	66
7.16	Detailed views of wind tunnel test plate	66
7.17	DR predictions for different permeability cases of the 3D-printed test plate	67
9.1	Wind tunnel facilities used	74
9.2	Schematics of the Hill measurement system	75
9.3	Test plates in the Hill	75
10.1	Direct force measurement results for the seal fur plate	79
10.2	Direct force measurement results for the continuous fibre plate	80
10.3	Direct force measurement measurement results for the 3D-printed plate	81
10.4	Significance estimation of force measurements	82
10.5	Comparison of wetted and dry seal fur	83
11.1	Schematic overview of PIV measurement locations	87
11.2	Calibration image examples	88
11.3	Setup of PIV experiments	89
11.4	Schematic of test plate mount with the leading edge assembly and wind tunnel floor	89
11.5	Effect of laser-cutter on laser sheet	90
11.6	Effect of laser-cutter on images	90
11.7	Example of PIV image pre-process step	90
12.1	Instantaneous velocity field results from cross-correlation for Station 4	94
12.2	Mean velocity field results for Station 4 at 30 m/s	94
12.3	FOV edge distortion effect on PIV data at Station 4	95
12.4	Schematic of averaging effect due to light incidence angle	96
12.5	Averaging effects near the wall on PIV data for the smooth wall at Station 4	97
12.6	Diagnostic plots for Station 4	98
12.7	Development of boundary layer thickness (δ) over the test plate for different velocities	100
12.8	Development of displacement thickness (δ^*) over the test plate for different velocities	100
12.9	Development of moment thickness (θ) over the test plate for different velocities	101
12.10	Development of shape factor (H) over the test plate for different velocities	101
12.11	Development of friction velocity (u_τ) over the test plate for different velocities	102
12.12	Development of freestream velocity normalised to the Station 1 value ($U_\infty/U_{\infty,S1}$) over the test plate for different velocities	102
12.13	Development of normalised friction velocity (u_τ/U_∞) over the test plate for different velocities	103
12.14	Development of friction coefficient (C_f) over the test plate for different velocities	103
12.15	Boundary layer mean velocity profiles at Station 4	104
12.16	Boundary layer profiles for $U_\infty \approx 5$ m/s at Station 4	106
12.17	Boundary layer profiles for $U_\infty \approx 10$ m/s at Station 4	106
12.18	Boundary layer profiles for $U_\infty \approx 20$ m/s at Station 4	107
12.19	Boundary layer profiles for $U_\infty \approx 30$ m/s at Station 4	107
12.20	Joint probability density function for Station 4	110
12.21	Weighted joint probability density function for Station 4	111
12.22	Reynolds stress contributions for Station 4	112
12.23	Visualisation of the instantaneous turbulent structures	113

12.24	Comparison of velocity profiles for similar streamwise permeability	114
12.25	Isometric view renders of different surfaces	114
12.26	One-point turbulent statistics from Gómez-de-Segura and García-Mayoral (2019)	116
13.1	Momentum loss profiles	122
13.2	Correlation of results from direct force measurements and PIV experiments	123
13.3	Schematic of potential extra drag sources in permeable substrate	124
13.4	Schematic of expected profile penetration depth and structure length scales	126
13.5	Schematic of permeable substrate with pores and solid objects of equal size	127
B.1	Difference in fibre orientation within fibrous substrates	145
B.2	Examples of different unit cells for fibrous substrates	146
C.1	Comparison of prints for Prusa SL1 and Formlabs Form 3	149
C.2	Microscope scans of small samples for exposure time assessment	150
C.3	Microscope scans of small samples for pore quality assessment	151
C.4	Partially clogged wind tunnel test plate parts	151
C.5	Non-clogged wind tunnel test plate part	152
C.6	Anti-aliasing feature of Prusa SL1	153
D.1	Schematics of permeability measurement systems	156
D.2	Two-piece permeability sample	157
D.3	Occurrence of thickness effect in permeability characterisation	158
D.4	Negative γ -permeability at high pressure drops	158
D.5	Complete results for final permeability measurements	159
E.1	Friction coefficient for reference cylinder in Taylor-Couette flow setup	162
E.2	Drag difference for seal fur compared to smooth reference cylinder in Taylor-Couette flow setup	163
F.1	Setup for pressure probe measurements	165
F.2	Pressure probe measurement locations	166
F.3	Results of pressure probe measurements	167
G.1	Instantaneous velocity magnitude fields for the cross-correlation benchmark test	170
H.1	Visualisation of wall estimation procedure	171
H.2	Effect of BL profile correction using smoothed wall estimate	172
H.3	Velocity profile first and second unit derivatives	173
H.4	Assessment of linear fitting in viscous sublayer for friction velocity estimation	174
H.5	Assessment of Clauser's indirect fitting for friction velocity estimation	175
H.6	Assessment of Spalding's law of the wall fitting for friction velocity estimation	175
H.7	Assessment of composite fitting for friction velocity estimation	176
H.8	Friction velocity (u_τ) for different velocities and estimation methods	177
H.9	Assessment of method similarity across measurements at Station 1, for different velocities and estimation methods	178
H.10	Percentage difference in normalised friction velocity (u_τ/U_∞) between different estimation methods, with composite method as reference, for different velocities	179
I.1	Example of raw image from PIV measurement of the seal fur	181
I.2	Boundary layer profiles at Station 4 (seal fur)	182
I.3	Visualisation of vibrating hairs of seal fur	183
I.4	Boundary layer profiles at Station 1	185
I.5	Boundary layer profiles at Station 2	186
I.6	Boundary layer profiles at Station 3	187
I.7	Boundary layer profiles at Station 4	188
I.8	Boundary layer profiles at Station 4 (zoomed-in view)	189
I.9	Premultiplied spatial spectra for reference smooth wall at Station 4	191

This page has been intentionally left blank.

List of Tables

3.1	Approaches to porous medium flow modelling and interface conditions in studies on turbulent drag reduction by means of anisotropic permeability.	19
3.2	Cases for defining the virtual origin of the turbulence ($\ell_{\omega_x}^+$).	25
3.3	Results of DNS studies on drag reduction through anisotropic permeable substrates.	27
3.4	Cross-checking the theoretical model predictions	28
3.5	Overview of the types of anisotropic permeable specimens made in this research	31
5.1	Results from scaling based on Itoh et al. (2006).	40
5.2	Overview of Re_τ for different scaling methods compared to test facilities	41
5.3	Seal fur thickness	44
6.1	Dimensions of fibre mould components	46
7.1	Settings for 3D-printing	55
7.2	Statistics on dimensions of wall-normal pores	56
7.3	Surface roughness metrics expressed in viscous units	60
7.4	Measurement equipment in the permeability characterisation setup	62
7.5	Permeability results	65
7.6	Comparison of pore area and permeability values for y -permeability samples	65
7.7	Different scenarios for wind tunnel test plate permeabilities	67
8.1	Summary of the types of anisotropic permeable specimens manufactured	70
8.2	Benefits and drawbacks of different test plates for wind tunnel experiments	70
9.1	Overview of conducted direct force measurements	74
11.1	Main experimental parameters for PIV measurements	88
11.2	PIV correlation settings and vector field resolutions	91
12.1	Averaging regions due to finite interrogation window and optical angle expressed in viscous units for different freestream velocities	96
12.2	Uncertainty estimations of turbulent statistics for Station 4.	99
12.3	ΔC_f (%) of permeable surface w.r.t. smooth wall based on u_τ estimation from direct linear fitting in viscous sublayer	115
13.1	Overview of methods via which C_D and C_f were obtained	123
B.1	Overview of (semi-)analytical permeability models for unidirectional fibrous substrates	148
C.1	Design parameters and permeability results of first design iteration	150
C.2	Statistics on dimensions of wall-normal pores for small sample parameter sweep	151
C.3	Large sample parameter sweep results	153
G.1	Overview of interrogation window settings in cross-correlation benchmark test	169
I.1	Fitted boundary layer parameters of outer layer composite fit optimisation	190

This page has been intentionally left blank.

Nomenclature

Acronyms and Abbreviations

AC	Average case	KH	Kelvin-Helmholtz
AE	Aerospace Engineering	LCD	Liquid-crystal display
AoA	Angle of attack	LCM	Liquid composite moulding
APG	Adverse pressure gradient	LE	Leading edge
APS	Anisotropic permeable substrate/surface	LED	Light-emitting diode
ASTM	American Society for Testing and Materials	LR	Low-speed regime
BC	Best case	LSL	Low Speed Laboratory
BL	Boundary layer	MSLA	Masked stereolithography
BW	Bandwidth	PIV	Particle image velocimetry
CC	Cross-correlation	POD	Proper orthogonal decomposition
cDAQ	Compact data acquisition	Pred.	Predicted
CFRP	Carbon-fibre reinforced polymer	PTU	Programmable timing unit
d.o.f.	Degrees of freedom	px	Pixels
DASML	Delft Aerospace Structures and Materials Laboratory	Q	Quadrant
DFM	Direct force measurement	QS	Quasi-streamwise
DNS	Direct numerical simulation	Rd	Reading
DR	Drag reduction	Reg.	Regular orientation
EIA	U. S. Energy Information Administration	REV	Representative elementary volume
FOV	Field of view	Rev.	Reversed orientation
FPG	Favorable pressure gradient	rms	Root mean square
FRC	Fibre-reinforced composite	RMSE	Root-mean-square error
FS	Full scale	RPM	Rotations per minute
HSL	High Speed Laboratory	S	Station (streamwise location) in PIV experiments (e.g. S1 denotes station 1)
HWA	Hot-wire anemometry	SEM	Scanning electron microscope/microscopy
IATA	International Air Transport Association	SLA	Stereolithography
IPA	Isopropyl alcohol	SOC	Sum of correlation
ISA	International standard atmosphere	STL	Surface Tessellation Language
JPDF	Joint probability density function	TBL	Turbulent boundary layer
		TE	Trailing edge
		TPM	Tri(propylene glycol) methyl ether
		TU Delft	Delft University of Technology

UD	Unidirectional	ϵ	Porosity, standard error
UV	Ultraviolet	η	Wall-normal distance normalised with boundary layer thickness
VANS	Volume-averaged Navier Stokes	κ	von Kármán constant
WC	Worst case	λ	Friction factor, molecular mean free path, wave length
WJPDF	Weighted joint probability density function	μ	Dynamic viscosity, mean
WT	Wind tunnel	ν	Kinematic viscosity
ZPG	Zero pressure gradient	ω	Vorticity
Dimensionless Groups			
C_D	Drag coefficient based on freestream flow conditions and test plate top area	ω_i	Amplification
C_f	Skin friction coefficient	ϕ	Fibre volume ratio, permeability ratio (expressed in viscous units)
Kn	Knudsen number	Φ_s	Sphericity
Re	Reynolds number	Π	Wake strength
Re_1	Reynolds number based on unit length (unit Reynolds number)	ρ	Correlation coefficient, density
Re_δ	Reynolds number based on boundary layer thickness	σ	Permeability ratio (expressed in physical units), standard deviation
Re_τ	Reynolds number based on wall shear stress (friction Reynolds number)	τ	Shear stress
Re_θ	Reynolds number based on momentum thickness	τ_w	Wall shear stress
Re_D	Reynolds number based on pipe diameter	θ	Momentum thickness
Re_m	Reynolds number based on bulk velocity	$\tilde{\nu}$	Effective viscosity
Re_s	Reynolds number based on the shear rate between the inner and outer cylinder in Taylor-Couette flow measurement (shear Reynolds number)	Latin Symbols	
Re_x	Reynolds number based on streamwise distance from boundary layer starting point	B	Forchheimer coefficient (tensor)
Greek Symbols			
α	Light incidence angle, statistical significance level	K	Permeability (tensor)
Δ	Difference	u	Velocity (vector)
δ	Boundary layer thickness	<i>A</i>	Area
δ^*	Displacement thickness	<i>B</i>	Turbulent boundary layer wall law intercept constant
δ_ν	Viscous length scale	<i>D</i>	Diameter
ℓ	Slip length	<i>d</i>	Distance
		$d_{a,o}$	Averaging region due to optical angle
		$d_{a,w}$	Averaging region due to finite interrogation window
		<i>F</i>	Force
		<i>f</i>	Frequency
		<i>f#</i>	F-stop
		F_p	Pressure force
		F_{null}	Null force

H	Height, shape factor	u, v, w	Velocity in streamwise, wall-normal and spanwise directions
h	Roughness height, substrate thickness	u', v', w'	Velocity fluctuation in streamwise, wall-normal and spanwise directions
K	Permeability (scalar)	U_∞	Freestream velocity
L	Characteristic length scale, length	U_a	Bulk velocity
L_e	Entrance length	V	Volume
Ln	Standard liter	W	Width
M	Molecular weight	x, y, z	Coordinates in streamwise, wall-normal and spanwise directions
N	Sample size	x_{TP}	Streamwise distance w.r.t. test plate leading edge
n	Sample size	Superscripts	
$O()$	In the order of	$+$	Expressed in viscous units
P	Pressure	Subscripts	
p	Kinematic pressure	0	Reference (smooth wall)
p_a	Absolute pressure	ω	Vortices
p_v	Vapor pressure	\parallel	Parallel direction
Q	Volumetric flow rate	\perp	Perpendicular direction
q	Dynamic pressure	Br	At point of breakdown of linear drag reduction regime
R	Universal gas constant	f	Fibre
R_a	Roughness profile absolute arithmetic mean	g	Groove
R_{xy}	Reynolds stress	i	Inlet
RH	Relative humidity	K	Permeability-based
S	Surface area	p	Pore-based
s	Spacing	T	Bulk, turbulence
T	Temperature	V	Void
t	Thickness, time		
T_0	Reference temperature (273.15 K)		

This page has been intentionally left blank.

I

Introduction and theoretical background

This page has been intentionally left blank.



Introduction

The seal is not the first animal that comes to mind when we think about speed and performance. Perhaps it should. More than a decade ago, a group of Japanese scientists found that the seal fur can reduce turbulent drag in water flows with up to 12% (Itoh et al., 2006). It is attributed to the fur's anisotropic permeability, a concept through which recent DNS studies have achieved friction reductions of up to 25% (Gómez-de-Segura and García-Mayoral, 2019; Li et al., 2020). Such figures are extremely interesting and relevant in the context of the required reductions in CO₂ emissions of aviation. Unfortunately, the academic research into this topic has been limited to theoretical and numerical studies. This thesis aims to experimentally explore the potential of using anisotropic permeability to reduce turbulent drag in air.

1.1. Relevance of drag reduction

Transportation of people and goods accounts for 25% of all energy consumption in the world (EIA, 2015). The majority of this energy is used to overcome drag in vehicles and fluid resistance in pipelines. Due to the heavy reliance on fossil fuels, this drag has not only a substantial economic cost but also a negative impact on the climate via greenhouse gas emissions, especially CO₂. To illustrate both aspects for the aviation industry: jet fuel consumption accounted for 23.7% of operating expenses of airlines in 2019, totalling to \$188 billion globally (IATA, 2019); and while aviation is responsible for 2.4% of the total CO₂ emissions (Graver et al., 2019), including non-CO₂ warming effects results in a net contribution to 5% of the problem of climate-warming (Nelson, 2018).

The economic and environmental impact of aviation will continue to grow in the coming decades with an expected doubling in air travel demand between 2019 and 2038 (Airbus, 2019). Therefore the International Aviation Transportation Board has set a non-binding goal of 50% reduction of CO₂ emissions by the aviation industry (IATA, 2013). The roadmap in Figure 1.1 shows that radical novel technologies are required to reach this goal. The faculty of Aerospace Engineering at the Delft University of Technology participates in an action plan of the Dutch aviation industry called "Slim en Duurzaam", aiming to reduce CO₂ by 35% by 2030. Considering that turbulent friction accounts for nearly 50% of the energy consumption of commercial aircraft, the author of this report believes that research into new technologies for reducing turbulent friction drag is highly relevant and fits well within the objectives of the faculty.

1.2. Introduction to flow control

Flow control is the artificial modification of fluid flow to achieve a certain goal, e.g. lift enhancement or drag reduction. The first to experimentally explore this concept was Prandtl (1904), who introduced the concept of the boundary layer and aimed to delay laminar-to-turbulent transition through suction. Through the Second World War and the Cold War, military aircraft design asked for high aerodynamic performance requirements and flow control became an important area of study. Efforts in this field shifted towards drag-reducing applications for amongst others commercial aviation after the rise of fuel prices during the energy crisis of the 1970s, and this focus remains important nowadays. The author recommends Fischer and Ash (1974), Szodruch (1991), Choi (2000), Bushnell (2003), and Spalart and McLean (2011) for further reading.

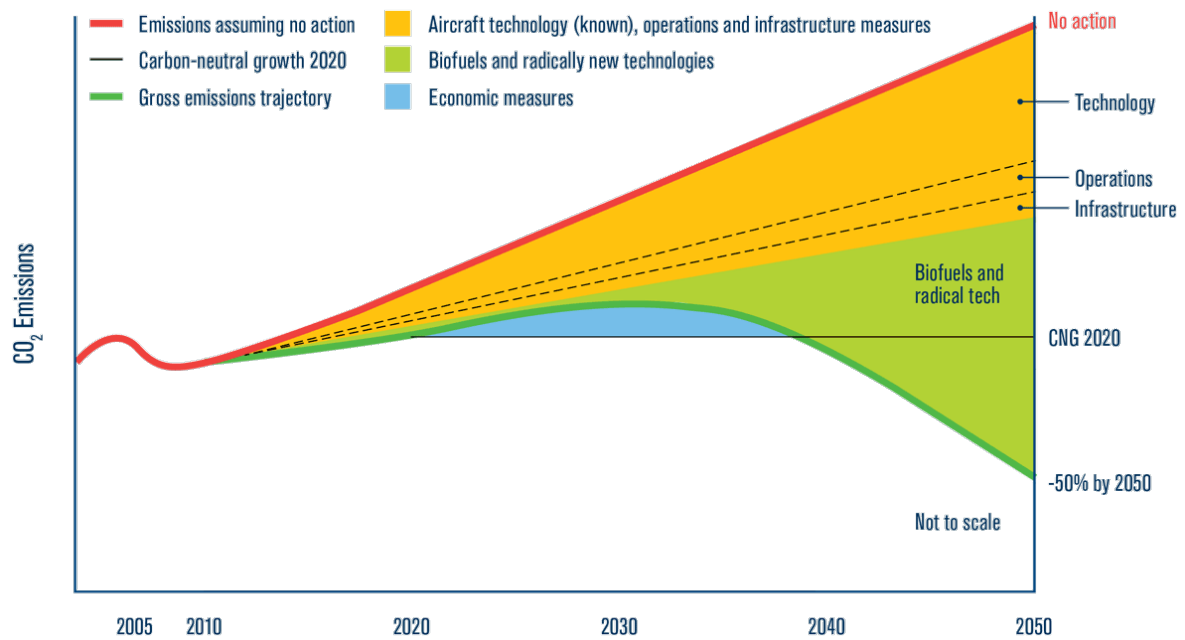


Figure 1.1: Roadmap on reduction of CO₂ emissions in aviation (IATA, 2013).

Flow control techniques can be classified in different ways. Distinguishing between active and passive methods is the most common approach and was proposed by Gad-el-Hak (2000) in his extensive work on modern flow control techniques. Active methods, such as plasma actuators, require an energy input. They can adjust to the flow and therefore offer flexibility. Passive methods do not need an energy input and are mostly in the form of a geometry modification to a surface. Successful examples of passive flow control techniques are vortex generators. These mix high momentum flow into the lower part of the boundary layer, which prevents flow separation. Consequently, aircraft can fly at higher angles of attack for improved lift coefficients.

Since passive methods do not require actuators and sensors, they are often lighter, cheaper and more manageable in maintenance than active methods. Consequently, the author believes that passive methods through surface modifications are interesting for realistic and practical applications to reduce turbulent drag. To come up with radical novel technologies required to follow the roadmap shown in Figure 1.1, it is necessary to look further than known methods and draw from new sources of inspiration.

1.3. From seal fur to anisotropic permeable substrates

The seal fur is a surprising but promising instance of passive flow control for turbulent drag reduction in nature. Itoh et al. (2006) found that the seal fur outperforms riblets in terms of turbulent friction reduction in water (12% vs. 7%). It is thought that this lower friction is caused by the anisotropic permeability (the resistance to fluid flow within a porous substance) of the fur (Gómez-de-Segura and García-Mayoral, 2019), which consists of flattened hairs aligned in streamwise direction (Erdsack et al., 2015). Over the last few years, different direct numerical simulation (DNS) studies have shown the potential of streamwise-preferential surfaces to reduce turbulent drag (Gómez-de-Segura and García-Mayoral, 2019; Li et al., 2020). Depending on the streamwise-to-spanwise permeability ratio and friction Reynolds number, these reductions were as high as 25%. Gómez-de-Segura and García-Mayoral (2019) developed a theoretical framework on the drag reduction working mechanism. In this model, permeability is related to a predicted drag reduction via slip lengths and virtual origins.

Different elements of living organisms have successfully found their way into methods of flow control for turbulent friction reduction, such as riblets (from the shark's skin) and superhydrophobic surfaces (from underwater plants). Emulating the seal fur's capabilities could be a new story of success at the intersection of biomimetics and fluid mechanics. To date, no further research has been done on the drag characteristics of the seal fur. Moreover, only one experimental study into turbulent flow over substrates with streamwise-preferential permeability has been performed (Efsthathiou and Luhar, 2020). Unfortunately, the permeability values in it were such that the hypotheses of the theoretical framework could not be fully tested. In fact, there is no consensus within the field on how to physically realise substrates with the required permeability characteristics. Given the potential for large drag reductions and the urgent need for CO₂ emission reductions in aviation, the author of this report believes that these unanswered questions form a highly relevant research gap that deserved an experimental study. A full literature study that lead to this conclusion is available upon request. It covers in more detail the topics of biomimetics for turbulent drag reduction, turbulent flow over permeable surfaces, and fibrous substrates and hairy surfaces in flow control applications.

1.4. Research scope and objectives

The concept around which this thesis revolves can be defined as follows:

Application of anisotropic permeability to wall-surfaces as a means of flow control for turbulent drag reduction.

Motivated by the experimental research gap on this topic, the **main objective** of this study is:

To experimentally investigate the potential of the application of anisotropic permeability to wall-surfaces as a means of boundary layer flow control for turbulent drag reduction, by performing permeability characterisation, direct force measurements and flow visualisation on practical implementations of substrates with streamwise-preferential permeability on flat plates in turbulent boundary layers of external flows in air.

"The potential" is a broad definition and can be interpreted as a combination of achievable drag reduction and practical feasibility. The use of this definition is justified from the viewpoint that the research concerns a highly novel concept and that there is little prior knowledge on how it materialises in experimental settings. "The theoretical framework" refers to the one proposed in the work by Gómez-de-Segura and García-Mayoral (2019). "Surfaces with streamwise-preferential permeability" will be referred to as "streamwise-preferential permeable surfaces" in the remainder of this report.

The main objective is further specified through the following three sub-objectives:

1. **Design and produce anisotropic permeable substrates with the required permeability characteristics and feasibility for use in wind tunnel experiments.**
2. **Find the design parameter space for an anisotropic permeable substrate which results in a drag reduction by correlating substrate topology and permeability characterisation results to direct force measurements.**
3. **Test the hypotheses on the flow modulation and subsequent drag reduction working mechanism proposed by Gómez-de-Segura and García-Mayoral (2019), by observing the flow behaviour over the streamwise-preferential permeable substrate implementation via planar PIV measurements.**

Research questions

To fulfil the research objectives, the following research questions ought to be answered:

1. **What anisotropic permeable substrates are viable for experimental aerodynamic research into turbulent boundary layers and friction drag?**
 - (a) What type of substrate can be produced with the required permeability characteristics?
 - (b) What is the relation between the design parameters and the substrate permeability tensor?
 - (c) How can these substrates be applied over a thin flat plate? What are the potential downsides considering the purpose of measuring friction drag in wind tunnel experiments?

2. How do streamwise-preferential permeable surfaces influence the change in drag?

- (a) What is the measured change in drag?
- (b) Can the measured change be fully attributed to a change in skin friction, or are other sources of drag at play?
- (c) What is the relation between the substrate permeability tensor and the change in drag?
- (d) To what extent does the change in drag agree with the theoretical framework predictions?

3. How do streamwise-preferential permeable surfaces influence the flow behaviour?

- (a) Is a shift in the log-law region of the boundary layer profile observed? Can this be related to the measured drag change via the theoretical framework?
- (b) Can the slip velocity at the substrate-flow interface be measured? If so, does the slip velocity relate to the log-law shift observed in (3a) in correspondence to the theoretical framework?
- (c) Can spanwise-coherent structures related to KH-instabilities ("rollers") be observed above the surface beyond the breakdown velocity?
- (d) How do (3b) and (3c) relate to the substrate permeability tensor? To what degree do these relationships agree with the theoretical framework?
- (e) How does the turbulent activity change compared to a smooth wall?
- (f) What (instantaneous) turbulent flow structures can be observed above the permeable surface? How do they differ from those observed above a smooth wall?

The theoretical framework and its predictions on drag reduction and flow modulation serve as the hypotheses for these research questions.

1.5. Report overview

This report consists of four parts. Supporting material that does not belong to the main body is provided in the appendices (Part V) and appropriately referenced whenever needed.

Part I shares the background knowledge required to understand the work presented in this thesis. Chapter 2 introduces the fundamental knowledge on turbulent boundary layers and friction drag, including relevant physical quantities, flow structures and analysis methods. Chapter 3 shares the literature on turbulent flow over permeable surfaces and explains the theoretical framework on the hypothesised working mechanism for drag reduction over streamwise-preferential surfaces specifically.

Part II explores the design, manufacturing and assessment of anisotropic permeable substrates. First, a general idea on the test specimen requirements for valuable wind tunnel experiments is established in Chapter 4. It covers the experimental circumstances for this research and subsequently establishes the permeability design space. Then, the three categories of test specimens are discussed in separate chapters: the seal fur in Chapter 5, continuous fibres in Chapter 6 and 3D-printed structures in Chapter 7. All categories are described in terms of the design rationale, manufacturing process, performed experiments to determine relevant characteristics and a final assessment on the hypothesised potential for turbulent friction drag reduction. A summary with concluding remarks is shared in Chapter 8.

Part III covers the wind tunnel experiments, through which the drag characteristics of the streamwise-preferential permeable surfaces and their influence on the overlying flow are investigated. Furthermore, the data is used to test the hypotheses of the theoretical framework. Direct force measurements for characterising the drag is covered first, establishing the methodology and subsequently presenting and discussing the results in Chapters 9 and 10 respectively. Particle image velocimetry (PIV) experiments for investigating the flow modulation are covered secondly and split up similarly in Chapters 11 and 12.

Part IV synthesises the findings of this research. Chapter 13 shares an overarching discussion, correlating the direct force measurements and PIV results first, and subsequently scrutinising the theoretical framework. Finally, Chapter 14 answers the research questions, sums up the conclusions and gives recommendations for further research.

2

Wall-bounded turbulence

This chapter provides the reader with relevant background knowledge on wall-bounded turbulence, to which often is referred in the remainder of this report. Section 2.1 covers the basic fundamentals and introduces definitions and parameters. Section 2.2 highlights the flow structures that are of main importance. Finally, Section 2.3 shares analysis methods used in this thesis.

2.1. Skin friction and boundary layer fundamentals

Fluid flow experiences viscous effects in the vicinity of a bounding surface (from hereon referred to as wall). At the fluid-wall interface, the no-slip condition imposes a zero velocity on the fluid; moving away from the wall, the local velocity component increases and approaches the freestream velocity sufficiently far away from the wall. This region is called the boundary layer (BL) and the resulting velocity profile is referred to as the boundary layer profile. Definitions and equations in the remainder of this section are from White and Corfield (2006).

2.1.1. Boundary layer properties

The boundary layer can be described by a several mean properties, sometimes referred to as integral BL properties.

Boundary layer thickness

The boundary layer thickness (δ) is defined as the distance (y) from the wall where the streamwise flow velocity (u) is 99% of the freestream velocity (U_∞):

$$\delta = y|_{u/U_\infty=0.99}. \quad (2.1)$$

For turbulent flow over a flat plate, the boundary layer thickness can be approximated by a power-law expression:

$$\frac{\delta}{x} \approx \frac{0.16}{Re_x^{1/7}}, \quad (2.2)$$

with the Reynolds number Re_x defined as

$$Re_x = \frac{\rho U_\infty x}{\mu} = \frac{U_\infty x}{\nu}, \quad (2.3)$$

with density (ρ), dynamic viscosity (μ) and kinematic viscosity (ν), and where x is the streamwise location with respect to the start of the boundary layer, i.e. $\delta = 0$ at $x = 0$. Note that this power-law approximation holds for a zero-pressure-gradient (ZPG) turbulent boundary layer (TBL).

Displacement thickness

The displacement thickness (δ^*) is the theoretical distance that the wall has displaced as experienced by a particle in the freestream. It is defined as the integrated velocity deficit of the boundary layer:

$$\delta^* = \int_0^{\lim Y \rightarrow \infty} \left(1 - \frac{u}{U_\infty}\right) dy. \quad (2.4)$$

Momentum thickness

The momentum thickness (θ) is an indication of the momentum loss due to friction forces within the boundary layer. It can be interpreted as the theoretical thickness of a fluid layer in the freestream carrying the amount of momentum equal to that lost in the boundary layer. It is defined as the integrated momentum loss in the boundary layer:

$$\theta = \int_0^{\lim Y \rightarrow \infty} \frac{u}{U_\infty} \left(1 - \frac{u}{U_\infty}\right) dy. \quad (2.5)$$

The momentum thickness is sometimes used to scale the Reynolds number (Re_θ):

$$Re_\theta = \frac{U_\infty \theta}{\nu}. \quad (2.6)$$

For flow over a flat plate, the momentum thickness directly relates to the friction drag via:

$$C_f = 2 \frac{d\theta}{dx}. \quad (2.7)$$

Shape factor

The shape factor (H) is an indication for the shape of the boundary layer velocity profile and is often used to assess the stability of the boundary layer. It is defined as the ratio of the displacement thickness to the momentum thickness:

$$H = \frac{\delta^*}{\theta}. \quad (2.8)$$

In general, a higher value for H corresponds to a stronger adverse pressure gradient, $dp/dx > 0$, and a lower value to a favourable pressure gradient, $dp/dx < 0$. Typical boundary layers have known shapes and thus shape factors: $H = 2.59$ for a laminar (Blasius) profile and $H = 1.3 - 1.4$ for a turbulent profile.

2.1.2. Non-dimensional analysis

The flow velocity and wall distance can be non-dimensionalised to compare boundary layer profiles under different flow conditions. Since the region near the wall is dominated by friction (shearing) forces, 'inner scaling' is performed using the friction velocity (u_τ):

$$u_\tau = \sqrt{\frac{\tau_w}{\rho}}, \quad (2.9)$$

where τ_w is the wall shear stress. The non-dimensionalised flow velocity (u^+) and wall distance (y^+) (also called 'inner variables') are then defined as:

$$u^+ = \frac{u}{u_\tau}, \quad y^+ = \frac{y u_\tau}{\nu}. \quad (2.10a, 2.10b)$$

The superscript '+' denotes 'expressed in viscous units' (also called wall units). The physical length of such a wall unit, or the viscous unit length (δ_ν), is given by:

$$\delta_\nu = \frac{\nu}{u_\tau}. \quad (2.11)$$

The friction velocity, combined with the boundary layer thickness, can be used to define the friction Reynolds number (Re_τ):

$$Re_\tau = \frac{u_\tau \delta}{\nu}. \quad (2.12)$$

Further away from the wall, boundary layer profiles can also be described in physical units or made dimensionless with the boundary layer thickness (for distances) and freestream velocity (for velocities), called 'outer scaling'. The former is often denoted as η :

$$\eta = \frac{y}{\delta}. \quad (2.13)$$

2.1.3. Turbulent boundary layer regions

The boundary layer in turbulent flow is schematically visualised in Figure 2.1a and can be divided into two main regions: the inner layer and the outer layer. The flow within the inner layer mainly depends on conditions near the wall and is, sufficiently close to the wall, dominated by viscous effects, whereas in the outer layer it mainly depends on freestream conditions and is dominated by (inertial) turbulence effects. The two regions have different mathematical descriptions for the boundary layer profile, namely the "law of the wall" for the inner layer, and the "defect law" for the outer layer. The inner layer is often described with inner variables while the outer layer is described with outer variables. A third region, which partially overlaps both the inner and outer layer, can be established to mathematically match these two laws. This is called the overlap layer, where the "logarithmic law" applies.

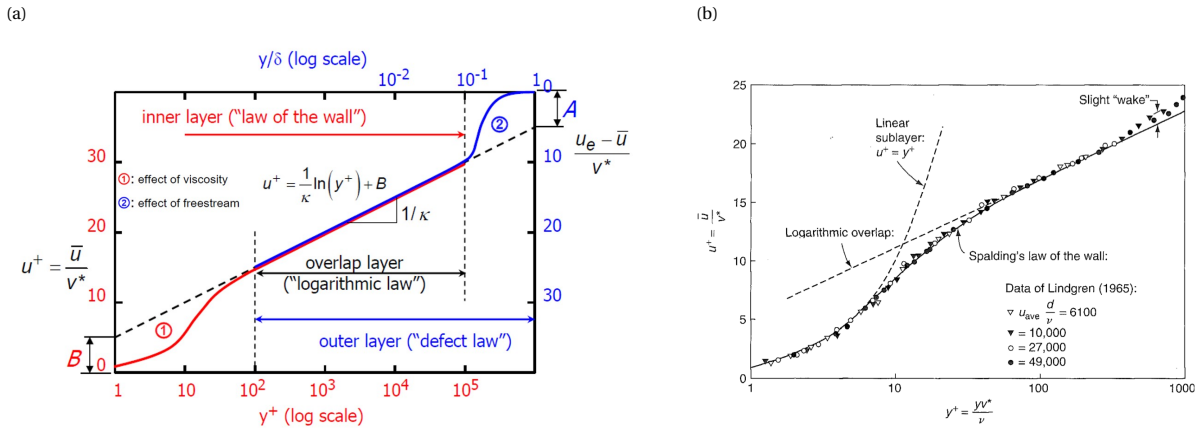


Figure 2.1: Regions within the boundary layer. (a) Schematic of full boundary layer (Van Oudheusden, 2020). (b) Inner layer, Spalding's law of the wall (White and Corfield, 2006).

Zooming in on the inner layer, three subregions can be distinguished. First, in immediate proximity to the wall, viscous effects are dominant and the velocity profile is linear, hence this region is called the viscous sublayer. Then, a "buffer layer" is present where the velocity profile smoothly transitions from linear to logarithmic, connecting the viscous sublayer to the third subregion in the inner layer: the overlap layer. Whereas the domains of the viscous sublayer and buffer layer can be expressed in inner variables only, the extent of the overlap layer also depends on the flow conditions in the outer layer, such as the freestream Reynolds number. The different regions within the inner layer and their corresponding wall-distance domains and mathematical descriptions can be summarised as follows:

$$\begin{array}{lll} 0 \leq y^+ \leq 5 & \text{Viscous sublayer} & u^+ = y^+ \\ 5 \leq y^+ \leq 30 & \text{Buffer layer} & \\ 30 \leq y^+ \leq 0.1\delta^+ & \text{Overlap layer} & u^+ = \frac{1}{\kappa} \ln y^+ + B \end{array}$$

where δ^+ is the boundary layer thickness expressed in wall units, κ is the von Kármán constant and B is also a constant. For canonical ZPG TBL, $\kappa \approx 0.39$ and $B \approx 5.0$ are often taken. Spalding has developed a single implicit expression that describes the boundary layer profile in the entire inner layer region, given in Equation (2.14). The empirical fit is valid up until $y^+ \approx 350$ (Figure 2.1b), depending on freestream conditions.

$$y^+ = u^+ + e^{-\kappa B} \left[e^{\kappa u^+} - 1 - \kappa u^+ - \frac{(\kappa u^+)^2}{2} - \frac{(\kappa u^+)^3}{6} \right] \quad (2.14)$$

The outer layer can be expressed using the defect law:

$$\frac{U_\infty - \bar{u}}{u_\tau} = g(\eta, \xi), \quad (2.15)$$

where ξ is the pressure-gradient parameter:

$$\xi = \frac{\delta}{\tau_w} \frac{dp_e}{dx}. \quad (2.16)$$

The deviation of the outer law w.r.t. the overlap law resembles a wave-like shape and is called the wake component. It can be added to the inner layer such that the entire velocity profile (excluding viscous sublayer) can be represented by a single expression:

$$u^+ \approx \frac{1}{\kappa} \ln y^+ + B + \frac{2\Pi}{\kappa} w(\eta), \quad (2.17)$$

where Π is the wake strength and $w(\eta)$ the wake function. Different forms of wake functions have been proposed in literature.

2.1.4. Skin friction drag

The total shear stress within a two-dimensional unsteady (turbulent) fluid consists of two components: the viscous stress and the Reynolds (turbulent) shear stress:

$$\tau = -\rho \overline{u'v'} + \mu \frac{du}{dy} \quad (2.18)$$

$$\text{Reynolds shear stress: } -\rho \overline{u'v'} \quad \text{Viscous stress: } \mu \frac{du}{dy} \quad (2.19a, 2.19b)$$

At the wall, the turbulent velocity fluctuations (u' and v') are zero, hence the wall shear stress (τ_w) or skin friction is dependent on the viscous stress only:

$$\tau_w = \mu \left. \frac{du}{dy} \right|_{y=0}. \quad (2.20)$$

Dividing the wall shear stress with the freestream dynamic pressure ($q = \frac{1}{2} \rho U_\infty^2$) yields the dimensionless skin friction coefficient (C_f), which can be used to compare friction characteristics of different surfaces in different flow conditions:

$$C_f = \frac{\tau_w}{\frac{1}{2} \rho U_\infty^2}. \quad (2.21)$$

Using the definition of the friction velocity (Equation (2.9)), the friction coefficient can be written as

$$C_f = 2 \left(\frac{u_\tau}{U_\infty} \right)^2. \quad (2.22)$$

For turbulent flow over a flat plate, the skin friction can be approximated by a power-law expression in a similar fashion as the boundary layer thickness:

$$C_f = \frac{0.027}{Re_x^{1/7}}. \quad (2.23)$$

The effect of the Reynolds shear stress on the friction is indirect. A higher value indicates more fluid mixing. Inside the boundary layer, this results in a higher fluid velocity near the wall, and consequently a higher velocity gradient and thus wall friction. The dependence of the turbulent skin friction drag on the viscous stress and the Reynolds shear stress shows the importance of studying the flow behaviour inside the boundary layer, and more specifically within the inner layer, near the wall.

2.2. Coherent structures

The seemingly chaotic nature of turbulent flow can be better understood through identification of so-called coherent structures. These are flow structures that are repeated throughout space and time. Several structures and their relationships have been defined, but cause and effect are often not well understood. This section deals with the near-wall cycle, which describes the flow behaviour near the wall in turbulent boundary layers, and with spanwise-coherent structures, specifically those related to Kelvin-Helmholtz-like (KH) instabilities (also called "rollers").

2.2.1. The near-wall cycle

Regular patterns near the wall of turbulent boundary layers occur at intervals of approximately $1,000\delta_v$, which is called the streamwise wavelength (λ_x) of the near-wall cycle. This cycle consists of several different events and structures which have mutual interactions and contribute to the shear stress. Figure 2.2 provides a schematic illustration of this process.

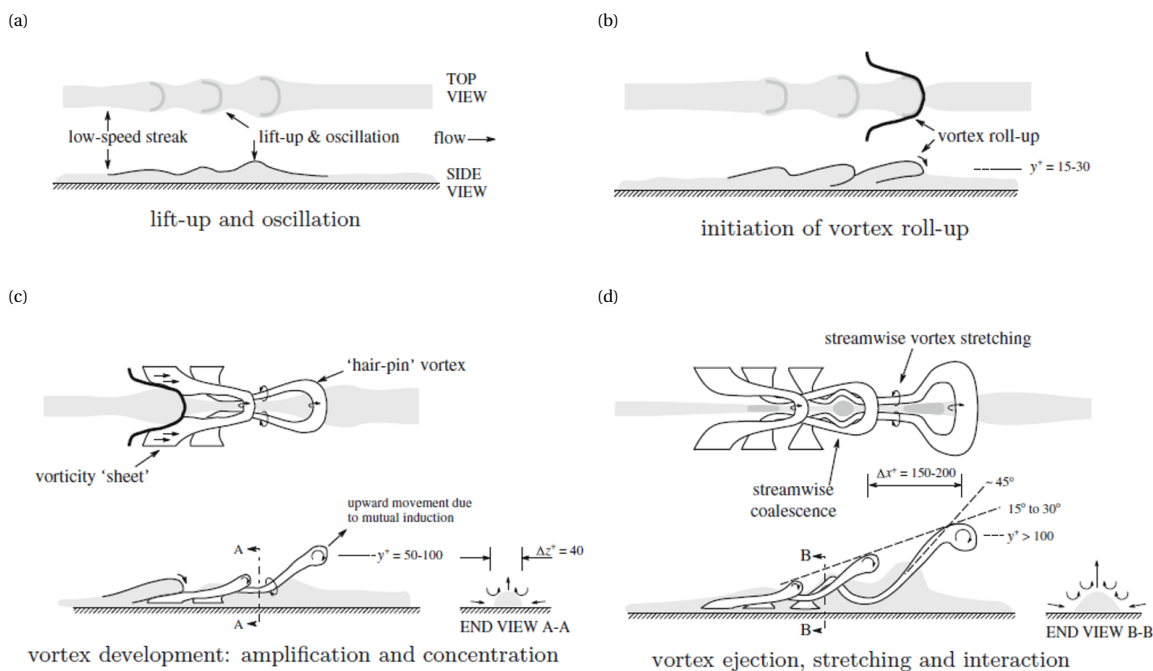


Figure 2.2: Visualisation of an instance of the near-wall cycle through the formation of hairpin vortices (Nieuwstadt et al., 2016). (a) Starting point: a perturbation of a low-speed streak and lift-off into buffer layer. (b) Growth and vortex roll-up due to instabilities. (c) Vortex development due to shear of overlying high-momentum flow and self-induced vortex motion. (d) Vortex ejection and stretching.

Low-speed streaks

The cycle starts with low-speed streaks in the buffer layer ($5 \leq y^+ \leq 30$). They arise due to local instabilities in the streamwise direction and form elongated pockets of low-momentum fluid spaced at regular intervals ($\lambda_x \approx 1,000$, $\delta z \approx 100$). These structures were one of the earliest to be identified and are a simple indicator of the turbulent state of the boundary layer (Kline et al., 1967; Smith and Metzler, 1983).

Burst, ejection, and sweep events

Due to the instabilities near the wall, streaks can lift from the surface and start to oscillate in the buffer layer (Figure 2.2a). If too unstable, these oscillations can lead to the breaking up of the uplifted streak into smaller structures, called burst events. The low-momentum fluid rolls up into a vortex filament in the spanwise direction (Figure 2.2b). Through a self-induced velocity field, this vortex can grow, stretch, and eventually lift away further from the wall (Figures 2.2c and 2.2d). This release of low-momentum fluid in higher layers of the boundary layer is called an ejection event. Simultaneously, high-momentum fluid from higher layers of the boundary layer approaches down towards the wall to replace the ejected low-speed streaks, called a sweep event. The bursting process (ejection and sweep events) are important contributors to the Reynolds stress and consequently friction drag.

Hairpin vortices and trains

The vortex-generation process of streak, burst, ejection, and sweep events shown in Figure 2.2 results in the formation of hairpin (or horseshoe) vortices. These structures form, as the low-momentum fluid in the form of rolled-up vortex filaments is brought away from the wall into higher momentum flow, which elongates the head of the vortex and pulls it further downstream. Consequently, the vortex legs induce an even stronger upward fluid motion, self-strengthening this cycle until it eventually breaks down. This process is also schematically depicted in Figure 2.3. Hairpin vortices often come together in streamwise aligned trains ('packets') along a virtual axis angled at $10 - 20^\circ$ (mean = 12°) with the wall surface (Adrian et al., 2000). Individual hairpins that are strong enough can create a new upstream hairpin by inducing low momentum fluid in the wall region. This starts a new instance of hairpin formation, and while the cycle continues, older hairpins grow and are lifted away from the surface along the inclined virtual axis.

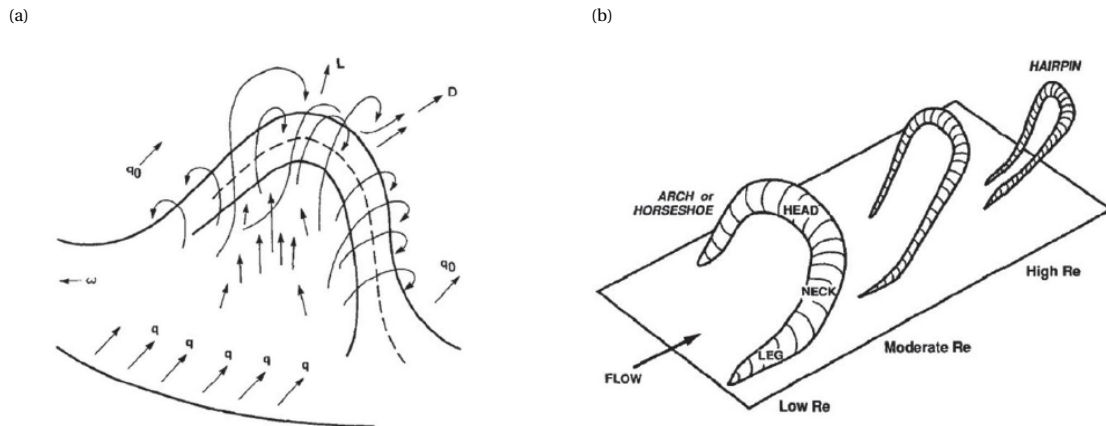


Figure 2.3: Hairpin vortex formation. (a) Theodorsen (1952). (b) Head and Bandyopadhyay (1981).

Quasi-streamwise vortices

Streamwise vortices were identified relatively early and found to be slightly tilted away from the wall ($3 - 7^\circ$), hence the name quasi-streamwise (QS) vortices (Kline et al., 1967). They occur in a large range of sizes ($d^+ \approx 5 - 110$ (Robinson, 1991)) but the majority is concentrated to buffer-layer sized vortices, with 73% within $d^+ \approx 10 - 40$ (Robinson, 1991) and an average of $\bar{d}^+ \approx 30$ (Kim et al., 1971; Blackwelder and Eckelmann, 1979; Kim et al., 1987). From Figures 2.2c and 2.2d they can be regarded as the legs of hairpin vortices (note the $\Delta z^+ = 40$). Since hairpin vortices constantly form and evolve, these legs trail behind each other, forming the QS-vortices. They occur at the interface between high-speed sweeps moving downwards, and low-speed ejections moving upwards. As previously mentioned, the cause-and-effect relation between QS-vortices and burst, ejection, and sweep events is unclear. Nevertheless, they form an important contribution to the Reynolds stress and friction drag. It is thought that riblets reduce turbulent skin friction by preventing the QS-vortices to reach the physical wall surface (Figure 2.4), effectively 'filtering out' turbulent activity (Bechert et al., 1986; Choi, 1989). This can be understood intuitively with the knowledge that effective riblets have a spanwise spacing and height of $s^+ & h^+ \approx 5 - 20$ respectively, which is smaller than the mean QS-vortex diameter (García-Mayoral and Jiménez, 2011a).

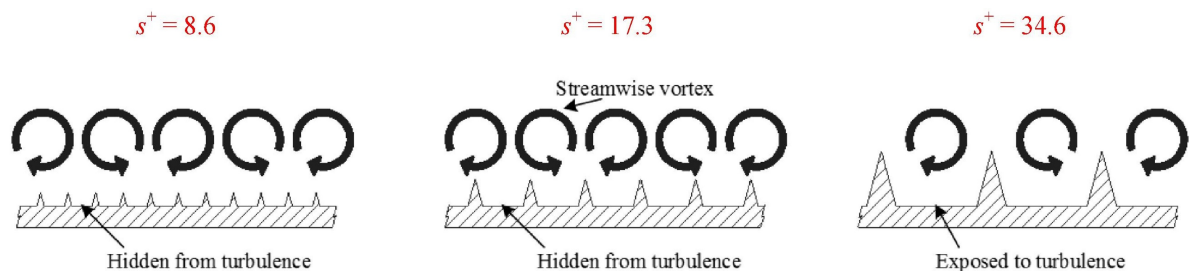


Figure 2.4: Schematic of QS-vortices above riblets of different sizes (Rowin et al., 2018).

2.2.2. Spanwise-coherent rollers

Spanwise-coherent rollers do not appear in canonical turbulent boundary layers over smooth walls, but are thought to play an important role at the surface-fluid interface of non-smooth surfaces, such as riblets or porous substrates. They are small, energetic vortices that 'roll' along the surface ($y^+ < 30$) in streamwise direction at regularly spaced streamwise intervals ($\lambda_x^+ \approx 100 - 200$) and extend over large widths ($\lambda_z^+ \approx 850$), hence the spanwise-coherence notation (see Figure 2.5). Their formation is linked to a Kelvin-Helmholtz-like (KH) instability. In smooth walls, the mean BL profile almost has an inflection point near the surface but remains stable due to the impermeability condition ($v = 0$). Once a surface allows for wall-normal transpiration ($v \neq 0$), the instability related to this inflection point reappears and can eventually result in rollers. This happens for riblets that are too large or porous substrates that have too large wall-normal permeability (further discussed in Sections 3.2 and 3.3.4). The formation of rollers contributes to the friction drag and is shown to cause the breakdown of the viscous (linear) part of the typical DR curve for riblets (García-Mayoral and Jiménez, 2011b).

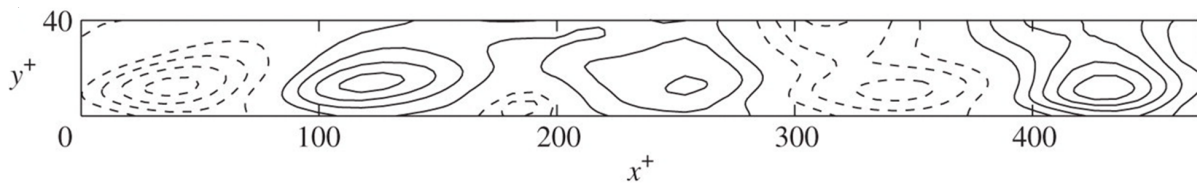


Figure 2.5: Identification of spanwise coherent rollers (García-Mayoral and Jiménez, 2011a). Instantaneous streamlines of the z -averaged perturbation $u - v$ flow, for $\ell_g^+ \approx 17$. $\ell_g = \sqrt{A_g}$, where A_g denotes the riblet groove area. Spanwise averaging domain of $L_z^+ \approx 850$. Solid lines correspond to clockwise-rotation rollers and the separation between streamlines is $1.3v$.

2.3. Analysis methods

Numerous methods exist for analysing turbulent boundary layers. This section covers those used in this thesis besides the already mentioned integral boundary layer and friction properties.

2.3.1. Boundary layer profiles and fitting

Boundary layer profiles show the values of parameters along the wall-normal direction. The most commonly assessed parameters are the streamwise mean velocity (u), streamwise and spanwise velocity fluctuations expressed as root mean square (u_{rms} & v_{rms}) and Reynolds stress ($-\overline{u'v'}$). The first indicates the mean state of the BL, the latter three indicate the degree of turbulence in the BL. Figure 2.6 shows an example based on DNS data from Schlatter and Örlü (2010).

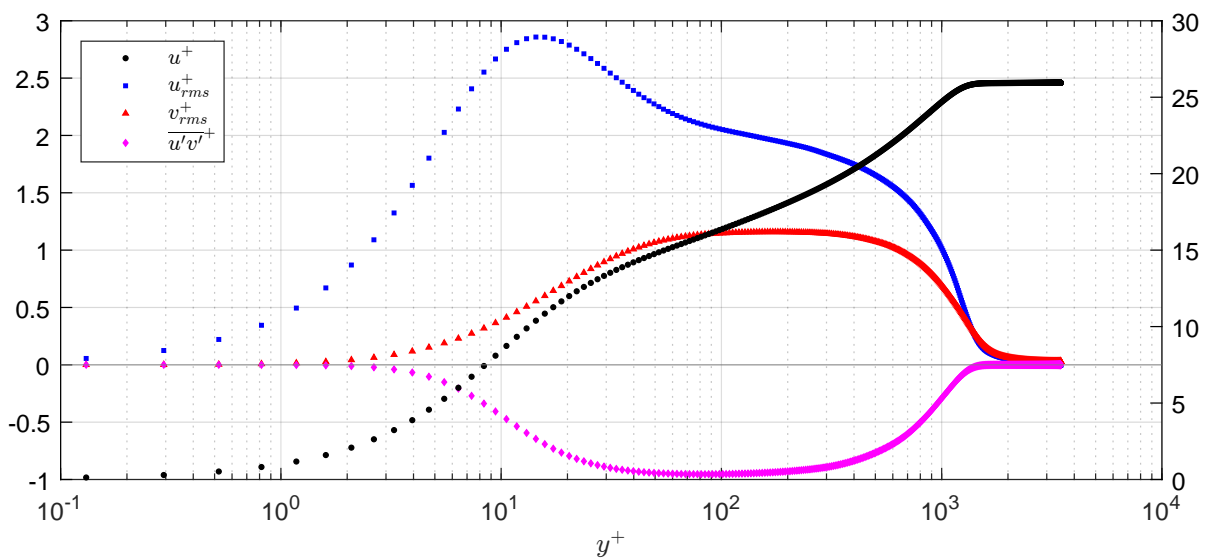


Figure 2.6: Example of boundary layer profiles. Left axis: u_{rms}^+ , v_{rms}^+ and $\overline{u'v'}$. Right axis: u^+ . $Re_\theta = 4,060$, data taken from Schlatter and Örlü (2010).

BL profiles can be plotted in inner variables (such as in Figure 2.6) or outer variables. For inner variables, an estimation of u_τ is required. There are different methods to do so: directly from linear interpolation in the viscous sublayer, the indirect method via the log-layer (Clauser's method), via Spalding's law of the wall, or by using any other method that optimises a fit based on an assumed (canonical) profile and different fitting parameters. A recently developed method by Rodríguez-López et al. (2015) fits to the entire BL profile based on all parameters of interest: δ , u_τ , κ , Π and dy , where dy allows for a wall-normal shift of the entire profile in case of uncertainty in the estimated wall location. In this method, B is not a fitting parameter but follows from the optimised fit.

2.3.2. Quadrant analysis

In quadrant analysis, turbulent events are divided into four quadrants according to the signs of the stream-wise and wall-normal velocity fluctuations. Their relative occurrence can be expressed with the joint probability density function (JPDF). Scatter plots (v' vs. u') are binned and subsequently the relative occurrence of each bin can be visualised via contour shading (Figure 2.7a). Their contribution to the Reynolds stress can be expressed with the weighted joint probability density function (WJPDF). The relative occurrence of each bin is multiplied by its bin coordinates (u' , v') (Figure 2.7b). Integration of the WJPDF leads to the total Reynolds shear stress within the BL:

$$-\overline{u'v'} = - \int_{-\infty}^{\infty} u'v'P(u',v') du' dv'. \quad (2.24)$$

An elegant method to visualise the relative contributions of different events to the Reynolds stress is via hole filter sampling. Data in the scatter plot is filtered via a hyperbola criterion (H) in each quadrant according to $|u'v'| \geq H|\overline{u'v'}|$ (see Figure 2.7c). Increasing H thus corresponds to keeping stronger events. The relative contributions of different events to the Reynolds stress can then be plotted against increasing H for each quadrant separately (Figure 2.7d). As such, turbulent events and their contribution to the Reynolds stress are broken down by type of event (quadrant) and strength (H). This shows quantitatively that the majority of the Reynolds stress is generated by ejection (Q2) and sweep (Q4) events.

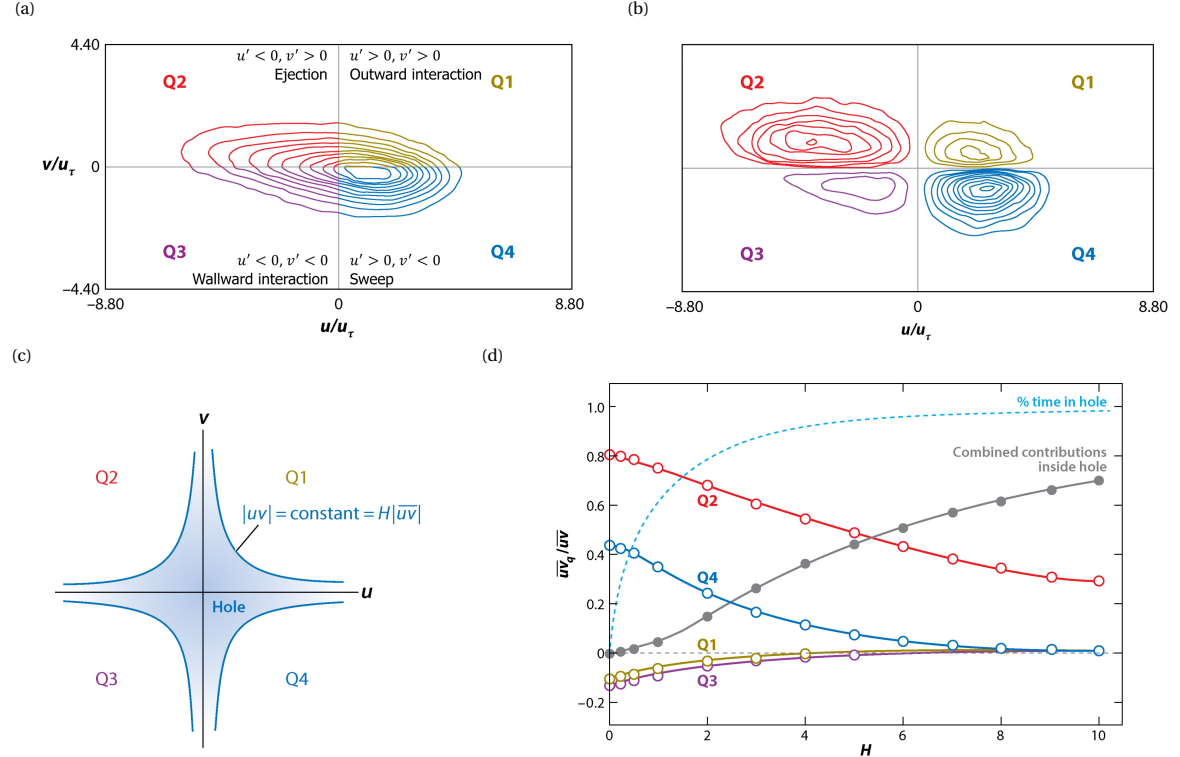


Figure 2.7: Example of quadrant analysis. JPDF (a) and WJPDF (b) at $y^+ = 45$, edited from Wallace and Brodkey (1977). (c, d) Hole filter sampling plots (Wallace, 2016).

2.3.3. Spectral analysis

Spectral analysis provides a quantitative assessment of the occurrence of certain turbulent structures within the boundary layer. Data obtained in the physical domain is expressed in the spectral domain (either as frequency or wavelength) via a Fourier transformation. This reveals the 'characteristic' structures as frequencies (f^+) or wavelengths (λ^+) with high signal energy. For turbulence, these peak regions correspond to the structures carrying the majority of the turbulent energy. The method has been used in research comparable to this study, both numerical and experimental, to identify the near-wall cycle and the occurrence of spanwise-coherent rollers. Figure 2.8 shows an example for riblets, visualising the near-wall cycle energy peak (dark shading towards $\lambda_x^+ \approx 1,000$) and the onset of spanwise coherent rollers (increasingly dark shading in the thin rectangle from left to right image).

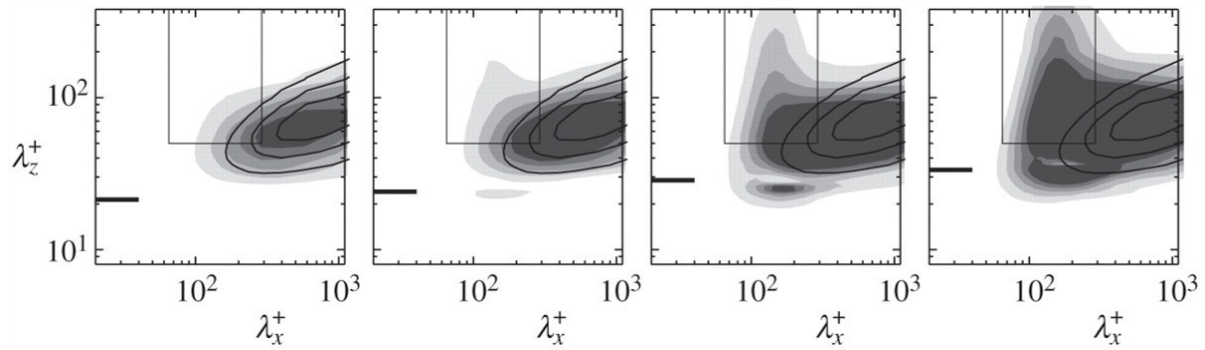


Figure 2.8: Premultiplied two-dimensional cospectra of the Reynolds shear stress at $y^+ \approx 4$ above the riblet tips (García-Mayoral and Jiménez, 2011a). Increasing riblet size from left to right, $\ell_g^+ \approx 13, 15, 17$ & 20 . Superimposed solid contour lines represent smooth-wall case. Thick horizontal line at the left of each plot marks the riblet spacing. Thin rectangle indicates region associated with spanwise coherent rollers.

This page has been intentionally left blank.

3

Anisotropic permeable substrates for turbulent friction reduction

Using anisotropic permeable substrates as a means of turbulent friction reduction is a novel academic topic. Recent studies have shown the potential of this concept, and a theoretical framework behind its working mechanism has been proposed by Gómez-de-Segura and García-Mayoral (2019). These studies formed the foundation of this experimental thesis. Therefore, this chapter dives deeper into the topic to give the reader a solid foundation for the rest of this report.

First, Section 3.1 covers the basics of flow modelling through porous media. Subsequently, Section 3.2 puts the novel topic of drag reduction through anisotropic permeable substrates in a broader perspective and sketches the history of research on turbulent flow over porous media in general. Section 3.3 explains the proposed drag reduction working mechanism, including the theoretical framework, elaboration on turbulent flow structures above the substrate and an assessment of the potential drag reduction. Finally, Section 3.4 summarises this chapter by presenting the main takeaways.

3.1. Flow modelling through porous media

A porous medium is a solid material that contains pores filled with fluid. The main parameter by which it usually is characterised is the porosity, which is a measure of the void spaces in the material:

$$\epsilon = \frac{V_V}{V_T}, \quad (3.1)$$

where V_V is the volume of void-space and V_T is the bulk volume of the material. It can be expressed as a fraction or percentage. For fluid flow, often the effective porosity is used, which is based on the amount of void-space accessible for fluid flow, changing the value of V_V in Equation (3.1). Another characteristic of interest is the (Darcy) permeability (\mathbf{K}). It is a measure of the ease with which fluids can pass through a porous medium and thus analogous to thermal conductivity. The permeability tensor is both symmetric and positive definite and therefore always diagonalisable. The eigenvectors will yield the principal directions of the flow. For perfectly isotropic materials, the permeability tensor reduces to a scalar. The permeability of a medium is dependent on porosity, but also other characteristics such as the pore shape, size and level of connectedness.

For fluid flow through porous media, the differences between the macroscopic scale (defined by the global size of the problem) and microscopic lengths (typically the pore or grain size of the porous medium) are usually large. There are two general approaches to treat this problem. The first approach is to perform a pore-scale numerical simulation of the flow throughout the medium. The geometry of the solid is closely reproduced, resembling an actual physical structure. This path has been followed by Kuwata and Suga (2016, 2017, 2019), for example. Such methods, unfortunately, come at a high computational cost. An additional disadvantage is that these simulations only provide a solution to a specific configuration of the porous medium.

The second approach is to conduct an effective macroscopic simulation without resolving the full microscopic structure. To do so, an auxiliary problem is introduced to characterise the pore-scale behaviour. It delivers a concise and rapid description of the fluid behaviour, which is satisfactory from a macroscopic point of view. This approach implicitly assumes that the coupled fluid-solid medium can be abstracted as a continuum for which an effective conductivity, permeability or viscosity can be defined. The method has been successfully used for studies into turbulent flow over porous substrates and will be further elaborated upon in this section.

3.1.1. Darcy's law and derivatives

One method to model the permeable behaviour without resolving the physical porous structure is via Darcy's law. It describes laminar, viscous (Stokes) flow through a porous medium and was deduced experimentally (Darcy, 1856). It essentially results from volume averaging the Stokes equation over many pores. The equation is a balance between the driving pressure gradient across a permeable medium on the one hand and the resistance to the flow exerted by the medium on the other hand:

$$\nabla p = -\nu \mathbf{K}^{-1} \mathbf{u}, \quad (3.2)$$

where p is the kinematic pressure. Volume averaging filters out diffusive effects that act over length scales larger than the averaging ones. If these effects are important, then a macroscopic diffusive term can be added, yielding Brinkman's equation (Brinkman, 1949):

$$\nabla p = -\nu \mathbf{K}^{-1} \mathbf{u} + \tilde{\nu} \nabla^2 \mathbf{u}, \quad (3.3)$$

where $\tilde{\nu}$ is the effective viscosity of the medium. For larger permeabilities and higher flow velocities inside the porous medium, but still within the laminar regime ($10 \lesssim Re_p \lesssim 375$), inertial effects also become important, resulting in form drag around the obstacles in the porous medium. These effects can be accounted for through addition of a Forchheimer term (Forchheimer, 1901):

$$\nabla p = -\nu \mathbf{K}^{-1} \mathbf{u} + \mathbf{B} |\mathbf{u}| \mathbf{u}, \quad (3.4)$$

where \mathbf{B} is the Forchheimer coefficient tensor. For porous media with length scales (L) similar to the molecular mean free path (λ) (hence $Kn = \frac{\lambda}{L} \approx 1$), slip effects between the fluid molecules and solid material play a role as well, giving rise to Knudsen friction. To illustrate: for airflow at ambient pressure and room temperature conditions, the molecular mean free path is 69 nm (Jennings, 1988). Porous media in the context of turbulent boundary layer research have had much larger characteristic length scales, and thus such effects did not need to be taken into account.

Different strategies have been developed over time to derive Equations (3.2) to (3.4) analytically. Deducing the macroscopic behaviour from a local description is called upscaling. It starts from a representative elementary volume (REV), from which an equivalent macroscopic continuous model is generated (homogenised model). One of the most used approaches is the Volume Averaging of the Navier-Stokes equations (VANS). This method is extensively described by Whitaker (1999). Another approach is the multiple-scale analysis, which is described by Mei and Vernescu (2010). The reader is referred to Davit et al. (2013) for an in-depth review of the topic.

3.1.2. Interface conditions

For studies into turbulent flow over porous media, not only the flow deep inside the substrate itself is relevant; also the interface between the substrate and the pure fluid flow is crucial in simulations. Three approaches to establishing interface conditions can be defined. The first approach involves pressure and velocities, which are linked over the interface directly, either via continuity or a jump. The jump condition by Beavers and Joseph (1967) is widely used, sometimes in a slightly adjusted form. They observed that the flow velocity penetrates to a depth proportional to the square root of the bed permeability (\sqrt{K}). The second approach involves the pressure and velocities indirectly, by linking the normal to the interface components of the stress tensor, such as done by Ochoa-Tapia and Whitaker (1995). The last approach is the use of a transition region towards the interface and applying a filter, e.g. shifting the porosity or permeability smoothly towards unity. A drawback is that there often is no general physical justification for the choice of filter (Zampogna and Bottaro, 2016). An overview of flow modelling and interface conditions approaches in studies on turbulent drag reduction by means of anisotropic permeability is given in Table 3.1.

Table 3.1: Approaches to porous medium flow modelling and interface conditions in studies on turbulent drag reduction by means of anisotropic permeability.

Study	Modelling in substrate	Interface conditions
Rosti et al. (2018)	Own derivation of the VANS equations.	Pressure and velocity continuity, jump in shear stress.
Gómez-de-Segura and García-Mayoral (2019)	Brinkman's equation, solved analytically. Assume infinitely small pores, such that continuum assumption holds up to interface.	Solution to Brinkman's equation form boundary conditions for free flow at interface, implicitly coupling velocity and pressure at the interface.
Li et al. (2020)	VANS equations, including Brinkman-Forchheimer terms.	Transition region applied where porosity shifts smoothly from its value to unity in the fluid domain

3.2. Historical overview

This section aims to give a complete historical overview of studies on turbulence over porous media. The storyline is roughly chronological, and split up into five subsections: experimental studies over porous walls, DNS studies over porous walls, the first efforts on anisotropic permeable substrates, the development of a theoretical framework and an assessment of the current status.

3.2.1. The beginning: experimental studies over porous walls

Beavers and Joseph (1967) performed one of the first studies into boundary layer behaviour over a permeable wall. They found a reduction in friction factor as a result of the permeable wall when the flow was laminar. In the following two decades, several experimental studies into turbulent flow over porous surfaces were conducted. There was a general consensus that for turbulent flow, in contrast to laminar flow, porous surfaces increase the friction factor (Lovera and Kennedy, 1969; Ruff and Gelhar, 1972; Ho and Gelhar, 1973; Zagni and Smith, 1976; Kong and Schetz, 1982; Zippe and Graf, 1983; Shimizu et al., 1990). Zagni and Smith (1976) investigated 20 different porous beds and attributed the increase in the friction factor to additional energy dissipation caused by an exchange of momentum across the channel-substrate interface. More details into the velocity profiles above the permeable surfaces were provided by the studies of Kong and Schetz (1982) and Zippe and Graf (1983), who found that velocity profiles over permeable substrates were more turbulent than over impermeable walls and that the logarithmic region of the wall law was shifted downwards, hence increasing the friction factor. Moreover, Kong and Schetz (1982) performed a direct comparison between permeable and impermeable surfaces with equivalent surface roughness, and found this increase in friction due to permeability to be an effect acting separately from, and in addition to, the surface roughness effect. Also interesting was the study by Shimizu et al. (1990), who, instead of above, looked within the porous bed, which was composed of glass beads. Using a tracer method, they found relatively large velocity gradients underneath the channel-substrate interface. It took a while before new experimental studies quite literally 'shed light' on the flow behaviour near the interface to a certain degree. Both Pokrajac and Manes (2009) and Suga et al. (2010) applied Particle Image Velocimetry (PIV) measurements which revealed that increasing permeability enhances turbulent fluctuations in the wall-normal velocity component. These newer studies provided further support for the earlier observations of Zagni and Smith (1976) that due to the permeability, momentum flux and hence the Reynolds stress was enhanced near the interface. A thorough understanding of the turbulent structures over porous surfaces, however, remained a question unanswered by experiments.

3.2.2. DNS studies over porous walls

The rise of computing power since the earlier 2000s accelerated the use of Direct Numerical Simulations (DNS) for investigating turbulent flow phenomena, also over porous walls. Breugem et al. (2006) did so by modelling the flow inside the porous wall as a continuum via volume-averaged Navier-Stokes (VANS) as described by Whitaker (1999), and then coupled this to the flow over the wall at the wall-channel interface. They found that above a highly permeable wall, no low- and high-speed streaks and quasi-streamwise vortices are present. The turbulence was dominated by relatively large vortical structures, which enhanced the exchange of momentum between the top layer of the porous medium and channel, resulting in a much higher Reynolds-shear stress and hence higher skin friction. These findings regarding momentum exchange and

increased skin friction are in accordance with prior experimental research. They thought these vortical structures to be of a Kelvin-Helmholtz (KH) type but had no direct evidence for this. The turbulence phenomena around and inside the porous layers could not be precisely reproduced, since their simulations included a model of the drag term and neglected the effect of dispersion. Furthermore, they assumed that permeability was a function of porosity, which is not necessarily the case as later research was able to show. Nevertheless, the work by Breugem et al. (2006) remains one of the most cited articles on this topic and can be considered an important milestone in understanding the turbulent phenomenon over porous walls.

Nearly a decade later, Rosti et al. (2015) also performed simulations by modelling the flow inside the porous wall as a continuum. In contrast to Breugem et al. (2006) however, they decoupled the effects of porosity and permeability. They also varied the porous wall thickness and a coefficient describing the momentum-transfer conditions at the channel-wall interface, which accounts for the effects of machining the interface would it have been an actual porous wall. From this parameter study, permeability emerged as the key parameter in determining the response of the channel flow to the porous wall, even at low permeabilities. The momentum-transfer coefficient was noticeably important too and mentioned to be also related to the porosity of the material.

3.2.3. First efforts on anisotropic permeable substrates

An even more detailed account of the turbulent behaviour over porous walls was given by a research group at the Department of Mechanical Engineering at Osaka Prefecture University in Japan (Kuwata and Suga, 2016, 2017; Suga et al., 2017, 2018). While experimental studies had been performed earlier (Suga et al., 2010), it was their use of the computationally much faster Lattice Boltzmann-based DNS method that enabled them to solve for the entire domain, including the porous structure, directly. They first used this to perform a 1-on-1 comparison between a porous layer and an equivalent rough wall (Kuwata and Suga, 2016). Using two-point auto-correlation, one-dimensional energy spectrum and proper orthogonal decomposition (POD) analyses, they proved the hypotheses from Breugem et al. (2006) by finding the influence of KH-instabilities to become more significant over the porous layer compared to the rough wall. These observations were also found experimentally, through PIV studies by Suga et al. (2017). Herein, three kinds of foamed ceramics with the same porosities but different permeabilities were tested. Again via two-point autocorrelation, they found that over the porous layer, much larger spanwise length scales were present. They considered these to be transverse roll cells as a result of KH-instabilities.

Kuwata and Suga (2017) continued the work of full DNS but applied to anisotropic permeable substrates. Their substrates were anisotropic in the sense that in the different investigated cases, they blocked out specific flow directions in the substrate completely. They took a porous wall with only wall-normal permeability as their baseline. From this view, they found that spanwise and especially streamwise permeability resulted in the development of KH-vortices, while the porous wall with only vertical permeability almost behaved like a smooth wall. Hence they suggested that the remarkable enhancement of turbulence could be attributed to streamwise permeability. They even mentioned that the impact of anisotropic permeability on turbulence might be in contrast to that of anisotropic rough walls, where spanwise roughnesses, such as riblets, were shown to reduce drag. Again they provided experimental support for their findings (Suga et al., 2018). The turbulence strength depended on the streamwise permeability rather than the wall-normal permeability, in the case when the wall-normal permeability is larger than the streamwise permeability. For these two studies, it is important to note that their starting point, namely considering a substrate with wall-normal permeability only, might have influenced the way they viewed their results. Would they have performed similar studies with only streamwise permeability as a baseline, and then increased the wall-normal permeability, they might have reached the opposite conclusion. Therefore, their suggestion that the impact of anisotropic permeability on turbulence may be in contrast to that of anisotropic rough walls is a highly questionable statement.

3.2.4. Development of a theoretical framework

More or less simultaneously with the efforts from Kuwata and Suga, a research group at the Department of Engineering at the University of Cambridge also studied turbulent flow over anisotropic permeable substrates, but with a completely different approach (Abderrahaman-Elena and García-Mayoral, 2017; Gómez-de-Segura et al., 2018a,b; García-Mayoral et al., 2019; Gómez-de-Segura and García-Mayoral, 2019). They explored the possibility of using anisotropic surfaces to reduce turbulent skin friction drag by promoting slip such as riblets or superhydrophobic surfaces do. As such, their hypothesis was opposite to the one suggested by Kuwata and Suga (2017) and Suga et al. (2018). This proposal was laid out by Abderrahaman-Elena and García-Mayoral (2017) and aimed particularly at external-flow applications.

Connecting anisotropic permeable surfaces to the idea of slip was not a new idea and had already been done fifteen years earlier by Jimenez et al. (2001) and Hahn et al. (2002). Jimenez et al. (2001) imposed non-slip conditions for the streamwise and spanwise velocities and set the wall-normal velocity to be proportional to the local pressure fluctuations, effectively only allowing wall-normal permeability, and found an increase in friction of 40%. Hahn et al. (2002) in turn set the wall-normal velocity to zero, allowing slip only in streamwise and/or spanwise direction. They found that streamwise slip is beneficial for drag reduction, while spanwise slip is deleterious. Abderrahaman-Elena and García-Mayoral (2017) acknowledged the importance of these findings but argued that real materials cannot be permeable solely in certain directions, only that they could have a preferential direction with higher permeability. Interestingly, they pointed out the seal fur as an example of such a material and explicitly referred to the study by Itoh et al. (2006) and the found drag reduction. Consequently, their efforts focused on developing a theoretical framework to predict the drag reduction potential of anisotropic permeable substrates by connecting material permeability to slip in all three directions. Up until then, it was commonly accepted that permeable substrates resulted in a drag increase because of the appearance of KH-like rollers (Jimenez et al., 2001; Breugem et al., 2006; Rosti et al., 2015; Kuwata and Suga, 2016). The results from Jimenez et al. (2001) suggested that the wall-normal permeability was the main driver of these spanwise coherent structures. Therefore, Abderrahaman-Elena and García-Mayoral (2017) also included the prediction of the onset of these drag-degrading mechanisms in their theoretical framework utilising linear stability analyses. They focused on highly connected materials, such as the one shown on the left in Figure 3.1, arguing that these offered better properties for drag reduction.

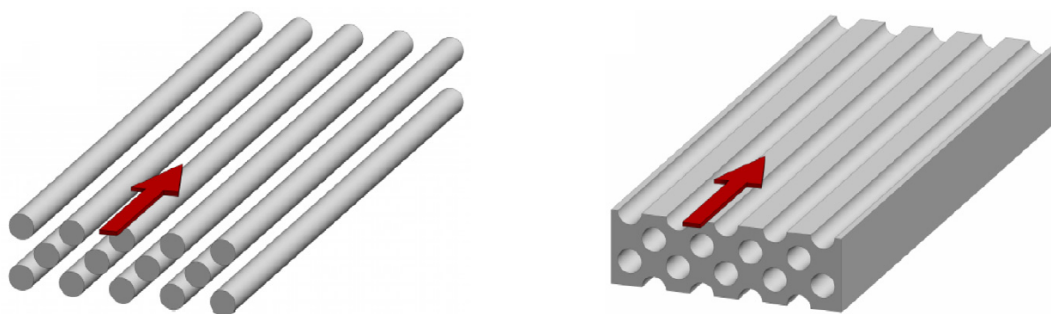


Figure 3.1: Difference between (left) a highly connected material which allows for propagation of diffusion effects, and (right) a poorly connected material, where no diffusive effects take place due to the disconnected pores (Gómez-de-Segura and García-Mayoral, 2019). Red arrow indicates the mean flow direction.

The first results were promising, showing a drag reduction of $O(10\%)$. Throughout several follow-up studies (Abderrahaman-Elena and García-Mayoral, 2017; Gómez-de-Segura et al., 2018a,b; García-Mayoral et al., 2019; Gómez-de-Segura and García-Mayoral, 2019), they further refined the different components of the framework employing DNS. Their findings were promising from a drag-reduction perspective, and in line with their prior expectations. Gómez-de-Segura and García-Mayoral (2019) found that streamwise-preferential anisotropic permeable substrates could reduce drag up to 25%. They concluded that the ratio between streamwise and spanwise permeabilities was the governing parameter dictating this drag reduction, indicating the resemblance with riblets and superhydrophobic surfaces. As they had anticipated, the breakdown of this regime was governed by the wall-normal permeability. Congruent with a lot of prior findings, both numerically and experimentally, they also attributed this breakdown to the spanwise-coherent structures associated with a KH-like instability. Although the theoretical framework was first proposed by

Abderrahaman-Elena and García-Mayoral (2017), it was fully worked out in subsequent studies, building up to a final publication by Gómez-de-Segura and García-Mayoral (2019) with an extensive set of results. Therefore in the remainder of this report, when discussing the concept and theoretical framework, Gómez-de-Segura and García-Mayoral (2019) will be referenced.

3.2.5. The current status

The theoretical framework and findings on drag reduction through anisotropic permeable substrates by Gómez-de-Segura and García-Mayoral (2019) currently seem to be the most elaborate in the field. Although their modelling approach using slip lengths does not allow for a detailed analysis of the turbulent structures under the substrate-channel interface such as the work of Kuwata and Suga (2016, 2017), they do provide the most comprehensive view on the working mechanism of the drag reduction. In fact, only two other studies explicitly mention the drag reduction potential of anisotropic permeable substrates (Rosti et al., 2018; Li et al., 2020). Rosti et al. (2018) considered equal streamwise and spanwise permeability (referred to as tangential permeability in their work), and only vary the tangential to normal permeability. For tangential-preferential permeability, a 20% drag reduction is obtained. They mention that the drag reduction does not seem to saturate in the range of anisotropy ratios considered. It should be noted however that in their tangential-preferential permeable cases, the wall-normal permeability was very low, rendering it in the same category as the work from Hahn et al. (2002), and hence it can be seen as a non-realistic permeable substrate. Li et al. (2020) did consider streamwise-preferential substrates and also achieved a drag reduction of 20%, albeit for shallow substrates.

The lack of experimental studies best captures the status quo on research into drag reduction through anisotropic permeable substrates. Although the drag increase over porous media in general has been proven both numerically and experimentally, the drag reduction over streamwise-preferential permeable substrates has not been shown experimentally. The work by Efstathiou and Luhar (2020) has been the only attempt, albeit with limited success. Their 3D-printed porous lattices had a too high wall-normal permeability to test the drag reduction hypothesis and small increases in friction were deduced from PIV measurements. They did observe an energetic footprint of spanwise-coherent structures linked to a KH-like instability, as well as a streamwise slip length related to the substrates streamwise permeability as predicted via the theoretical framework. Moreover, only a very limited amount of suggestions have been given for how such a substrate could be made or even should look like in practice. Gómez-de-Segura and García-Mayoral (2019) mention the seal fur of Itoh et al. (2006) as a possible implementation, Rosti et al. (2018) imagine a grid of rods parallel to the streamwise and spanwise directions and Suga et al. (2018) did experiments with anisotropic permeable substrates using polymer nets, albeit not being streamwise preferential. From the findings up until now however, it can be inferred that both the anisotropy ratios and the absolute values of the permeabilities are relevant and that consequently, the design of such substrates is not a trivial task.

The importance of the anisotropic permeability effects is also explicitly mentioned in the latest study of Kuwata and Suga (2019), who acknowledge that their chosen parameter for the flow characterisation - Re_K , based on the mean of the streamwise, spanwise and wall-normal permeabilities - might not be the most suitable one because of the anisotropic nature of the substrates investigated. Although their insights into the actual turbulent structures in and over porous substrates in general have been highly valuable (Kuwata and Suga, 2016; Suga et al., 2017), this provides further support for the doubts raised on their interpretation of the impact of anisotropic permeability on turbulence (Kuwata and Suga, 2017; Suga et al., 2018).

3.3. Drag reduction working mechanism

The previous section gave a broader understanding of the research field through a historical overview. This section provides a deep dive into the hypothesised drag reduction working mechanism. It first explains the rationale behind the theoretical model, split up according to its different components in Sections 3.3.1 to 3.3.4. Then, Section 3.3.5 discusses the drag reduction results obtained in DNS studies, and subsequently shares a verification of the proposed theoretical model based on these results.

3.3.1. The effect of small surface manipulations on turbulent drag

According to the classical theory of wall-bounded turbulence, the only noticeable effect of surface manipulations on the flow sufficiently far away from the wall is to modify the intercept of the logarithmic law, while both the von Kármán constant and wake function remain unaltered (Clauser, 1956). Hence, the freestream velocity in the logarithmic area can be written as

$$U^+ = \frac{1}{\kappa} \log y^+ + B + \Delta U^+ = U_0^+ + \Delta U^+, \quad (3.5)$$

where the subscript '0' in the expression U_0^+ indicates a reference smooth channel. This shift is visualised for an anisotropic permeable substrate in Figure 3.2.

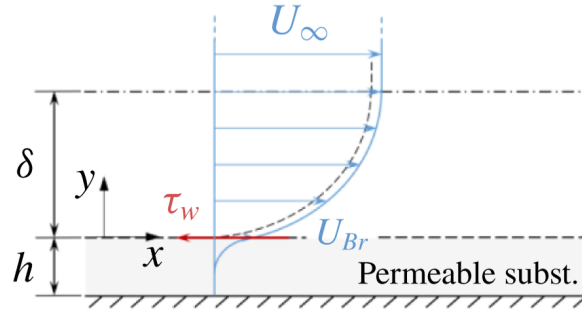


Figure 3.2: Mean velocity profile for an anisotropic permeable substrate (Gómez-de-Segura and García-Mayoral, 2019). The black-dashed line represents the smooth wall case.

Equation (2.22) can be rewritten in terms of the freestream velocity expressed in viscous units only:

$$C_f = 2 \left(\frac{U_\tau}{U_\infty} \right)^2 = \frac{2}{(U_\infty^+)^2}. \quad (3.6)$$

Hence, the drag reduction can be expressed in terms of the change in the intercept of the velocity profile:

$$DR = -\frac{C_f - C_{f,0}}{C_{f,0}} = 1 - \frac{1}{(1 + \Delta U^+ / U_0^+)^2}. \quad (3.7)$$

From these relationships, one can infer that if $\Delta U^+ > 0$, the logarithmic region is shifted upwards and drag is reduced, while the opposite is true if $\Delta U^+ < 0$. The reason for using ΔU^+ as a measure of drag reduction is because it fully captures the surface effect while being independent of Re_τ (Gatti and Quadrio, 2016). Hence, for a given surface texture with fixed viscous units, ΔU^+ remains the same, and consequently, results can be compared across different flow conditions (García-Mayoral and Jiménez, 2011a; García-Mayoral et al., 2019). To illustrate this benefit, Figure 3.3 shows the logarithmic dependence of the drag reduction on Re_τ (through the term U_0^+). When directly reviewing drag reduction results from numerical studies (often conducted at lower Re_τ), one should keep in mind that these do not translate directly to industrial applications (often with higher Re_τ), making comparisons between studies more cumbersome.

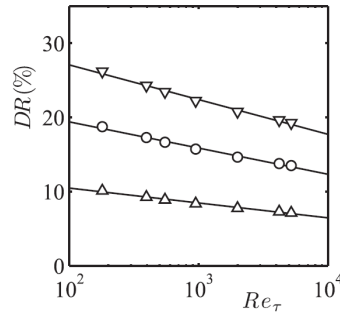


Figure 3.3: Dependence of drag reduction on Reynolds number for constant ΔU^+ according to Equation (3.7) (García-Mayoral et al., 2019). Δ , $\Delta U^+ = 1$; \circ , $\Delta U^+ = 2$; ∇ , $\Delta U^+ = 3$.

3.3.2. Virtual origins and slip lengths

Building on three decades of prior knowledge, García-Mayoral et al. (2019) postulated that the drag reduction mechanism of non-smooth surfaces with small characteristic length scales, such as riblets, superhydrophobic surfaces and anisotropic permeable substrates, is the result of a virtual-origin effect. The decrease in drag relies on the difference between the virtual origins of the mean flow and overlying turbulence, i.e. the turbulence is 'pushed away' from the virtual wall perceived by the mean flow.

The concept of a virtual origin for the mean flow was already proposed for riblets by Bechert and Bartenwerfer (1989), who called it the protrusion height (ℓ_u), and defined it as the depth below the riblet tips where the mean velocity would be zero, hence forming the 'virtual' origin of the velocity profile. Since the velocity profile in the viscous sublayer near a wall is essentially linear, this concept can be expressed through a Navier slip condition, $u = \ell_u \partial u / \partial y$, where u denotes the slip velocity. Another common name for ℓ_u is the slip length, which is used in the context of superhydrophobic surfaces. Luchini et al. (1991) further expanded this concept by proposing a spanwise protrusion height (ℓ_w) as well, which would resemble the virtual origin perceived by the quasi-streamwise vortices. They argued that the drag reduction in riblets was the result of the different virtual origins for the mean flow and the turbulent fluctuations, especially the quasi-streamwise vortices of the near-wall cycle. If these vortices experience a virtual origin less deep than the mean flow does, they are effectively pushed away from the 'virtual wall' for the mean flow. By including a spanwise slip length, they could express the riblet drag reduction as $\Delta U^+ = \ell_u^+ - \ell_w^+$. Later, this expression was refined to $\Delta U^+ \propto \ell_u^+ - \ell_w^+$ with a proportionality constant between 0.6 and 1 (Jiménez, 1994; Luchini, 1996; Bechert et al., 1997; Luchini, 2015).

Different studies, however, found that the given relationship did not always hold, because the adverse effect of ℓ_w^+ on ΔU^+ saturates for larger values of ℓ_w^+ (Min and Kim, 2004; Busse and Sandham, 2012). Gómez-de-Segura et al. (2018a) found that this was the result of the impermeability condition on the wall-normal velocity at the interface, $v = 0$, effectively impeding the displacement of quasi-streamwise vortices further towards the surface. They proposed including a virtual origin for the wall-normal velocity (ℓ_v^+) as well and found the most successful method being the implementation of a Robin boundary condition, similar to the approach for ℓ_u^+ and ℓ_w^+ . This has the consequence that the virtual origin for the turbulence, or the quasi-streamwise vortices, as ℓ_T^+ and $\ell_{\omega_x}^+$ are used interchangeably in the literature, is a function of both ℓ_v^+ and ℓ_w^+ . Gómez-de-Segura et al. (2018a) thus generalised the earlier found proportionality to

$$\Delta U^+ \propto (\ell_u^+ - \ell_{\omega_x}^+). \quad (3.8)$$

This general case is visualised in Figure 3.4. Three specific cases exist for defining the virtual origin of the turbulence ($\ell_{\omega_x}^+$), which are outlined in Table 3.2. Note that from hereon, the streamwise, spanwise and wall-normal slip lengths are denoted as $\ell_u = \ell_x$, $\ell_w = \ell_z$ and $\ell_v = \ell_y$ respectively. Overall, the results from Gómez-de-Segura et al. (2018a) suggest that $\ell_{\omega_x}^+$ is determined by the smallest origin between ℓ_y^+ and ℓ_z^+ , i.e. the one that is more restrictive on the cross-flow induced by the vortices. The first case, $\ell_y^+ = \ell_z^+$, yields the original relationship from Jiménez (1994). The second case, $\ell_y^+ < \ell_z^+$, is based on an empirical fit to the results for zero wall-normal permeability, obtained by Busse and Sandham (2012). The third case, $\ell_y^+ > \ell_z^+$, is based on the work from Choi et al. (1994), from which it appears that the origin of vortices is governed by that of the shallowest of ℓ_y^+ and ℓ_z^+ . However, Gómez-de-Segura et al. (2018a) explicitly stresses the necessity of further investigation on this conclusion. When linking virtual origins to permeability, they assume substrates with equal spanwise and wall-normal permeabilities and apply the first case laid out in Table 3.2:

$$\Delta U^+ \propto (\ell_x^+ - \ell_z^+). \quad (3.9)$$

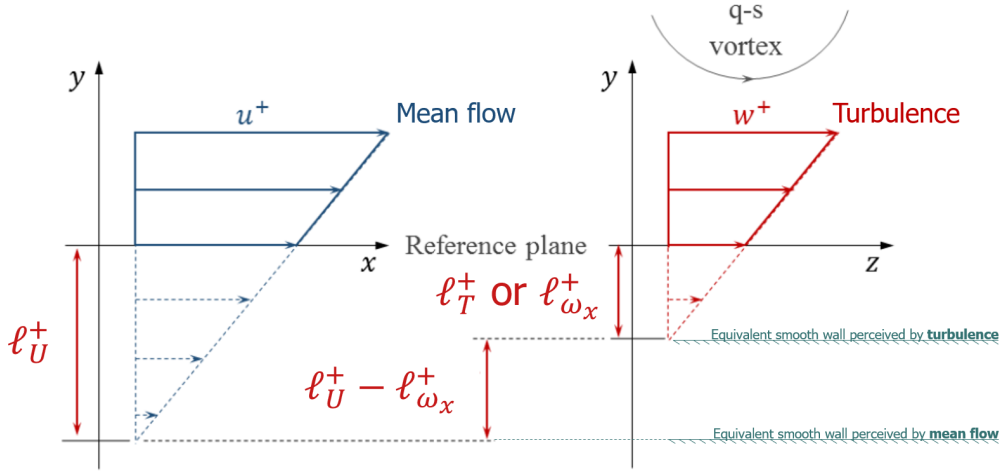


Figure 3.4: Schematic representation of streamwise and spanwise slip lengths, edited from Gómez-de-Segura and García-Mayoral (2019).

Table 3.2: Cases for defining the virtual origin of the turbulence ($\ell_{\omega_x}^+$).

Case	Virtual origin turbulence	DR relationship
$\ell_v^+ = \ell_w^+$	$\ell_{\omega_x}^+ = \ell_z^+$	$\Delta U^+ \propto (\ell_x^+ - \ell_z^+)$
$\ell_v^+ < \ell_w^+$	$\ell_{\omega_x}^+ = \ell_y^+ + \frac{(\ell_z^+ - \ell_y^+)}{1 + (\ell_z^+ - \ell_y^+)/4}$	$\Delta U^+ \propto (\ell_x^+ - \ell_y^+) - \frac{(\ell_z^+ - \ell_y^+)}{1 + (\ell_z^+ - \ell_y^+)/4}$
$\ell_v^+ > \ell_w^+$	$\ell_{\omega_x}^+ = \ell_z^+$	$\Delta U^+ \propto (\ell_x^+ - \ell_z^+)$

3.3.3. The connection between permeability and virtual origins

The work of Abderrahaman-Elena and García-Mayoral (2017) was the first to link permeability and virtual origins, such that the slip theory could be applied to anisotropic permeable substrates, which were assumed to have equal spanwise and wall-normal permeability. The authors derived expressions for ℓ_x^+ and ℓ_z^+ by solving Brinkman's equation analytically, in response to an overlying homogeneous shear:

$$\ell_x^+ = \xi \sqrt{K_x^+} \tanh\left(\frac{h^+}{\sqrt{K_x^+}}\right), \quad \ell_z^+ = \xi \sqrt{K_z^+} \tanh\left(\frac{h^+}{\sqrt{K_z^+}}\right), \quad (3.10a, 3.10b)$$

where $\xi = \sqrt{\nu/\bar{\nu}}$. They further simplify this expression by assuming highly connected substrates, $\xi \approx 1$, which are thought to be more relevant for drag reduction purposes, and deep substrates, $h^+ > \sqrt{K_x^+}$ and $h^+ > \sqrt{K_z^+}$. Consequently, the slip lengths can be expressed as

$$\ell_x^+ = \sqrt{K_x^+}, \quad \ell_z^+ = \sqrt{K_z^+}, \quad (3.11a, 3.11b)$$

and thus the drag reduction relation becomes

$$\Delta U^+ \propto \left(\sqrt{K_x^+} - \sqrt{K_z^+}\right). \quad (3.12)$$

The provided expression neglects the effect of pressure drag within the substrate. Abderrahaman-Elena and García-Mayoral (2017) argue that this effect is negligible in most industrial applications, especially in external flows such as aircraft fuselages. With a mild to zero pressure gradient, the flow near the substrate interface is driven by overlying shear and the effect of the mean pressure gradient within the substrate is negligible. Furthermore, with an expected substrate thickness of $h \sim O(100\mu m)$ - for comparison, the paint thickness is of $O(300\mu m)$ - the size and shape of the fuselage would not significantly change.

3.3.4. Drag degradation effects due to permeability

Equation (3.12) suggests an unbounded drag reduction potential in a linear regime, dependent on only the spanwise and streamwise permeabilities. However, based on common knowledge of spanwise coherent turbulent structures over porous materials in general, Gómez-de-Segura et al. (2018b) made efforts to bound the design space of anisotropic permeable substrates a priori. Through linear stability analysis, similar to the work performed by García-Mayoral and Jiménez (2011b) on riblets, they predicted the onset of KH-like instabilities based on the effect of substrate topology on amplification of instability. An empirically fitted parameter (K_{Br}^+) was proposed to capture this effect:

$$K_{Br}^+ = K_y^+ \tanh\left(\frac{\sqrt{2K_x^+}}{9}\right) \tanh^2\left(\frac{h^+}{\sqrt{12K_y^+}}\right). \quad (3.13)$$

Again, under the assumption of deep substrates, $h^+ > \sqrt{K_x^+}$, and a high streamwise permeability, $\sqrt{K_x^+} > 5$, this simplifies to

$$K_{Br}^+ \approx K_y^+, \quad (3.14)$$

revealing that the wall-normal permeability is the governing parameter for the onset of these instabilities, which is in accordance with earlier work (Jimenez et al., 2001). Figure 3.5 shows the amplification of the most unstable modes as function of $\sqrt{K_{Br}^+}$. Whereas Gómez-de-Segura et al. (2018b) predicted the onset of these rollers would start at $\sqrt{K_{Br}^+} \approx 1$, they later found that this actually happened at $\sqrt{K_{Br}^+} \approx 0.38$ for deep substrates (Gómez-de-Segura and García-Mayoral, 2019). For shallow substrates, it should be noted that the onset of KH-rollers is delayed to higher values of $\sqrt{K_{Br}^+}$ due to the wall-blocking effect, making the permeable substrates more robust to KH-instabilities.

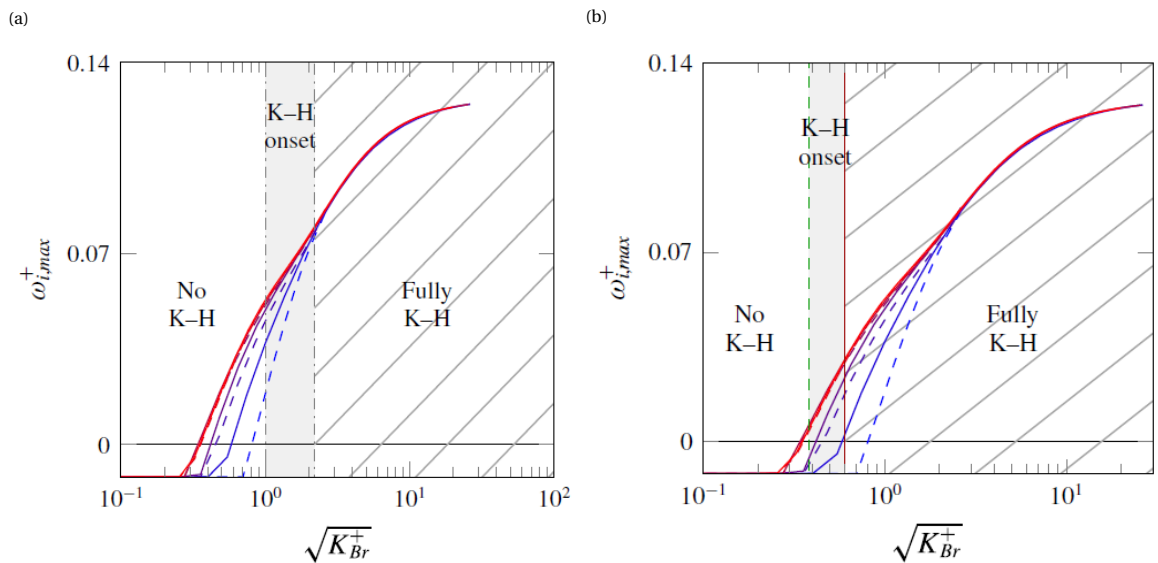


Figure 3.5: Maximum amplification ($\omega_{i,max}^+$) versus permeability length scale ($\sqrt{K_{Br}^+}$) for different permeable substrates (Gómez-de-Segura and García-Mayoral, 2019). - - -, $h^+ = 10$; —, $h^+ = 100$; from blue to red, anisotropy ratios increase as $\phi_{xy} \approx 1, 3, 10, 30$. The shaded region corresponds to the estimated range for the onset of Kelvin–Helmholtz rollers (K–H). (a) Predictions: onset instabilities in range $\sqrt{K_{Br}^+} \approx 1.0 - 2.2$. (b) Results: onset instabilities in range $\sqrt{K_{Br}^+} \approx 0.38 - 0.60$.

Figure 3.6 visualises the turbulent flow structures above the anisotropic permeable substrate. For low wall-normal permeability (A), the flow field is comparable to that of a smooth wall, with streamwise streaks visible in the u -velocity field, and quasi-streamwise vortices in the v -velocity field. For high wall-normal permeability (B), spanwise coherent structures are visible through all three velocity fields.

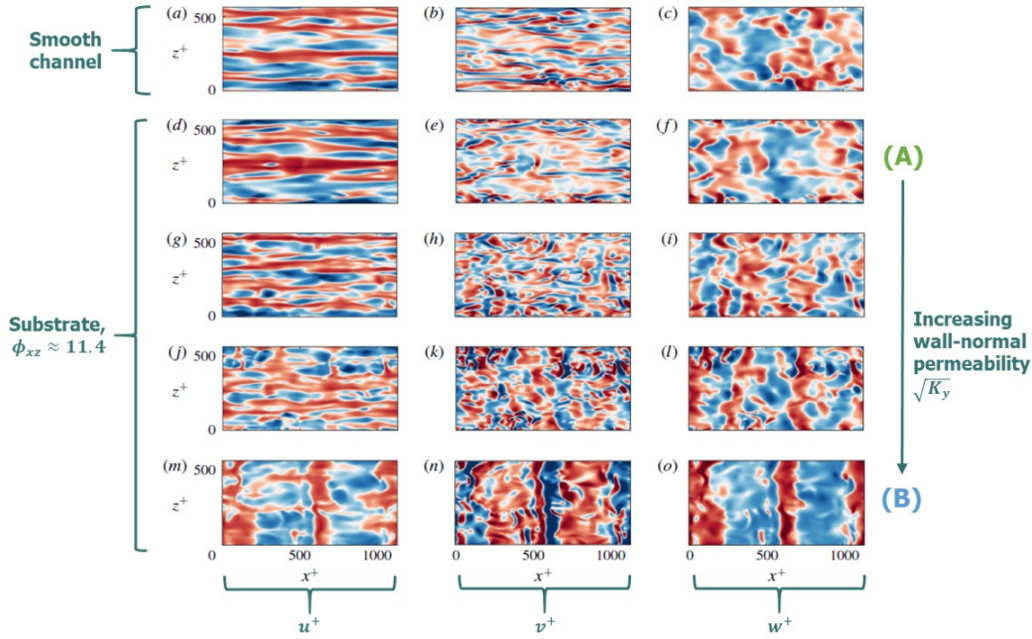


Figure 3.6: Comparison of flow structures above anisotropic permeable substrate to smooth flat plate, edited from Gómez-de-Segura and García-Mayoral (2019). Flow from left to right.

3.3.5. Drag reduction potential and assessment of theoretical model

In the last two years, three different groups of authors have performed DNS to study the drag reduction potential of anisotropic permeable substrates. Table 3.3 summarises these studies, including values for permeability, Re_τ and the obtained drag reductions. The first notable observation is that the study of Rosti et al. (2018) yields a drag reduction of 18% through a substrate with equal streamwise and spanwise permeabilities. This is not in line with the drag reduction model and is caused by an effective impermeability in the wall-normal direction. Gómez-de-Segura and García-Mayoral (2019) and Li et al. (2020) explicitly refer to this configuration as an 'impermeable' substrate, in which the displacement of quasi-streamwise vortices further towards the surface is impeded, as explained in Section 3.3.2.

The author of this report thinks that the results obtained by Gómez-de-Segura and García-Mayoral (2019) and Li et al. (2020) have a higher validity and are more relevant when considering 'real' anisotropic permeable substrates. Two important notes can be made here. Firstly, for similar streamwise to spanwise permeability ratios, $\phi_{xz} = \sqrt{K_x^+} / \sqrt{K_z^+} \approx 10$, drag reductions of the same order, $O(20\%)$, are obtained. Note that this definition of permeability ratio (ϕ) is chosen by Gómez-de-Segura and García-Mayoral (2019), and that $\phi_{xz} = 10$ corresponds to a ratio of 100 when expressed in actual Darcy permeabilities, i.e. K_x / K_y . Furthermore, both studies show that with shallow(er) substrates, higher values of wall-normal permeabilities $\sqrt{K_y^+}$ can be used before the degradation effect due to KH-instabilities kicks in (not shown in Table 3.3). The study of Gómez-de-Segura and García-Mayoral (2019) shows this directly: for $h^+ / K_y^+ \approx 5.7$ for example, the maximum value of the drag reduction (and hence the point where the drag degradation effects start) is obtained for $\sqrt{K_y^+} \approx 0.62$. In the case of Li et al. (2020), the wall-normal permeability is kept constant in all simulations. However, a similar effect can be deduced from the fact that for equal wall-normal permeabilities, increasing the substrate depth from its 'optimal value' of $h^+ \approx 9$ reduces the obtained drag reduction.

Table 3.3: Results of DNS studies on drag reduction through anisotropic permeable substrates. h = substrate thickness.

Study	DR _{max} (%)	$\sqrt{K_x^+}$	$\sqrt{K_y^+}$	$\sqrt{K_z^+}$	ϕ_{xz}	ϕ_{xy}	h	Re_τ
Rosti et al., 2018	18	2.62	2.62	0.01	1	256	$h_p = 0.2h$	164
Gómez-de-Segura and García-Mayoral, 2019	25	4.48	0.39	0.39	11.4	11.4	$h^+ = 39$	180
Li et al., 2020	20	1.8	0.18	0.18	10	10	$h^+ = 9$	180

According to the theoretical drag reduction model by Gómez-de-Segura and García-Mayoral (2019), for substrates with equal spanwise and wall-normal permeability (Equation (3.12)), the highest drag reductions can be obtained by maximising the streamwise-to-spanwise permeability ratio, and keeping the spanwise (and thus wall-normal) permeability just below the value at which KH-rollers emerge. To verify the theoretical model, results from Li et al. (2020) are compared to predictions using the permeabilities from Li et al. (2020) as input values. These are presented in Table 3.4. ΔU^+ is calculated via Equation (3.12), and the corresponding drag reduction is deduced using the drag reduction results of Gómez-de-Segura and García-Mayoral (2019) for similar values of ΔU^+ . In general, there is a good agreement between the predictions and obtained results. There are a few possible explanations for the differences:

- It is given in Gómez-de-Segura and García-Mayoral (2019) that for a general case where $K_z^+ \neq K_y^+$, one can expect $\ell_T^+ \neq \ell_z^+$. This uncertainty in how to define the virtual origin of the turbulence in the specific case of $\ell_z^+ < \ell_y^+$ (which is equivalent to the case of Li et al. (2020) where $K_z^+ < K_y^+$) is discussed in Section 3.3.2.
- Li et al. (2020) model the influence of the porous medium on the overlying flow in a different way than Gómez-de-Segura and García-Mayoral (2019) do in their theoretical model.

Table 3.4: Cross-checking the theoretical model predictions by Gómez-de-Segura and García-Mayoral (2019) ('Predicted drag reduction') with input values ('Case') and actual results ('Found drag reduction') from Li et al. (2020).

Case	Predicted drag reduction	Found drag reduction
$\sqrt{K_x^+} = \sqrt{K_y^+} = 1.8, \sqrt{K_z^+} = 0.18, h^+ = 9$	$\Delta U^+ = 1.62 \rightarrow DR \approx 16\%$	$DR \approx 20\%$
$\sqrt{K_x^+} = \sqrt{K_y^+} = 1.8, \sqrt{K_z^+} = 0.8, h^+ = 9$	$\Delta U^+ = 1.0 \rightarrow DR \approx 10\%$	$DR \approx 9\%$

All in all, the comparison gives confidence in the theoretical model as a useful tool for estimating the drag reduction potential of possible anisotropic permeable substrate configurations in a preliminary design phase. The predictions and DNS results are in a similar range. The fact that this is true not only within the study of Gómez-de-Segura and García-Mayoral (2019) but also via a cross-checking to Li et al. (2020) gives even more confidence. Nevertheless, the assumptions in the theoretical framework should not be forgotten when applying it to experimental settings.

3.4. Concluding remarks

The main takeaways regarding the literature on turbulent boundary layers over anisotropic permeable substrates are as follows:

- For turbulent flows over porous surfaces, permeability is the key parameter dictating the flow response.
- In general, permeable substrates have a drag-increasing effect. The wall-normal permeability facilitates momentum exchange between the substrate and the free flow, which enhances wall-normal velocity fluctuations that contribute to an increased Reynolds stress.
- Under the right conditions, streamwise-preferential permeable substrates show potential for significant (25%) reductions in friction. The results are limited to a few DNS studies only.
- A theoretical framework by Gómez-de-Segura and García-Mayoral (2019) links permeability to drag reduction through the use of slip and virtual origins. It has been verified using DNS results from studies by other authors.
- The only experimental study performed on streamwise-preferential surfaces (Efstathiou and Luhar, 2020), used 3D-printed lattices which did not have permeability values capable of achieving drag reductions based on the theoretical framework.

The main takeaways regarding the theoretical framework are as follows:

- Two important assumptions are made:
 - Pores are much smaller than the smallest turbulent length scales. In the analytical model of the substrate, they are taken as infinitely small, such that Brinkman's equation remains valid in the substrate up to the substrate-free flow interface.
 - The effect of pressure drag within the substrate is neglected.
- The framework is built up through four steps:
 - The (friction) drag reduction results from surface manipulation through a shift in the intercept of the velocity profile (ΔU^+).
 - An anisotropic, streamwise-preferential substrate introduces slip. Through the virtual origin model, this slip results in a shift of the log-law region which is proportional to the difference in streamwise and spanwise slip lengths: $\Delta U^+ \propto (\ell_x^+ - \ell_z^+)$.
 - Solving Brinkman's equation for flow through the substrates yields a simplified relationship between slip lengths and substrate permeabilities: $\ell_x^+ \approx \sqrt{K_x^+}$ and $\ell_z^+ \approx \sqrt{K_z^+}$. It follows that the change in ΔU^+ is proportional to the difference between the streamwise and spanwise permeability: $\Delta U^+ \propto (\sqrt{K_x^+} - \sqrt{K_z^+})$.
 - For $\sqrt{K_y^+} > 0.38$, spanwise coherent structures emerge associated with a Kelvin-Helmholtz-like instability. The linear DR trend breaks down.
- The working mechanism relates to a difference in the perceived wall by the mean flow and QS-vortices. As such, the contribution of the QS-vortices to the surface friction decreases. These turbulent structures are effectively 'filtered out'. It is therefore similar to the working mechanism behind the drag reduction obtained by riblets.


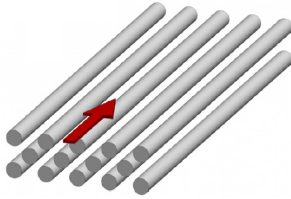
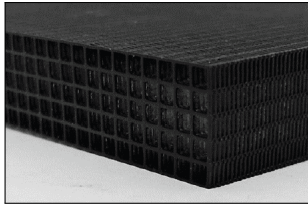
This page has been intentionally left blank.

II

Design, production, and assessment of anisotropic permeable substrates

Anisotropic permeability for flow control and turbulent friction reduction is a relatively unexplored topic in the domain of experimental aerodynamics. There is no established knowledge or best practice on what the physical characteristics of anisotropic permeable substrates should be (other than the required permeability in viscous units), and more specifically, how they should be realised, for use in wind tunnel experiments that can lead to insightful results. This part aims to address these gaps and builds on the limited resources available in literature. Within the frame of the research scope, it serves to meet and answer the first research objective and question respectively as outlined in Section 1.4. To do so, three different types of anisotropic permeable specimens were made, which are shown in Table 3.5 along with the source of inspiration and example images.

Table 3.5: Overview of the types of anisotropic permeable specimens made in this research, including source of inspiration and example images (taken from source).

Seal fur	Continuous fibres	3D-printed structures
Itoh et al. (2006)	Gómez-de-Segura and García-Mayoral (2019) and Wood et al. (2020)	Efstathiou and Luhar (2020)
		

First, a general idea on the test specimen requirements for valuable wind tunnel experiments is established in Chapter 4. It covers the experimental circumstances in this study and subsequently establishes the permeability design space. Then, the three categories of test specimens are discussed in separate chapters: the seal fur in Chapter 5, continuous fibres in Chapter 6 and 3D-printed structures in Chapter 7. All categories are described in terms of the design rationale, manufacturing process, performed experiments to determine relevant characteristics and a final assessment on the hypothesised potential for turbulent drag reduction. A summary with concluding remarks is finally shared in Chapter 8.

This page has been intentionally left blank.

4

General considerations for test plate production

Based on literature, three types of anisotropic permeable substrates were chosen to experimentally investigate: the seal fur, continuous fibres, and 3D-printed structures. The latter two needed to be designed based on a range of target permeabilities. In addition, all three types needed to be formed into a standardised test specimen corresponding to the direct force measurement setup which was used to assess their drag characteristics. Therefore this chapter covers two general aspects. First, it is necessary to establish the experimental circumstances for the wind tunnel measurements, and the test specimen limitations, which is done in Section 4.1. Subsequently, these experimental circumstances can be combined with the theoretical model discussed in Section 3.3, to yield a permeability parameter space which is hypothesised to result in drag reductions. This analysis is presented in Section 4.2 and guides the design and assessment of the continuous fibres and 3D-printed structures in later chapters.

4.1. Experimental circumstances and test specimens

Wind tunnel experiments were performed in the M-tunnel at the Low Speed Laboratory (LSL) at the Delft University of Technology (TU Delft). The tunnel has a maximum freestream velocity of approximately 35 m/s. Drag measurements were performed with a force balance called 'the Hill', a patent-pending system designed and manufactured by Dimple Aerospace B.V. for skin friction measurements of flat plates. For these measurements, a lower velocity limit of 5 m/s is generally taken. The reason is twofold. First, the absolute friction forces are small at this speed (~ 0.01 N). This results in a higher measurement spread and uncertainty compared to high velocities, which in turn makes it more challenging to assess drag differences in the order of a few per cent. Secondly, prior experiments with the Hill in the M-tunnel have shown that velocities lower than 5 m/s sometimes yield unstable boundary layers. Therefore, the range of testable freestream velocities was established as: $5 \text{ m/s} < U_\infty < 35 \text{ m/s}$. A full description of the M-tunnel and the Hill is given in Section 9.2, while the measurement uncertainty is covered in Section 10.4.1.

The Hill requires test specimens (referred to as test plates from now on) of a fixed dimension: $881.3 \text{ mm} \times 366.1 \text{ mm} \times 5.0 \text{ mm}$ (width \times length \times thickness). All test plates are compared to a smooth aluminium reference plate in drag measurements. Thinner plates are possible but need to be raised with spacers such that the plate top is flush with the wind tunnel wall. A test plate needs to have a solid, one-piece bottom, such that it can be inserted in and released from the Hill. The leading edge of a test plate inserted in the Hill is located approximately 0.6 m downstream from the point where the flow is tripped and a fresh turbulent boundary layer starts.

A priori knowledge on several quantities is useful: δ_ν and u_τ for inner scaling, Re_τ for comparing between different experimental circumstances, and δ for determining the field of view (FOV) for PIV measurements. Figure 4.1 shows these parameters for a test plate in the Hill in the M-tunnel subject to the conditions and dimensions described in the previous paragraphs. A ZPG TBL over a smooth plate plate and standard sea-level atmospheric conditions ($\rho = 1.225 \times 10^3 \text{ kg/m}^3$, $\mu = 1.81 \times 10^{-5} \text{ Ns/m}^2$ and $\nu = 1.51 \times 10^{-5} \text{ m}^2/\text{s}$) are assumed.

All required equations are given in Section 2.1. x_{TP} indicates the streamwise location along the test plate: $x_{TP} = x + 0.6$ where x is the streamwise coordinate w.r.t. the start of the BL. Two noteworthy observations can be made. First, it is clear that δ_v is relatively constant along the test plate, but highly dependent on U_∞ . Secondly, both δ and Re_τ show a high dependence on both U_∞ and x_{TP} . This is because the development length of the boundary layer upstream of the test plate is relatively short with 0.6 m. Dedicated turbulent boundary layer wind tunnels often have development lengths in the order of 5 m or longer.

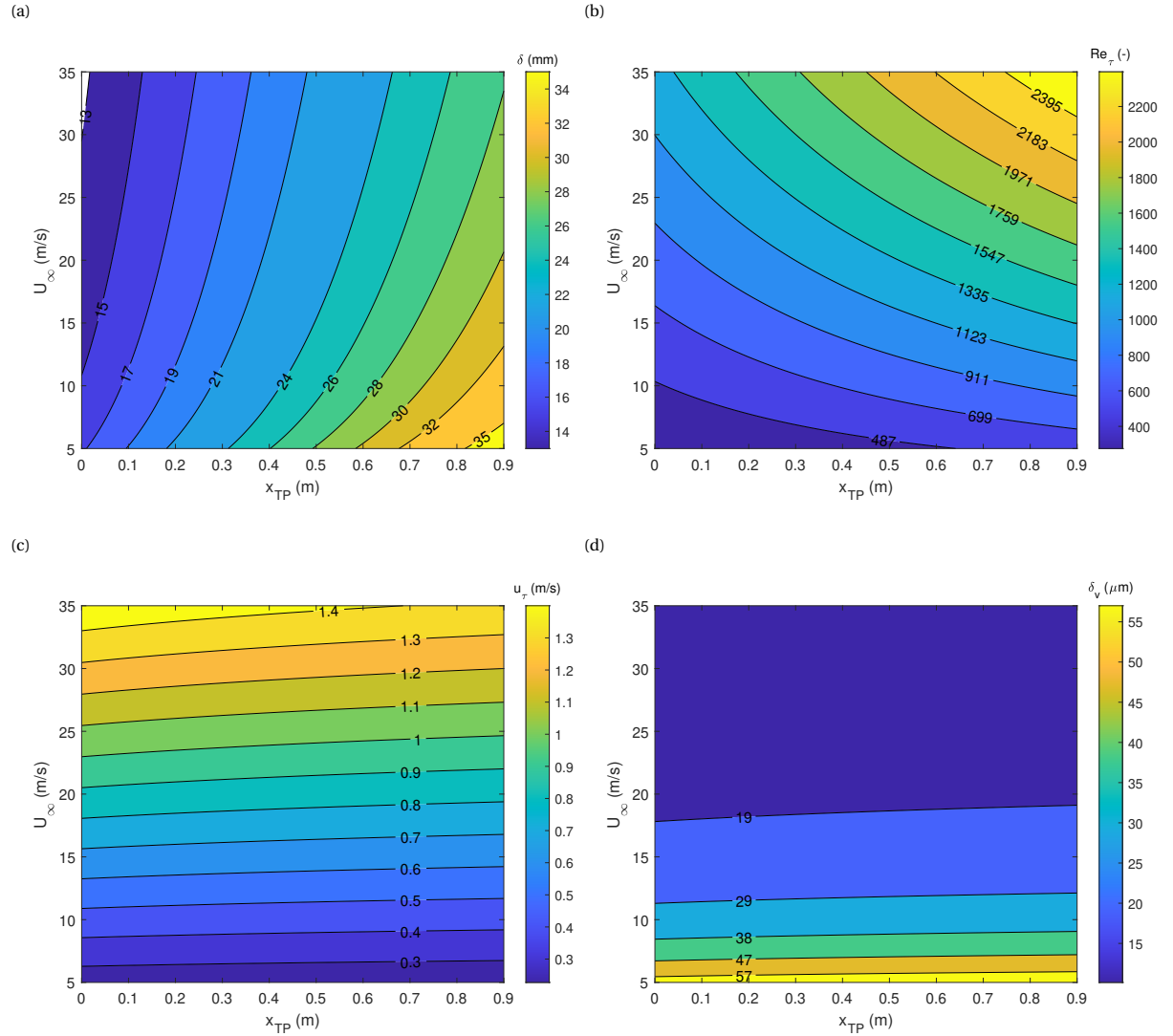


Figure 4.1: Theoretical values of δ (a), Re_τ (b), u_τ (c) and δ_v (d) for a ZPG TBL over a smooth plate in the Hill in the M-tunnel.

To illustrate this effect, Figure 4.2 shows the theoretical development of a turbulent boundary layer at $U_\infty = 35$ m/s, where items in blue correspond to the current setup, and items in red to a setup in which an additional 5 m of development length would be used upstream of the test plate. Although the absolute difference in boundary layer thickness between the end and the beginning of the test plates is similar (15.1 vs. 11.7 mm), it is clear that the relative difference is much larger for the test plate with the shorter upstream development length (119.3%), compared to a test plate with a longer upstream development length (13.6%). Similar trends apply to the friction Reynolds number as well. Consequently, it is challenging to capture the results from this setup within a single friction Reynolds number and therefore they require careful consideration when compared to other experiments. Increasing the development length upstream of the test plate was not feasible within the scope of this research.

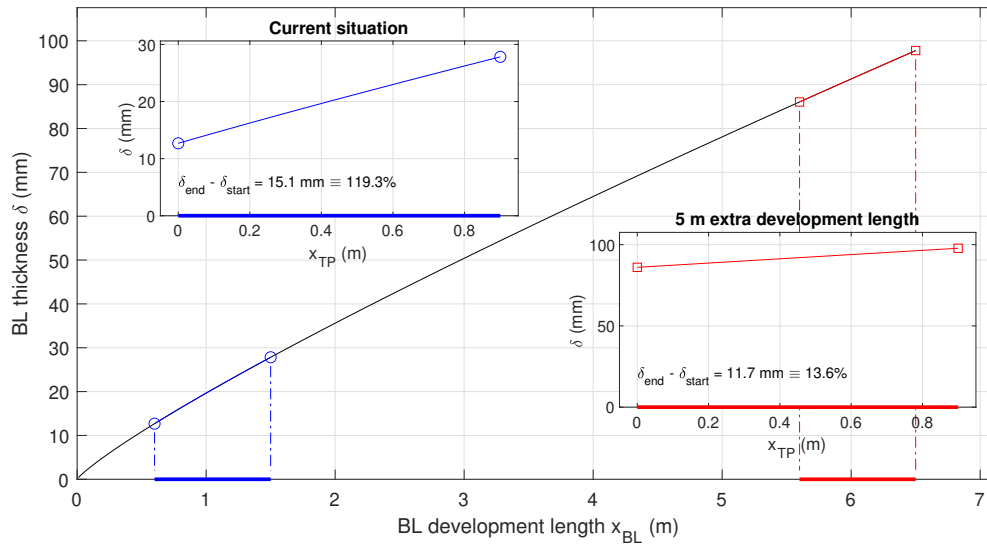


Figure 4.2: Theoretical development of a zero-pressure-gradient turbulent boundary layer over a smooth flat plate at $U_\infty = 35$ m/s. Blue indicates the location of a test plate in the Hill in the M-tunnel. Red indicates a theoretical location with 5 m extra upstream boundary layer development length.

4.2. Characterisation of permeability design space

The permeability of a substrate has three principal components. When placed in the wind tunnel reference frame, these components align with the streamwise (K_x), spanwise (K_z), and wall-normal (K_y) directions. In line with the theoretical framework, for achieving drag reduction, one wants to have a substrate with the following permeability characteristics:

1. A high streamwise permeability (K_x);
2. A low spanwise permeability (K_z), which can also be interpreted as a high streamwise to spanwise permeability ratio ($\sigma_{xz} = K_x/K_z$);
3. A low wall-normal permeability (K_y), more specifically below the threshold value above which spanwise coherent structures (KH-rollers) are predicted to emerge.

Gómez-de-Segura and García-Mayoral (2019) defined their theoretical framework and permeability design space in viscous units, i.e. $\sqrt{K_x^+}$, $\sqrt{K_y^+}$ and $\sqrt{K_z^+}$ (and similar for the permeability ratios, e.g. $\phi_{xz} = \sqrt{K_x^+}/\sqrt{K_z^+}$). Physical substrates have fixed, absolute permeability values in physical units (m^2). Consequently, in this experimental research, the design space had to be established in physical units. This required a translation between the design space and theoretical model in viscous units on the one hand and the design space in physical units on the other hand. This was done using δ_ν from the experimental circumstances discussed in Section 4.1.

Figure 4.3 shows the dependence of theoretical DR predictions on the flow conditions in the wind tunnel for a hypothetical test plate with fixed permeability. Since both U_∞ and the x_{TP} affect δ_v , they also affect the predicted drag reduction, although the effect is relatively small for x_{TP} . Therefore, from hereon, drag reduction predictions will be given as the mean value taken over x_{TP} .

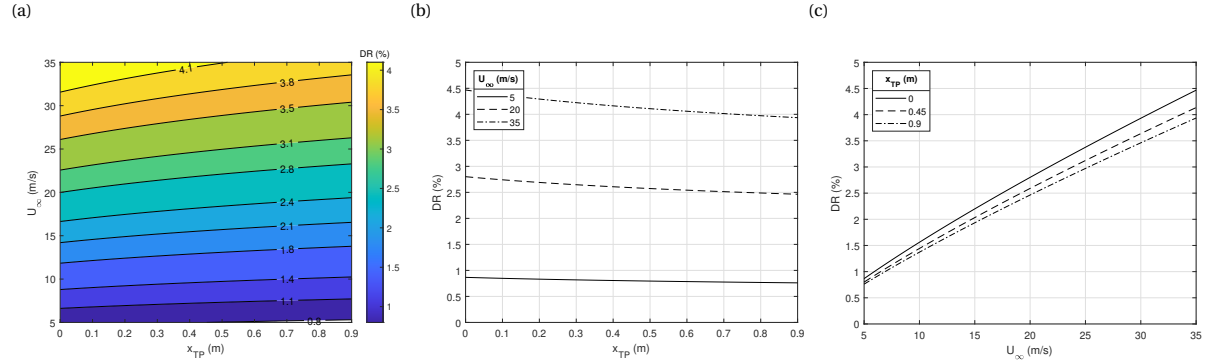


Figure 4.3: Dependence of theoretical DR predictions on flow conditions for $K_x = 1 \times 10^{-10} \text{ m}^2$ and $\sigma_{xz} = 10$. (a) Varying U_∞ and x_{TP} . (b) Varying x_{TP} , fixed U_∞ . (c) Varying U_∞ , fixed x_{TP} .

The influence of the first two permeable test plate design parameters (K_x and σ_{xz}) on the drag reduction prediction is shown in Figure 4.4 for $U_\infty = 20 \text{ m/s}$. The effect of the K_y is not taken into account yet. Two observations can be made. First, the positive effect of σ_{xz} saturates at higher values: increasing from 2 to 10 provides a larger gain than an increase from 10 to 100. Secondly, the opposite is true for the K_x : increasing from 10^{-9} m^2 to 10^{-8} m^2 yields a similar relative gain and higher absolute gain compared to increasing from 10^{-10} m^2 to 10^{-9} m^2 . This shows that obtaining the right absolute permeability range is of first priority, given that a reasonable degree of anisotropy is established in the design.

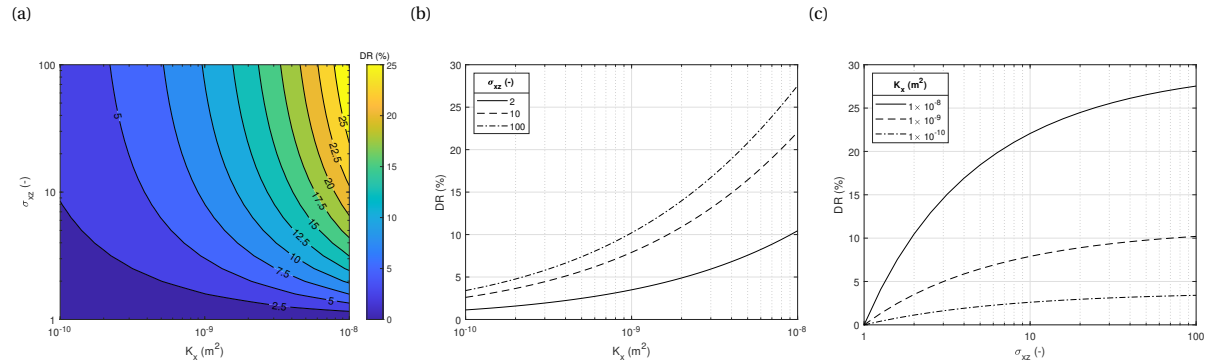


Figure 4.4: Dependence of theoretical DR predictions on permeability parameters for $U_\infty = 20 \text{ ms}^{-1}$. Effect of K_y not taken into account. (a) Varying K_x and σ_{xz} . (b) Varying K_x , fixed σ_{xz} . (c) Varying σ_{xz} , fixed K_x .

The prediction drag reduction does not continue indefinitely. Above a certain threshold value of K_y , the drag reduction trend breaks down with the appearance of spanwise coherent structures. Gómez-de-Segura and García-Mayoral (2019) predicted that this would happen at $\sqrt{K_y^+} = 1$, while their DNS results showed that this limit was $\sqrt{K_y^+} = 0.38$. Figure 4.5a shows the threshold value of K_y above which rollers start. A decreasing trend with respect to U_∞ can be observed. This is because δ_v decreases with increasing flow velocity, and consequently, for a fixed $\sqrt{K_y^+}$, K_y also decreases. This suggests that a porous material should have smaller pores to provide drag reductions at higher velocities. This is analogous to riblets, since larger riblets are used for slow oil-flow experiments and smaller riblets for flight conditions.

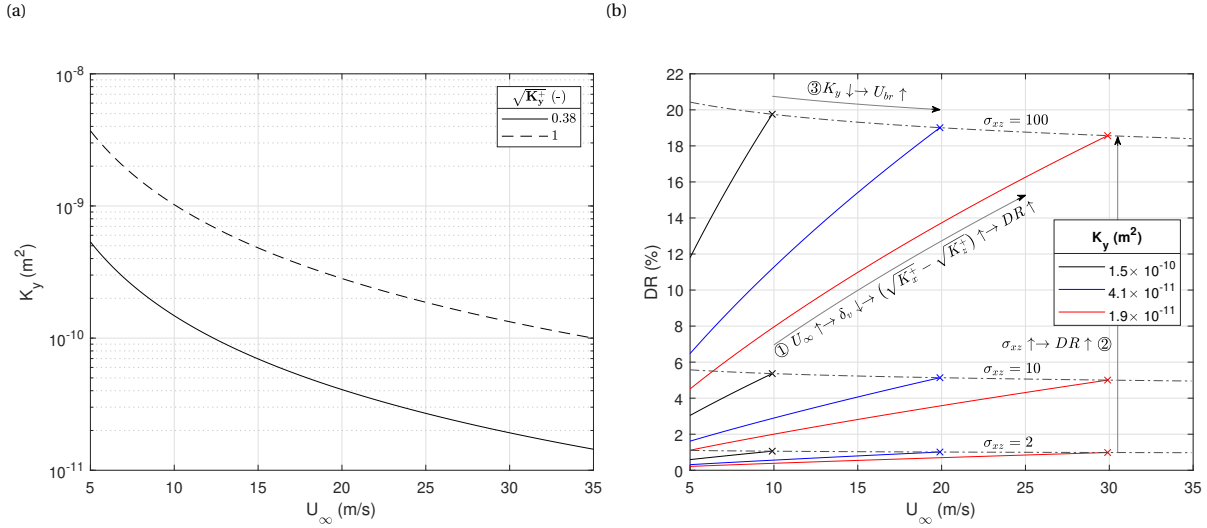


Figure 4.5: Demarcating the permeability design space including the K_y . (a) U_{Br} as function of K_y . (b) Theoretical DR predictions as function of U_{∞} , σ_{xz} and K_y , assuming $K_y = K_z$.

Combining the permeabilities in all three directions yields the drag reduction predictions presented in Figure 4.5b. Herein, $\sqrt{K_y^+} = 0.38$ and it is assumed that $K_y = K_z$. This assumption is made to ease the interpretation of the data. Gómez-de-Segura and García-Mayoral (2019) also assumed equal $\sqrt{K_y^+}$ and $\sqrt{K_z^+}$ in their simulations. Furthermore, it was expected that the design of anisotropic permeable substrates will be close to symmetrical around the streamwise axis, yielding similar values for K_y and K_z . Three distinct trends can be observed. The first is that of increasing DR with increasing U_{∞} for a given design, i.e. when traversing along a line as indicated by ①. This is the same trend as in Figure 4.3c, and the consequence of a decreasing δ_v with increasing U_{∞} , such that the difference between K_x and K_y in viscous units increases for fixed values in physical units. The second trend is increasing drag reduction for increasing σ_{xz} given a constant K_y , indicated by ②. This is the same trend as in Figure 4.4c; for a given K_y and thus given K_z , K_x is higher for higher σ_{xz} , increasing $K_x - K_z$ and thus $\sqrt{K_x^+} - \sqrt{K_y^+}$. The last trend is an increase in velocity at which KH-rollers emerge and the drag reduction breaks down, with decreasing K_y , as indicated by ③. This is the same trend as in Figure 4.5a. An additional consequence is that, for a fixed σ_{xz} the drag reduction obtained at the point of breakdown, slightly decreases. This is because a reduction in K_y means a reduction in K_x (since $K_z = K_y$ and σ_{xz} is constant) and thus a decrease in drag reduction as shown in Figure 4.4b. The decrease remains limited however by a simultaneous increase in U_{Br} .

Although all values used here are indicative and based on a canonical ZPG TBL, they do provide an understanding of how the theoretical model translates to the experimental settings. A priori, it is thought that the K_y will be limiting and to be able to achieve a measurable drag reduction at approximately 10 m/s, it should be below approximately $1.5 \times 10^{-10} \text{ m}^2$. Assuming $K_y = K_z$, $\sigma_{xz} \approx 10$ would result in a drag reduction in the order of 5%. These rough target values were kept in mind while designing and evaluating the different types of test plates manufactured.

This page has been intentionally left blank.

5

Seal fur

Gómez-de-Segura and García-Mayoral (2019) hypothesise that the drag reduction of seal furs found by Itoh et al. (2006) is an example of the streamwise-preferential permeability effect. No other studies into the effect of seal fur on fluid flow have been performed, let alone in air. As such, it was deemed interesting to do so in this research. Unfortunately, no information on the permeability characteristics of the seal was found in literature. In addition, characterising the seal fur's permeability with conventional measurement techniques is challenging due to the presence of the impermeable leather skin and therefore could not be done within the scope of this research. Section 5.1 presents the case why testing a real seal fur in the available wind-tunnel was deemed interesting even without knowing the exact permeability characteristics, mainly by considering the flow conditions compared to the work by Itoh et al. (2006) and for seals in nature. Two test plates were manufactured with real seal furs provided by the Pieterburen Seal Centre, which is discussed in Section 5.2. Finally, an assessment of the test plates is given in Section 5.3.

5.1. Scaling from prior experiments

Scaling of the flow conditions related to seals was performed to explore whether it would be interesting to perform experiments on real seal fur in the M-tunnel. Re_τ was chosen as the relevant scaling parameter for two reasons. First, in the theoretical framework, it is used as the governing parameter for defining different flow conditions. Secondly, it is a relatively straightforward parameter that can be directly calculated both based on experimental data and theoretical predictions and requires no knowledge of the seal fur itself. The goal was to check whether the obtained Re_τ would be in the same range as theoretical values across a test plate in the Hill in the M-tunnel, which was shown in Section 4.1 to be approximately $Re_\tau \approx 500 - 2500$. Three different scaling approaches were taken. Firstly, the experiments of Itoh et al. (2006) were scaled based on the available friction coefficient and flow measurement data. These were then checked against theoretical values obtained using power-law expressions. Lastly, the same power-law expressions were applied to data corresponding to the swimming conditions of seals in nature.

5.1.1. Scaling based on Itoh et al. (2006)

Not all flow conditions were explicitly mentioned in the paper, but they can be back-calculated using the given expressions. Firstly, the flow velocity (in their work referred to as bulk velocity (U_a)) is calculated via

$$Re_m = \frac{d_h U_a}{\nu}, \quad (5.1)$$

where Re_m is the bulk Reynolds number and $d_h = 2HW/(H+W)$ is the equivalent channel diameter based on the effective channel height (H) and channel width (W). ν was calculated for the 40 wt. % glycerol-water mixture via ρ and μ taken from Takamura et al. (2012). A temperature of 20 °C was assumed.

With the calculated U_a and C_f values for the seal fur between $z/W = 0.14$ and 0.30 , given in Figure 5.1, a mean friction velocity (\overline{u}_τ) is calculated via

$$\overline{u}_\tau = U_a \sqrt{\frac{C_f}{2}}. \quad (5.2)$$

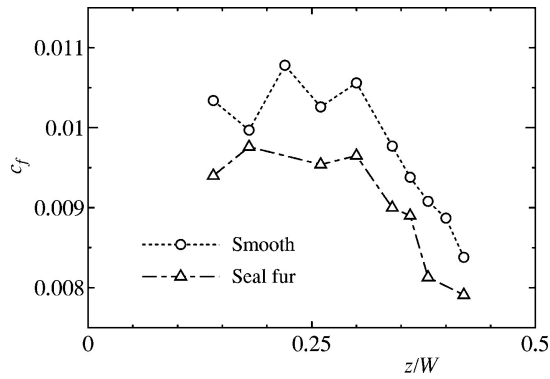


Figure 5.1: Spanwise distribution of local skin friction coefficient on smooth and seal fur surfaces at $Re_m = 7,000$ for the glycerol-water mixture (Itoh et al., 2006).

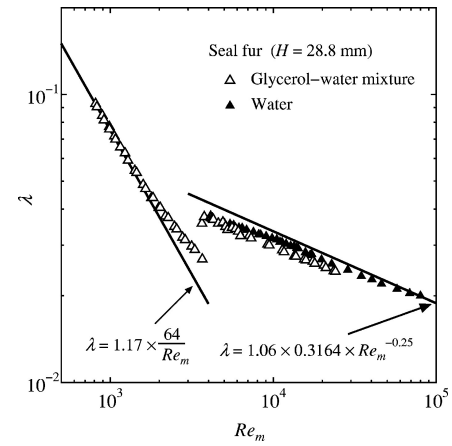


Figure 5.2: Friction factor versus Reynolds number on the seal fur surface (Itoh et al., 2006).

Finally Re_τ is based on an expression given by Itoh et al. (2006):

$$Re_\tau = \frac{(H/2) \overline{u_\tau}}{\nu}. \quad (5.3)$$

This yields $Re_\tau = 146$ for $Re_m = 7000$ in the glycerol-water mixture. This unfortunately is too low to reproduce with the experimental setup of this research. Luckily, drag reduction was also found at the highest tested Reynolds number of $Re_m = 25,000$. Therefore, since Figure 5.1 presents C_f for $Re_m = 7,000$, an extra step was performed for calculating Re_τ at $Re_m = 25,000$. This consisted of calculating the decrease in overall friction factor (λ) from Figure 5.2, and subsequently applying the same decrease factor to the C_f obtained from Figure 5.1. This implicitly assumes equal changes in λ and C_f .

Table 5.1 presents the results obtained via the outlined procedure. The found Re_τ corresponding to $Re_m = 7,000$ for the glycerol-water mixture is very close to the given $Re_\tau = 150$ for $Re_m = 7,000$ in water Itoh et al. (2006).

Table 5.1: Results from scaling based on Itoh et al. (2006).

Case	Re_m	U_a (m/s)	Re_τ
Maximum drag reduction	7,000	0.48	146
Highest tested velocity	25,000	1.73	451

5.1.2. Scaling based on Itoh et al. (2006) via power-law expressions

A second method for scaling based on Itoh et al., 2006 is via the power-law expressions. This is similar to what was done for the Hill and M-tunnel setup in Section 4.1, and thus yields a direct comparison between the two experimental setups. This procedure was performed for the full length of the tested flat plate (900 mm) and for velocities $\pm 20\%$ w.r.t. the calculated U_a as given in Table 5.1. The results are shown in Figures 5.3a and 5.3b. It can be seen that this method produces results approximately 19% and 7% higher than those obtained in Section 5.1.1. It is especially interesting to see that the Re_τ values for $Re_m = 25,000$ are relatively close to one another, as that these values are also close to the range obtainable with the Hill in the M-tunnel.

5.1.3. Scaling based on seals in nature via power-law expressions

The procedure outlined in Section 5.1.2 can also be applied to data corresponding to swimming conditions of seals in nature. If the seal fur reduces turbulent friction drag, then from an evolutionary point of view, it would make sense that it does so for their common swimming conditions, such as water viscosity and swimming speeds. Performing these calculations was done for a harbour ("common") seal, which lives in the Dutch Waddenzee and forms the main group of seals at the Sealcentre Pieterburen.

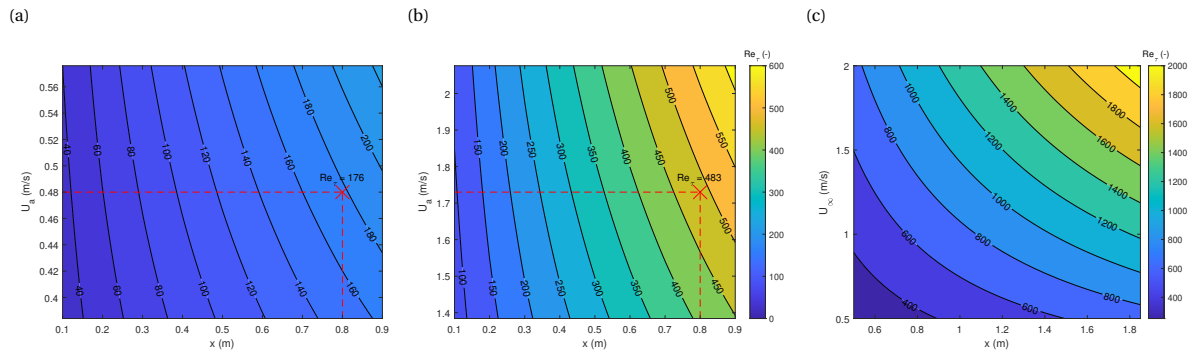


Figure 5.3: Re_τ for different seal circumstances. Function of U_a and x for $Re_m = 7,000$ (a) and $Re_m = 25,000$ (b). Colorbar of (b) also applies to (a). Values for the calculated bulk velocities in Section 5.1.1 at the LDV measurement location $x = 800$ mm are indicated with a red cross. (c) Function of U_∞ and x for the harbour seal in salt water at $T = 10$ °C.

For this scaling, the following assumptions were made:

- A seal is modeled as a flat plate where a ZPG TBL develops, starting at the tip of the snout.
- Based on a yearly average, minimum and maximum temperature in the Dutch Waddenzee of 10.4, 2.8 and 18.6 °C respectively (Wadkanovaren, 2011), a temperature of 10 °C was considered.
- Corresponding water density and viscosity were taken from ITTC (2011) for standard sea water.
- Adults can reach a length of up to 1.85 m (Wilson and Burnie, 2001).
- Typical swimming velocities are in the range of 0.5 to 2.0 m/s (Davis et al., 1985; Lesage et al., 1999).

Figure 5.3c presents the obtained results for the power-law method applied to seals in nature. The range of Re_τ over the entire body and in the entire speed regime overlaps with the range obtainable with the Hill in the M-tunnel.

5.1.4. Concluding remarks

Scaling of the flow conditions related to seals was performed to explore whether it would be interesting to perform direct force measurements on the seal fur in the available facilities. Re_τ was used as scaling parameter. Table 5.2 shows that the results of the three different methods are in line with the conditions in the available facilities. Therefore it was concluded that testing real seal furs was an interesting case to pursue.

Table 5.2: Overview of Re_τ for different scaling methods compared to test facilities.

Method	Re_τ
Scaling based on Itoh et al. (2006)	146 - 451
Scaling based on Itoh et al. (2006) via power-law expressions	176 - 483
Scaling based on seal in nature via power-law expressions	400 - 2000
Test facilities: The Hill in M-tunnel	500 - 2500

5.2. Manufacturing process

Two real seal furs were used to manufacture test plates: one from an adult harbour seal (*Phoca vitulina*), also known as the common seal, and one from a four-month-old grey seal (*Halichoerus grypus*). Both seals died of natural causes and the furs were provided by the Pieterburen Sealcentre for academic research purposes. Consequently, the use of these specimens is in line with the TU Delft Code of Conduct and guidelines on academic integrity.

The skins were removed from the carcasses by a veterinarian at the Pieterburen Sealcentre and subsequently treated by a taxidermist to remove excess fat and subcutaneous tissue and perform chemical treatment for preservation of the specimens. This treatment was performed with a liquid mixture of water, salt, aluminium dioxide and magnesium. The result of this process can be seen in Figure 5.4. The furs were quite stiff, had numerous folds and holes, and could not cover a full test plate at once. This necessitated stretching, cutting and patching before attaching the seal furs to a flat plate. The harbour seal fur was notably softer and thicker, i.e. the hairs were oriented upwards more, than the grey seal fur.

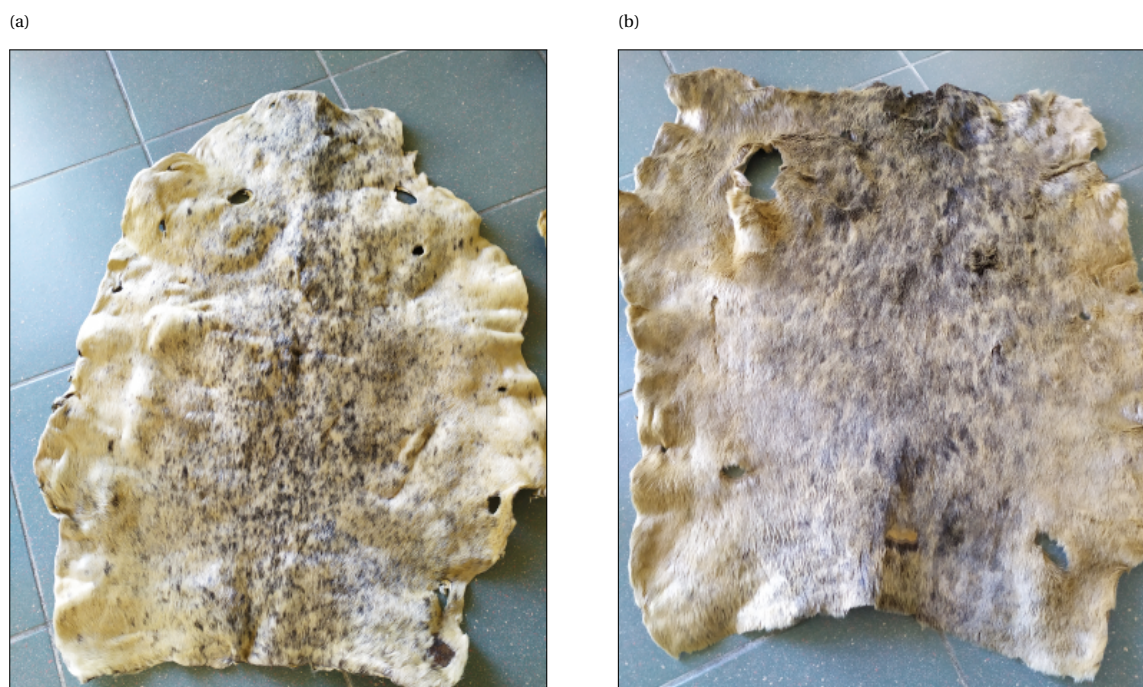


Figure 5.4: Seal furs after treatment. (a) Grey seal, streamwise direction from bottom to top. (b) Harbour seal, streamwise direction from top to bottom.

The seal furs were stretched within a wooden octagonal frame using lashing straps, tension ratchets and canvas clamps. The ratchets were continuously tightened over the course of 24 hours while slightly wetting the leather (seal fur bottom part) with water to maintain flexibility. After stretching, the furs were cut into pre-measured pieces with a Stanley knife. Figure 5.5 shows the setup for stretching and cutting of the seal furs.

With the grey seal fur, it was possible to cover an entire test plate; for the harbour seal fur, the entire width of the test plate could be covered over a length of approximately 60 cm. The thickness of the cut pieces, with the hairs squeezed flat against the skin leather, was measured around the perimeter with a digital calliper. Subsequently, the required thickness of the aluminium baseplate was determined to be 2 mm. This thickness analysis is further discussed in Section 5.3. Finally, the seal fur parts were glued to the baseplate with Scotch Weld EC-9323 B/A (from hereon referred to as Scotch Weld) and covered with a plate with heavy weights on top, to ensure a flat adherence of the seal fur to the baseplate and glue layer, for 24 hours. An aluminium plate of 3 mm was glued to the baseplate for the area uncovered by the harbour seal fur.

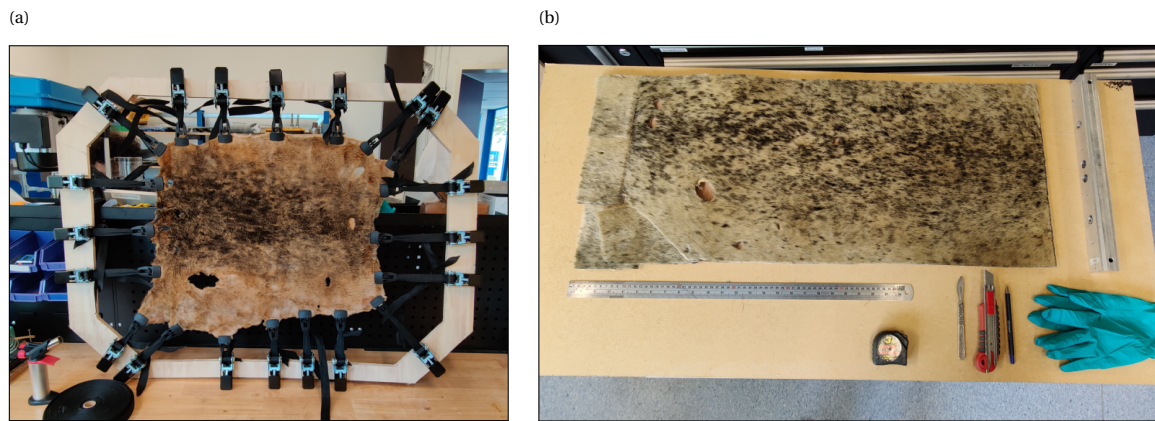


Figure 5.5: Seal fur test plate manufacturing process steps. (a) Stretching. (b) Cutting.

5.3. Test plate assessment

Figure 5.6 shows the final result of the two seal fur test plates. The furs adhered properly to the aluminium base plate, including the smaller pieces that served as patches to the holes. In some cases, these patches are visible, although all of them have hairs aligned in the streamwise direction. Another irregularity is the thickness of the fur, more specifically the skin leather. This was analysed for both furs, for which the results are shown in Table 5.3. With an aluminium base plate of 2 mm, this means that if squeezed completely flat, some portions of the plate would be thinner than the standard 5 mm for test plates in The Hill. However, in practice, the seal fur hairs do not lie completely flat as they would when submerged in water. Especially the harbour seal has hairs standing up straight. As an analogy, the grey seal can be compared with a short pile carpet and the harbour seal with a long pile carpet.

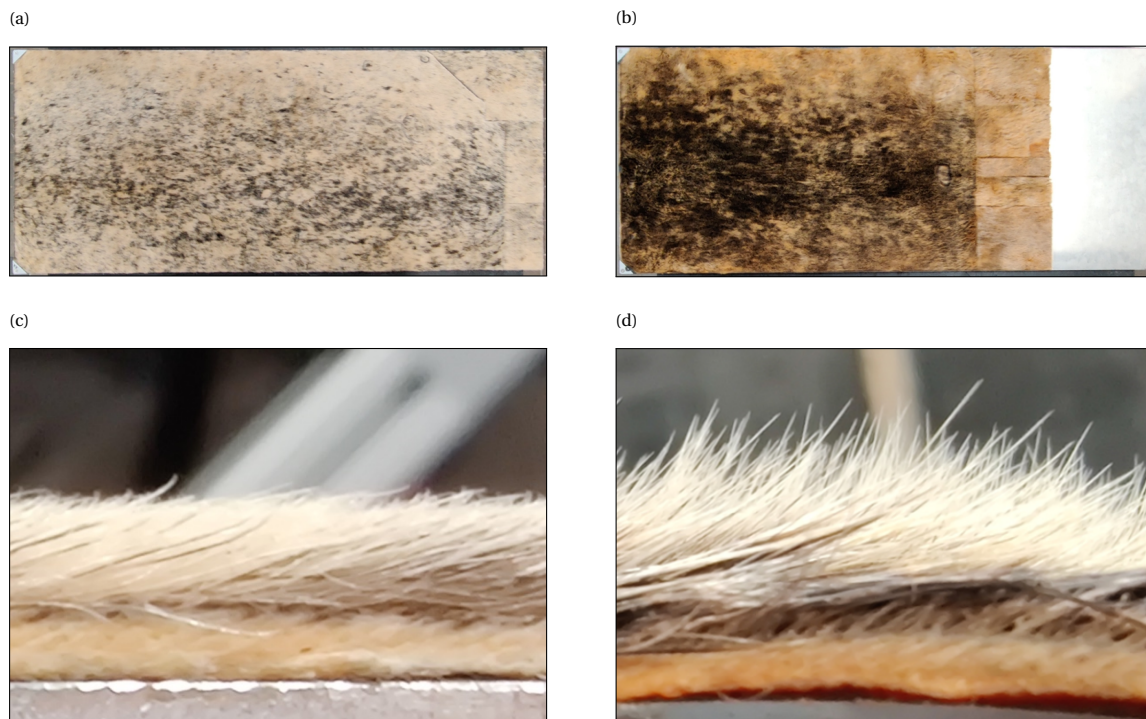


Figure 5.6: Seal fur test plates. Oriented w.r.t. a flow from left to right. (a, c) Grey seal. (b, d) Harbour seal. (a, b) Top view. (c, d) Detailed view.

Table 5.3: Seal fur thickness (in mm). Measurements were performed with a digital calliper around the perimeter of the cut parts. Thickness was measured by squeezing the fur flat against the skin leather.

Seal	Data points (#)	Mean	Min.	Max.	Std.
Grey	38	2.3	1.6	3.1	0.4
Harbour	36	2.6	1.6	3.6	0.1

Images with a scanning electron microscope (SEM) were taken to assess the shape of individual hairs. The JEOL JSM-7500F SEM in the Delft Aerospace Structures and Materials Laboratory (DAMSL) was used. Figure 5.7 shows that the seal fur is composed of two types of hairs, with the main hairs having an elliptical cross-sectional shape. This corresponds to findings in literature such as by Erdsack et al. (2015), who analysed the hairs and skin of harbour seals. They found that the seal fur is composed of 'flattened' guard hairs with an elliptical cross-section, and shorter circular underhairs, which all grow in the flow direction and are aligned with the skin. Contrary to popular belief, this fur does not keep the seals warm. Phocid seals, to which the harbour and grey seal belong, mainly rely on their blubber for thermal insulation (Scholander et al., 1950). Moreover, adult seals lose almost all of their underhairs while ageing.

Although their study focused on fur and skin characterisation, Erdsack et al. (2015) believe that the flattened guard hairs could play a role in drag reduction. They regard such a surface as a 'smooth surface' however, and based on that assumption argue that this would be in contrast with the established theory on drag reduction of shark skins. The author of this study agrees with the thought that the flatness of the hairs could be beneficial for turbulent drag reduction, but does not see the seal fur as a 'smooth surface', and in this regard agrees with Itoh et al. (2006) on the actual similarity to riblets. The flattened shape of the guard hairs could aid in enhancing the streamwise permeability while simultaneously limiting the wall-normal permeability, fitting in the theoretical framework of Gómez-de-Segura and García-Mayoral (2019). The view of Erdsack et al. (2015) on the 'smoothness' of the seal fur surface is understandable, given that none of the authors is specialised in the field of fluid dynamics.

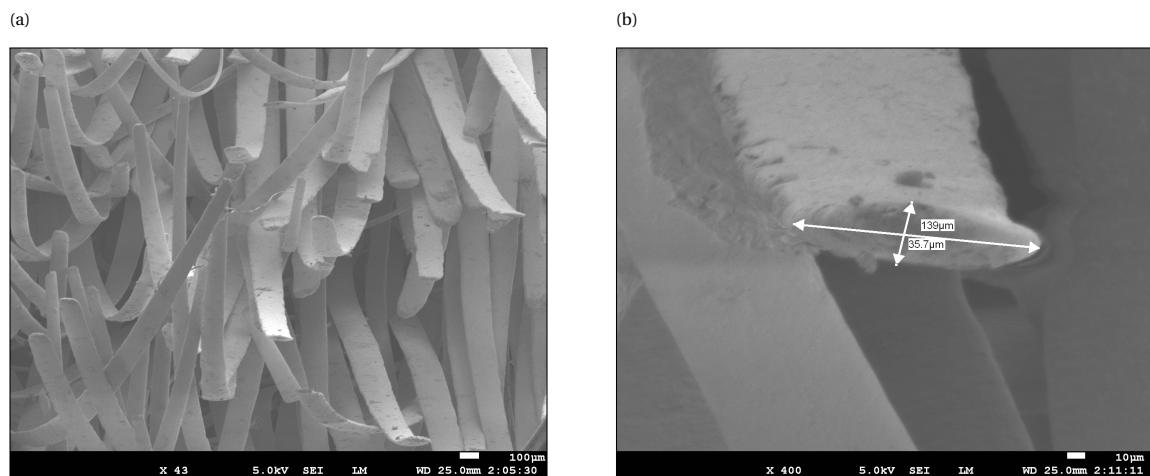


Figure 5.7: SEM images of the harbour seal fur. (a) Zoomed out view. Guard hairs are visible as wide, 'flat' hairs, underhairs are visible as thin, circular hairs. (b) Detailed view of an individual guard hair.

6

Continuous fibres

Gómez-de-Segura and García-Mayoral (2019) envisioned a highly connected substrate with rods in the longitudinal direction as a practical example of an anisotropic permeable substrate, while Wood et al. (2020) mentioned a similar structure, specifically an anisotropic fibrous medium. As such, the second type of test plate manufactured is a plate covered with several layers of continuous streamwise-aligned fibres, from hereon referred to as "continuous fibre(s) plate". First, Section 6.1 presents the design of the test plate. Subsequently, Section 6.2 goes through the manufacturing process. Finally, an assessment of the test plates is given in Section 6.3. The reader is referred to Appendix B for more background information on fluid flow through unidirectional fibre substrates.

6.1. Test plate design

The continuous fibre plate consists of several layers of fibres running in the lengthwise direction across a flat, aluminium plate. Figure 6.1 shows a schematic image of this conceptual design. After consultation with experts from Centexbel, a highly regarded research institute in the field of textile and plastic processing, it was concluded that using a filament winding production procedure was the most feasible solution for this design case.

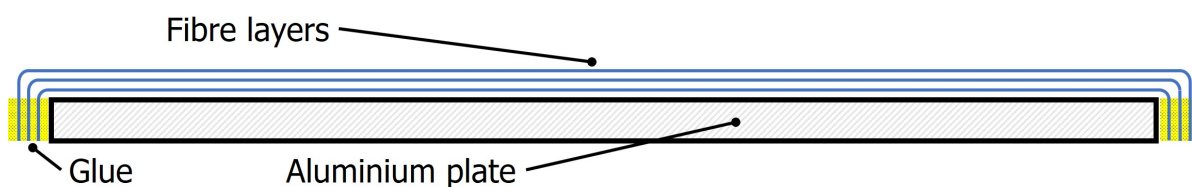


Figure 6.1: Conceptual design of continuous fibre test plate. Side view. Not to scale.

Two options of filament winding were explored in a preliminary experiment: winding around an open frame vs. a closed frame (plate). The open frame was expected to have the benefit of creating unidirectional (UD) fabrics after stitching the fibre sheets together in the transverse direction at the inner side of the frame. These fabrics could then be attached to a different plate, offering a higher degree of freedom in the design. The preliminary experiment however showed that fibres in the UD fabric lost tension after removing the fabric from the open frame, as can be seen in Figure 6.2. Therefore it was decided to continue with winding around a closed frame.

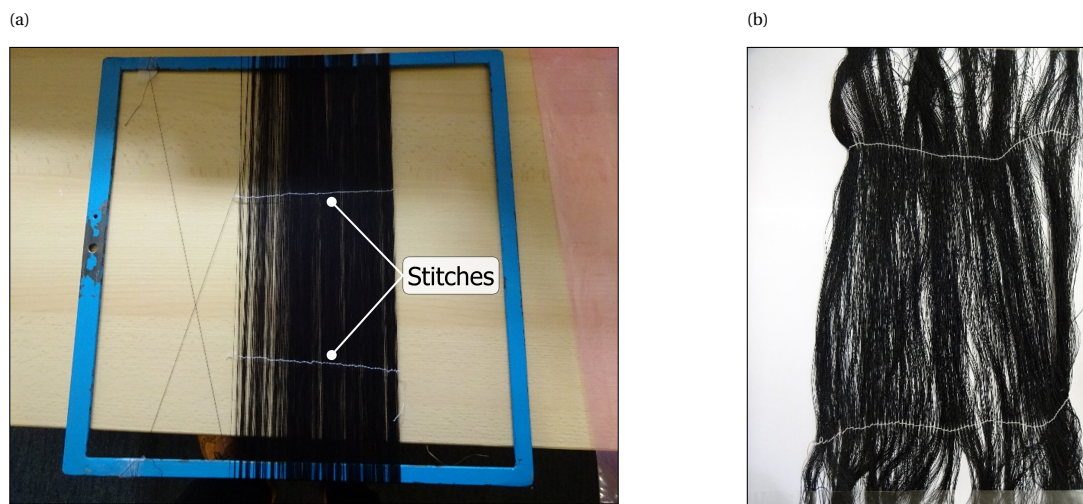


Figure 6.2: Filament winding around an open frame. (a) Fibres attached to open frame with stitches in transverse direction. (b) After removal from open frame.

The filament winding procedure posed several constraints on the test plate design. Firstly, the machine used at Centexbel has a clearance height of 30 cm, meaning that the maximum size of a plate that could be used was 60 cm, hence it was not possible to cover a full test plate at once. Therefore, the test plate was designed to consist of two frames, interconnected in lengthwise direction and assembled on a bottom plate. These frames have side strips to keep the fibres in place. Also, a leading edge and trailing edge strip are attached to the bottom plate to have a smooth, closed off perimeter. Figure 6.3 shows a schematic exploded view of this continuous fibre test plate mould, while the dimensions of the different components are given in Table 6.1.

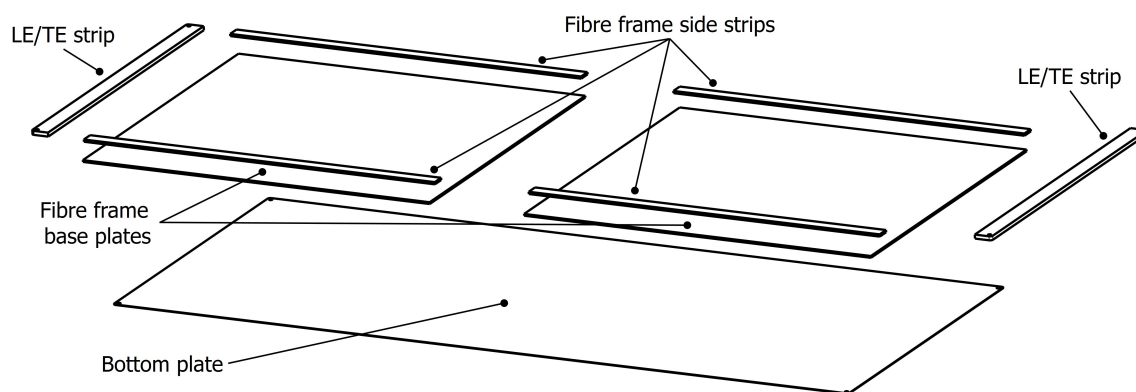


Figure 6.3: Schematic exploded view of continuous fibre test plate aluminium mould.

Table 6.1: Dimensions of fibre mould components.

Item	Quantity (#)	Length (mm)	Width (mm)	Thickness (mm)
Bottom plate	1	881.3	366.3	0.5
Fibre frame base plate	2	415.65	366.3	2
Fibre frame side strip	4	420.65	15	2.5
LE/TE strip	2	20	366.3	4.5

Other constraints were the fibres used and the fibre-to-fibre spacing (sideways) direction. The fibre used was Güterman sewing thread, which is a multifilament. A smoother monofilament was preferred but unfortunately not feasible within the project budget. Fibres could be of diameter between 0.2 and 1.0 mm, while the fibre-to-fibre spacing could be any integer multiple of 0.3 mm up to 3.0 mm. Through a priori estimation of permeability and potential drag reduction (further discussed in Section 6.3), it was decided to use 0.25 mm diameter fibres and a 0.3 mm fibre-to-fibre spacing. Assuming perfect hexagonal packing it was estimated that nine fibre layers would be laid to form a sheet of 2.5 mm.

6.2. Manufacturing process

The filament winding production procedure covers two sides of a plate, whereas the final test plate only required fibres on the top side of the plate. Figure 6.4 shows how this incompatibility was addressed. Two fibre frames were mirrored such that their bottoms faced each other. These frames were clamped together with another plate in between, which could be connected to the winding machine. In the winding procedure, glue was deposited only on the fibre frame front and rear edges so that after the winding procedure, the fibres could be cut through along the plane separating the two fibre frames. This ultimately yielded the two fibre frames which are required to form one full test plate. Figure 6.5 shows a schematic exploded view of the assembly that was attached to the winding machine. The spacing plate has the same thickness as the winding machine attachment plate and provides integrity to the whole assembly when clamped.

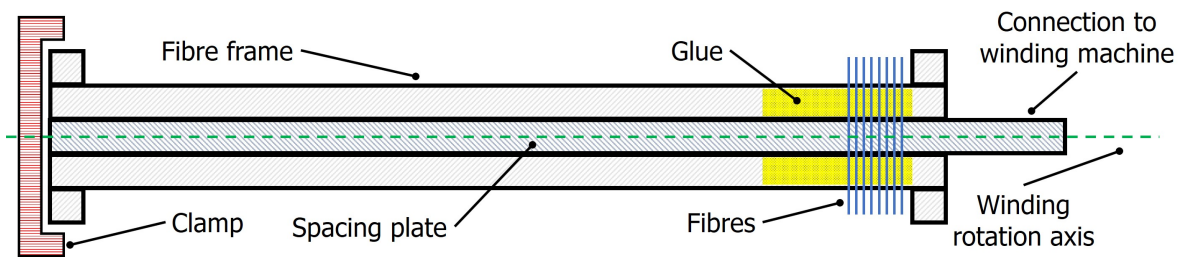


Figure 6.4: Conceptual design of continuous fibre winding frame for filament winding process. Front view. Not to scale.

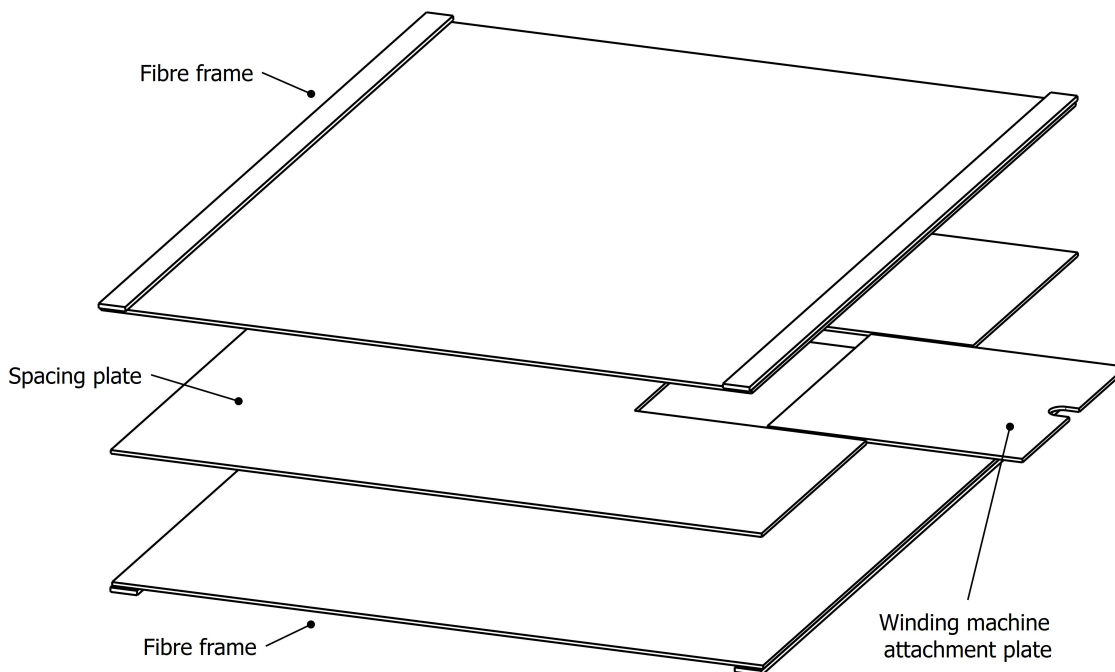


Figure 6.5: Schematic exploded view of continuous fibre frame assembly for filament winding process.

The whole manufacturing process consisted of roughly four phases: (1) preparing the assembly for the filament winding procedure, which included gluing the fibre frame side strips to the fibre frame base plates with Scotch Weld; (2) winding the filament around the fibre frame assembly, done at Centexbel in Kortrijk; (3) cutting the fibre sheets to separate the two fibre frames and cleaning the bottom of the fibre frame base plates; and (4) assembling the full test plate and performing some finishing touches.

The filament winding process was performed at the Kortrijk location of Centexbel. Figure 6.6a shows the setup. An electromotor rotates a clamp holding the fibre frame assembly at a constant rotational velocity, with a maximum of 237.5 RPM. With the relatively heavy assembly however, a rotational velocity of approximately 25 RPM (~ 10%) was set. The rotation axis is coupled to a screw thread via gears and a chain. The screw thread provides lateral movement to the filament guiding wheels, such that at every rotation, the new fibre is laid next to the previous one. The fibre-to-fibre spacing can be set via the gearbox connected to the guiding rails and screw thread; values range between 0.3 and 3.0 mm with steps of 0.3 mm. The fibre is drawn from a filament spool which provides 500 m of filament per spool. The winding machine was paused every time the filament spool had to be replaced. Fibres of the old and new spools were tied together with a knot negligibly thicker than the fibres.

Stopping points on the guiding rails force the gearbox to switch direction, i.e. switching from left-to-right to right-to-left and vice versa. A full 'pass', corresponding to one fibre layer, took approximately an hour. After every pass, a fresh layer of glue was deposited on the front and rear edges of the fibre frames. Consequently, the fibres of a new layer were laid in the wet glue layer prior to curing, as shown in Figure 6.6b. Special care was taken to ensure glue was removed in the centre line between the fibre frame edges for easier cutting later on. Eight passes were performed, hence resulting in eight layers of fibre.

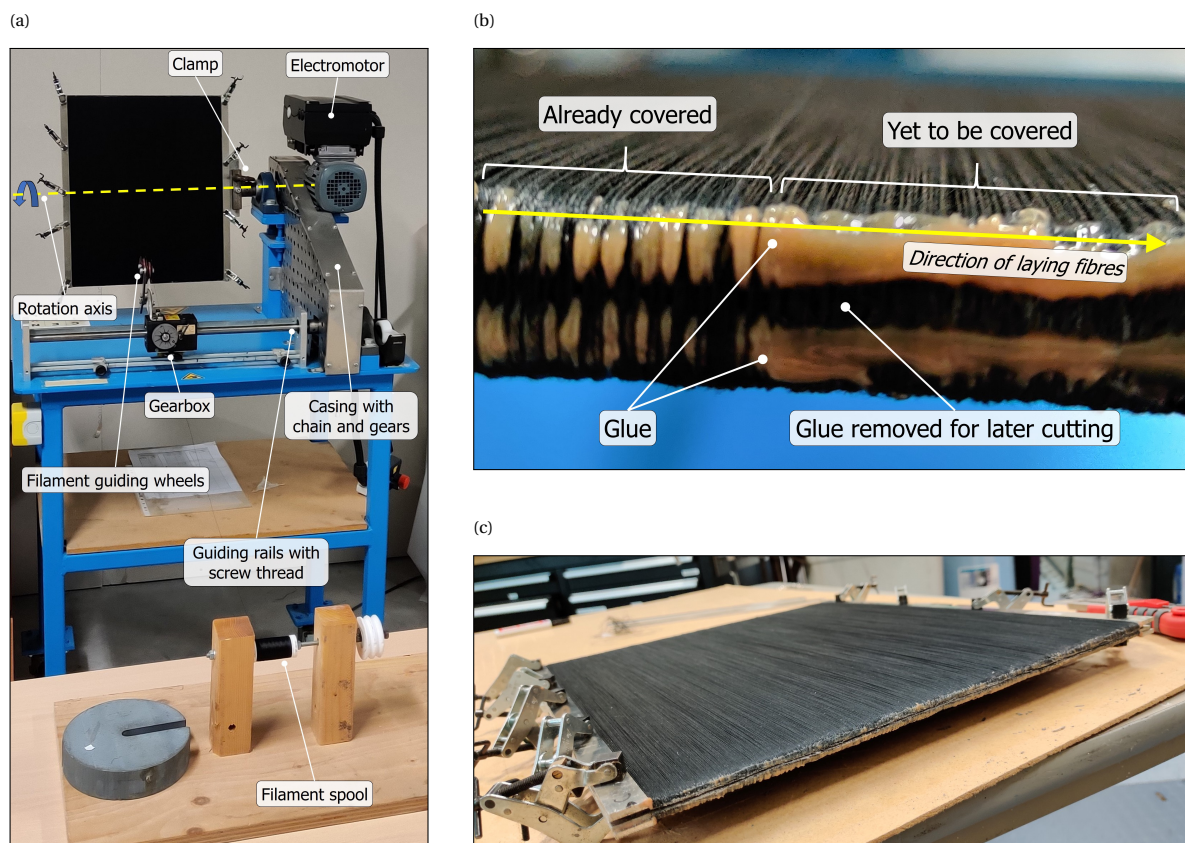


Figure 6.6: Filament winding and cutting procedure. (a) Filament winding setup at Centexbel. (b) Close-up view of plate front-edge with glue. (c) Cutting through the fibres at the plate front-edge.

After the glue was completely cured, the fibres were cut in between the fibre frame edges, both at the front and at the rear, as shown in Figure 6.6c. The fibre-gluе mixture remained attached to the plate at the front and rear edges as shown in Figure 6.7. Excess material was sheared away such that the fibre-gluе mixture was flush with the fibre frame plate bottom. Finally, the two fibre frames were glued onto a bottom plate, together with a leading- and trailing edge strip, using Scotch Weld, forming one whole test plate. Gaps at the LE, in the middle, and at the TE were filled with moulding clay to ensure smooth transitions between edges and the fibre sheet.



Figure 6.7: Bottom of fibre frame. The fibre-gluе mixture is attached to the plate front and rear edges and sheared to be flush with the bottom.

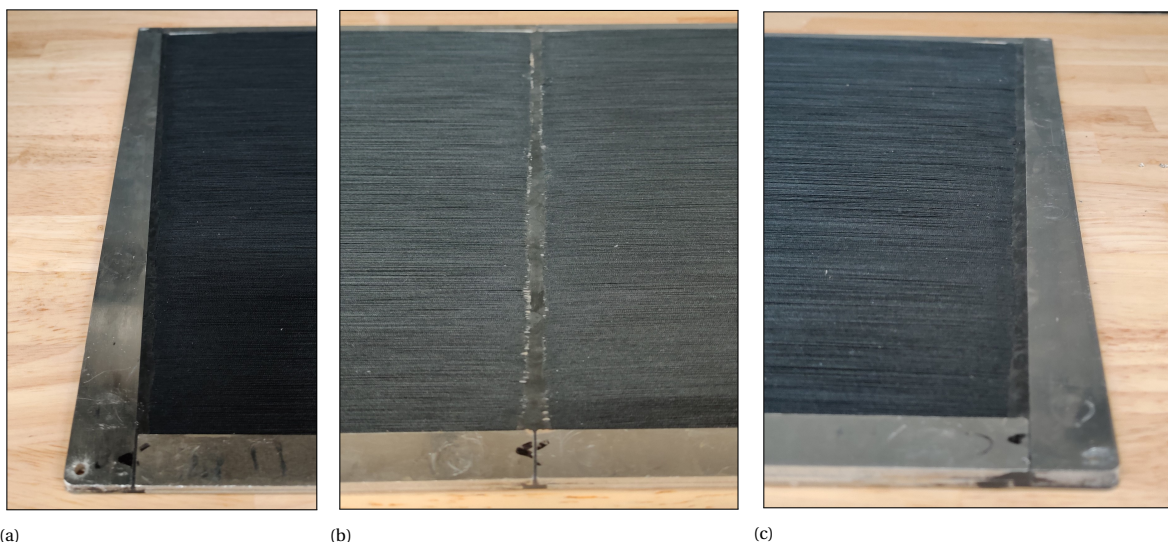


Figure 6.8: Leading edge (a), mid (b) and trailing edge (c) locations finished with moulding clay.

6.3. Test plate assessment

The final test plate deviates from an ideal continuous fibre substrate design in a few ways. The most obvious difference is the solid strip of glue and moulding clay in the middle of the test plate. Fluid flowing through the fibre substrate cannot pass here, and as such it acts as a forward- and backward-facing step. It might result in pressure drag, although the effect was not quantified upfront. A second noticeable difference is the 'bulging' of fibres, depicted in Figures 6.9a and 6.9b. At a quarter and three-quarters of the test plate (streamwise direction), the fibre sheet is thicker (approximately 5 mm) than at the LE, mid-plate and TE (2.5 mm), leading to an approximately 2.5 mm thicker plate at the quarter and three-quarter locations. This bulging is caused by the natural tendency of the fibre sheets to expand when not compressed, and also results from winding around sharp, thin edges. This translates into fewer sheets per unit thickness and thus a higher porosity at these locations. Thirdly, the fibres, being multi-filaments, are not homogeneous in thickness. The theoretical fibre diameter is 250 μm , while using an optical microscope showed a fibre diameter of 200 μm . Lastly, the fibres have inherent roughness, as can be seen in Figure 6.9c. The exact roughness was not quantified.

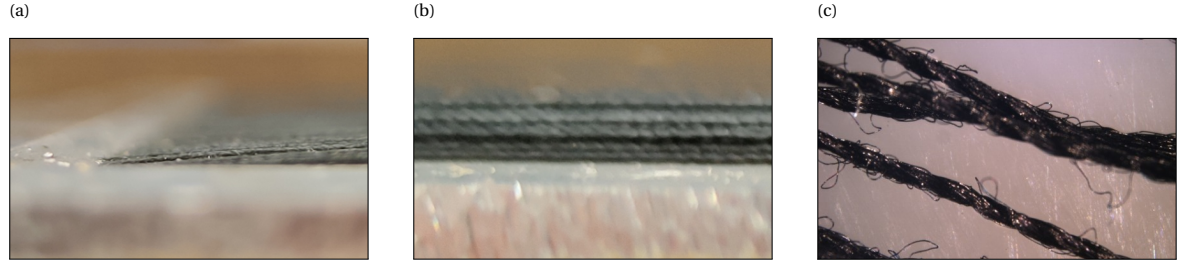


Figure 6.9: Continuous fibre plate imperfections. Fibre sheet thickness at thinnest (a) and thickest (b) locations. (c) Fibre roughness, image taken by Centexbel.

Estimations of the permeability are done with two different analytical models for the streamwise (fibre-parallel) permeability (Equation (6.1)) and the wall-normal and spanwise (fibre-normal) permeabilities (Equation (6.2)), taken from der Westhuizen and Du Plessis (1996) and Brusckke and Advani (1993) respectively. These models were chosen after an extensive literature search, which is discussed in Appendix B and of which the results are summarised in Table B.1. Unfortunately, no suitable setup was found to experimentally determine the permeability of the fibre sheets.

$$\frac{K_{\parallel}}{D_f^2} = \frac{(5.299 - 2.157\varepsilon)\varepsilon^2}{192(1 - \varepsilon)^2} \quad (6.1)$$

$$\frac{K_{\perp}}{D_f^2} = \frac{1}{3\sqrt{3}} \frac{(1 - l_h^2)^2}{l_h} \left(\frac{3 \tan^{-1}(\sqrt{(1 + l_h)/(1 - l_h)})}{\sqrt{1 - l_h^2}} + \frac{1}{2} l_h^2 + 1 \right)^{-1}, \quad (6.2)$$

where D_f is the fibre diameter, ε is the substrate porosity, and $l_h^2 = \frac{2\sqrt{3}}{\pi}(1 - \varepsilon)$.

With the permeability estimates from the above-mentioned models, and the theoretical model linking permeability and drag reductions as described in Section 3.3 and linked to experiments in Section 4.2, drag reduction predictions were computed. Due to variability in the fibre sheet thickness (and hence porosity) and uncertainty in the fibre diameter, different scenarios were devised. These are shown in Figure 6.10. Overall, it can be observed that all scenarios yield permeabilities that would lead to substantial drag reductions based on the theoretical model predictions. With the exception of two, all scenarios also would lead to a point of breakdown in the measurable velocity regime. In the case of a larger fibre diameter, the maximum drag reduction decreases, while the breakdown velocity increases. For decreasing fibre sheet thickness (and hence lower porosity), the maximum drag reduction decreases, while the breakdown velocity increases. It should be stressed that these predictions are based on an ideal unidirectional fibrous substrate and with the use of three analytical models (two for the permeability, one for the drag reduction predictions), without experimental validation.

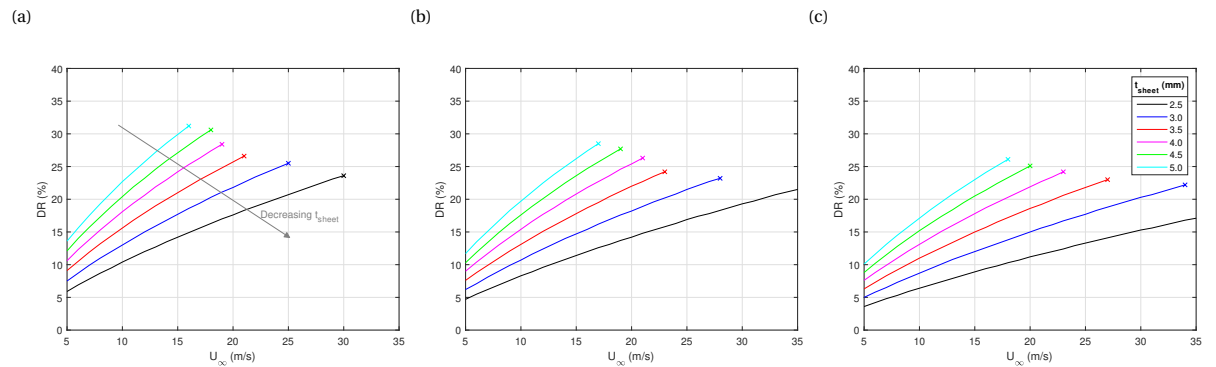


Figure 6.10: DR predictions for different continuous fibre substrate configurations. (a) $D_f = 200 \mu\text{m}$, (b) $D_f = 225 \mu\text{m}$, (c) $D_f = 250 \mu\text{m}$.

7

3D-printed structures

To date, the only experimental study into turbulent boundary layers over streamwise-preferential permeable substrates has utilised a substrate that was 3D-printed (Efstathiou and Luhar, 2020). This method enables a large design space and allows an iterative prototyping process. It also makes it possible to produce samples with different purposes, namely for permeability characterisation or as part of the final wind tunnel test plate, based on the same unit cell design. The combined benefits of iterative prototyping and experimental characterisation of the permeability was important since no analytical models exist that predict the permeability of an arbitrarily designed structure. This chapter presents the topics related to the design, manufacturing and assessment of the test-plate covered in a 3D-printed porous structure, from hereon referred to as "3D-printed plate". For sake of brevity, only the final design is covered in this chapter. A description of the full prototyping phase is given in Appendix C. Section 7.1 shares this design and the design process and covers the unit cell, permeability sample and final test plate designs. Section 7.2 describes the printing methodology. Section 7.3 presents the methods and results of the topography characterisation, specifically the pore size and surface roughness analyses. Section 7.4 presents the method and results of the permeability characterisation. Finally, an assessment of the test plate is given in Section 7.5.

7.1. Design and design process

The design process of the 3D-printed test plate included a prototyping phase in which different designs and print settings were examined. This process and the lessons learnt are discussed in Appendix C. Overall, it was challenging to obtain small pores that yielded the desired permeability, without the pores being too small such that printed samples would be clogged. This section deals with the final design, going through the conceptual design (Section 7.1.1), the design process (Section 7.1.2), the permeability sample (Section 7.1.3) and the wind tunnel test plate (Section 7.1.4).

7.1.1. Conceptual design

Figure 7.1 shows the unit cell design. It is a hexagon with an extra wall connecting two vertices and is therefore dubbed a 'half-hexagon'. All hexagon faces and the extra wall have square pores. There are four design parameters: (1) the hexagon diameter (1.35 mm), (2) the wall thickness (0.2 mm), (3) the pore diameter (0.25 mm) and (4) the pore-to-pore streamwise spacing (1.25 mm). The extra wall was added during the prototyping phase to further limit the wall-normal permeability. Square pores were used to improve file preparation time and pore quality. The wall thickness was chosen as thin as possible while maintaining enough structural integrity. The pore size was chosen as small as possible while ensuring that pores were not clogged anywhere in the permeability sample or the wind tunnel test plate parts.

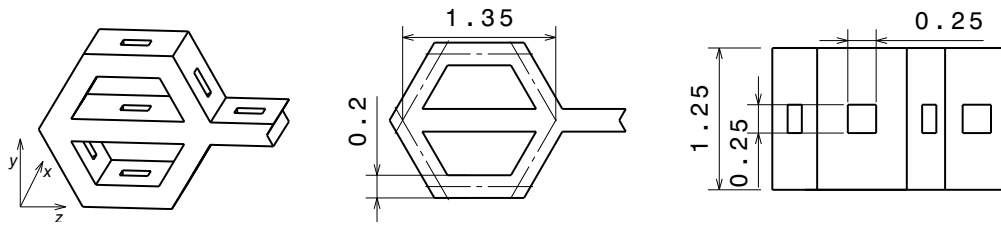


Figure 7.1: Unit cell design. From left to right: isometric view, front view and top view. Axis system in isometric view represents principal permeability directions K_x , K_y and K_z , corresponding to streamwise, wall-normal and spanwise directions in wind tunnel experiments. Dimensions in mm.

7.1.2. Design process

Figure 7.2 illustrates the different steps of the design process. Unit cell and small sample designs were created in CATIA. For the permeability samples, the outer ring was designed in nTop Platform. STL files (triangular meshes) from CATIA and nTop Platform were (repeated and) merged in Rhino 6 to create the final STL files for use in dedicated 3D-printing software. This step was required since neither CATIA nor nTop Platform was able to render STL files for large scale structures with small details within the available computational resources.

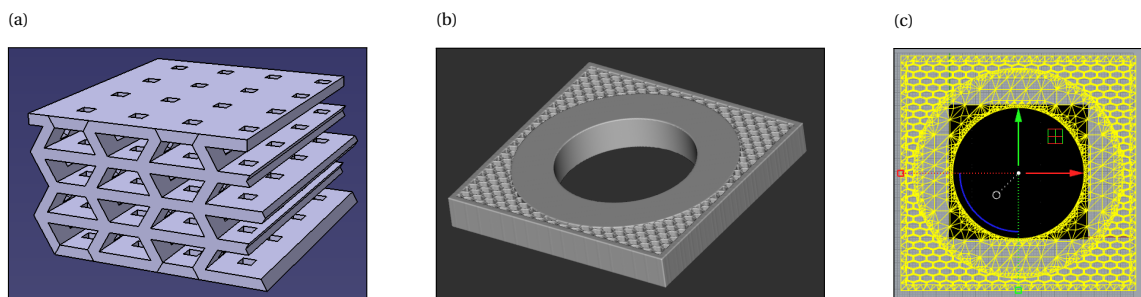


Figure 7.2: Design process steps. (a) Unit cell and small samples in CATIA V5R21. (b) Permeability sample outer region in nTop Platform. (c) Mesh merging in Rhino 6.

7.1.3. Permeability sample design

Figure 7.3 shows an example of a permeability sample, more specific in the y -direction, with a thickness of approximately 10 mm. The sample's permeable region matches the permeability measurement setup pipe inner diameter (50 mm) and fits exactly in the dedicated measurement chamber (100 mm \times 100 mm) (further described Section 7.4.1). The outer honeycomb structure was chosen for material saving purposes. Samples with different thicknesses were produced and measured, which is further covered in Section 7.4.2.

7.1.4. Test plate design

The build volume of the printer used (covered in Section 7.2) is smaller than the test plate dimensions. Therefore, the test plate was manufactured by assembling multiple 'tiles' within one mould. The mould was taken from a similar study into compliant coatings and therefore known to fit well in the experimental setup. A rectangular volume of 797.3 mm \times 342.3 mm \times 3.7 mm was filled by the 3D-printed permeable structure, consisting of eighteen parts (3.7 mm thick) in a 6 \times 3 grid. Fifteen parts were as large as possible (approximately 146 \times 56 mm) and constrained by the printer build volume, while the last three parts were tailored to fill up the remainder. Figure 7.4 shows an example of such a wind tunnel test plate part.

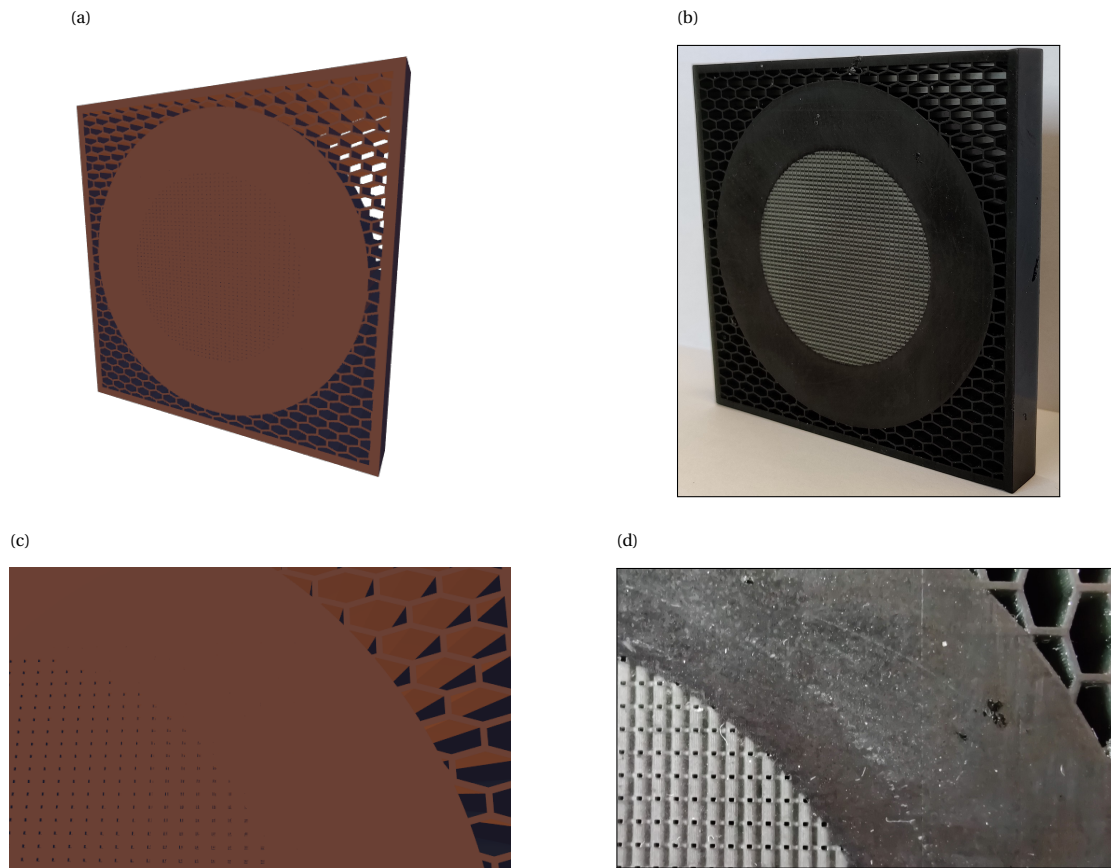


Figure 7.3: Example of permeability sample (y -direction, $t \approx 10$ mm). (a, c) Schematic render. (b, d) Physical realisation. (a, b) Full view. (c, d) Zoomed-in view.

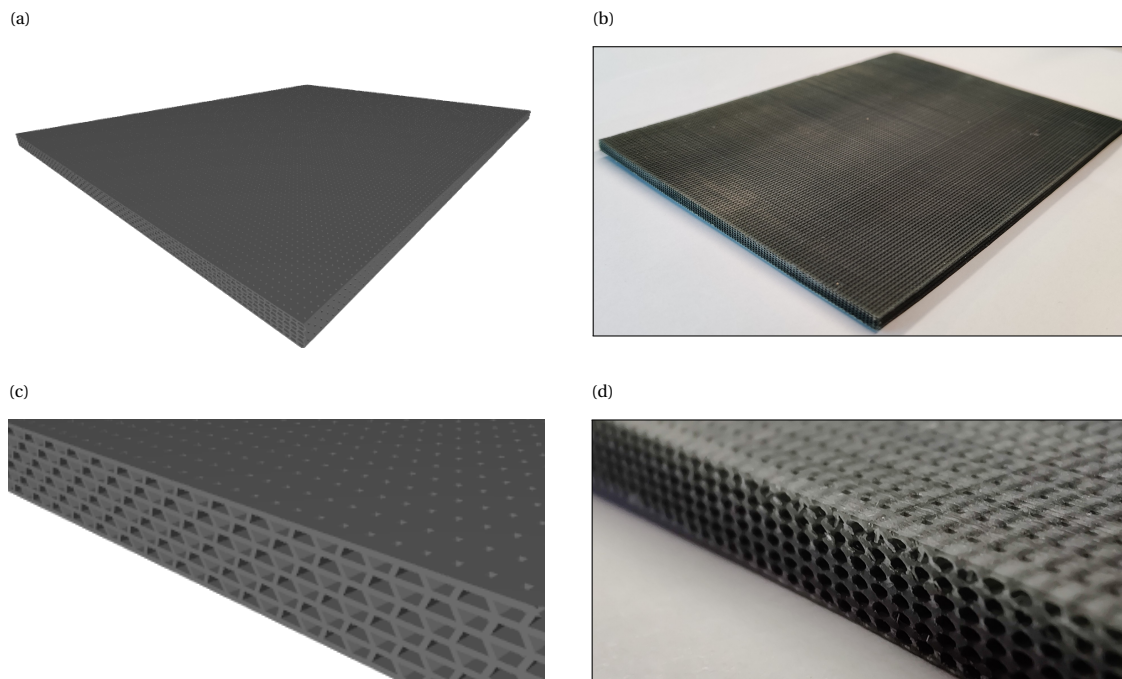


Figure 7.4: Example of wind tunnel test plate part. (a, c) Schematic render. (b, d) Physical realisation. (a, b) Full view. (c, d) Zoomed view.

7.2. Printing methodology

The designed structures were printed with a Prusa SL1 in the Shaping Matter Lab at the AE Faculty of TU Delft. This printer outperformed the Formlabs Form 3 in terms of printing resolution and speed in the preliminary prototyping phase, and was found to be the best printer available for this research. It is based on the Mask Stereolithography (MSLA) working principle, which is briefly explained in Section 7.2.1. Then, the printing and post-processing procedures are laid out in Section 7.2.2.

7.2.1. Theoretical background

3D printing, or additive manufacturing, is a rapidly growing manufacturing technique that enables the design and production of structures with shapes or specific properties that cannot be achieved through conventional manufacturing techniques such as cutting or milling. SLA printing is one of the many different methods used in additive manufacturing, whereas MSLA is yet another subset within the SLA printing technology. The field is extensive and for further information on the topic, the reader is referred to Gibson et al. (2010). Given the scope of this thesis, the theoretical background on MSLA addresses only the basic, relevant concepts.

Figure 7.5 illustrates the working principle of MSLA printing. Objects are printed in upside-down orientation in discrete steps ("layers") on a solid plate ("build plate") that moves upward during the printing process. For every layer, a bath ("tank") of liquid photopolymer resin is selectively exposed to UV-light masked by an LCD screen in which individual pixels can be turned on and off. This light cures the resin in the bottom of the tank on a transparent film (Fluorinated Ethylene Propylene Polymer, or FEP), creating the designed pattern for that layer. In the curing process, the layer fuses to the previous layer. Subsequently, the new layer is "peeled" from the FEP film, often by a slightly tilting resin tank. The build plate then moves up slightly, creating a small gap between the FEP film and the just-printed layer, where new liquid resin enters that can be cured in the next layer. This process of light exposure, peeling and moving up the build plate is repeated until the entire solid object is printed.

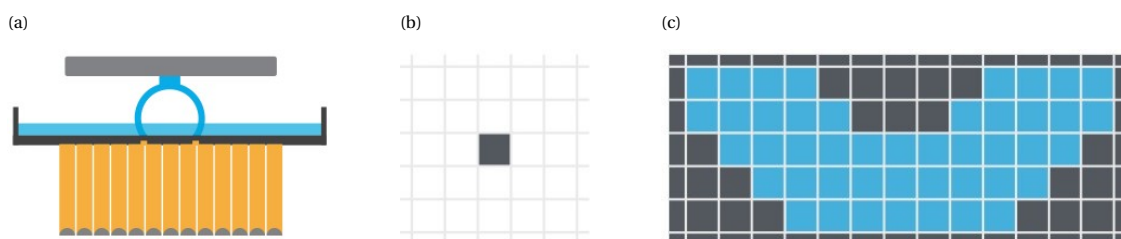


Figure 7.5: Working principle of MSLA printing. Images taken from Formlabs (2017). (a) Front view: selective exposure to light masked by LCD. (b) Top view: minimum pixel size. (c) MSLA deactivates pixels on an LCD photomask to let light through.

The highest achievable resolution (or smallest level of detail) depends on the resin and the printer. In general, resins consist of a monomer, photoinitiator and UV absorber. The absorber is used to control the penetration depth of the UV light and thus influences to what extent light 'bleeds' through a layer to the previous layer, where one might aim to have no cured resin. As such, the absorber can influence the resolution in the build (z -)direction. The smallest possible discrete step of the build plate is the other parameter dictating the z -resolution. For MSLA printing, the xy -resolution is mainly dictated by the pixel size. A general rule of thumb is that the smallest achievable pore size is approximately four times the pixel size (Gong et al., 2015, 2017). These studies have shown the possibility of reliably printing true microfluidic channels (cross-sections of $18 \mu\text{m} \times 20 \mu\text{m}$) with custom-made SLA printers and specially tuned resin. Lastly, the light exposure time also influences the level of detail of the printed object. A higher exposure time ensures a higher degree of solidification, but can come at the cost of excessively curing around the targeted area and potentially closing off intended pores.

7.2.2. Printing and post-processing procedure

Print files were prepared and generated with PrusaSlicer, dedicated for Prusa printers and based on the open-source project Slic3r. Supports were not necessary except for the x -permeability sample, since the building orientation aligned with the direction of highest strength in all other prints. Table 7.1 gives the main print settings. Within the scope of this research, it was decided to use stock resin best suited for high detailed prints on the Prusa SL1 (Prusa Tough Black). The decision for these settings was based on the prototyping phase described in Appendix C. Printing time was approximately 10 hours for the permeability samples (a maximum of two per print) and approximately 15 hours for the wind tunnel test plate parts (a maximum of three per print). More parts per print required a resin refill, which in turn caused misalignment of the two layers before and after the refill was performed.

Table 7.1: Settings for 3D-printing.

Support thickness (mm)	Penetration depth (mm)	Pad thickness (mm)	Layer height (μm)	Exposure time (s)
0.6	0.4	1	4.0	25

All prints were post-processed via at least three multi-stage cleaning cycles followed by a 24-hour drying period in a food drying oven. Cleaning consisted of a five-minute bath in isopropyl alcohol (IPA) (the first time in a Formwash, all subsequent times manually), followed by a three-minute period in an ultrasonic cleaner with tri(propylene glycol) methyl ether (TPM) and finally a thorough drying with pressurised air (4 bar). The multiple cycles ensured that all residue (uncured resin) was removed from the porous structures. Permeability samples were also post-cured (30 minutes at 60°C) to ensure structural rigidity in the permeability measurements. The wind tunnel test plate parts were not post-cured, as their flexibility aided in the process of attaching them to the test plate mould.

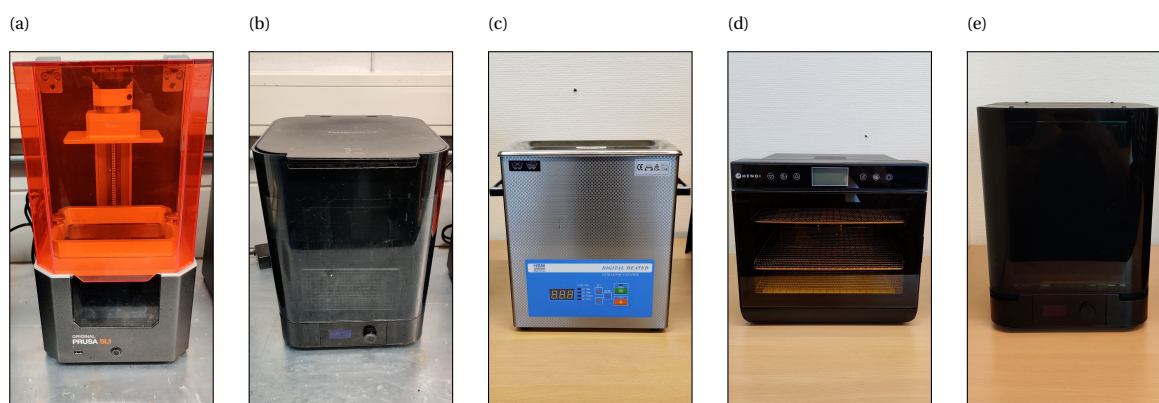


Figure 7.6: Apparatus used in printing process. (a) 3D-printer: Prusa SL1. (b) Washing machine: Formlabs Form wash. (c) Ultrasonic cleaner: HBM GL Serie 4 Liter. (d) Drying oven: HENDI Food dehydrator, item 229064. (e) Curing device: Formlabs Form cure.

7.3. Topography characterisation

The topography of the 3D-printed structures was characterised through two analyses: a pore dimension analysis and a surface roughness analysis, covered in Sections 7.3.1 and 7.3.2 respectively. The former is relevant to assess the reliability of the printing process. The surface roughness analysis is relevant to be able to assess potential surface roughness effects in the wind tunnel experiments. Scans were performed with an optical microscope (Keyence One-Shot 3D VR-5200) at 80x & 120x magnification and pore dimensions and surface profiles were measured within the supplier software (Keyence VR-5000). Data post-processing and computation of statistics was performed with MATLAB.

7.3.1. Pore dimension analysis

The reliability of the printing process is determined through the pore dimension analysis. This analysis has three objectives. Firstly, it is crucial to determine whether the pores are similar in the permeability sample and the wind tunnel test plate parts. Large discrepancies could mean that results from the permeability characterisation do not translate to the wind tunnel measurements. Secondly, it is relevant to know whether pores are consistent in terms of size throughout the printed parts. Large inconsistencies could lead to differences in permeability across the WT test plate. Lastly, it is valuable to know whether the printed objects accurately reflect the design. This could aid in future design and production processes.

The pore dimension analysis is performed on the wall-normal pores for three reasons. First, the wall-normal permeability is expected to be the limiting factor in the wind tunnel experiments, dictating the region in which a potential drag reduction can be detected. Secondly, the wall-normal pores are identical to the spanwise pores and smaller than the streamwise pores, on which therefore similar or better printing reliability is expected. Lastly, the wall-normal pores are perfectly orthogonal to the microscope optical axis when laying the wind tunnel test plate parts down flat. In contrast, the spanwise pores are angled at 60° due to the hexagonal structural design. Therefore the wall-normal pores are the most accessible to characterise. The three y -permeability samples were scanned on both sides, at three locations with twelve pores per location. The eighteen wind tunnel test plate parts were scanned on the top side, which forms the permeable surface in the wind tunnel experiments, also at three locations with twelve pores per location. Figure 7.7 shows examples of scanned images.

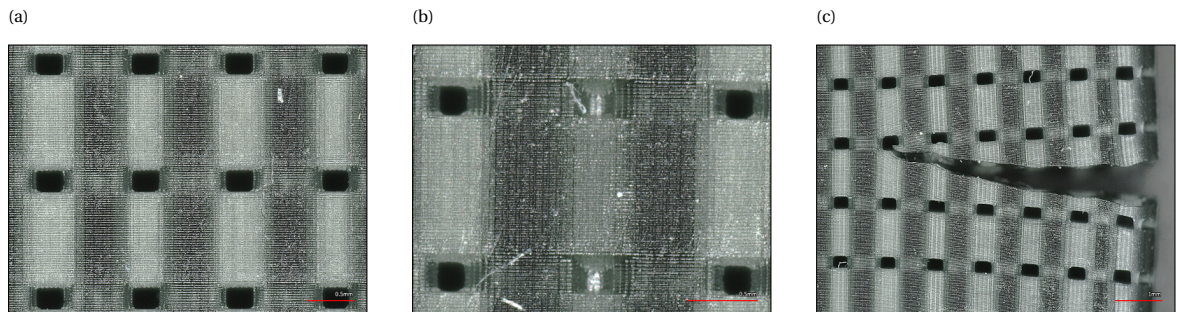


Figure 7.7: Examples of scanned images for topography characterisation of 3D-printed samples. Successful (a), partially clogged (b) and cracked (c) regions.

Table 7.2: Statistics on dimensions of wall-normal pores. Mean (μ), different w.r.t. target (Δ) and standard deviation (σ). Δ in %, length (L) and width (W) in μm , area (A) in $10^4 \mu\text{m}^2$.

Measurement	Datapoints (#)	μ_L	Δ_L	σ_L	μ_W	Δ_W	σ_W	μ_A	Δ_A	σ_A
Permeability samples	216	238	-4.8	10	304	+21.6	29	7.3	+16.8	0.9
Wind tunnel test plate parts	645	234	-6.4	13	290	+16.0	34	6.8	+8.8	1.2
Difference in mean (%)		-1.7			-4.6			-6.8		

Table 7.2 presents the main statistical results of the pore dimension analysis. Overall, the pores are slightly shorter and significantly wider than the design, resulting in a rectangular rather than a square shape on average. The relationship between pore length and width is visualised in Figure 7.8. Nearly all data points lie under the imaginary line passing through the origin with unity slope, while the trend also has a slope smaller than unity. The former observation confirms the rectangular, wide shape of all pores, while the latter indicates that the variability in pore width is larger than in length. This is also reflected in the standard deviations of the length and width. The difference between the mean length and target length is approximately half a layer height, as is its standard deviation. The difference between the mean and target widths is approximately one print display pixel size. It is thought that the deviation in width is caused by the fact that the print display pixels at the pore edges are partially turned off to selectively let some light through (anti-aliasing). This intensity might not be enough to solidify the resin enough such that the pore ends up wider than it is supposed to, on average one pixel.

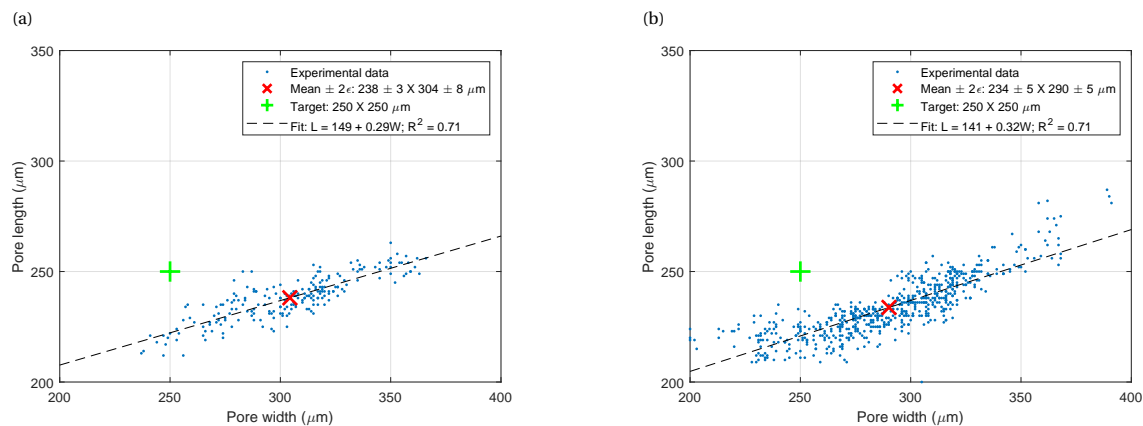


Figure 7.8: Dimensions of wall-normal pores. (a) Permeability samples. (b) Wind tunnel test plate parts.

The pores for the wind tunnel test plate parts are slightly smaller than those of the permeability samples, especially in terms of width. This leads to an overall difference in pore area of approximately -6.8% . The direct relationship between pore size and permeability is unknown, but a plausible rule of thumb is that the permeability is proportional to the pore area in the case of identical pores throughout the permeable material. This is because the pore area facilitates the flow passage. Also, the permeability is expressed in area units. Therefore the wind tunnel test plate parts on average might have a lower permeability than those given by the measurements described in Section 7.4. Figure 7.9 visualises the statistics of all individual pore dimension measurements. The difference in overall mean values between the permeability samples and wind tunnel test plate parts is on par or even smaller than the differences between part mean values (across three measurements), between some individual measurements (within a part) or even within some individual measurements (one box in the figure). In general, variability between and in measurements are larger than the expected measurement error that can arise from an incorrect determination of the pore edge, which is done by hand in the Keyence software and conservatively estimated to be not more than 5%. For the permeability samples, four part mean values of the pore area lie very close to the overall mean, providing confidence in this mean value. For the wind tunnel test plate parts, a slightly higher degree of variability is observed. This could be due to the fact that the permeability samples were printed on the same location on the printer build platform, whereas the wind tunnel test plate parts were printed at different locations simultaneously.

Overall, three main takeaways of the pore size analysis are:

- The pores of the prints deviate from the design. They are slightly shorter, significantly wider and overall have a larger area.
- The pores of the wind tunnel test plate part are sufficiently close to those of the permeability sample in terms of size. It is expected that on average, the results from the permeability characterisation will reflect the permeability of the wind tunnel test plate.
- A relatively large variance exists between wind tunnel test plate parts and even within a part. This could result in local differences in permeability across the test plate.

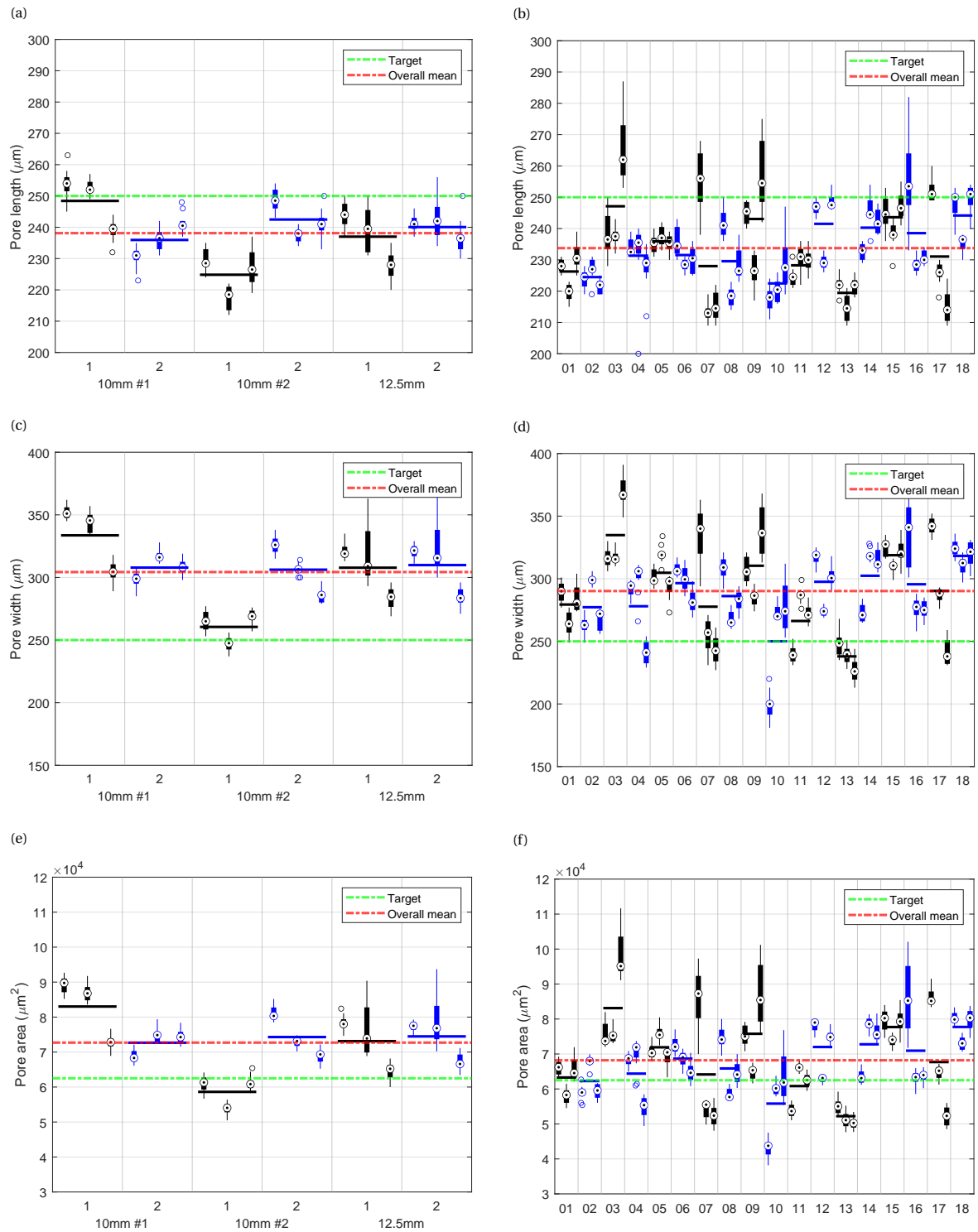


Figure 7.9: Statistics on dimensions of wall-normal pores. Each box denotes a measurement of twelve pores at one location. (a, b) Pore length. (c, d) Pore width. (e, f) Pore area. (a, c, e) Permeability samples: three parts, two sides per part, three locations per side, twelve pores per location. (b, d, f) Wind tunnel test plate parts: eighteen parts, three locations per part, twelve pores per location.

7.3.2. Surface roughness analysis

Whether the roughness of a surface influences the friction drag depends on the ratio of the surface roughness to the viscous length scale. Therefore a surface roughness analysis of the wind tunnel test plate parts has been conducted. Roughness profiles 2.84 mm in length were sampled along the streamwise direction. All eighteen test plate parts were sampled at three locations on the surface exposed to the freestream, with three profiles per location, yielding a total of 162 measured profiles. In some profiles, outliers occurred as local transparencies resulting from the thin walls were perceived by the optical microscope as a trough in the profile. Outliers larger than six times the median residual were removed. This relatively high threshold ensured that true, locally increased roughness would not be unjustly discarded. The cleaned profile was subsequently filtered using a moving average filter (21 points ≈ 0.078 mm). This process is shown in Figure 7.10a and yielded a filtered roughness profile, shown in Figure 7.10b. Peaks and troughs were identified as points with an absolute value larger than the absolute arithmetic mean of the roughness profile (R_a). The distance between the mean peak and trough heights was estimated to be the bandwidth of the roughness profile. Figure 7.10c shows the absolute roughness profile including R_a . R_a is the most widely used one-dimensional roughness parameter, but one could argue that the roughness height (h) as defined in Raupach et al. (1991) would be more accurately reflected by the profile bandwidth. As such, both metrics are used to assess the surface roughness.

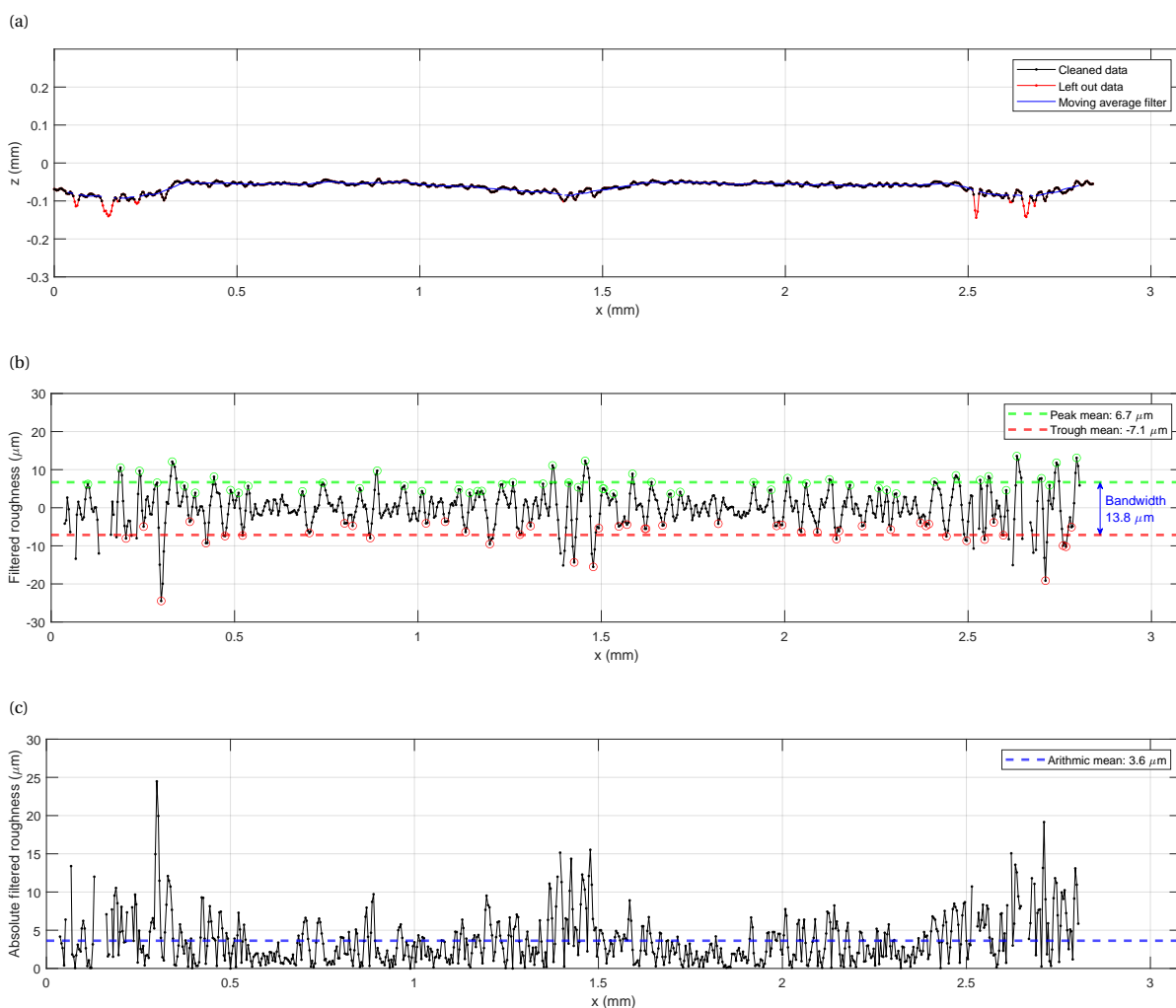


Figure 7.10: Example of roughness profile and determination of roughness metrics. Example taken to have a bandwidth value closest to the overall mean bandwidth. (a) Raw profile, including left out data and moving average filter. (b) Roughness profile, including identification of peaks and troughs and bandwidth computation. (c) Absolute roughness profile, including mean absolute roughness computation.

Figure 7.11 shows the overall statistics on the wind tunnel test plate part roughness in terms of R_a and roughness profile bandwidth. Both histograms resemble a normal distribution, symmetric around mean values of 3.6 and 13.8 μm respectively. Table 7.3 translates these mean values in terms of viscous units at the four freestream velocities tested during PIV experiments and for which u_τ was determined. With the exception of the bandwidth at 30 m/s, all values are smaller than a viscous length scale. Even when considering all values for the bandwidth larger than the mean value, the roughness height stays within the range for which dynamically smooth flow can be expected, i.e. $0 < h^+ < 5$ (Nikuradse, 1950). In conclusion, the 3D-printed wind tunnel test plate parts are smooth enough to assume dynamically smooth flow during the wind tunnel experiments.

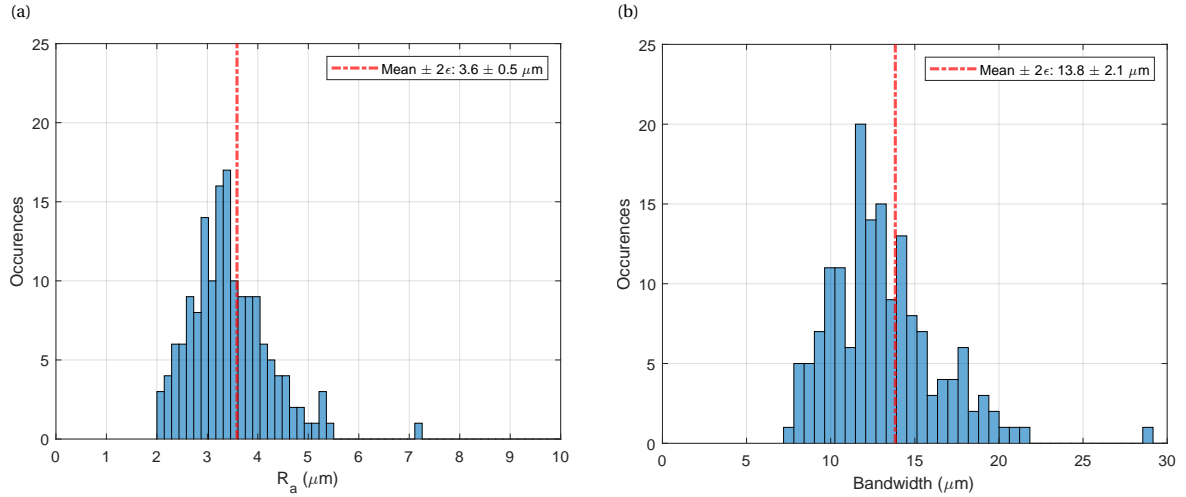


Figure 7.11: Statistics on wind tunnel test plate part roughness. $N = 162$. (a) Arithmetic absolute mean roughness (R_a). (b) Bandwidth (mean peak-valley distance).

Table 7.3: Surface roughness metrics expressed in viscous units. R_a = arithmetic absolute mean, BW = bandwidth. Viscous length scale based on PIV measurements over 3D-printed surface at Station 4. Inconsistencies in ratio between R_a^+ and BW^+ due to rounding.

U_∞ (m/s)	5	10	20	30
R_a^+	0.05	0.11	0.20	0.30
BW^+	0.21	0.41	0.78	1.13

7.4. Permeability characterisation

The permeability of the 3D-printed structures was characterised experimentally in a gas flow rate - pressure drop setup. Simultaneously measuring these two quantities across a sample yields its permeability. Further background information on this measurement technique is given in Appendix D, and the design of the samples for these measurements is discussed in Section 7.1.3. The method, including physical setup, measurement procedure, data processing procedure and measurement plan, is explained in Section 7.4.1. The results are presented and discussed in Section 7.4.2.

7.4.1. Experimental methodology

The setup used for characterising the permeability (from now on referred to as 'permeability rig') was developed and validated in prior work at the LSL of the TU Delft (Hemmen, 2018). The initial purpose of the rig was to measure pressure drops across perforated sheets, in the context of hybrid laminar boundary layer control. Other studies used the experimental rig explicitly for determining the permeability of porous aluminium used in airfoil trailing edges for noise abatement. As such, the rig was considered suitable for characterising the permeability of the 3D-printed structures.

Physical setup

Figure 7.12a gives a schematic representation of the permeability rig. It is supplied with pressurised air at ten bar which then is down-regulated to five bars, matching the operating specifications of the subsequent mass flow controller. Via flexible hoses and a diffuser pipe, the air is lead into the main pipe with an inner diameter of 50 mm. This main pipe consists of two parts; in between, the test section holding the permeability sample is clamped. Pressure taps connected to a differential pressure transducer are located up- and downstream of the test section. Air flow is exhausted at the end of the pipe into the ambient. The pipes and other components are mounted vertically on an X-beam construction as shown in Figure 7.12b.

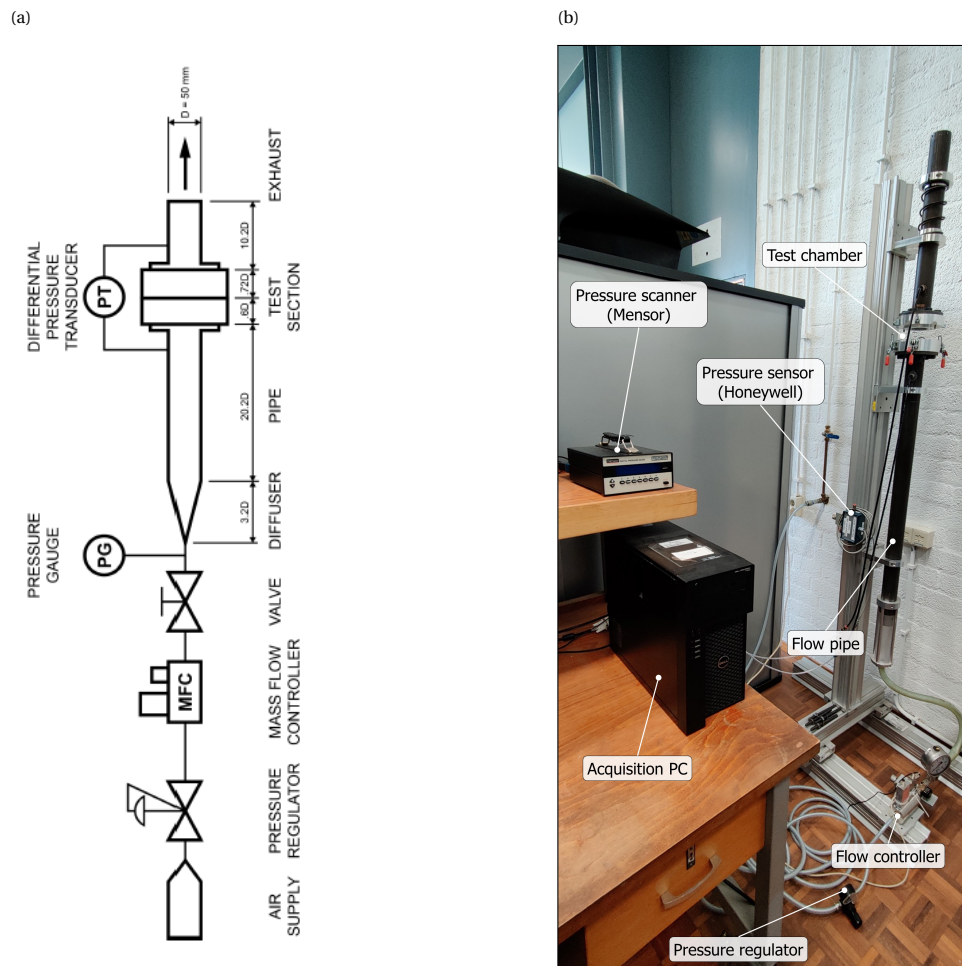


Figure 7.12: Setup for permeability characterisation. (a) Schematic (Hemmen, 2018). (b) Image.

Figure 7.13a shows how the test section sample holders are bolted to the main pipe, and how the downstream pipe component is assembled to the X-beam. The interior design of the holders is shown in more detail in Figure 7.13b. They can accommodate square and circular samples, with sides and diameters of 100 mm and 90 mm respectively. The inner diameter matches the main pipe diameter. The holders are clamped together by four adjustable clamps, allowing samples of varying thicknesses. O-rings are used at all points of connection to prevent air leakage: one between the holders and the main pipes, and two between the holders and the samples. In closed position, a spring connected to the downstream pipe is compressed; when opening the test section, the spring decompresses and holds the downstream pipe and sample holder in position. As a result permeability samples can be swapped with two free hands.

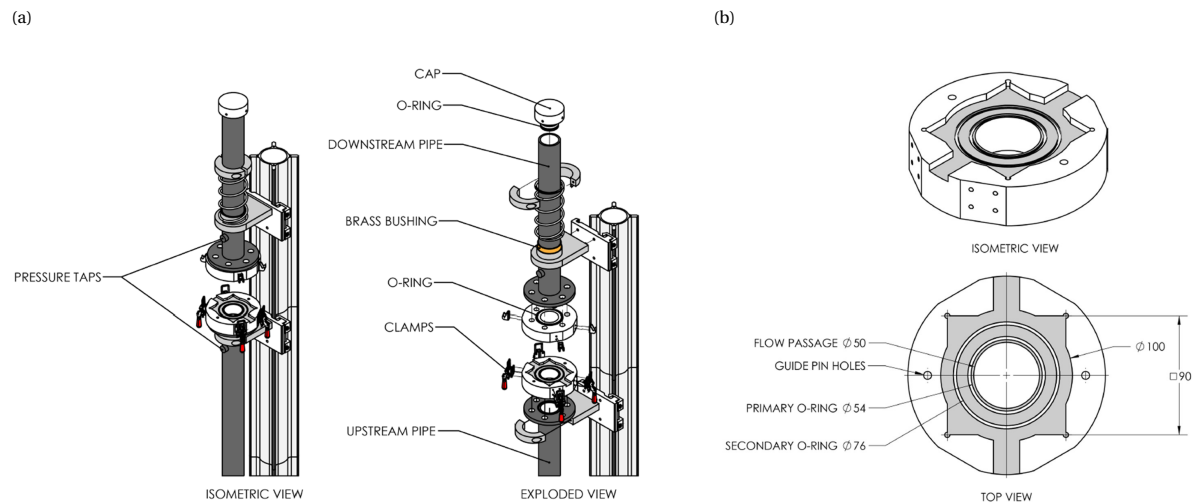


Figure 7.13: Technical drawings of permeability setup test section. (a) Assembly of test section sample holders, pipes and X-beam. Cap only used for leakage tests. (b) Test section sample holder. Grey shading indicates seating surface for permeability samples. Both images adapted from Hemmen (2018).

Two types of measurement equipment were used: a mass flow controller and a differential pressure transducer. The mass flow controller is a Bronkhorst F-202AV-M20-DGD-55-V, with a maximum capacity of 270 Ln/min. It is computer-actuated and registers mass flow rate and flow temperature at an acquisition rate of 5 Hz. Two differential pressure transducers were used: a Mensor 2101 and a Honeywell SSC-SAAN600MDAA5, for low and high ranges of pressure drops, respectively. This enabled the ability to characterise both low permeabilities, for which high pressure drops are required, and higher permeabilities, for which accurate readings of low pressure drops are necessary. Table 7.4 summarises the measurement equipment properties. All equipment was connected to, and controlled via, LabVIEW.

Table 7.4: Measurement equipment in the permeability characterisation setup.

Type	Equipment	Range	Rated accuracy
Mass flow controller	Bronkhorst F-202AV-M20-DGD-55-V	up to 270 Ln/min	$\pm (0.5\%Rd + 0.1\%FS)$
Differential pressure transducer	Mensor 2101	-1 to 16 kPa	$\pm 0.010\%FS$
Differential pressure transducer	Honeywell SSCSAAN600MDAA5	± 60 kPa	$\pm 0.25\%FS$

Hemmen (2018) discusses several aspects concerning the validity of the setup: pressure tap placement, airtightness and the state of flow. The main conclusions are summarised here. Pressure tap placement upstream was performed according to standards described in literature. The downstream pressure tap placement was assessed by comparing its measurements to static pressure probe measurements at locations between the test section and the pressure tap, and downstream of the pressure tap. The variation in pressure at all measured locations was less than 0.3%, indicating that the pressure recovery was completed at all locations, and thus also at the downstream pressure tap. Airtightness was confirmed in an overnight leakage test downstream of the mass flow controller.

Regarding the state of the flow, Hemmen (2018) mentions that the entrance length is of importance, to assess whether the flow has fully developed, i.e. the BL velocity profile remains unchanged. In this, he assumes laminar flow, giving Equation (7.1) as the definition for the entrance length (L_e). The state of pipe flow, laminar or turbulent, depends on the diameter-based Reynolds number (Re_D), defined as Equation (7.2), where D is the pipe inner diameter. Pipe flow is laminar for $Re_D < 2300$, transitional for $2300 < Re_D < 4000$, and turbulent for $Re_D > 4000$.

$$\frac{L_e}{D} = 0.06Re_D \quad (7.1)$$

$$Re_D = \frac{\rho U D}{\mu} \quad (7.2)$$

Based on the rig dimensions, fully developed pipe flow at the test section is guaranteed up to $Re_D = 347$. Hemmen (2018) however argues that the BL already starts developing at the flexible hoses and throughout the diffuser section, and concludes that it is likely that nearly fully developed pipe flow is reached up to $Re_D = 2000$. Regardless of whether this assumption holds, he does not address whether the flow in this particular setup will be laminar or turbulent, which is thought by the author of this report to be a shortcoming of his assessment. In fact, based on the main pipe inner diameter and assuming sea level standard atmospheric conditions, it can be shown that the flow is laminar only up until approximately 30% of the full range of the flow controller, and is turbulent above 50%.

Measurement procedure

In general, the measurements consisted of setting a desired mass flow rate and measuring the consequential pressure drop across the 3D-printed permeability sample. Every permeability sample was measured at least twice (once in each orientation). Before each measurement, the pressure differential was zeroed. This is necessary to account for pressure differences between the two pressure taps resulting from hydrostatic effects, since they are located at a height difference of approximately 20 cm. This difference is approximately 2 Pa and thus non-negligible for the low pressure drops measured in the samples with higher permeability.

For each measurement, a sequence of linearly-spaced mass flow rates was defined as an input, with values increasing from zero to a set maximum value, and subsequently decreasing back to zero. This increasing-decreasing sequence was done to check for potential hysteresis effects. The maximum flow rate was set to 30% of the flow controller capacity. Preliminary measurements showed that for certain samples, higher flow rates (and thus higher pressure drops) yielded inconsistent and sometimes non-physical (negative) permeability values. Although this occurred only for specific samples, it was decided to keep the flow rates within the same range for all samples in the final measurements. A further discussion of this topic including the preliminary permeability measurement results is provided in Appendix D.2. For each measurement point, data recording started when the measured mass flow rate was within 0.5% of the set value. Each recording took 15 seconds at 5 Hz, yielding 75 raw data points per measurement point. Mass flow rate, flow temperature and pressure differential across the permeability sample were recorded. One measurement took approximately 20 minutes.

Data processing procedure

Processing of the measurement data was performed in MATLAB. Each measurement point was consolidated by taking the mean of the 75 raw data points. For each measurement, a transformed version of the compressible Forchheimer's equation (Innocentini et al., 2000) was fitted to all measurement points through linear regression, evaluating P_0 , μ_0 and ρ_0 at the inlet (denoted with subscript i):

$$Y = \alpha X_1 + \beta X_2, \quad (7.3)$$

where

$$Y = \frac{P_i^2 - P_a^2}{2P_i \Delta x} \quad (7.4)$$

and

$$X_1 = \mu_i u_d, \quad X_2 = \rho_i u_d^2. \quad (7.5a, 7.5b)$$

Subsequently, permeability values were extracted from the fitting parameters α and β :

$$\alpha = \frac{1}{k_1}, \quad \beta = \frac{1}{k_2}. \quad (7.6a, 7.6b)$$

This fitting procedure was validated on experimental data collected by Rubio Carpio et al. (2019), yielding a permeability of 2.6×10^{-9} , within $\pm 5\%$ of the published value of 2.7×10^{-9} . All fitted models were evaluated on the quality of the fit (R-squared) and the statistical significance of fitting parameters α and β (p -values). The reader is referred to Appendix A for more details on these statistical parameters.

Measurement plan

For all the 3D-printed designs, the permeability was characterised in the three directions, i.e. K_x , K_y and K_z . As such, every sample represented a different design-direction pair. Repeatability was tested by measuring the same sample in different orientations ('normal' and 'flipped'), the same sample on different dates, and different samples of the same design-direction pair. Furthermore, samples of the same design-direction pair but with different thicknesses were tested to assess whether the obtained permeability indeed is independent of sample thickness and thus solely dependent on the design. All performed measurements can be found in the overall results in Table 7.5.

7.4.2. Results and discussion

Figure 7.14 shows examples of experimental data and the fitted models for all three permeability directions. Uncertainty in the experimental data is mainly caused by the pressure scanner in the x -permeability measurements, and by the flow controller in the y - and z -permeability measurements. No hysteresis effects occur, as the data points for increasing flow rate overlap with the data points for decreasing flow rate. All fits to the experimental data are considered to be of high quality with a high coefficient of determination ($R^2 > 0.999$) and statistical significance of the permeability fitting parameter ($p < 10^{-30}$). The complete set of results (with all plots) is shared in Appendix D.3. All fits pass through the experimental data points within the error margins and have a y -axis intercept close to the origin ($< \pm 0.5$ Pa for x -direction, $< \pm 10$ Pa for y -direction and $< \pm 5$ Pa for z -direction), which should be the case from a physical point of view since no pressure differential means no flow rate. The slight deviation is to be expected given that the fit minimises the error w.r.t. all data points, which have some measurement uncertainty. Forcing the fit through the origin resulted in slightly higher permeability estimates (3–7%) for all cases, but a lower fitting quality. For the x -sample, a clear linear relationship is observed, whereas for the y - and z -samples, including the Forchheimer term is indeed necessary to account for non-linear effects. The quality of the fits gives confidence in the method for extracting the permeability characteristics.

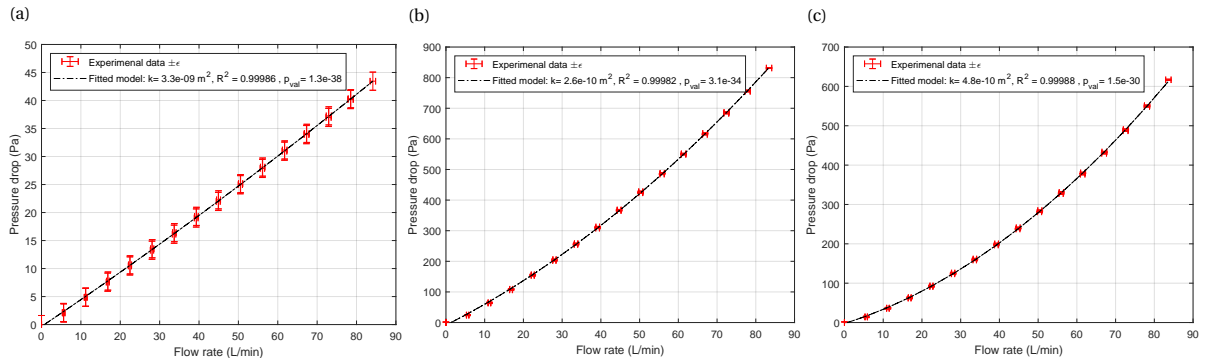


Figure 7.14: Examples of pressure drop - flow rate experimental results and fitted models for permeability characterisation. ϵ = uncertainty based on measurement equipment rated accuracy (Table 7.4). (a) x -direction, 10 mm. (b) y -direction, 10.7 mm. (c) z -direction, 9.7 mm. All data is from sample #1, regular orientation.

Table 7.5 shows the results of all the permeability measurements. Overall, measurements are repeatable, with near-identical values for the regular and flipped orientations of each individual sample. No clear thickness effect can be distinguished, with higher, similar, and lower permeability values for the thicker samples in the x -direction, y -direction and z -direction respectively. Moreover, the difference in permeability values for two different samples with the exact same thickness ($y-1$ and $y-2$ of 10.7 mm) is larger than the difference for varying thicknesses. As such, it is believed that differences in permeability arise due to differences between individual samples, and not due to thickness differences. This implies that the samples were thick enough to contain sufficient repeating unit cells in the flow direction for a homogenised view over which the permeability can be determined. Lastly, the x -permeability is approximately an order of magnitude larger than the y - and z -permeability, hence the design yields a sufficient degree of anisotropic permeability. How this translates into the predicted drag reduction is discussed in Section 7.5.

Table 7.5: Permeability results for the different directions, thicknesses, samples and orientations, as well as averaged values. Orientation: R = regular, F = flipped.

Direction	Thickness (mm)	Sample (#)	Orientation	Permeability ($\times 10^{-10} \text{m}^2$)	Δ w.r.t. avg. (%)
<i>x</i>	10	1	R	32.6	-7.3
<i>x</i>	10	1	F	32.9	-6.4
<i>x</i>	10	1	sample average	32.7	-6.8
<i>x</i>	12.5	1	R	37.4	6.4
<i>x</i>	12.5	1	F	37.7	7.3
<i>x</i>	12.5	1	sample average	37.5	6.8
<i>x</i>	overall average			35.1	
<i>y</i>	10.7	1	R	2.6	11.2
<i>y</i>	10.7	1	F	2.6	12.1
<i>y</i>	10.7	1	sample average	2.6	11.7
<i>y</i>	10.7	2	R	2.0	-15.7
<i>y</i>	10.7	2	F	2.0	-12.0
<i>y</i>	10.7	2	sample average	2.0	-13.8
<i>y</i>	10.7	thickness average		2.3	-1.1
<i>y</i>	13.1	1	R	2.3	0.6
<i>y</i>	13.1	1	F	2.4	3.8
<i>y</i>	13.1	1	sample average	2.4	2.2
<i>y</i>	overall average			2.3	
<i>z</i>	9.7	1	R	4.8	-3.6
<i>z</i>	9.7	1	F	4.8	-3.3
<i>z</i>	9.7	1	sample average	4.8	-3.5
<i>z</i>	11.7	1	R	4.5	3.5
<i>z</i>	11.7	1	F	4.5	3.5
<i>z</i>	11.7	1	sample average	4.5	3.5
<i>z</i>	overall average			4.7	

A last interesting observation is the correspondence between the values for the *y*-permeability and the pore area (Figure 7.9e), which are combined in Table 7.6. The first thinner sample has a larger-than-average pore area, the second thinner sample has a smaller-than-average pore area, and the thicker sample is very close to the average pore area, where the average pore area is taken across all pores of these three samples. This trend corresponds to a larger-than-average permeability, lower-than-average permeability, and close to average permeability, for the first thinner, second thinner, and thicker samples, respectively. Moreover, the differences w.r.t. the average values are similar. It suggests that the relationship between pore area and permeability is proportional, where a given percentage change in pore area yields 1.5 times that percentage change in permeability. This makes intuitive sense as both characteristics are of unit area. It also strengthens the thought that differences in permeability values of the same direction result from differences between individual samples (due to deviation in average pore size), and not due to differences in sample thicknesses.

Table 7.6: Comparison of pore area and permeability values for *y*-permeability samples. Δ calculated w.r.t. overall average. K = permeability, A = pore area.

Direction	Thickness (mm)	Sample (#)	Pore area		Permeability		Δ_K/Δ_A
			($\times 10^4 \text{mm}^2$)	$\Delta(\%)$	($\times 10^{-10} \text{m}^2$)	$\Delta(\%)$	
<i>y</i>	10.7	1	7.8	7.1	2.6	11.6	1.6
<i>y</i>	10.7	2	6.6	-8.6	2.0	-13.8	1.6
<i>y</i>	13.1	1	7.4	1.5	2.4	2.1	1.4
Overall average			7.3		2.3		1.5

With the found relationship between difference in pore area and difference in permeability, it is possible to perform a rough estimation on the difference in γ -permeability of the permeability samples and the wind tunnel test plate parts, given their differences in pore area as presented in Section 7.3.1. A 6.8% smaller average pore area then yields an approximately 10% lower γ -permeability for the wind tunnel test plate parts. This difference is within the variability range of measured γ -permeability values of the permeability samples (Table 7.5). The drag reduction predictions in subsequent analyses take this variability into account by including different scenarios (best-, average- and worst-case), given in Table 7.7. Consequently, no further corrections on the (γ -)permeability of the wind tunnel test plate are performed, and its values are estimated to be equal to the mean overall average values from the permeability measurements. Lastly, it should be kept in mind that the high variability in pore area between the different wind tunnel test plate parts ($\pm 30\%$ from mean value) could translate to large differences in permeability locally ($\pm 50\%$ from mean value).

7.5. Test plate assessment

Figure 7.15 shows the final wind tunnel test plate while Figure 7.16 shows some detailed views. Overall, the test plate is of satisfactory quality. Gaps between individual parts were kept to a minimum and if present, sealed with Scotch Weld Crystal tape. With a $50\ \mu\text{m}$ thickness, this tape is smaller than $5\delta_v$ and therefore not expected to have a significant effect on the measurements. In Section 7.3.2 it was already established that the surface roughness of the 3D-printed parts is such that the plate can be considered hydrodynamically smooth. Parts were flush with the outer rim of the mould.



Figure 7.15: Wind tunnel test plate. Image taken before sealing minor unwanted cavities with tape.

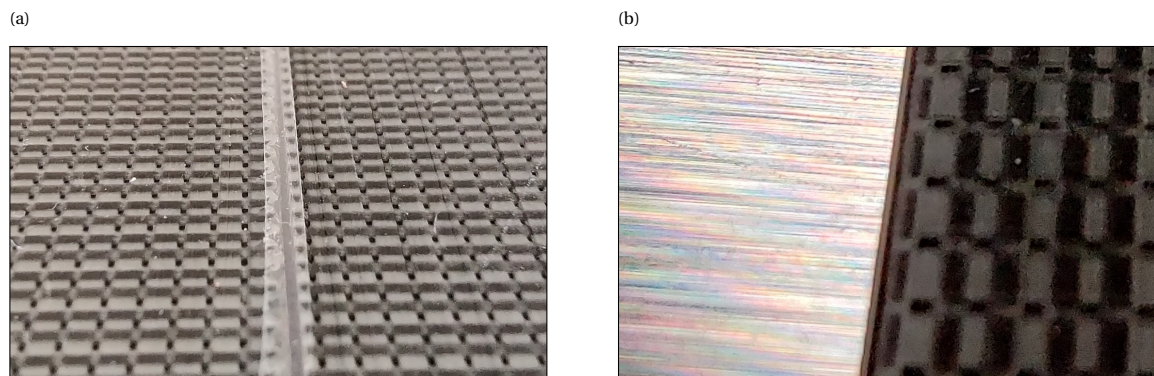


Figure 7.16: Detailed views of wind tunnel test plate. (a) Example of sealing unwanted cavity with tape (flow from left to right). (b) Example of alignment of 3D-printed test plate part with mould edge (flow from bottom to top).

With the permeability characteristics shared in Section 7.4.2, and the theoretical model linking permeability and drag reductions as described in Section 3.3 and linked to experiments in Section 4.2, drag reduction predictions were computed. Due to the slight variability in the permeability measurements, three scenarios were devised. The permeability values are given in Table 7.7 and the predicted DR are shown in Figure 7.17. Overall, it can be observed that the scenarios lie close to one another. The variability in the permeability measurements does not translate to large differences in predicted drag reductions, which are moderate with values of approximately 5 – 7%. It is clear that the best case, with the highest streamwise permeability and lowest wall-normal and spanwise permeabilities, leads to the highest predicted drag reduction and breakdown velocity. Furthermore, the point of breakdown is predicted to be before 10 m/s, relatively low. This can complicate reliably measuring differences in drag, as the error margin of the force sensor increases at lower speeds (where absolute forces are lower).

Table 7.7: Different scenarios for wind tunnel test plate permeabilities to account for variability in permeability characterisation. Permeabilities in 10^{-10} m^2 .

Case	K_x	K_y	K_z
Best	38	2.0	4.5
Average	35	2.3	4.7
Worst	33	2.6	4.8

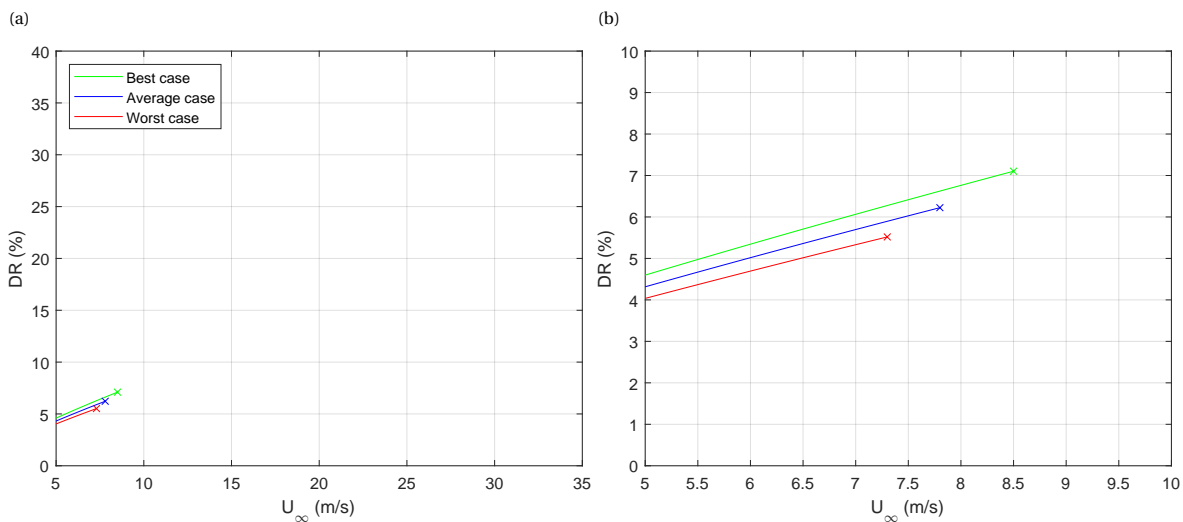
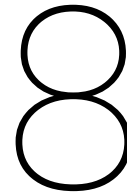


Figure 7.17: DR predictions for different permeability cases of the 3D-printed test plate. (a) View on same scale as Figure 6.10, showing the measurable range of velocities for the drag measurements. (b) Zoomed-in view.

This page has been intentionally left blank.



Concluding remarks on manufacturing of anisotropic permeable substrates

Test plates with three different types of anisotropic permeable substrates were manufactured: two plates covered with different seal furs, one with several layers of continuous streamwise-aligned fibres, and one with 'tiles' of 3D-printed structures. This brief chapter aims to summarise the main findings relating to the manufacturing process and resulting test plates.

First of all, in general, the process was time-consuming, both in terms of the total time window and actual time dedicated to design and manufacturing activities. The time between the first contact and the start of test plate manufacturing was three months for Pieterburen and the seal fur plate, and four months for Centexbel and the continuous fibre plate. The prototyping phase for 3D printing lasted nearly half a year (including a six-week period waiting for printer replacement parts), while the manufacturing of the final 3D-printed test plate took two weeks. Although these activities were performed concurrently, it illustrates the necessity of starting early with experimental preparations, especially when covering new terrain or dealing with external parties. Given these circumstances, unfortunately, not more test plates were manufactured and thus no extensive design parameter sweep could be performed in the wind tunnel experiments.

Table 8.1 shows the three types of anisotropic permeable specimens made in this research, including the predicted maximum drag reduction and breakdown velocity based on the theoretical model, using the estimated permeabilities and assuming a canonical ZPG TBL development. The continuous fibre and 3D-printed plates are predicted to result in moderate to high drag reductions and a breakdown velocity within the research velocity sweep regime, which would render it possible to test the hypothesis of the emergence of spanwise coherent structures and the subsequent breakdown of the DR regime. Note that the permeabilities for the continuous fibre plate were estimated via analytical models, giving a lower certainty in these predictions than for the 3D-printed plate, for which the permeabilities were estimated via experimental characterisation. Other benefits and drawbacks considering the wind tunnel experiments are summarised in Table 8.2 for the different the test plates.

Without consulting the actual wind tunnel results, the 3D printing approach is upfront deemed the most viable option for this (type of) research. It has a large design space, allows for experimental permeability characterisation and rapid prototyping, and yields a test plate with the least imperfections that could influence the measurements. However, the design is limited in terms of the level of detail, yielding a smallest reliable pore size of 250 μm . For higher predicted DR and breakdown velocities (e.g. 10% at 20 m/s), pores would need to be up to an order of magnitude smaller. The build volume of the printer is also a limitation for the manufacturing of a large test plate required for the direct force measurements.

Table 8.1: Summary of the types of anisotropic permeable specimens manufactured in this research, including predicted maximum DR and breakdown velocity based on theoretical model and assuming a theoretical ZPG TBL development.



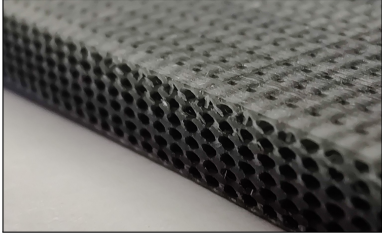
Seal fur	Continuous fibre	3D-printed structures
$DR_{max} = n/a$ $U_{br} = n/a$	$DR_{max} = 22 - 32\%$ $U_{br} = 16 - > 35 \text{ m/s}$	$DR_{max} = 5.5 - 7.0\%$ $U_{br} = 7.3 - 8.5 \text{ m/s}$
		

Table 8.2: Benefits and drawbacks of different test plates for wind tunnel experiments.

Plate type	Benefits	Drawbacks
Seal fur	+ Closest resemblance of structure with proven DR	- Inhomogeneous thickness - Hairs of fur stand up straight - No known permeability characteristics
Continuous fibre	+ High predicted DR + Breakdown velocity in research velocity sweep regime	- Permeable region obstructed halfway - Inconsistent plate thickness - Fibre roughness - Permeability from analytical relations, lower certainty
3D-printed	+ Hydrodynamically smooth surface + Permeability from experiments, higher certainty + Breakdown velocity in research velocity sweep regime	- Local imperfections (minor steps between plate parts) - Pore size (and thus permeability) not consistent over plate - Predicted DR at low velocities, challenging to measure

III

Wind tunnel experiments with streamwise-preferential permeable surfaces

Little experimental work has been done on turbulent boundary layers over streamwise-preferential substrates. The only study to date (Efstathiou and Luhar, 2020) was based on substrates with permeability values through which the hypotheses of the theoretical framework by Gómez-de-Segura and García-Mayoral (2019) could not be fully tested. Specifically, the wall-normal permeability was out of the range (too high) required to make drag reduction predictions based on the theoretical model. In Part II it was concluded that in this research, wind tunnel test plates are made with the right permeabilities to test the hypotheses of the theoretical framework. Hence, this part aims to address those research gaps. Within the frame of the research scope, it serves to meet and answer the second and third research objectives and questions respectively as lined out in Section 1.4.

This part presents the performed wind tunnel experiments. Through these experiments, the drag characteristics of the streamwise-preferential permeable surfaces and their influence on the overlying flow are investigated. Furthermore, the data is used to test the hypotheses of the theoretical framework. Direct force measurements for characterising the drag is covered first, establishing the methodology and subsequently presenting and discussing the results in Chapters 9 and 10 respectively. Particle image velocimetry (PIV) experiments for investigating the flow modulation are covered secondly, and are split up in a similar fashion in Chapters 11 and 12.

This page has been intentionally left blank.

9

Direct force measurements - Methodology

Direct force measurements were performed to investigate the drag characteristics of the test plates with streamwise-preferential permeable surfaces. The measurement setup is designed for accurate measurement of surface friction. The measurement plan is given in Section 9.1 The experimental setup is elaborated upon in Section 9.2. The methods used in data processing are shared in Section 9.3.

9.1. Measurement plan

Direct force measurements were performed on three different designs of anisotropic permeable surfaces: the seal fur, continuous fibrous substrates, and 3D-printed surfaces (see Chapter 8 for a summary on these three test plates). Two different seal fur plates were tested, one with seal fur from the grey seal, and one from the harbour seal. Seal fur tests were performed twice with an interval of four months during which the plates were stored on top of each other in a box, squeezing the plates firmly together and flattening the hairs. A last set of measurements was performed with a wet grey seal test plate, which was wetted using a plant sprayer and tap water and rubbed flat before every single measurement. The continuous fibre and 3D-printed plates were tested in regular and reversed orientation. The 3D-printed plate measurement was performed three times, once with more data points in a low-velocity regime. A last measurement was performed on an empty mould used for the 3D-printed plate, and which is similar in dimensions to the mould for the fibrous plate. A solid, spanwise strip was placed halfway in the streamwise direction of the mould. As such, the fibre plate without fibres, but with the glue halfway the plate, was resembled in comparison drag measurements. An overview of the measurements performed is seen in Table 9.1. For the continuous fibre and 3D-printed plate measurements, the measured velocity regime included the predicted breakdown velocity.

All drag measurements were compared against a reference smooth plate. Each measurement set consists of seven velocity sweeps from low to high freestream velocity. At every odd-numbered sweep, the reference plate is installed and at every even-numbered sweep, the test plate of interest (the "target") is installed. Each target sweep is compared to the average of the prior and posterior reference sweeps. To save time, multiple targets can be tested between two reference sweeps. Prior experiments have shown that conditions do not change so much as to significantly influence the results when simultaneously measuring up to three targets. Such a measurement routine would be referred to as a 'triple sandwich'. A typical measurement set takes between two and three hours depending on the number of target plates.

Table 9.1: Overview of conducted direct force measurements. MN = Measurement Number.

Test plate	MN (#)	Orientation	Comments
Grey seal	1	Regular	
Harbour seal	1	Regular	
Grey seal	2	Regular	Conducted after four months storage in flat box
Harbour seal	2	Regular	Conducted after four months storage in flat box
Grey seal	3	Regular	Wetted fur
Continuous fibre	1	Regular	
Continuous fibre	1	Reversed	
Empty mould	1	Regular	Control for step at mid-plate location
3D-printed	1	Regular	
3D-printed	1	Reversed	
3D-printed	2	Regular	
3D-printed	2	Reversed	
3D-printed	3	Regular	Low-velocity regime ($U_\infty = 3.0 - 11.0$ m/s)
3D-printed	3	Reversed	Low-velocity regime ($U_\infty = 3.0 - 11.0$ m/s)

9.2. Experimental setup

This section presents the experimental setup for the direct force measurements. It covers the wind tunnel and test section, and the measurement equipment. The complete setup has been validated in prior experiments, proving the capability of reliably measuring changes in friction drag in TBL (van Nesselrooij et al., 2021). Validation was performed both for drag reductions, with riblets, and drag increases, with dimpled surfaces.

9.2.1. Wind tunnel and test section

Experiments were performed in the M-tunnel at the LSL of the TU Delft. The tunnel operates at a maximum fan speed of 2,900 RPM and maximum freestream velocities of approximately 35 m/s and 50 m/s in open-loop and closed-loop configurations respectively, with a freestream turbulence intensity of approximately 0.7%. The closed-loop configuration suffers from rapid flow heating and therefore the open-loop configuration was used for this research. The tunnel is operated through LabView, either integrated within the Hill control program when performing direct force measurements or as a stand-alone program when performing PIV experiments. The measurement equipment is installed in an auxiliary test section with a 400×400 mm cross-section. A fresh TBL is created in front of the measurement equipment by a modular assembly. It consists of an elliptic LE that deflects the upstream developed BL downwards and ejects it through an opening in the wind tunnel floor. The undisturbed flow is tripped by a carborundum strip to start a new TBL approximately 600 mm in front of the test plate LE.

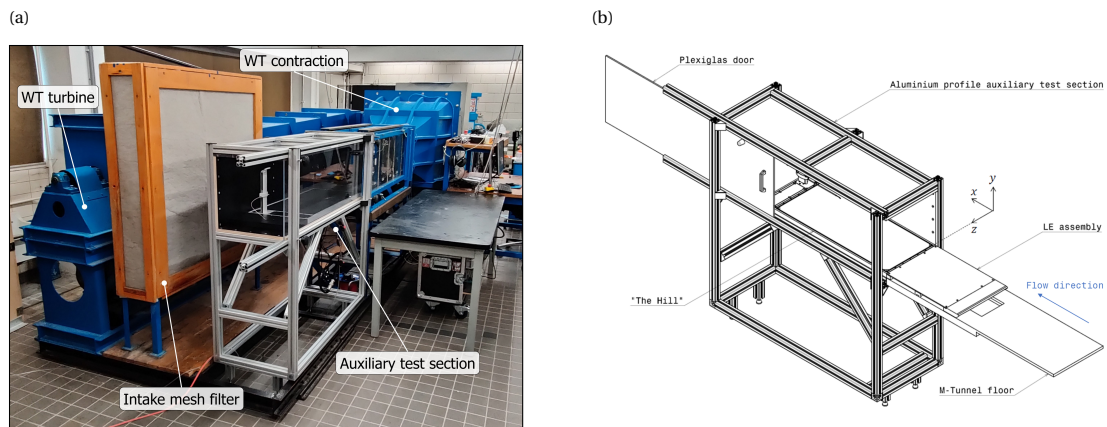


Figure 9.1: Wind tunnel facilities used. (a) Image of M-tunnel at the LSL of the TU Delft. (b) Schematic of auxiliary test section, image adapted from Lai (2021).

9.2.2. Direct force measurement equipment

Direct force measurements were performed in a dedicated patent-pending flat plate aerodynamic friction drag measurement device provided by Dimple Aerospace BV and called "the Hill". It is capable of calibrated direct force measurements in flow velocities up to Mach 1 that are corrected for pressure forces acting on the streamwise-facing surfaces within the cavities between the connector tray (holding the test plate) and the rest of the device. It also is capable of performing automated hot-wire anemometry (HWA) measurements with an integrated, motorised traverse. Measurement repeatability in terms of root mean square is typically less than 0.2% C_D . Validation tests with riblets suggest an accuracy of at least 1% C_D . An extensive description of the system and its validation is provided by (van Nesselrooij et al., 2021). This section is confined to the direct force measurement capabilities of the Hill and does not cover the HWA measurement unit.

Figure 9.2 shows schematic images of the Hill. The core element dimensions are 1,020 mm \times 395 mm \times 30 mm (L \times W \times H), fitting exactly in the M-tunnel test section. For larger wind tunnels, tapered extensions can be fitted to ensure a smooth flow guidance towards the test plate. Twelve Shore 00-30 Sorbothane[®] vibration isolators prevent transmission from tunnel vibrations into the system. The connector tray is made of an aluminium frame and carbon-fibre reinforced polymer (CFRP) base and holds test plates of dimensions 881.3 mm \times 366.3 mm \times 5.0 mm (L \times W \times H). It rests on 0.3 mm thick titanium flexures that have a minimal influence on the direct force measurements. To prevent lifting of the test plate during measurements, six small screw connections can be used to attach the test plate to the connector tray. The test plate can be lifted out of the tray by pneumatically activating three small air pistons in the base. Figure 9.3 shows images of the Hill with test plates.

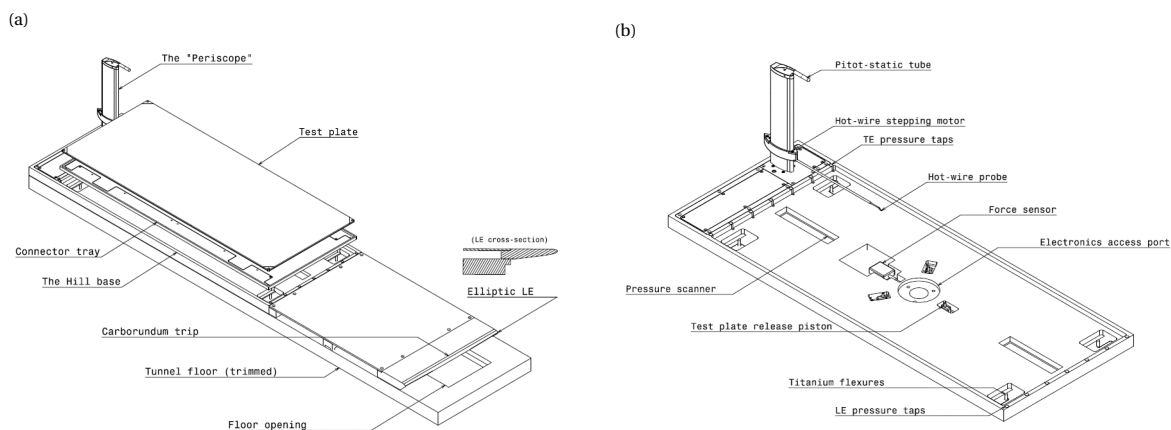


Figure 9.2: Schematics of Hill measurement system. (a) Overall view of positioning in test section. (b) Detailed view of systems internal architecture. Images adapted from Lai (2021).

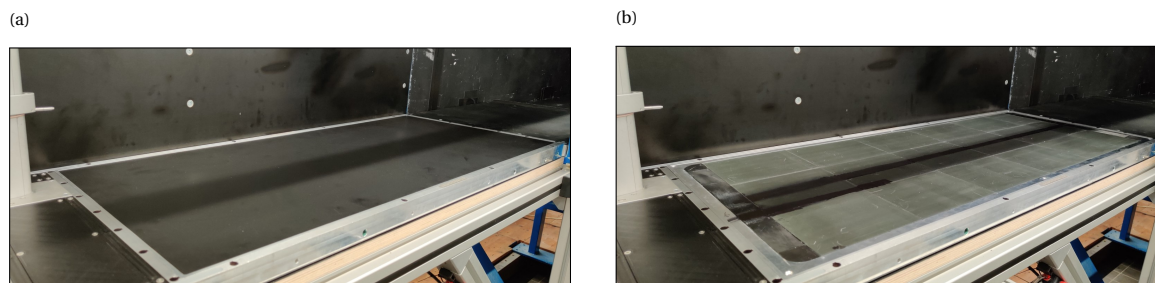


Figure 9.3: Test plates in the Hill. (a) Reference smooth plate. (b) 3D-printed plate.

The force sensor used is of the ME-systeme KD40S series and has a 25 kHz sampling rate and ± 2 N range with 0.1%FS rated accuracy. It makes contact with a pin that extends from the bottom of the connector and can be engaged and retracted between measurements using an electrical linear actuator. This connection can be tailored to have a small positive force reading at zero velocity (the Null force). The force sensor inherently measures the total force acting on the connector, including those arising from pressure differences in the air gap between the connector tray and the rest of the core. To correct for this, the pressure force is monitored via four pressure scanners connected to 23 pressure taps around the perimeter: seven at the LE, eight at the TE, and four on each of the sides. Pressure data is channelled to a custom printed circuit board that incorporates four scanners with up to 10 Honeywell RSC sensors with a 2 kHz sampling rate and ± 250 Pa range with 0.1%FS accuracy. Temperature-corrected differential pressure data is computed with respect to the static pressure port from the pitot tube, for which a ± 1245 Pa range sensor was used. Besides force and pressure signals in the system core, the Hill system also acquires data in the periscope (total pressure, static pressure, WT temperature and humidity) and at the control box (ambient temperature and pressure). The control box houses the control system of the Hill and a compact data acquisition (cDAQ) system from National Instruments and is computer-controlled via LabVIEW.

9.3. Data processing

Processing of the measurement data was performed using MATLAB. Environmental conditions were calculated using Buck's empirical relation (Buck, 1981) for vapor pressure from the relative humidity (RH), temperature (T) and absolute pressure (p_a) via Equations (9.1) to (9.3) where $T_0 = 273.15$ K. Based on the environmental conditions and measured dynamic pressure (q), the freestream velocity and unit Reynolds number (Re_1) were calculated via Equations (9.4) and (9.5) respectively. In general, the main reason for using the unit Reynolds number is to be able to compare concepts with different characteristic length scales. In this research, an additional argument for using the unit Reynolds number for the direct force measurements is that the friction Reynolds number (Re_τ) changes significantly along the streamwise direction on the test plate, rendering it impossible to link integrated drag coefficients to a single Re_τ .

$$p_v = 0.61121 \cdot 10^{-3} RH \cdot \exp \left[\frac{18.678 - T/234.84}{257.14 + T} \right] \quad (9.1)$$

$$\rho = \frac{0.028964(p_a - p_v) + 0.018016p_v}{8.314(T + T_0)} \quad (9.2)$$

$$v = \frac{4.18528 \cdot 10^{-4} \cdot (T + T_0)^{2.5}}{p_a \cdot (110.4 + T + T_0)} \quad (9.3)$$

$$U_\infty = \sqrt{\frac{2q}{\rho}} \quad (9.4)$$

$$Re_1 = \frac{1U_\infty}{v} \quad (9.5)$$

Drag coefficients are calculated via Equation (9.6) after performing pressure force (F_p) and null force shift corrections (ΔF_{null}) to the total measured force (F), where S is the test plate surface (0.32 m^2). The former is calculated by integration of the pressure readings in the air gaps along the streamwise-facing leading and trailing edge. The latter correction is necessary because the measured force without flow is slightly different before and after the velocity sweep due to sensor temperature sensitivity and creep. It is applied proportionally to the measured force. Reference measurements are interpolated at the Reynolds number of target measurements before calculating the difference in drag coefficients. Error estimates are calculated as the RMSE over the measurements of the same target.

$$C_D = \frac{F - F_p - \Delta F_{null}}{qS} \quad (9.6)$$

10

Direct force measurements - Results and discussion

This chapter presents and discusses the results of the direct force measurements. The seal fur, continuous fibre and 3D-printed plates are covered separately in Sections 10.1 to 10.3 respectively. All results are assessed in terms of the calculated drag coefficient (C_D), difference in drag coefficient w.r.t. the smooth reference plate (ΔC_D , expressed in %), effects of pressure and null force shift corrections (in terms of ΔC_D , expressed in %) and the uncertainty in ΔC_D (expressed in %) in terms of RMSE across measurements in a measurement set. Section 10.4 shares a discussion on these results and presents intermediate conclusions on the direct force measurements.

10.1. Seal fur

The drag results for the seal fur are shown in Figure 10.1. The drag increase is extremely high. At the highest value, it is nearly 90% for the wetted grey seal fur, and 330% for the first harbour seal measurement, with the other measurements reaching a maximum increase of between 170% and 260%. The second measurements (denoted as #2) both lie below their first counterparts. The wetted grey seal fur measurement lies below all other measurements.

Figure 10.1a shows that all seal fur measurements have a seemingly constant, but subtle decreasing and then increasing trend in C_D for increasing Re_1 . This trend is best visible for the wetted grey seal fur. The sudden drop at the last two data points of the first harbour and grey seal measurements are thought to be outliers. Frequency analysis on the force signal showed an anomalous peak frequency, different to usual ones observed at measurement points at different Re_1 . This could result from tunnel vibrations and resonance not sufficiently dampened and/or filtered out by the drag measurement system, for example, if the connector is in direct contact with the outer frame of the Hill. Checking the raw force measurements showed that the null force was lower for the measurements at which the drop in C_D occurs compared to the other measurements. Also, the maximum measurable force was not yet reached, as the issue occurred at different C_D and thus F for the two different seal furs. Consequently, these outliers are believed to be related to the tunnel vibrations that change with changing fan rotation speed (and hence Re_1).

The null force shift correction is small (Figure 10.1c), with the exception of one measurement. Likely, the connector tray was not perfectly able to oscillate freely, influencing the readings of the force sensor in the first and final null measurement. The pressure drag correction is very large (Figure 10.1d), with absolute values of 10-60% ΔC_D . Considering the magnitude of the overall change in drag, they are deemed acceptable. The RMSE is generally within 2% for all dry fur seal measurements, indicating repeatable measurements and confidence in the results. The wetted seal fur measurement has a higher RMSE which grows with increasing Re_1 and ultimately decreases again.

10.2. Continuous fibre substrates

The drag results for the continuous fibre plate and empty reference mould are shown in Figure 10.2. The drag increase is very high. The continuous fibre drag increase grows from 30% to 90% with increasing Re_1 , while for the empty mould it grows from approximately 50% to 75%. The regular and reversed measurements for the continuous fibre substrates overlap well.

Figure 10.2a shows that the continuous fibre substrates have a slight increase in C_D for increasing Re_1 in the beginning, before tapering off to a constant value. The empty mould measurement shows a decreasing C_D for increasing Re_1 , which tapers off to a constant value at higher Re_1 . This is in contrast to the reference smooth plate measurements, which show a continuously decreasing trend common for smooth wall friction.

The null force shift correction is small (Figure 10.2c). The pressure drag correction is moderate to large (Figure 10.2d), with values between -2 and $-13\% \Delta C_D$ depending on test plate and Re_1 . Considering the overall change in drag, they are deemed acceptable. The RMSE is generally within 0.75% for all and within 0.5% for most measurements, indicating repeatable measurements and confidence in the results.

10.3. 3D-printed surfaces

The drag results for the 3D-printed plate are shown in Figure 10.3. The shaded region indicates non-valid measurements, as the drag coefficient does not show the typical decreasing behaviour expected from pure surface friction (Figure 10.3a). These two measurement points were part of the low regime velocity sweep and taken at extremely low flow velocities (3.0 & 3.9 m/s), which has three potential drawbacks. First, it is uncertain whether a stable TBL has formed. Secondly, the slow-turning wind tunnel fan might have rotor-wake effects that are measurable downstream in the test section. Lastly, the forces acting on the test plate (both friction and pressure drag) are so small that they become more susceptible to measurement error.

Figure 10.3e shows that the 3D-printed plate has a slight to moderate drag increase: approximately 2% at lower Re_1 and 7% at higher Re_1 . In terms of absolute C_D , a decreasing trend with increasing Re_1 can be observed (Figure 10.3a) that resembles the trend of pure skin friction. Both the null force shift and pressure drag corrections are relatively small, with absolute values within 1% and 2% respectively (Figures 10.3c and 10.3d). For $Re_1 \gtrsim 0.5 \times 10^6$, the RMSE is generally within 0.75% for all and within 0.5% for most measurements, indicating repeatable measurements and confidence in the results for $Re_1 \gtrsim 0.5 \times 10^6$.

For $Re_1 \lesssim 0.5 \times 10^6$, the null force shift and pressure drag corrections are in the same order of magnitude as the computed difference in drag coefficient. The same is true for the RMSE. As such, there is a high degree of uncertainty in the computed drag differences for $Re_1 \lesssim 0.5 \times 10^6$. This can also be observed directly in Figure 10.3e. The difference between measurement sets is large, with some measurement sets showing a decreasing trend for decreasing Re_1 (the first regular and reversed measurements) while others show a constant trend (low regime regular and reversed measurements). Also, all measurements and their RMSE considered, the uncertainty bound is relatively large, ranging from -2.5% to $+2.5\% C_D$ at the lowest Re_1 . The lower bound gets above 0% for $Re_1 > 0.5 \times 10^6$ (≈ 8.3 m/s), indicating that the measured drag increase from thereon is relatively certain.

The theoretical model drag reduction predictions are computed with respect to the drag coefficient from the different reference measurements ($C_{D,0}$), while using the corresponding flow conditions to determine δ_v required for expressing the permeabilities in viscous units. Predictions for different reference measurements are denoted with different marker shapes and correspond to the same marker shapes as for the experimental drag difference data. Lines continue until the point of breakdown, above which $\sqrt{K_y^+} > 0.38$. The effect of the spread in the results of the permeability measurements is taken into account by considering three scenarios (best, average and worst case). Across all scenarios, maximum drag reductions of approximately 5.6 – 7.3% are predicted, with the worst-case point of breakdown at lower maximum drag reduction (DR $\approx 5.8\%$) and lower breakdown velocity ($Re_1 \approx 5.2 \times 10^5$ or $U_{Br} \approx 7.7$ m/s), and the best-case point of breakdown at higher maximum drag reduction (DR $\approx 7.2\%$) and higher breakdown velocity ($Re_1 \approx 6.2 \times 10^5$ or $U_{Br} \approx 9.2$ m/s). To summarise, the experimental conditions - that is, reference smooth wall drag and flow conditions - combined with the theoretical model, predicts moderate drag reductions (6 – 7%) at low velocities (8 – 9 m/s). These values are similar to the predictions based on an assumed canonical ZPG TBL as calculated in Section 7.5.

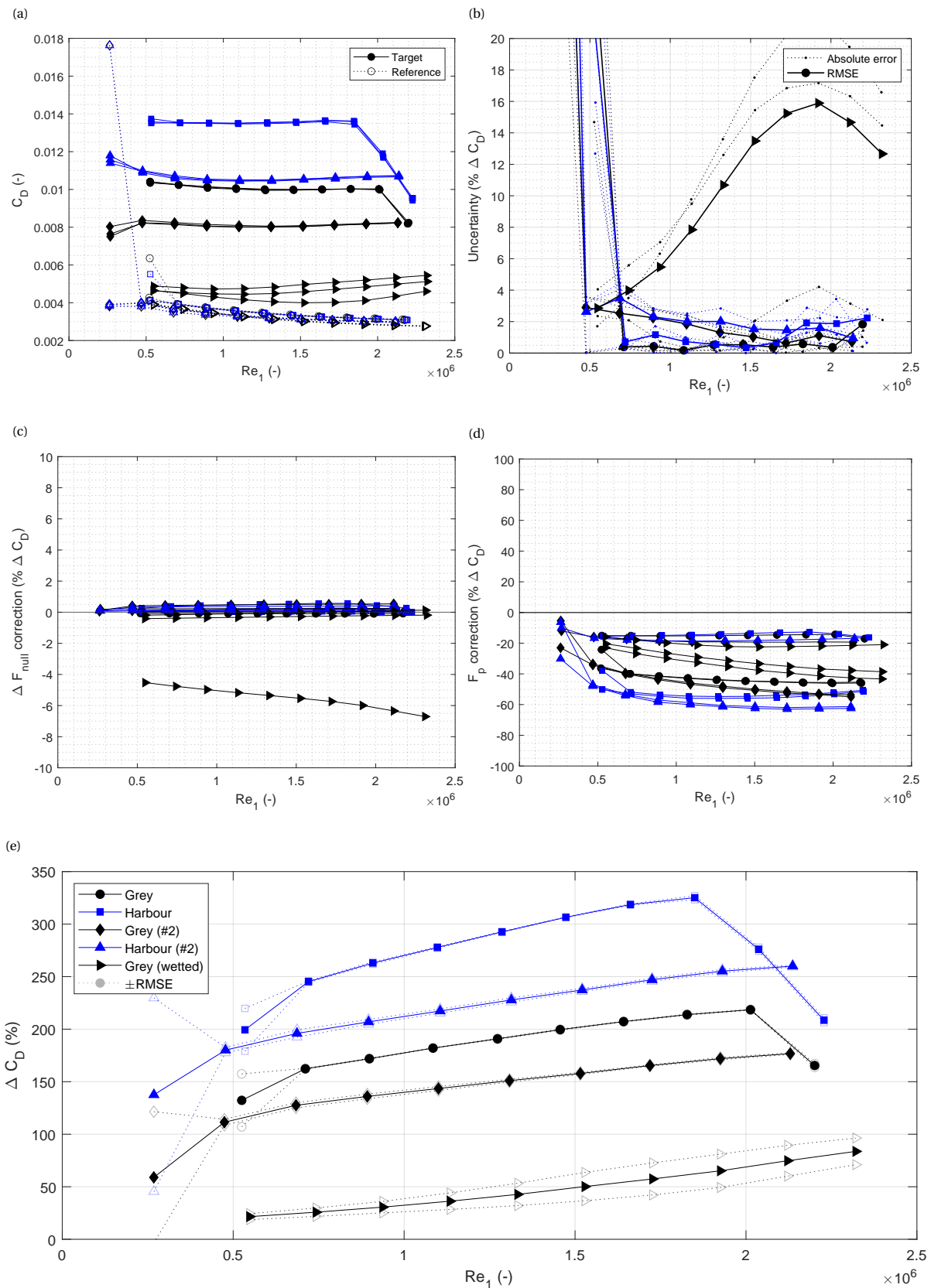


Figure 10.1: Direct force measurement measurement results for the seal fur plate. (a) Drag coefficient (C_D). (b) Uncertainty expressed as absolute error for each individual measurement and RMSE for a measurement set. (c) Null-force shift correction. (d) Pressure drag correction. (e) Drag change w.r.t. reference plate.

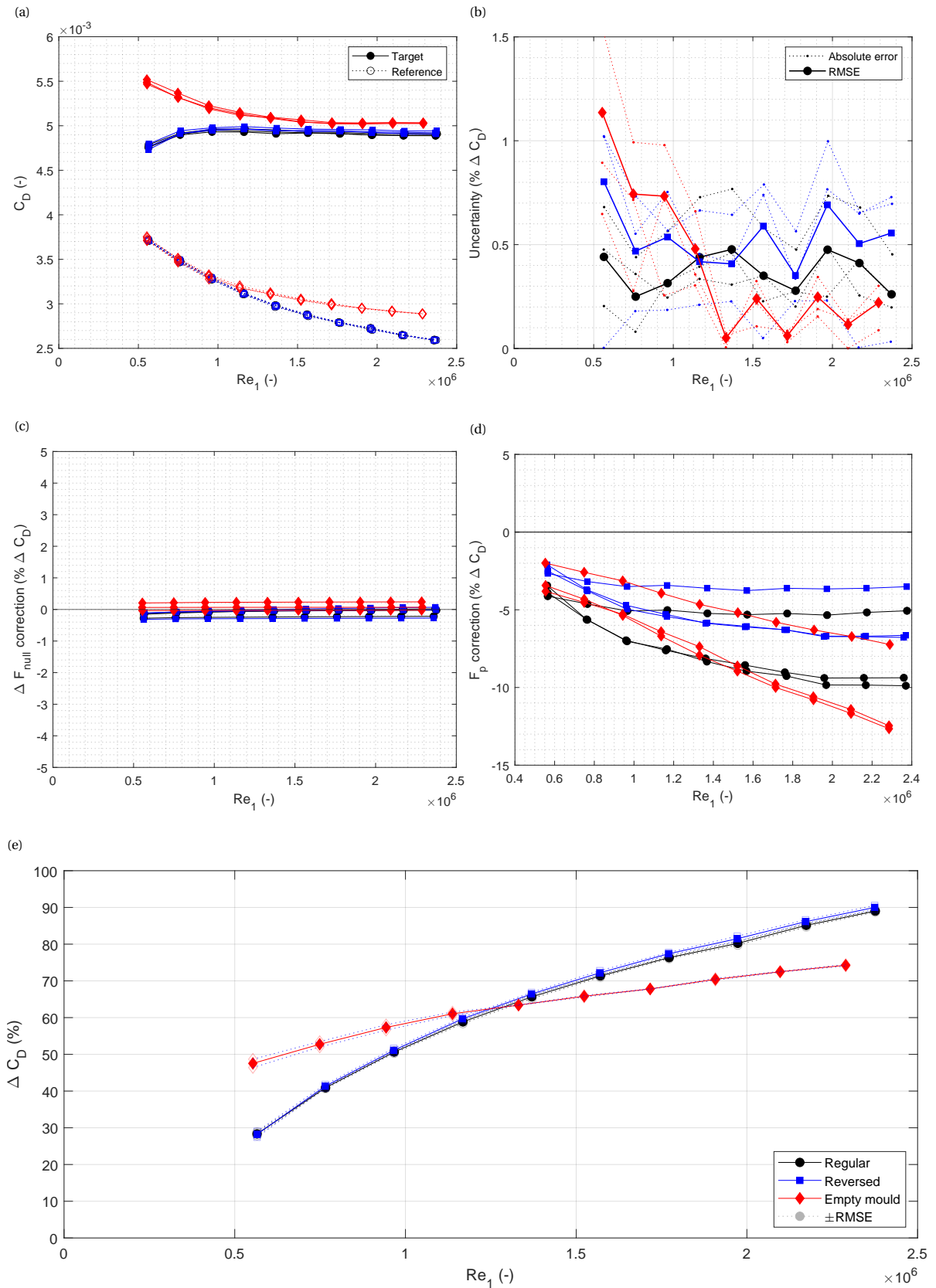


Figure 10.2: Direct force measurement results for the continuous fibre plate. (a) Drag coefficient (C_D). (b) Uncertainty expressed as absolute error for each individual measurement and RMSE for a measurement set. (c) Null-force shift correction. (d) Pressure drag correction. (e) Drag change w.r.t. reference plate.

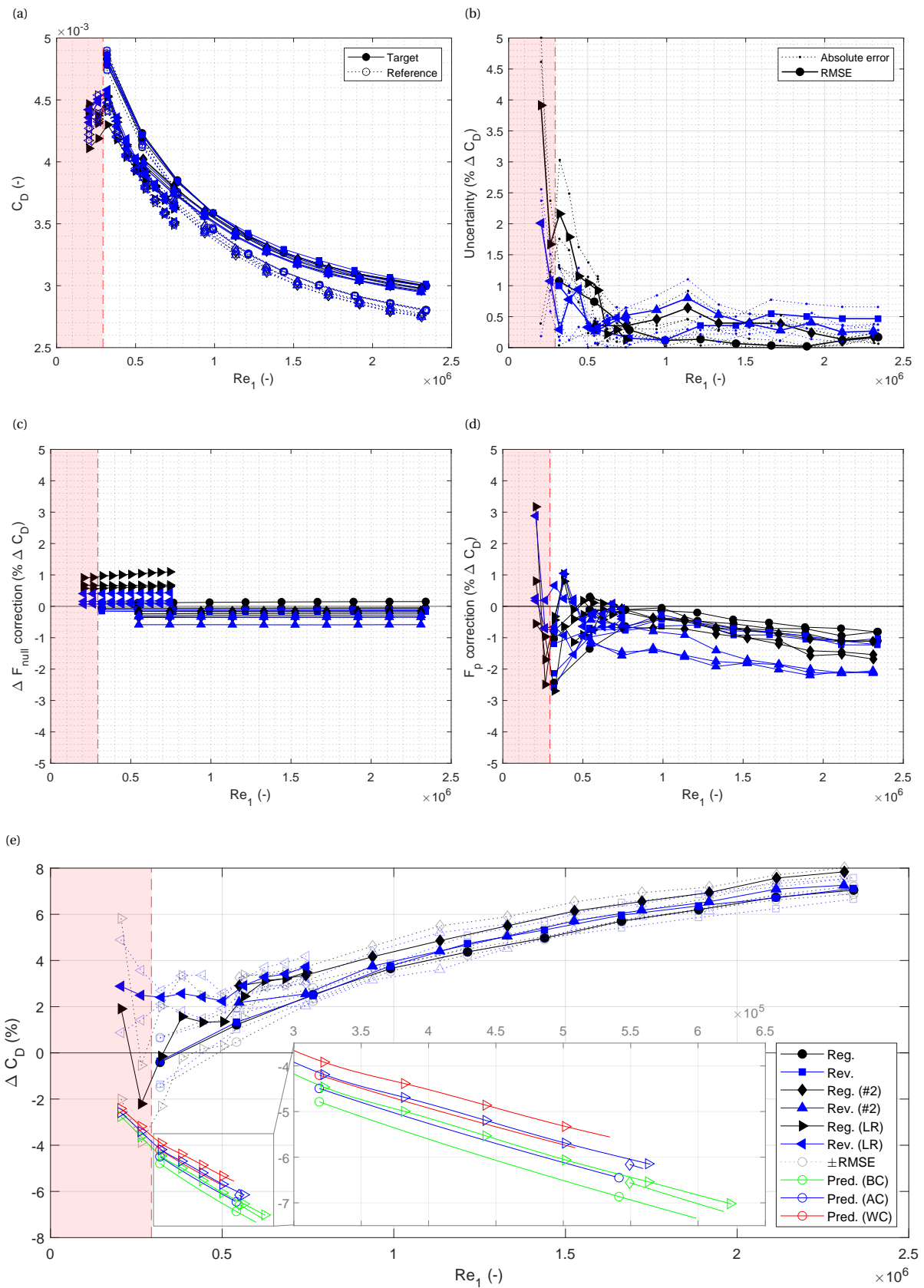


Figure 10.3: Direct force measurement measurement results for the 3D-printed plate. (a) Drag coefficient (C_D). (b) Uncertainty expressed as absolute error for each individual measurement and RMSE for a measurement set. (c) Null-force shift correction. (d) Pressure drag correction. (e) Drag change w.r.t. reference plate. Reg.: Regular orientation. Rev.: Reversed orientation. LR: Low-speed regime. Pred.: Prediction based on theoretical model. BC: Best case. AC: Average case. WC: Worst case.

10.4. Discussion

The drag results are further discussed in this section. Their general significance is first covered in Section 10.4.1. Then, the seal fur, continuous fibre and 3D-printed plate results are discussed separately in Sections 10.4.2 to 10.4.4.

10.4.1. General significance of results

The general significance is assessed on two aspects: the uncertainty in the measured drag force at the lowest absolute values, and what differences in measured drag can be considered statistically significant. This assessment is done using the smooth reference plate data from the three measurement sets of the 3D-printed plate measurements. The force sensor has a 0.1%FS rated accuracy, translating into 2×10^{-3} N. Figure 10.4a shows the measured force and corresponding measurement accuracy. The accuracy improves for increasing F (and hence increasing Re_1) and is better than 1% for $Re_1 > 1.2 \times 10^6$. This stresses two points: the importance of repeated measurements to correct for the inherent error of single measurements and using the corresponding RMSE as error metric; and the larger uncertainty for lower velocities, which naturally translates into a larger RMSE. Figure 10.4b shows the minimum required difference in C_D between a reference and target measurement to yield a statistically significant result ($\alpha = 0.99$). It has been computed using Welch's t-test (see Appendix A) under the assumption that the target measurement has the same signal variability as the reference measurement. It can be seen that overall, differences are significant if they are at least 0.5% C_D ; this can be interpreted as the minimum drag difference that can be measured with sufficient certainty. Since this value is nearly an order of magnitude smaller than the drag differences found in this research, it is considered that the found drag differences are significant.

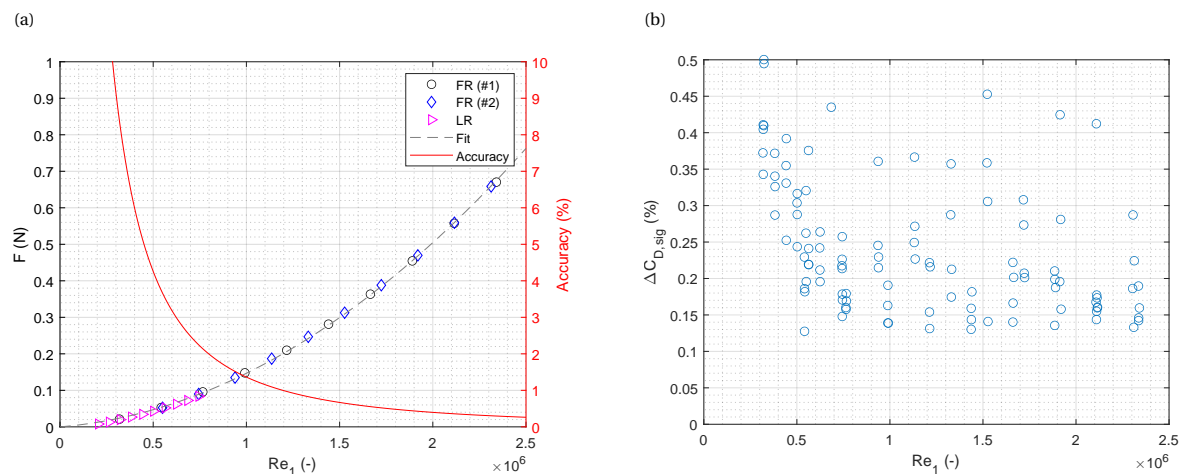


Figure 10.4: Significance estimation of force measurements. (a) Measurement accuracy. (b) Required difference in C_D for a statistically significant ($\alpha = 0.99$) result.

10.4.2. Seal fur

Unfortunately, a drag reduction as found by Itoh et al. (2006) was not observed in this study. The difference in medium seems to be a logical explanation for this. Therefore, extra friction measurements in water using a Taylor-Couette flow setup were conducted in collaboration with the Fluid Mechanics section from the Laboratory for Aero & Hydrodynamics (part of the Process & Energy department, 3ME faculty, TU Delft). A significant drag increase ($\Delta C_D > 100\%$) was observed, with a linear trend for increasing Re . A description and the results of these measurements are shown in Appendix E. Regardless of the difference in medium, it remains worthwhile to discuss the results of the WT measurement in more detail. In their dry state, the seal furs form a carpet-like surface, where the hairs are relatively upright (Figures 5.6c and 5.6d). This is in contrast with the wetted state, wherein the hairs stick together and the fur is nearly perfectly flat with small grooves between the hairs, almost riblet-like (Figure 10.5). This observation is in line with those by veterinarians in the Pieterburen Seal Centre:

"The difference of the seal fur appearance in dry and wet states is remarkable and especially well visible when the seal is partially wet. The wet part is dark and seems smooth. The dry part is much lighter and appears furry, similar to a regular pet animal such as a cat."

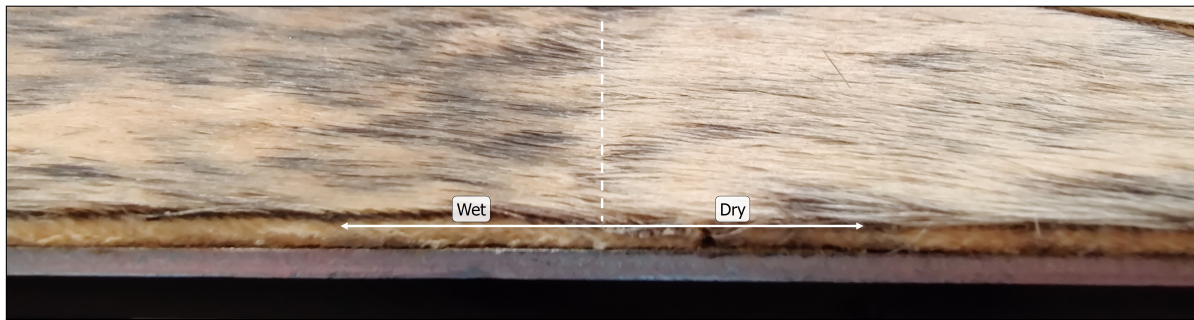


Figure 10.5: Comparison of wetted and dry seal fur. Grey seal. Picture taken after fur was stored in box for a long period, consequently the dry seal fur looks flatter than it was during drag measurements.

It is thought that in this dry state, the hairs are upright to such a degree, that the high permeability of the fur as a whole allows air to flow through the fur and experience significant friction and pressure drag by the hairs. Furthermore, it was visually observed that individual hairs vibrate in the flow. This could enhance turbulent mixing, generate Reynolds stress and thus contribute to momentum loss in the flow. Both then would be reflected in an increase in drag compared to a smooth surface. Vibrating hairs and increased Reynolds stresses were also observed in the PIV experiments (Appendix I.1).

The above-mentioned line of thought is supported by multiple observations. Firstly, the results (C_D and ΔC_D) of the second set of measurements follow the same trend as the first set of measurements, but are shifted downwards, for both the grey and the harbour seal. Between these two sets of measurements, the seal furs were stored on top of each other in a box, squeezing the plates firmly together and flattening the hairs. The same can be observed for the wetted seal, where the hairs are flattened even further than in the dry state. Secondly, the drag coefficient shows a constant and even slight increasing trend for increasing Re_1 , whereas a decreasing trend occurs for the smooth reference plate. This increasing trend is especially true for the wetted seal fur measurement. In this case, it can be expected that the wind tunnel acts as a hairdryer, removing excess water from the seal fur and consequently decreasing the flatness during the measurement itself. For the dry seal furs, the slight increase in C_D hints at non-friction related sources of drag that are more severe at higher Re_1 . Lastly, the spread in the data (interpreted as the RMSE) is largest for the wetted seal fur. This could be due to the 'hairdryer' effect. Its influence could differ between measurements, such that at given Re_1 , in one measurement the seal fur is still wetter, hence flatter, than in the other. The deviation between measurements hence is expected to first increase when the 'hairdryer' effect gets stronger, and ultimately converge when the seal furs are dried to a similar degree.

Although not beneficial for turbulent friction on flat surfaces, the vibrating hairs might be beneficial for other flow control applications, such as prevention of flow separation. Different studies into this topic have been performed, finding significant increases in lift (up to 30%) and decreases in drag (9 – 15%) in the stall regime (Favier et al., 2009; Niu and Hu, 2011; Venkataraman and Bottaro, 2012). Most notably are the studies performed by a research group from the Aachen University, who decided to perform PIV experiments on accurate 3D replicas of a scanned owl wing (Klän et al., 2008; Klän et al., 2012; Winzen et al., 2013). Applying a velvet structure that closely resembled the actual owl wing surface onto the suction side significantly reduced the size of the separation bubble compared to a clean wing configuration (Klän et al., 2008). Longer and thinner filaments, with a preferred orientation coinciding with the mean freestream direction, performed even better than the original velvet at higher Reynolds numbers (Klän et al., 2012). Reynolds shear stresses were reduced, while the shear stress distribution indicated a quick transition to an equilibrium turbulent boundary layer (Winzen et al., 2013). The authors attribute these effects to the roughness of the surface: filaments split large vortical structures into several small vortices which enhance mixing with the free shear layer and reduce separation. The hairs in these studies used were an order of magnitude larger, smaller and smaller respectively, compared to the seal fur. Nevertheless, it remains an interesting topic and shows promise for a different application of hairy surfaces in the field of flow control.

10.4.3. Continuous fibre

The drag increases for the continuous fibre plate (30 to 90%) and empty mould (50 to 75%) are similar in order of magnitude but different in trend. Also, the source of the drag increase is thought to be different. Given that the empty mould material and surface characteristics are similar to the reference smooth plate, it can be assumed that its surface friction is similar. Therefore, it is likely that the increase in drag is solely caused by the forward- and backward-facing steps at the LE, TE and mid-way of the test plate. The drag components that arise here cannot be (fully) corrected by the pressure sensors around the perimeter of the connector tray. For the continuous fibre plate, the effect of the steps is expected to be smaller than for the empty mould. Pressure probe measurements showed that the dynamic pressure within the fibrous substrate is significantly lower than for the empty mould at a similar wall-normal distance (see Appendix F). This means that the flow encountering the forward-facing steps carries less momentum and thus the overall effect on the drag of these steps is less.

The increase in drag for the continuous fibre plate is thought to have five potential causes:

1. **Friction drag due to increased wetted surface area.** Pressure probe measurements showed that close to the fibre-free flow interface, there is a significant flow velocity. This means that the flow does penetrate the fibre sheet with a relatively high velocity. As such, the wetted surface area of the fibre plate is higher than the smooth reference plate, increasing the friction drag.
2. **Pressure drag due to increased frontal area.** The fibre plate has a larger thickness at the quarter- and three-quarter positions than the reference plate due to bulging of the fibre sheets (discussed in Section 6.3). As such, the fibre plate is not completely flush with the wind tunnel wall and hence the flow experiences a frontal area at these two locations. This results in pressure drag that cannot be corrected for by the pressure sensors around the perimeter of the connector tray.
3. **Incorrectly estimated permeability.** It might be the case that the wall-normal permeability is higher than estimated, and in fact too high, such that the point of breakdown lies before the first measurement point. This however would mean that even the most conservative wall-normal permeability estimate ($6.2 \times 10^{-11} \text{ m}^2$) is more than an order of magnitude too high (the permeability at which the point of breakdown lies before the first measurement point is approximately $2 \times 10^{-10} \text{ m}^2$), or that the theoretical model is not valid in this experimental setting.
4. **Increased turbulent mixing due to fibre vibration.** If the fibres vibrate in the flow and enhance turbulent mixing, extra Reynolds stress is generated that contributes to momentum loss in the flow, similarly to the seal fur. This behaviour was not observed during the measurements.
5. **Friction drag due to fibre roughness.** The fibres were drawn from a non-smooth multi-filament (Figure 6.9c). This roughness was not accurately quantified but estimated to be not more than $5\delta_v$ at the highest velocities and thus hydrodynamically smooth for the majority of the measurement regime. Therefore its effect should be limited.

Summarised, there are a large number of possible causes for the significant drag increase. It is possible that all these causes are present and that their drag increases are combined. Given the magnitude of the drag increase, it was decided not to accurately quantify the contributions of all individual components. The main takeaway is that this continuous fibre configuration has numerous challenges that render it impractical for this experimental setting.

10.4.4. 3D-printed

Overall, the drag results for the 3D-printed test plate are clear for $Re_1 \gtrsim 0.5 \times 10^6$ with an increase from approximately 2% at $Re_1 \approx 0.5 \times 10^6$ to 7% at $Re_1 \approx 2.3 \times 10^6$. The data points in the lower regime ($0.3 \times 10^6 \lesssim Re_1 \lesssim 0.5 \times 10^6$) hint at a minor drag increase of 1–2%, but the uncertainty, in terms of force corrections and RMSE, is too large to be conclusive in this velocity regime. The trend in the lower regime does not correspond to the theoretical predictions, wherein first a drag decrease would be expected before the point of breakdown. The trend in the higher regime does correspond to what is expected qualitatively. At higher velocities, the viscous length scale decreases. For a fixed absolute permeability, this means that the permeability expressed in viscous length scale increases. Consequently, the deleterious drag increase effects after the point of breakdown are more pronounced at higher velocities.

The incongruence between the theoretical predictions and the experimental results at the lower regime could arise from different causes, for which five potential explanations are:

1. **Other drag sources.** There could actually be a reduction in friction in the lower regime, but that other sources of drag result in a net drag increase. This can be further broken down into three possibilities: (1) pressure drag within the permeable structure, this can happen with flow entering the surface through the pores and exerting a pressure force on the wall in the downstream direction, creating extra net drag, and at the TE where the permeable structure ends in a solid wall; (2) friction drag due to the viscous flow within the permeable structure; and (3) pressure drag on the surface due to local plate imperfections. This hypothesis was tested in the PIV experiments through estimation of the pure surface friction (C_f). These results are presented and discussed in Sections 12.2.2 and 12.6.2 respectively. An overall discussion correlating these drag measurements and the PIV measurements is given in Section 13.1.
2. **Incorrectly characterised permeability.** If the actual permeability is higher than the average estimate, then it could be the case that the point of breakdown lies before the first reliable measurement point. This however would require the permeability to be approximately $5 \times 10^{-10} \text{ m}^2$ (Figure 4.5a), more than twice as high as characterised, which is well outside the spread in the measurement data (Figure 7.9 and Table 7.5). This scenario is therefore deemed unlikely.
3. **Inconsistent permeability over test plate.** Locally, the permeability could be too high, such that the point of breakdown at that location is already reached. This could affect the flow further downstream and render the working principle inoperable there as well. However, even the region with the largest measured pore area would have a breakdown velocity and measurable drag reduction above the first reliable measurement velocity. It could also be the case that the locally deviating permeabilities in general affect the overlying flow in such a way that the hypothesised DR working principle does not work.
4. **BL not fully developed.** The BL needs time to adapt from the smooth wall to the permeable surface. This adaption length might render the overall working mechanism inoperable over a large portion of the test plate, or even the rest downstream as well. Literature suggests that flow development over porous substrates requires a streamwise distance of approximately $40h$, where h is the substrate thickness (Efstathiou and Luhar, 2018; Efstathiou and Luhar, 2020). For this research, with $h = 3.7 \text{ mm}$, that would translate into 148 mm, or approximately 22% of the entire test plate (taking smooth LE region into account). As such, this cause is deemed unlikely.
5. **Theoretical framework assumptions not satisfied.** The spanwise and wall-normal pores have a 1.25 mm spacing and are larger than the viscous length scale at all velocities. This is at odds with the continuous, infinitesimally small pore assumption of the theoretical framework. A final discussion on the theoretical model, its assumptions and applicability in experimental settings is shared in Section 13.2.

Summarised, the incongruence between theoretical predictions and experimental results is most likely caused by other drag sources, or as a result of not having satisfied the theoretical framework assumptions. The former is assessed through PIV experiments, the latter is assessed through an in-depth discussion of the theoretical model itself.

This page has been intentionally left blank.

Particle image velocimetry - Methodology

Particle image velocimetry (PIV) is an optical, non-intrusive and quantitative method of fluid flow visualisation. It is used for instantaneous velocity measurements and related flow characteristics. The working principle is as follows. A laser beam is focused by optical lenses to generate a laser sheet covering the region of interest within the flow field. Tracer particles are released into the flow and scatter the laser light, which is captured by a high-speed camera. The snapshots are divided into smaller interrogation windows containing a few particles. For every interrogation window of two subsequent snapshots, cross-correlation is applied to statistically determine the mean displacement and consequently velocity vector of the (particles in the) interrogation window. Raffel et al. (2018) is an excellent source for further reading on the method. In this research, PIV experiments were performed to study the flow behaviour in the boundary layer above anisotropic permeable surfaces. The rationale behind the experiments is given in Section 11.1. The experimental setup is elaborated upon in Section 11.2. The methods used in data processing are shared in Section 11.3.

11.1. Measurement plan

The general purpose of the PIV experiments is to characterise the flow and assess the effect of streamwise-preferential permeable surfaces on the state of a TBL. Characteristics of interest are the integral BL properties, friction-related parameters, mean velocity profiles and turbulent statistics (velocity fluctuations and Reynolds stress). In addition, two elements of the theoretical framework by Gómez-de-Segura and García-Mayoral (2019) are aimed to be tested against experimental data as well. The first is whether a streamwise-preferential permeable surface provides slip near the wall which is related to its permeability via $\ell_x^+ \approx \sqrt{K_x^+}$. Secondly, whether spanwise coherent structures related to KH-instabilities ('rollers') can be identified above the breakdown velocity (U_{Br}). For these purposes, planar (2D-2C) PIV in the xy -plane suffices (Efstathiou and Luhar (2020) used this setup as well). A setup with the laser sheet in the xz -plane was briefly considered for identifying the spanwise coherent structures but was ultimately discarded due to the large averaging region in the wall-normal direction (equivalent to the laser sheet thickness of at minimum 1 mm). Efforts were focused on achieving a high resolution with reliable data near the wall.

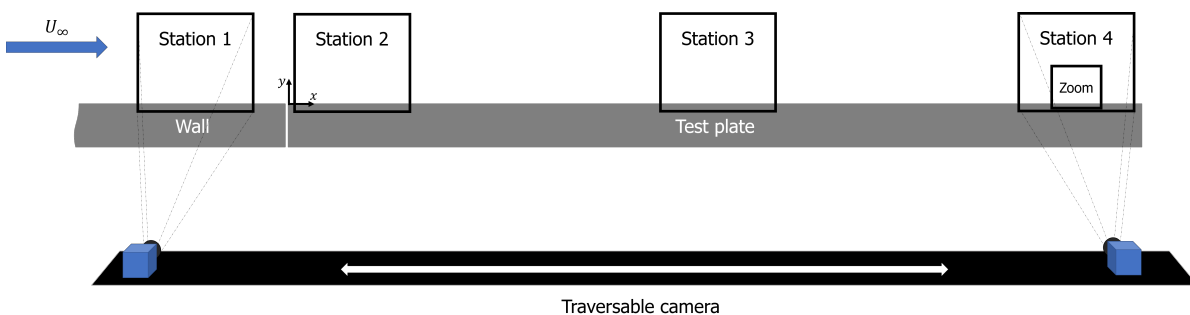


Figure 11.1: Schematic overview of PIV measurement locations. Mirrored vertically w.r.t. experimental setup, i.e. flow moves from right to left in reality. Image not to scale. Image adjusted from Lai (2021).

Figure 11.1 shows the locations at which measurements were performed: three on the test plate, namely at the leading edge (2), mid-plate (3) and at the trailing edge (4), for an assessment of the BL development along the test plate; and one in front of the test plate (1), to check similarity of flow conditions for different test plates. These locations are from hereon referred to as stations. The FOV was established in such a way that the entire BL was captured. Furthermore, an extra measurement was performed at the trailing edge (4) with a zoomed-in view to capture the maximum amount of detail realistically possible with this experimental setup. This location was chosen since the BL has developed the furthest here.

Measurements were conducted at four wind tunnel fan rotation speeds, tailored to match U_∞ of 5, 10, 20 and 30 m/s. The actual U_∞ slightly deviated from these targets depending on the measurement location, but in the remainder of the report, these target values are referred to for sake of clarity. The laser pulse separation time (Δt) was chosen such that the particles in the freestream would have 20 and 30 px displacement per image-pair, for the full BL and zoomed-in view, respectively. This was done to prevent pixel-locking at lower velocities near the wall. Table 11.1 presents an overview of the main experimental parameters.

Table 11.1: Main experimental parameters for PIV measurements.

	Full BL view				Zoomed-in view			
FOV, w × h (mm × mm)	43.5 × 36.7				22.3 × 18.8			
Locations	1, 2, 3, 4				4			
Test plates	Smooth (ref.), 3D-printed, grey seal				Smooth (ref.), 3D-printed, grey seal, riblets			
WT speed (RPM)	420	840	1680	2520	420	840	1680	2520
U_∞ (m/s)	5	10	20	30	5	10	20	30
Δt (μs)	69	34.5	17.2	11.5	52.2	26.1	13.1	8.7
Laser sheet location	Centre-plane				5 cm from centre-plane			
Lens focal length (mm)	105				105			
Resolution (px/mm pair)	58				115			
Particle displacement (px/image pair)	20				30			
f# (-)	8				16			

11.2. Experimental setup

Figure 11.3 shows the experimental setup of the PIV measurements. Measurements were performed in the M-tunnel (described in Section 9.2). An sCMOS CLHS camera (LaVision GmbH), with a pixel size of $6.5 \mu\text{m}$ and sensor size of $2560 \text{ px} \times 2160 \text{ px}$, was screwed onto a three-axis mount and attached to a rail. This enabled traversing the camera parallel to the test plate and measuring at different streamwise locations. Recording was done in double frame mode with $10 \mu\text{s}$ exposure time. An AF Micro Nikkor 105 mm was used for all measurements, at aperture $f/8$ and $f/16$ for the full BL and zoomed-in views respectively. Images were calibrated using a millimetric paper calibration board as shown in Figure 11.2.

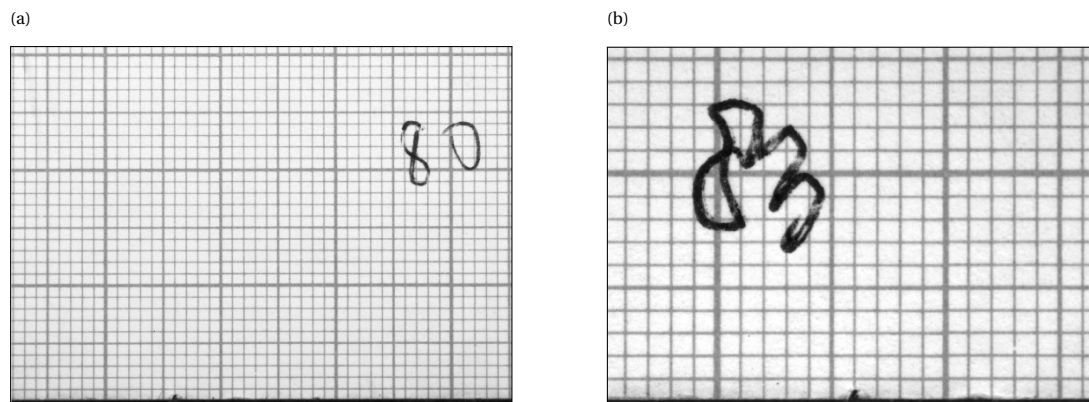


Figure 11.2: Calibration image examples, cropped at top and bottom. (a) Full BL view. (b) Zoomed-in view.

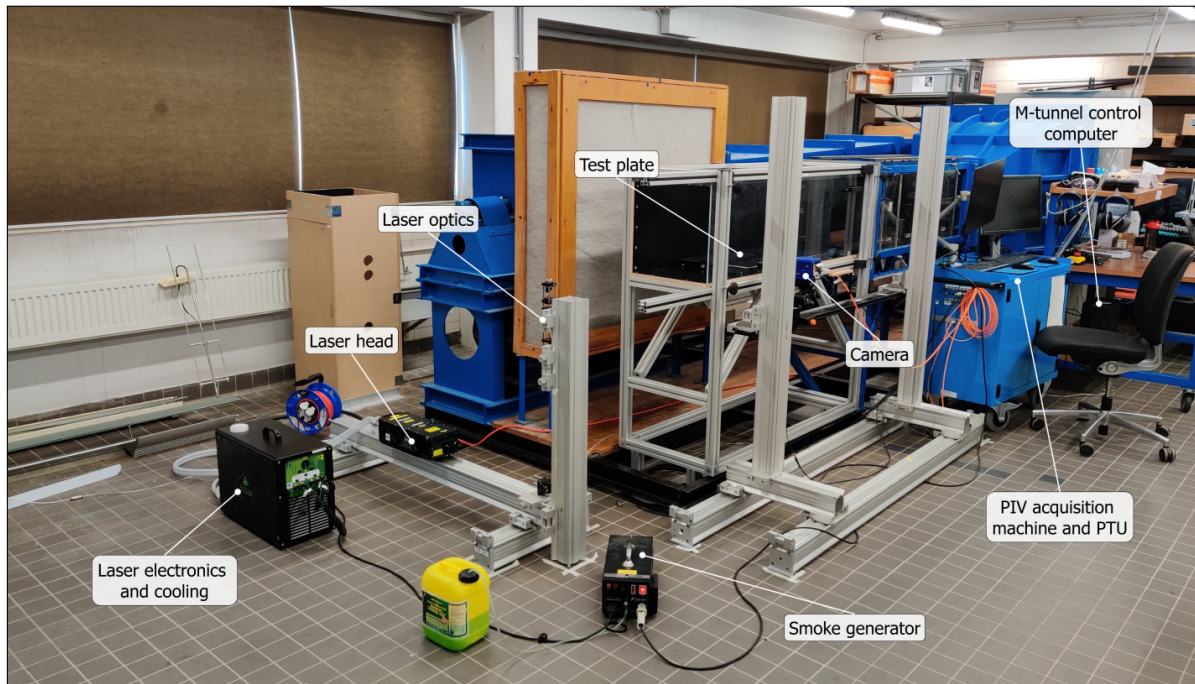


Figure 11.3: Setup of PIV experiments.

Tracer particles were generated by a SAFEX Fog 2010+ smoke generator and have a mean diameter of approximately $1\ \mu\text{m}$. These were illuminated with a double-pulsed ND:Yag Evergreen 200 (Quantel Laser) providing a 532 nm laser-pulse. This light beam is formed into a laser sheet of approximately 1.5 – 2.0 mm thickness via a set of spherical and cylindrical lenses. These optics were attached to an x-beam with a traversable mount, enabling flexibility in and ease of adjusting the laser sheet aim. The camera and laser were controlled from DaVis 10 software and timed and triggered via a programmable timing unit (PTU) from LaVision GmbH.

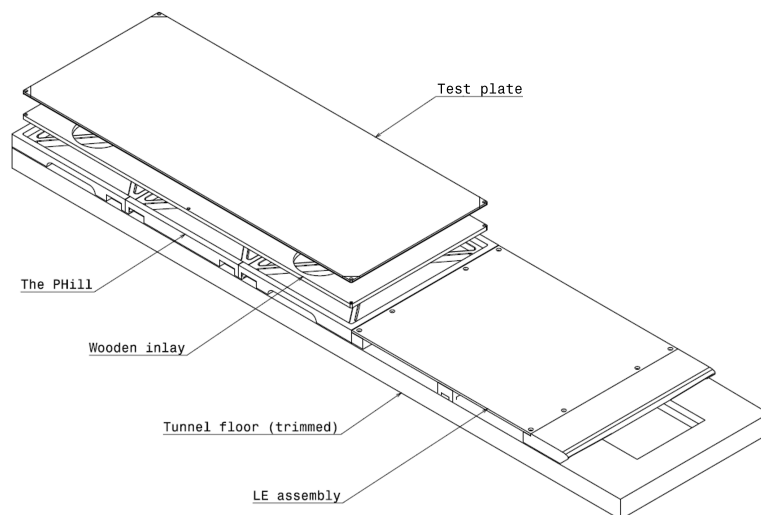


Figure 11.4: Schematic of test plate mount with the leading edge assembly and wind tunnel floor. Image adjusted from Lai (2021).

The test plate was placed in a mount, the 'PHill', developed by Lai (2021) and shown in Figure 11.4. This mount replicates the placement of the test plate in the Hill to ensure similar flow conditions between the direct force measurements and PIV experiments. An aluminium strip with a chamfered top edge was mounted onto the rear of the test plate mount. This 'razor-blade' can be slid up and down and consequently cut the laser sheet at the desired height, minimising reflections on the test plate surface further upstream. The effect of this 'laser-cutter' can be seen in Figures 11.5 and 11.6.

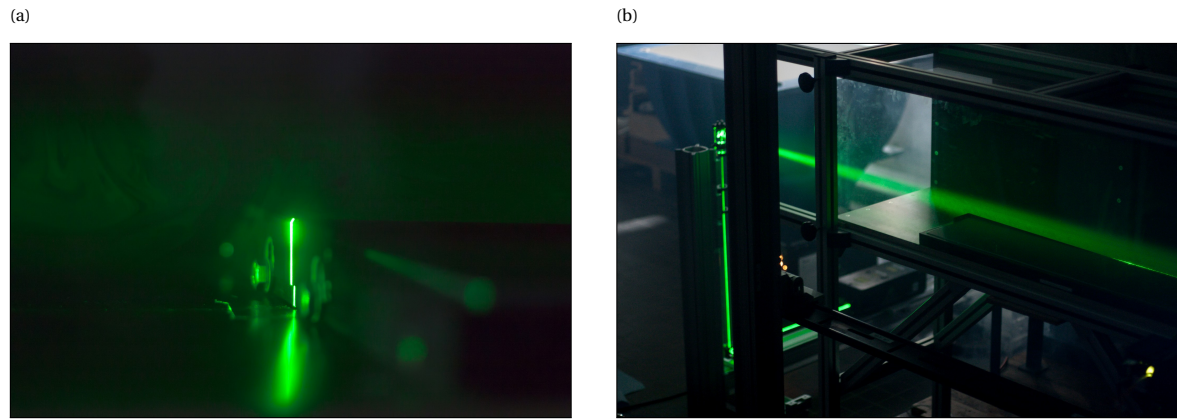


Figure 11.5: Effect of laser-cutter on laser sheet. (a) Detailed view from the back. (b) Overview from the front.

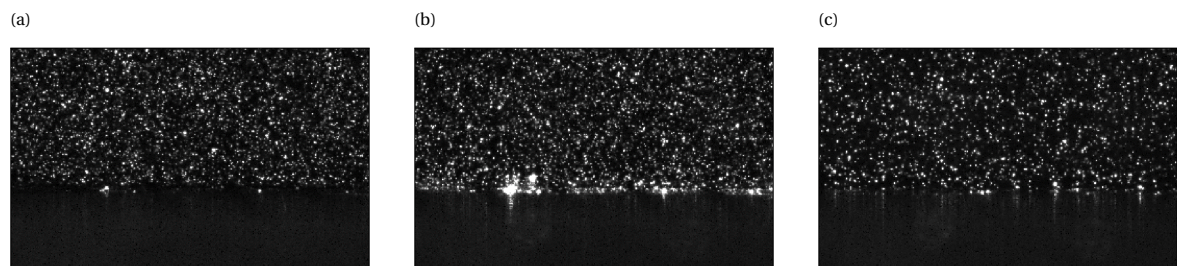


Figure 11.6: Effect of laser-cutter on images. Cropped images. (a) Laser-cutter too high, loss of information near the wall. (b) Laser-cutter too low, strong reflection at wall. (c) Laser-cutter right, slight reflections of individual particles visible.

11.3. Data processing

Processing of the PIV data was performed using LaVision DaVis 10 and MATLAB software. The sequential steps required to convert raw images into vector fields and subsequently extract relevant quantities such as velocity profiles and turbulent statistics are discussed in this section.

11.3.1. Image pre-processing

Raw measurement images were pre-processed within DaVis to improve their suitability for subsequent correlation methods. The quality of the images from the performed experiments was already relatively high. A Butterworth high-pass filter (filter length of seven images) was applied to filter out background noise, reflections and other stationary sources of light from the image. The effect of this step can be seen in Figure 11.7. Other steps such as converting to relative intensities or performing contrast stretching (as used by Van Nes-selrooij (2015), Van Campenhout (2016), and Lai (2021)), did not improve the output of the correlation step.

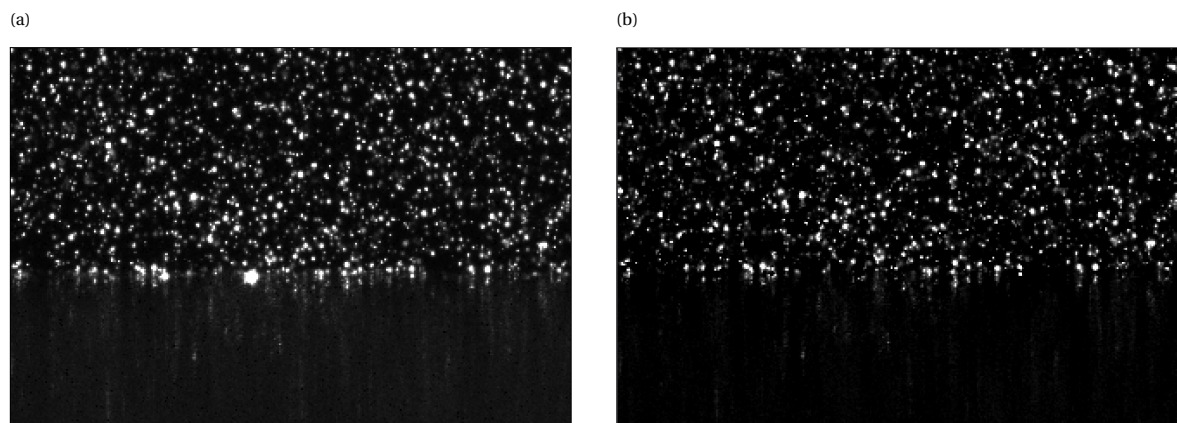


Figure 11.7: Example of PIV image pre-process step. Cropped images. (a) Raw image. (b) After Butterworth filter.

11.3.2. Correlation and vector post-processing

Converting raw images into velocity vector fields is done via statistical correlation methods within DaVis. Two different correlation methods were used in this study: cross-correlation (CC) and sum of correlation (SOC). CC performs cross-correlation and returns instantaneous velocity vector fields for every single image pair. SOC performs cross-correlation on all image pairs and sums these correlation fields, before returning one, mean velocity vector field. The benefit of this method is that smaller window sizes can be used and hence the vector field resolution is increased. It does not return velocity fluctuations or instantaneous velocity vector fields however; for this, regular CC is required. Table 11.2 presents the settings used in the different correlation methods. Correlation settings were decided on after a brief benchmark test (Appendix G). For CC, this revealed that window sizes smaller than 16×16 pixels became too noisy. All methods used multipass processing outlier detection ($1 \times$ median filter outlier detection, $remove > 2.0$, $reinsert < 3.0$, $filter\ region\ 5 \times 5$, $min.\ vectors: 3$) and vector post-processing ($1 \times$ median filter outlier detection, $remove > 2.0$, $reinsert < 3.0$, $filter\ region\ 5 \times 5$, $min.\ vectors: 3$; $remove\ groups\ with < 3\ vectors$, $fill-up\ empty\ spaces\ (interpolation)$). These settings were based on best practices from prior research within the Aerodynamics department.

Table 11.2: PIV correlation settings and vector field resolutions. ov = overlap.

	Cross-correlation	Sum of correlation
Initial pass window	96×96 , elliptical 2:1, 75% ov	16×16 , square, 75% ov
Final pass window	16×16 , elliptical 2:1, 75% ov	4×4 , circular, 75% ov
Final passes (#)	2	2
Vector pitch, full BL view (μm)	68	17
Vector pitch, zoomed-in view (μm)	34.8	8.7
Δy^+ at 30 m/s, full BL view (-)	5.6	1.4
Δy^+ at 30 m/s, zoomed-in view (-)	2.9	0.7

11.3.3. Vector field processing

Vector fields were exported from DaVis and further processed with MATLAB. A wall-profile ($y_w(x)$) was estimated via a minimum velocity search-and-interpolate method. This wall-estimate was used to correct for non-horizontal walls and potential camera roll angle (tilts around the optical axis). This procedure is further explained in Appendix H.1. Wall-normal profiles were calculated through spatial averaging along x in the entire FOV. Spatial averaging regions were 1.5δ and 2.1δ for 5 m/s and 30 m/s respectively. As such it was assumed that no BL development takes place within one FOV. BL properties such as BL thickness (δ) and momentum thickness (θ) were calculated as the mean for the entire FOV. The friction velocity (u_τ) was estimated with a BL fitting routine adapted from Rodríguez-López et al. (2015). An extensive assessment of different methods for estimating u_τ is presented in Appendix H.2. Uncertainty quantification is discussed in Section 12.1.4.

This page has been intentionally left blank.

12

Particle image velocimetry - Results and discussion

This chapter presents and discusses the results of the particle image velocimetry (PIV) experiments. The seal fur PIV results were not extensively scrutinised given the high drag increase found in the direct force measurements and the challenge of acquiring 'near-wall' data due to heterogeneity of the seal fur. A quick assessment showed that the Reynolds stresses above the seal fur were much higher compared to a smooth wall. This is in line with the high increase in drag. It is not clear to what extent permeability and vibrating hairs of the seal fur play a role. It is expected that both contribute to an increase in turbulence mixing. When dry, the seal fur is not completely flattened in streamwise direction as it is in water, hence increasing wall-normal permeability. Furthermore, raw images acquired with PIV showed vibration of individual hairs of the seal fur, especially at higher velocities. These results can be found in Appendix I.1. Unfortunately, the continuous fibre plate was damaged while preparing the experiments and could therefore not be measured with PIV.

This chapter focuses on the comparison between the reference smooth plate and the 3D-printed plate (from hereon referred to as permeable plate). Drag measurements showed a small to moderate drag increase over the permeable plate above $Re_1 \gtrsim 0.5 \times 10^6$, while at lower velocities, the data was inconclusive. Furthermore, the 3D-printed plate allows for acquiring data close to the surface, such that near-wall effects can be investigated. These reasons justified the choice to focus on the 3D-printed plate in the analysis and discussion of the results from the PIV experiments. First, the quality of the results is assessed in Section 12.1. This includes the effects of the experimental setup visible in the data and uncertainty quantification of calculated metrics. Subsequently, Section 12.2 covers the BL development along the test plates. Section 12.3 goes into detail on the BL profiles at the location where the BL has developed the fullest, near the trailing edge. Quadrant analysis at this location provides further detail on the state of the BL in terms of turbulent events and is elaborated on in Section 12.4. Section 12.5 covers the turbulent structures observed in the instantaneous velocity vector fields. Finally, a discussion of the complete set of PIV results is presented in Section 12.6.

12.1. Data quality assessment and uncertainty quantification

Assessing the quality of the data and, where possible, quantifying uncertainty, is a necessary prerequisite for a reliable assessment of the validity, significance and implications of experimental results. This section discusses the correlation output in Section 12.1.1, effects of the experimental setup visible in the data in Section 12.1.2, quality of the resulting profiles in Section 12.1.3 and uncertainty quantification in Section 12.1.4.

12.1.1. Correlation output

Figure 12.1 shows two examples of instantaneous velocity field results obtained with CC. The images capture the entire boundary layer since the velocity is equal to the freestream velocity in a large enough region at the top of the FOV. Small-scale 'grainy' patterns in the images are the result of the relatively small window size and do not reflect actual physical structures. It is key that these structures do not appear in the freestream, which indeed is not the case as seen in the images. Correlation values for the instantaneous vector fields were generally above 0.9, while some local pockets had values between 0.6 and 0.8.

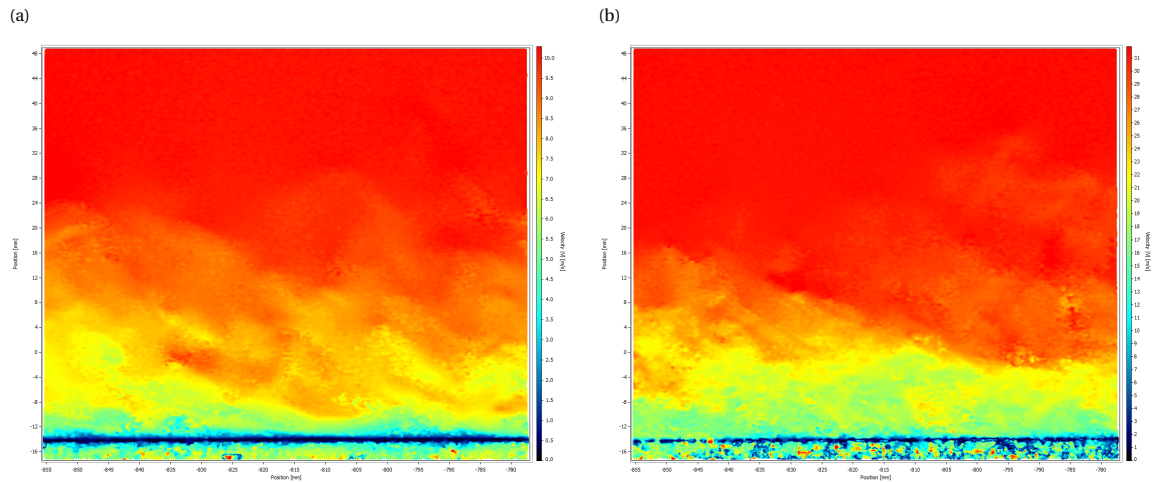


Figure 12.1: Instantaneous velocity field results from cross-correlation for Station 4. (a) 10 m/s (b) 30 m/s. Images taken directly from DaVis export. Flow from right to left.

Figure 12.2 shows two examples of mean velocity field results obtained with CC and SOC methods respectively. The CC mean field is smooth, which indicates good convergence of the results. The SOC mean field is somewhat noisy, indicating that the results have not yet fully converged. This is deemed acceptable since wall-normal mean velocity profiles are generated through spatial averaging along the streamwise direction, increasing the number of data points and reducing the potential error in the estimated mean velocity. This intuition was confirmed with two statistical tests. A one-sample t -test showed that the mean value derived at every wall-normal coordinate (y) indeed was the true mean of the entire set of \bar{u} taken along the streamwise coordinate x at that specific y . Also, a two-sample (Welch's) t -test was performed on two sets of data points ($N = 320$) uncorrelated within the set and between the sets, for every y . This confirmed that for all y , the mean values of these sets were equal within statistical significance. Furthermore, note the similarity between the mean velocity fields obtained with the different correlation methods. A clear, horizontal region with low velocity is visible, wherein the wall lies.

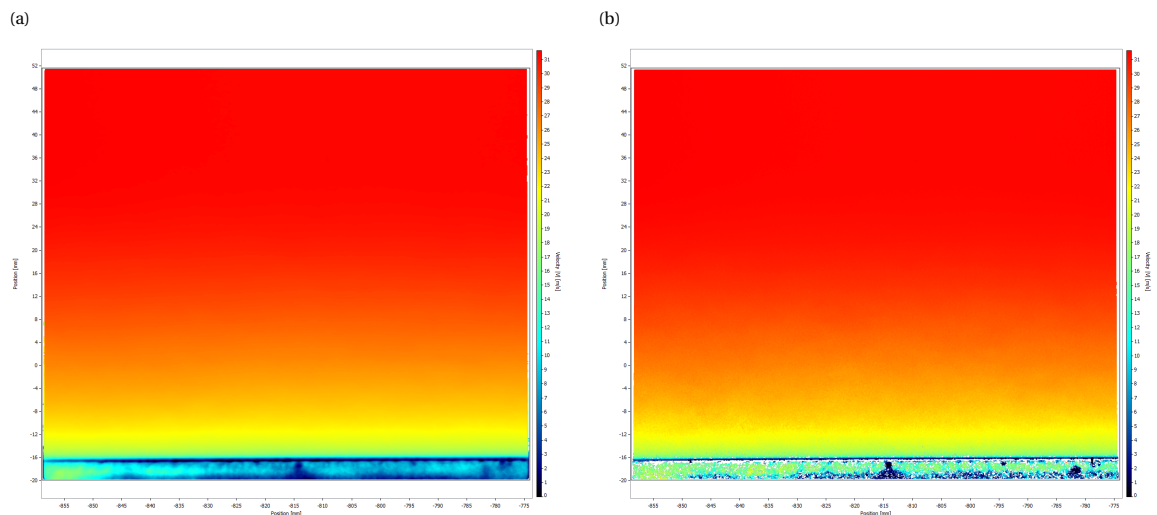


Figure 12.2: Mean velocity field results for Station 4 at 30 m/s. (a) Cross-correlation. (b) Sum of correlation. Images taken directly from DaVis export. Flow from right to left.

12.1.2. Effects of experimental setup

Experimental setups are not ideal and imperfections can have a measurable influence on the data. Two of such effects were identified in the data processing routine and are discussed here. The first is the effect of the camera lens curvature, the second an averaging effect, specifically near the wall.

Camera lens curvature effect

The camera lens is spherical and therefore slightly distorts the image. An extreme example of this is the fish-eye lens, where objects near the edge of the FOV appear smaller than in the middle. In the case of the PIV experiment, this means that the resolution, the number of pixels per length unit, is higher in the centre than at the edges. Image calibration in DaVis however is performed assuming a constant resolution throughout the entire FOV. Consequently, distances, and thus flow velocities, are underestimated in the centre and overestimated towards the edges. The degree to which this happens depends on the region of the calibration image that is used for determining the image resolution.

Figure 12.3a shows how the camera lens affects the estimated U_∞ at every streamwise location in the FOV. Compared to the mean estimate as taken over the entire FOV ($\overline{U_\infty}$), the locally estimated U_∞ is slightly lower near the centre of the FOV, and higher towards the edges. This effect is the same for different absolute values of the U_∞ , as can be seen from the overlapping profiles. This is expected as the raw data is processed based on the same calibration image. The differences are considered small enough to neglect, also given the spatial averaging performed to obtain wall-normal velocity and turbulent statistics profiles for further analysis.

Figure 12.3b shows an example of how an estimated integral BL parameter, in this case the momentum thickness, is affected. The momentum thickness is calculated based on a normalised velocity profile. If the local velocity profile (at a given x) is normalised with the mean freestream velocity as taken over the entire FOV, then the momentum thickness estimate is higher near the centre, and lower near the edges. However, if the local velocity profile is normalised with the U_∞ at that same x , then the momentum thickness shows a slight upward trend, which is expected in a developing boundary layer. When taking the mean momentum thickness in the entire FOV, both methods yield the same result. Therefore, it is considered safe to neglect this effect also when calculating BL parameters.

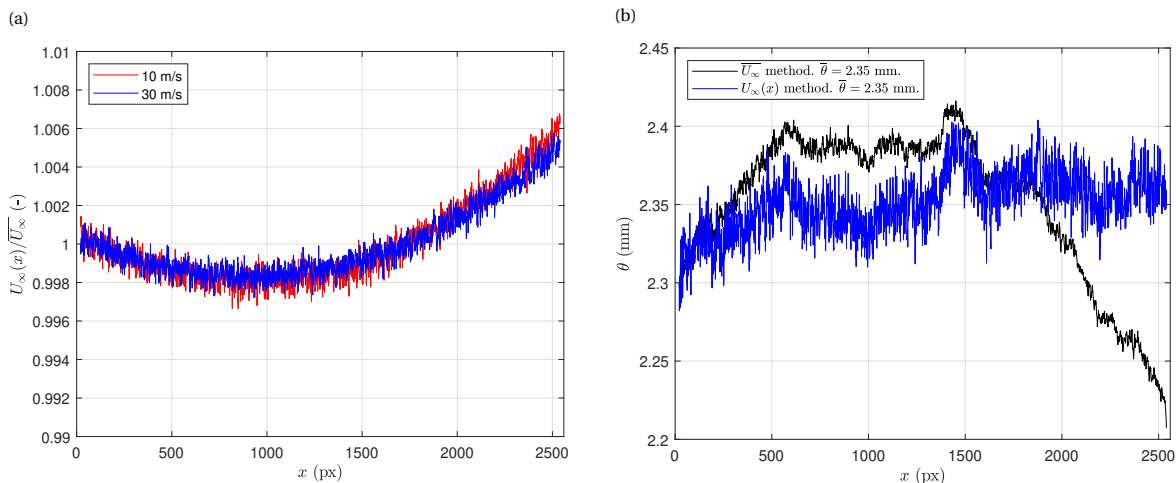


Figure 12.3: FOV edge distortion effect on PIV data at Station 4. (a) Freestream velocity normalised with the mean freestream velocity, averaged along x for the entire FOV. (b) Momentum thickness for $U_\infty = 30$ m/s as determined with the x -dependent and FOV averaged freestream velocities, respectively.

Near-wall averaging effect

Averaging effects can result in biased velocity profiles, especially in regions with high velocity gradients such as near the wall in a TBL. Two of such effects are considered here: averaging due to a finite interrogation window size, and averaging due to a finite laser sheet thickness in the case of a non-horizontal optical path from camera to laser sheet. The first effect is relatively straightforward. Interrogation windows have a finite size and the resultant velocity vector inherently is an average across the interrogation domain. This leads to biased estimates in the case of strong, non-linear velocity gradients or directly at the wall, where an average is taken over a domain that includes wall reflections (Kähler et al., 2012).

The second effect is visualised in Figure 12.4. Since the camera is positioned close to the laser sheet, light beams from the bottom of the FOV travel towards the camera at a small angle. When following this optical path through the laser sheet, it becomes evident that the particles seen at the front of the laser sheet are located at a higher wall-normal position than the particles seen at the back of the laser sheet. In the image, these particles appear to be at the same height. The computed mean velocity at this location therefore is an average of the true velocity profile between the two wall-normal positions of the particles seen at the front and rear of the laser sheet respectively. As such, the averaging effect is similar to that of the finite window size, but decreases towards the centre and increases again towards the top of the FOV. The averaging effect at the top of the FOV is negligible when a full BL is captured since the mean velocity is constant in the freestream.

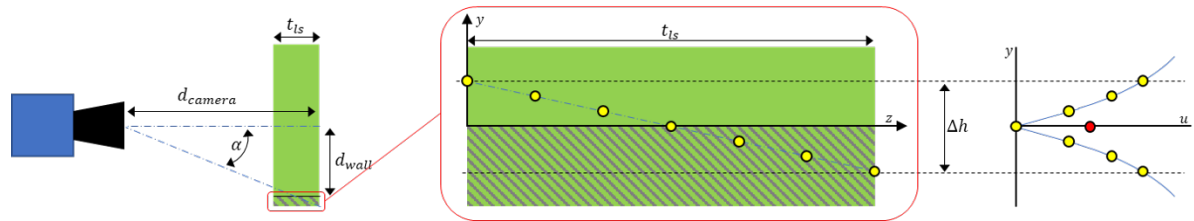


Figure 12.4: Schematic of averaging effect due to light incidence angle (α). $\alpha = \arctan(d_{wall}/d_{camera})$, where d_{wall} denotes the distance between the camera optical axis (mid of FOV) and the wall, d_{camera} the distance between camera and optical plane (laser sheet) and t_{ls} the laser sheet thickness. Δh denotes the averaging region. The red dot indicates the resulting average velocity.

The experimental data were investigated to assess to what extent averaging effects play a role in the inner-layer ($y^+ < 30$), where the velocity gradients are the largest. Two different freestream velocities for the reference plate at Station 4 were taken as a case. Two biased velocity profiles were recreated by applying the averaging effects to the profile fitted to the experimental data. The first case only considers the window averaging effect, the second case also includes the averaging effect because of the non-horizontal optical path. The averaging region of the interrogation window is equal to 4 pixels ($\approx 68 \mu\text{m}$). Based on a camera - laser sheet distance of 25 cm and laser sheet thickness of 2 mm, an incidence angle of 3.8° and consequently averaging region of approximately $133 \mu\text{m}$ is assumed. Note that this is nearly double the averaging region of the interrogation window. Table 12.1 expresses this averaging region in terms of viscous units at the different flow velocities.

Table 12.1: Averaging regions due to finite interrogation window ($d_{a,w}$) and optical angle ($d_{a,o}$) expressed in viscous units (δ_ν) for different freestream velocities.

U_∞ (m/s)	5	10	20	30
$d_{a,w}$	1.0	2.0	3.8	5.6
$d_{a,o}$	2.0	3.9	7.5	10.9

Figure 12.5 shows the results of the averaging effect assessment. The experimental data deviate from the fitted profiles, more so for the higher velocity. Only considering the window averaging effect does not heavily bias the data. A small deviation can be observed in the first two data points at the wall, after which the data follows the fitted profile well. A very small deviation can be seen in the buffer layer for the 30 m/s case, since the velocity gradient is non-linear and still relatively large. Nevertheless, the window averaging effect alone does not account for the large deviation between the experimental data and the fitted profile.

When considering the total averaging effect, it can be seen that the recreated biased profile follows the experimental data remarkably well for both cases. The bias is stronger at higher velocities, since the velocity gradient is larger in physical units. This is similar to saying that the averaging region is larger in viscous units, which can be seen in Table 12.1. As such, the experimental data points contain more bias due to averaging in the high velocity case. This is visible in both the experimental data and the recreated biased profile. The velocity is overestimated directly at the wall due to particle reflections, but underestimated in the rest of the near-wall region. The main implication of this bias is that u_τ cannot be determined from the slope (du/dy) of the velocity profile in the viscous sublayer for all freestream velocities. Averaging along a linear profile yields a new linear profile with a similar slope. For 5 and 10 m/s, the averaging region is smaller than the extent of the viscous sublayer. Therefore, there will be a region within the viscous sublayer where the slope of the biased profile is equal to the true slope, and where therefore u_τ can be estimated directly from the slope. This is not the case for higher velocities, where the estimated slope will be lower than the true slope. This is also visible in Figures 12.5a and 12.5c. Further discussion on estimation of u_τ via this method is given in Appendix H.2.

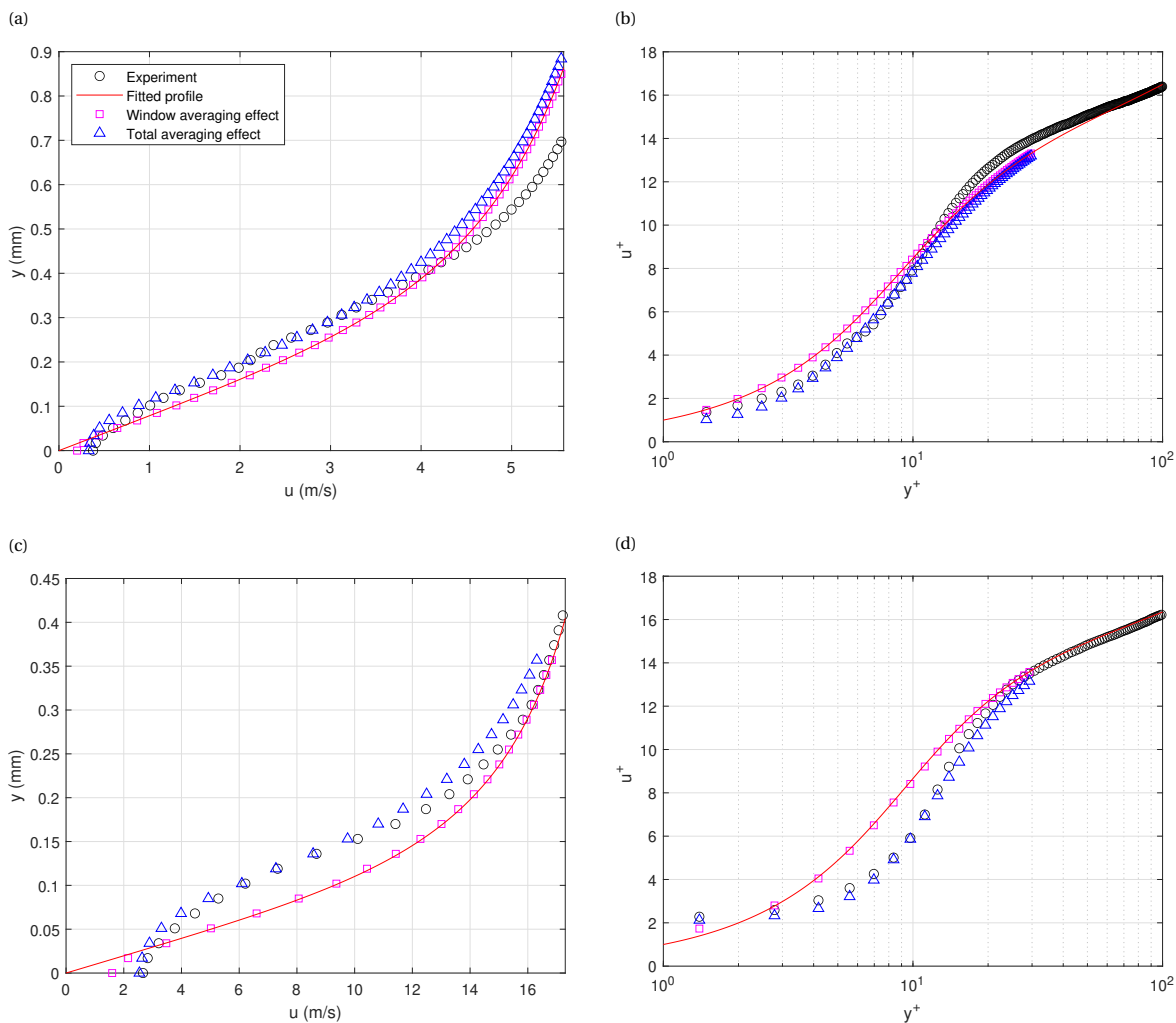


Figure 12.5: Averaging effects near the wall on PIV data for the smooth wall at Station 4. (a, b) 10 m/s. (c, d) 30 m/s. (a, c) Regular units. (b, d) Viscous units.

12.1.3. Diagnostic plot

The diagnostic plot is a method to assess the quality of wall-bounded turbulence data in terms of mean and rms of streamwise velocity (Alfredsson and Örlü, 2010). It is used to check the data near the wall, around the peak in the rms, and in the outer region, and does not require u_τ nor the exact wall location. Figure 12.6 shows the diagnostic plot for the smooth wall measurement at Station 4 (after performing wall-corrections as outlined in Appendix H.1). The data directly near the wall is only reasonably reliable for the lowest velocity, since for the other velocities, the first few data points do not follow the tangent as with the lowest velocity. It is expected that this is due to averaging effects which were discussed in Section 12.1.2. Around the peak in the rms, the data looks reliable. The peak value is slightly lower than the predicted value for all except $Re_\theta = 1020$, again most probably due to averaging effects. In general, the location of the peak corresponds well to what is predicted except for $Re_\theta = 1020$. This could be due to the fact that Alfredsson and Örlü (2010) estimated u_τ via the Coles-Fernholz skin friction relation (Nagib et al., 2007), which might not be valid for low Re_θ . The outer region data collapses well for $u/U_\infty > 0.7$ for all except $Re_\theta = 1020$, although the deviation is relatively small. For this case, it might be possible that the BL has not properly and fully developed into a natural state. All things summarised, the diagnostic plot reveals that in general, the data appears reliable, with the exceptions of the immediate near-wall data (that is, the first few data points); and that for $U_\infty = 5$ m/s, the BL might not have fully developed into a natural state.

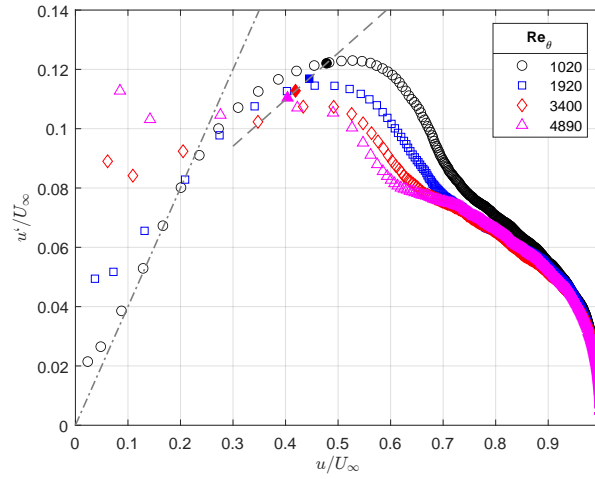


Figure 12.6: Diagnostic plots for Station 4. u from SOC (interpolated on CC vector pitch), u' from CC. Increasing Re_θ corresponds to $U_\infty = \{5, 10, 20, 30\}$ m/s. Dash-dotted line indicates tangent to near-wall data with a slope of 0.40. Dashed line represents $\max(u'/U_\infty) = 0.047 + 0.157U/U_\infty$ while filled symbols represent the expected point of $\max(u'/U_\infty)$ for every Re_θ (Alfredsson and Örlü, 2010).

12.1.4. Uncertainty quantification

Uncertainty is defined as the standard error (ϵ) and performed on the instantaneous velocity vector based on a 0.1 pixel correlation error (Raffel et al., 1998), and on the mean velocity, velocity fluctuation and Reynolds stress components following Sciacchitano and Wieneke (2016), via Equations (12.1) to (12.4) respectively. The latter three are defined for a given (x, y) -location in the vector field. N represents the number of sample points and, for a single measurement, is equal to the number of image-pairs (N_{im}).

$$\epsilon_u = \epsilon_{\text{corr}} \frac{\Delta x_{px}}{\Delta t} \quad (12.1)$$

$$\epsilon_{\bar{u}} = \frac{u_{\text{rms}}}{\sqrt{N}} \quad (12.2)$$

$$\epsilon_{u'} = \frac{u_{\text{rms}}}{\sqrt{2(N-1)}} \quad (12.3)$$

$$\epsilon_{R_{xy}} = u_{\text{rms}} u_{\text{rms}} \sqrt{\frac{1 + \rho_{uv}^2}{N-1}} \quad (12.4)$$

Spatial averaging of these quantities along the streamwise coordinate (x) reduces the standard error proportional to the inverse square root of the number of uncorrelated data points along x (Sciacchitano and Wieneke, 2016). Neighbouring vectors are correlated because of the overlapping interrogation windows. Determining the exact degree of correlation is complex for multi-pass windows of different window shapes and considered out of the scope of this research. Given a 75% overlap, it is assumed that vectors at an interval of four data points are uncorrelated. Hence the standard error (ϵ_T) for any streamwise spatially averaged turbulent statistic (T) at a given wall-normal coordinate (y) is given by:

$$\epsilon_T = \frac{\frac{1}{N_x/4} \sum_{\xi=1}^{N_x} \epsilon_T(\xi)}{\sqrt{N_x/4}} \quad \text{with} \quad \xi = \{x(1), x(5), \dots, x(N_x - 3)\} \quad (12.5)$$

and where N_x represents the number of pixels in the streamwise direction within the FOV.

Table 12.2 presents the uncertainty estimations for the different metrics. Overall the uncertainties are low with all values below 1%. The uncertainty in mean velocity is higher for the permeable plate data, especially in the inner layer ($y^+ < 30$). The uncertainty in velocity fluctuations, when expressed in percentage error, is independent from test plate or U_∞ and is directly related to the number of sampled data points ($\propto (2(N_{im} - 1)N_x/4)^{-1/2}$). For this study, $N_{im} = 600$ and $N_x = 2,560$.

Table 12.2: Uncertainty estimations of turbulent statistics for Station 4. Mean uncertainty percentage along streamwise averaged wall-normal profiles, where percentages are calculated w.r.t. local value, e.g. $(\epsilon_{u_{rms}}/u_{rms}) \times 100$ for a given (x, y) .

Plate	U_∞ (m/s)	ϵ_u (m/s)	$\epsilon_{\bar{u}} _{y^+ < 30}$ (%)	$\epsilon_{\bar{u}}$ (%)	$\epsilon_{u_{rms}}$ (%)	$\epsilon_{v_{rms}}$ (%)	$\epsilon_{\overline{u'v'}}$ (%)
Reference	5	0.025	0.16	0.028	0.23	0.23	0.81
Permeable	5	0.025	0.27	0.037	0.23	0.23	0.81
Reference	10	0.049	0.17	0.023	0.23	0.23	0.83
Permeable	10	0.049	0.31	0.028	0.23	0.23	0.84
Reference	20	0.099	0.19	0.019	0.23	0.23	0.85
Permeable	20	0.099	0.81	0.032	0.23	0.23	0.86
Reference	30	0.15	0.22	0.019	0.23	0.23	0.87
Permeable	30	0.15	1.1	0.031	0.23	0.23	0.88

12.2. Boundary layer development

This section covers the BL development over the tested surfaces. Integral BL properties - BL thickness, displacement thickness, momentum thickness and shape factor - are discussed in Section 12.2.1. Friction and velocity related properties - friction velocity, freestream velocity, normalised friction velocity and friction coefficient - are discussed in Section 12.2.2. All properties are assessed on their absolute values as well as on the relative difference between the permeable and smooth surface, for all measured stations and velocities. Since it is assumed that the flow at Station 1 is unaffected by the type of test plate measured, the maximum difference between the permeable and reference measurements at this station is taken as the uncertainty bound for the calculated differences at the other stations. The complete set of BL fitting parameters (κ , B and Π) is given in Appendix I.2.2.

12.2.1. Integral boundary layer properties

Figure 12.7a shows the development of the BL thickness (δ) over the test plates. The expected general characteristics can be observed: it grows with a close to linear trend and a slightly decreasing slope; and for a given location, an increase in velocity corresponds to a decrease in δ . Figure 12.7b shows the percentage difference over the permeable plate w.r.t. the reference plate. For the first station, the BLs have identical δ for both test plate measurements. This is to be expected since this station is located in front of the test plate. The 10 m/s measurement forms an exception with a 2% decrease. For the other locations, the 10 m/s measurement does not show any significant deviation w.r.t. the other measurements. The decrease is caused by the reference data point, which deviates from the trend observed in Figure 12.7a. Therefore, and given the other results at the first station, it is assumed that this deviation either is an anomaly or arises from a measurement error. Overall, the permeable plate has a δ which is very close to that of the reference plate.

Figures 12.8a and 12.9a show the development of the displacement (δ^*) and momentum thicknesses (θ) respectively. Both trends are similar to the trend observed in the development of δ . In Figures 12.8b and 12.9b it can be seen that for both parameters, the permeable plate has slightly higher values for the majority of the measurements, especially at higher velocities. Fluid particles experience a slightly larger displacement w.r.t the wall, and more momentum is extracted from the flow. This higher loss of momentum for the permeable plate is qualitatively in line with the increase in drag observed in the direct force measurements. Nevertheless, it should be noted that most data points lie within the uncertainty region, that no clear trend is visible, and thus that no definitive conclusions can be made based on these observations.

Figure 12.10a show the development of the shape factor (H). Values between 1.3 and 1.4 are typical for TBL. This requires sufficiently long development lengths and high Reynolds numbers, which is evident from the results: at station 4, all measurements except for 5 m/s have an H between 1.35 and 1.4; and H decreases along the streamwise direction and also decreases with increasing velocity. Figure 12.10b shows a pattern in the difference in H between the plates. H is consistently higher for the permeable plate, and this difference gets larger at higher velocities. The largest differences are observed at station 3. Generally speaking, higher H corresponds to a less favourable pressure gradient. No pressure data was collected during the PIV measurements, but the development of the freestream velocity can serve as an indication of the pressure gradient.

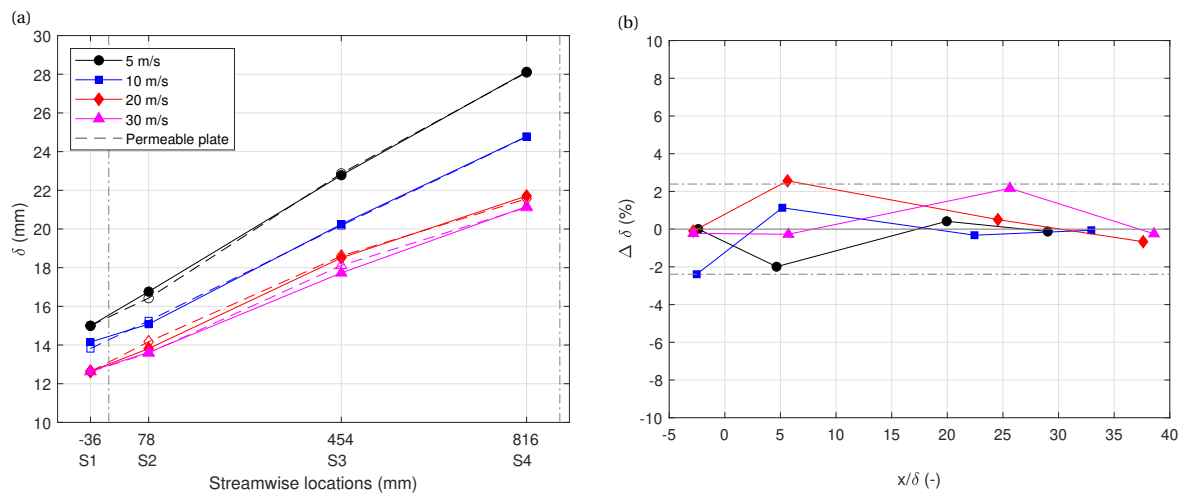


Figure 12.7: Development of boundary layer thickness (δ) over the test plate for different velocities. (a) Absolute values for reference and permeable plate for different absolute streamwise locations. (b) Percentage difference of permeable w.r.t. reference plate for normalised streamwise locations x/δ .

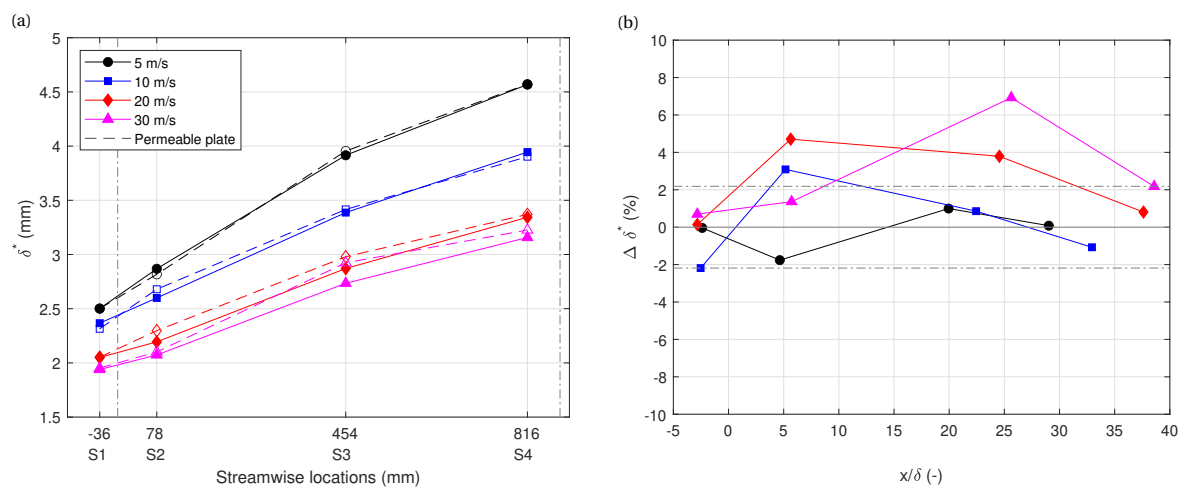


Figure 12.8: Development of displacement thickness (δ^*) over the test plate for different velocities. (a) Absolute values for reference and permeable plate for different absolute streamwise locations. (b) Percentage difference of permeable w.r.t. reference plate for normalised streamwise locations x/δ .

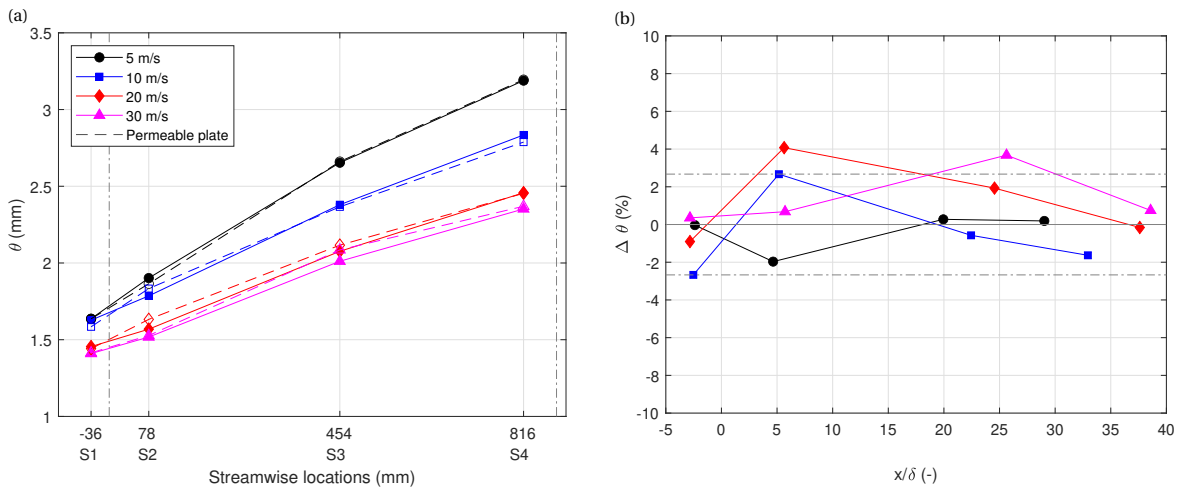


Figure 12.9: Development of moment thickness (θ) over the test plate for different velocities. (a) Absolute values for reference and permeable plate for different absolute streamwise locations. (b) Percentage difference of permeable w.r.t. reference plate for normalised streamwise locations x/δ .

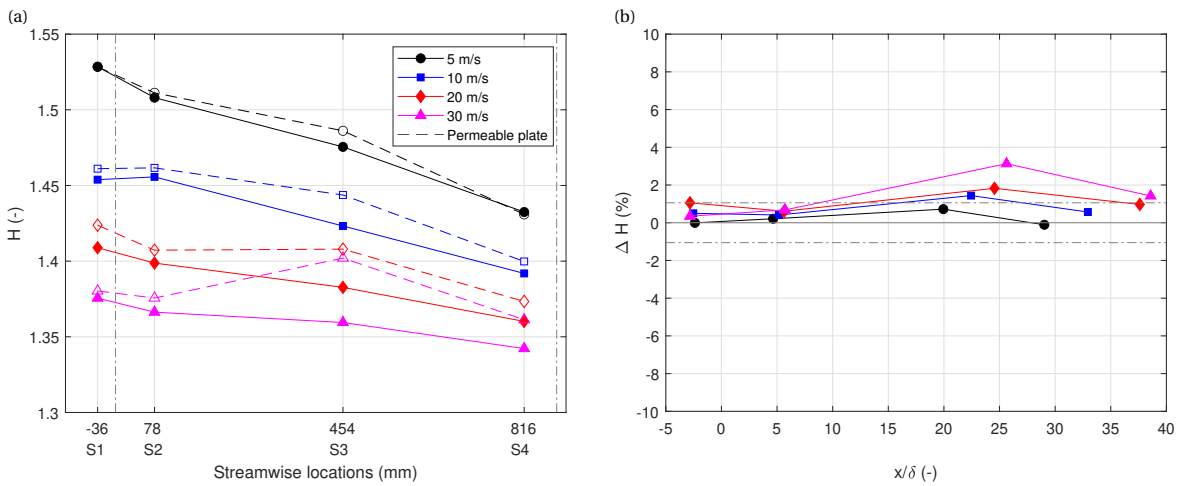


Figure 12.10: Development of shape factor (H) over the test plate for different velocities. (a) Absolute values for reference and permeable plate for different absolute streamwise locations. (b) Percentage difference of permeable w.r.t. reference plate for normalised streamwise locations x/δ .

12.2.2. Friction parameters

Figure 12.11a shows the development of the friction velocity (u_τ). It increases with increasing velocity and seems to remain constant over the test plate. While the first is expected, the second observation is not in line with the common knowledge that u_τ slightly decreases with increasing development length. Comparing the permeable and reference plates (Figure 12.11b), no consistent differences can be observed. u_τ values are slightly lower for the permeable plate at station 3, but the differences lie within the uncertainty bounds.

Figure 12.12a shows the development of the freestream velocity, established as percentage difference w.r.t. the freestream velocity as measured at the first station ($U_\infty/U_{\infty,S1}$). The flow accelerates along the test plate, for both the reference and the permeable plates. Regardless of the absolute values, the velocity is between 4 and 5% higher at the end of the test plate compared to the front. This could explain the lack of decreasing trend in u_τ , since a higher U_∞ corresponds to a higher u_τ . Furthermore, differences can be observed between the permeable and reference cases. Firstly, the flow accelerates over the LE for the permeable case, whereas the flow remains at constant velocity for the reference case. This is followed by a lower acceleration between Stations 2 and 3/4 for the permeable plate, and a higher acceleration for the reference plate. This last observation indicates a more favourable pressure gradient for the reference plate and thus could explain the earlier observations on the slightly higher H for the permeable case.

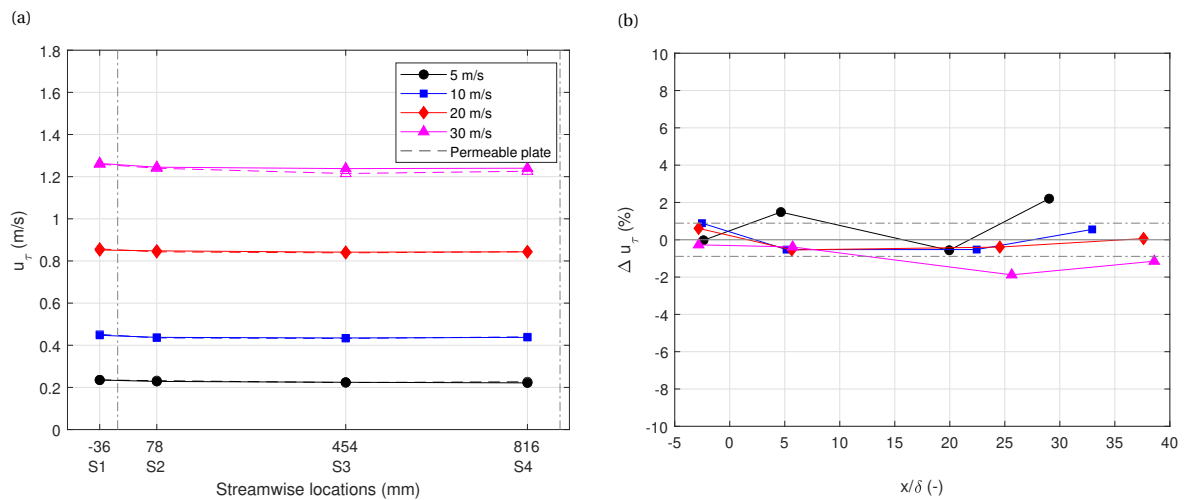


Figure 12.11: Development of friction velocity (u_τ) over the test plate for different velocities. (a) Absolute values for reference and permeable plate for different absolute streamwise locations. (b) Percentage difference of permeable w.r.t. reference plate for normalised streamwise locations x/δ .

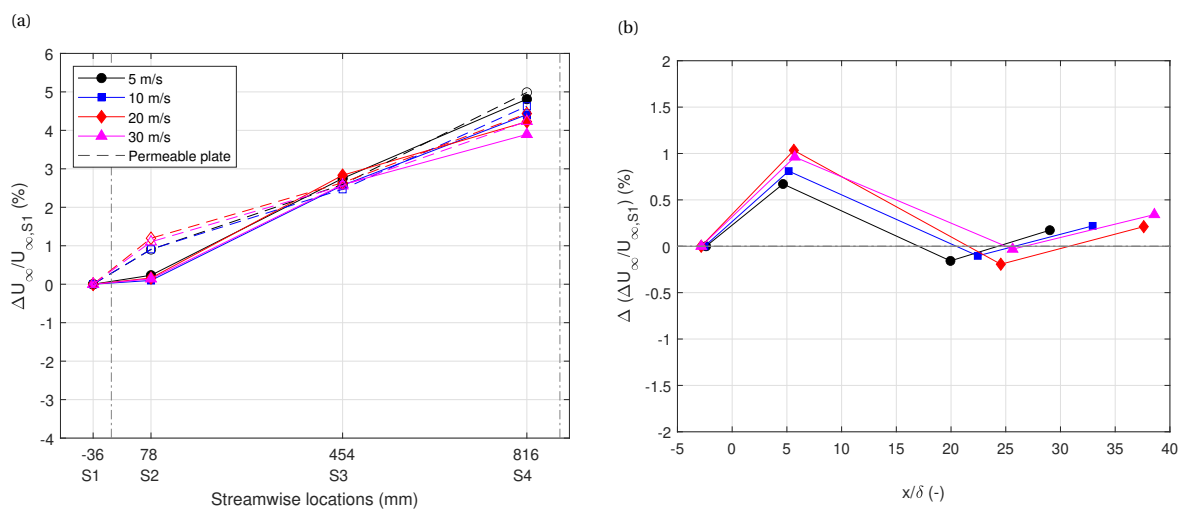


Figure 12.12: Development of freestream velocity normalised to the Station 1 value ($U_\infty/U_{\infty,S1}$) over the test plate for different velocities. (a) Absolute values for reference and permeable plate for different absolute streamwise locations. (b) Percentage point difference of permeable w.r.t. reference plate for normalised streamwise locations x/δ .

Figures 12.13a and 12.14a shows the development of the normalised friction velocity (u_τ/U_∞) and friction coefficient (C_f). They follow identical trends since these parameters are related via Equation (2.22): decreasing values for increasing velocities, and decreasing values for increasing development length, both in line with expectations for TBL. Three observations can be made when assessing the differences between the permeable and reference plates (Figures 12.13b and 12.14b). Firstly, at Station 2, all velocities except 5 m/s show a decrease in C_f between 2% and 3%. This could be the result of the sudden increase in U_∞ while the BL might not have had time to fully adapt, such that an unchanged u_τ is normalised with an increased U_∞ . Secondly, for 30 m/s, C_f is between 2% and 2.5% lower for all stations on the test plate (2 through 4). This value is relatively close to the uncertainty bound. Lastly, at Station 4, the difference in C_f is most positive for the lowest velocity, and decreases to most negative for the highest velocity. Based on the theoretical framework, only for $U_\infty = 5$ m/s a drag prediction can be made. The other velocities are beyond the breakdown velocity. This is done for the final station only since the predicted values do not differ much along the streamwise direction.

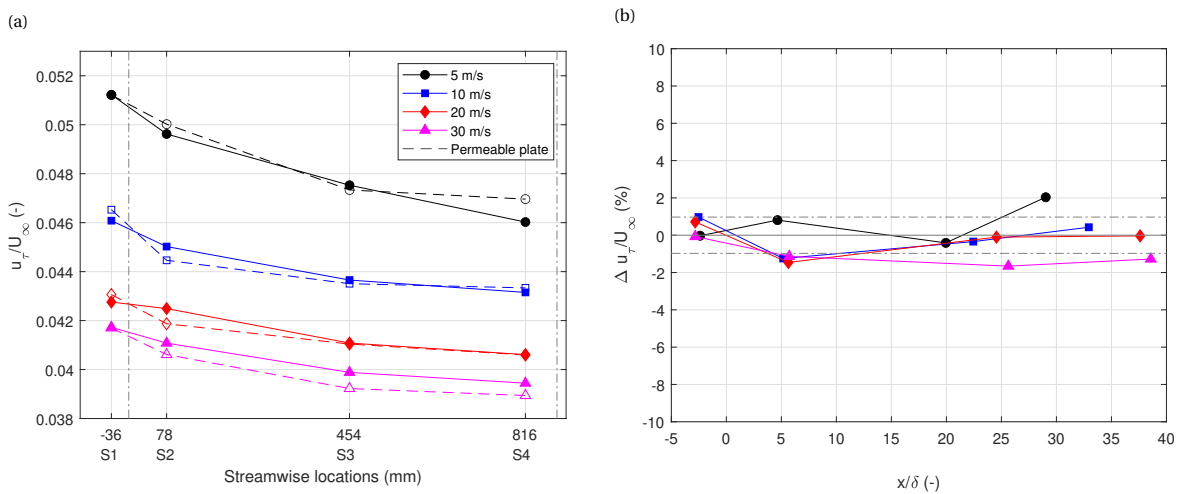


Figure 12.13: Development of normalised friction velocity (u_τ/U_∞) over the test plate for different velocities. (a) Absolute values for reference and permeable plate for different absolute streamwise locations. (b) Percentage difference of permeable w.r.t. reference plate for normalised streamwise locations x/δ .

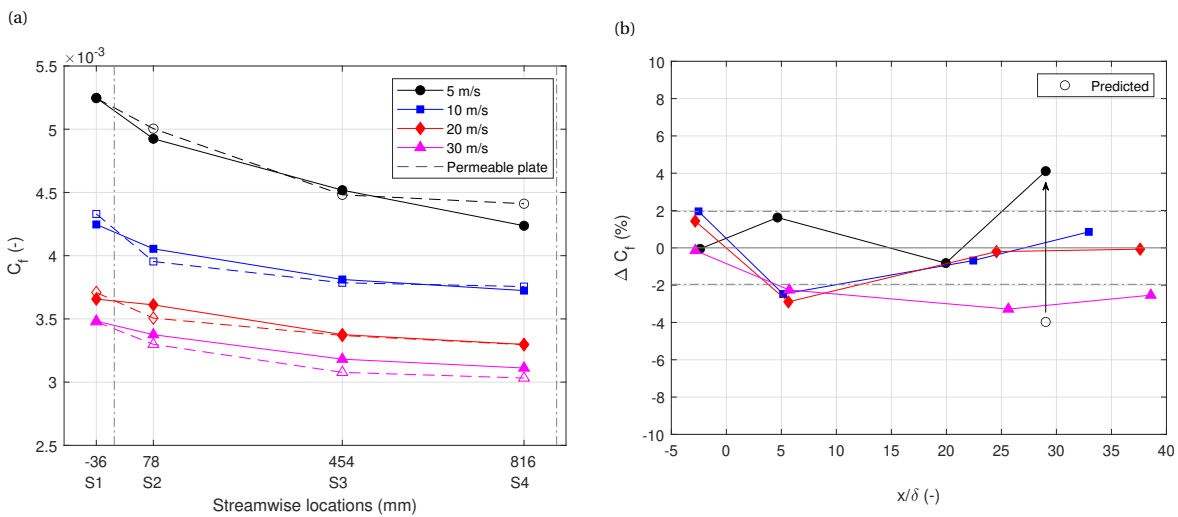


Figure 12.14: Development of friction coefficient (C_f) over the test plate for different velocities. (a) Absolute values for reference and permeable plate for different absolute streamwise locations. (b) Percentage difference of permeable w.r.t. reference plate for normalised streamwise locations x/δ . Prediction assuming average case for permeability estimates ($K_x = 3.5 \times 10^{-9} \text{ m}^2$, $K_y = 2.3 \times 10^{-10} \text{ m}^2$, $K_z = 4.7 \times 10^{-10} \text{ m}^2$).

12.3. Boundary layer profiles: mean velocity and turbulent statistics

This section discusses the BL profiles of the mean velocity and turbulent statistics in more detail. All data is taken from Station 4 since this location represents the most developed BL. The regular zoom data is taken such that the entire BL is captured.

Figure 12.15 presents the mean velocity profiles for different Reynolds numbers (Re_τ) separated by test plate. For both the smooth and permeable plates, the profiles show expected behaviour. The profiles collapse well in the overlap layer, especially for the permeable surface. For increasing Re_τ , two changes can be observed. Firstly, the overlap layer grows in length and so does the entire BL when expressed in viscous units. This is typical as the freestream (Reynolds) effects increase. Secondly, the profile in the inner layer shifts further downwards, and for $y^+ < 5$, further away from the theoretically expected profile. This is due to the averaging effects which increase in strength with increasing U_∞ , as discussed in Section 12.1.2.

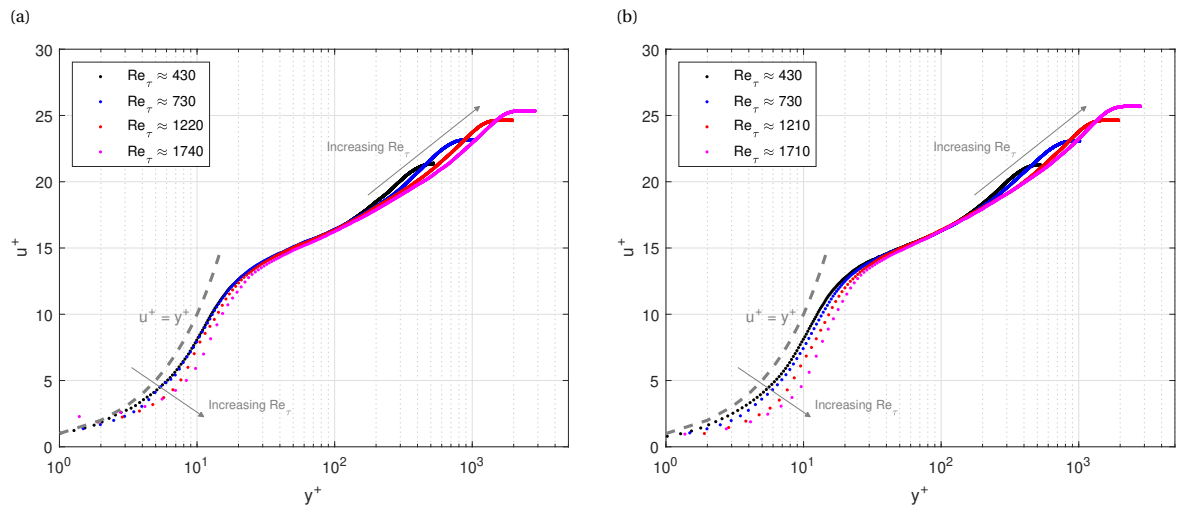


Figure 12.15: Boundary layer mean velocity profiles for $U_\infty \approx 5, 10, 20$ & 30 m/s at Station 4. (a) Smooth wall. (b) Permeable surface.

Figures 12.16 to 12.19 show the mean velocity, streamwise velocity fluctuation, wall-normal velocity fluctuation and Reynolds stress profiles, for 5, 10, 20 and 30 m/s respectively. The mean velocity profile is based on the SOC data, the other statistics on the CC data, explaining the discrepancy in vector pitch of the profiles. For validation and comparison, DNS data by Schlatter and Örlü (2010) is included. Unfortunately, for 30 m/s, no good match in terms of Re_τ or Re_θ was available in this data set. For the higher velocities, a clear bias in the first data points can be seen, also for the turbulent statistics profiles. In general, all profiles have similar shapes when comparing the two test plates. Especially the mean velocity profiles are near identical.

The mean velocity profiles show good agreement with DNS data (Figures 12.16a, 12.17a, 12.18a and 12.19a). At lower velocities, there is a slightly larger 'bump' in the buffer layer visible in the experimental data. Furthermore, in all cases, the wake is slightly less strong for the experimental data. In the inner layer, the mean velocity profile for the permeable plate consistently lies slightly below that of the reference plate. Two causes could explain this observation. First, the reflections on the plate surface may be less strong for the 3D-printed plate compared to the reference plate. Consequently, the averaging region near the wall will contain less reflected velocity vectors, lowering the resultant mean velocity near the wall. Secondly, the 3D-printed plate may be slightly tilted around the streamwise rotation axis. This would mean that the wall at the back of the laser sheet is slightly higher than at the front, which strengthens the optical path averaging effect. All in all, it is clear that no slip velocity can be observed for the permeable surface. This is in contrast to what is predicted by the theoretical model (dash-dotted lines in the inner layer).

In the streamwise velocity fluctuation profiles (Figures 12.16b, 12.17b, 12.18b and 12.19b), a clear peak is present at $y^+ \approx 15$ for 5 and 10 m/s. For 20 m/s this peak is still just visible, but for 30 m/s the averaging effect is too strong to yield a clear peak at $y^+ = 15$. This peak location is typical for streamwise velocity fluctuations in wall-bounded turbulence and also visible in the DNS data. This gives confidence in the velocity fluctuation data, and also in the method for determining the wall location. The peak strength is slightly lower than the DNS data for increasing velocity, which can be ascribed to a larger influence of averaging effects. Compared to the smooth wall, at 5 m/s, the peak is lower for the permeable plate whereas for higher velocities, this peak is increasingly higher. Between $y^+ \approx 15$ and $y^+ \approx 200$, the permeable profile lies below the reference profile for 5 and 10 m/s and above for higher velocities. Near the BL edge, the profiles are higher than the DNS data for 5 m/s. This is in line with the findings from the diagnostic plot in Section 12.1.3.

In the wall-normal velocity fluctuation profiles (Figures 12.16c, 12.17c, 12.18c and 12.19c), a wider peak is observable, shifting from $y^+ \approx 100$ for 5 m/s further away from the wall to $y^+ \approx 250$ for 30 m/s while simultaneously getting wider. Differences between the permeable and reference plates are similar to the streamwise fluctuations. The peak is lower for the permeable plate at 10 m/s and higher at higher velocities. In the inner layer ($y^+ < 30$), the wall-normal velocity fluctuations are consistently higher for the permeable plate. This could be because fluid can be exchanged across the permeable surface, increasing the occurrence and strength of velocity fluctuations near the wall. In all cases, the profiles are significantly attenuated and lie below the DNS data, an effect that grows stronger with increasing velocity. This is true for both the smooth and permeable wall, and can be attributed to the spatial averaging effects. Turbulent flow structures with length scales smaller than the window size of the CC method (approximately $\{4, 8, 15, 22\} \delta_\nu$ for $U_\infty \approx \{5, 10, 20, 30\}$ m/s) are not properly resolved. These small-scale structures have a significant contribution to the energetic content of the wall-normal fluctuations, and consequently, their magnitude is underestimated. The streamwise fluctuation profiles do not suffer from this since they are typically associated with larger-scale flow features than the wall-normal velocity fluctuations. Similar observations were made by Efstathiou and Luhar (2020).

In the Reynolds stress profiles (Figures 12.16d, 12.17d, 12.18d and 12.19d), the peak also shifts away from the wall with increasing freestream velocity, from $y^+ \approx 60$ for 5 m/s to $y^+ \approx 200$ for 30 m/s. The profiles go to zero towards the edge of the boundary layer, indicating that no Reynolds stresses are generated in the freestream. At 5 and 10 m/s, it is clear that the permeable plate yields a lower peak in the Reynolds stress. For 20 m/s no significant difference can be observed, and for 30 m/s, the permeable plate has a larger peak in Reynolds stress. As with the wall-normal velocity fluctuations, the profiles all lie below the DNS data. This can be attributed to the underestimation of wall-normal velocity fluctuations as a consequence of window averaging effects. Apart from that, the profiles match the DNS data reasonably well.

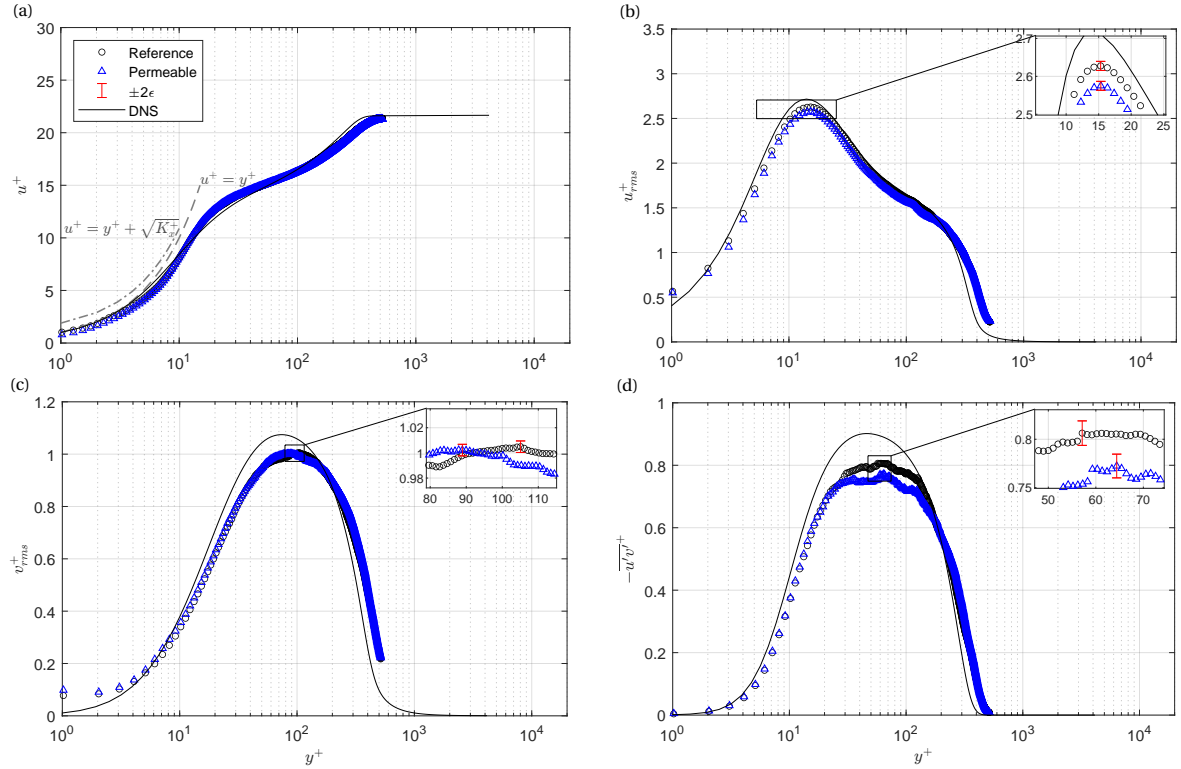


Figure 12.16: Boundary layer profiles for $U_\infty \approx 5$ m/s at Station 4. $Re_\tau \approx 420$ & 420 and $Re_\theta \approx 1,020$ & $1,020$ for smooth wall and permeable surface respectively. $\sqrt{K_x^+} \approx 0.9$. DNS data for $Re_\tau \approx 1,010$ and $Re_\theta \approx 360$ from Schlatter and Örlü (2010). (a) Mean velocity (u^+). (b) Streamwise velocity fluctuations (u_{rms}^+). (c) Wall-normal velocity fluctuations (v_{rms}^+). (d) Reynolds stress ($-\overline{u'v'}$).

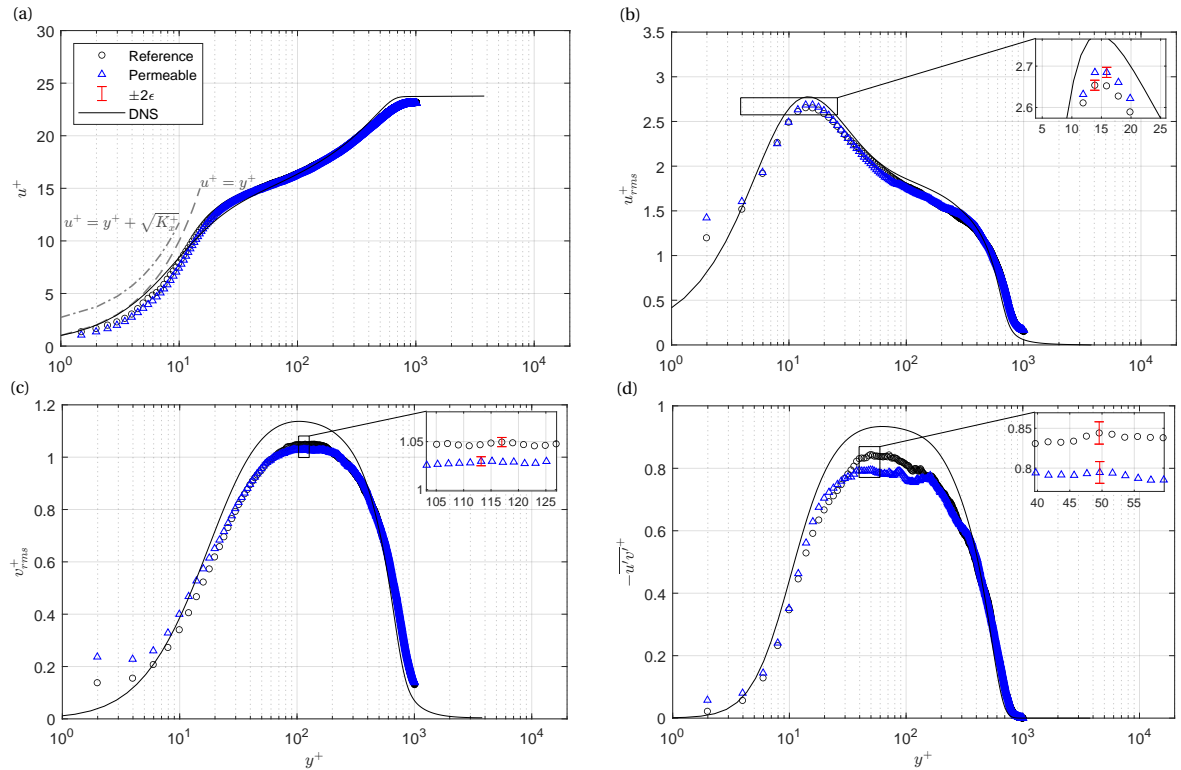


Figure 12.17: Boundary layer profiles for $U_\infty \approx 10$ m/s at Station 4. $Re_\tau \approx 720$ & 720 and $Re_\theta \approx 1,920$ & $1,880$ for smooth wall and permeable surface respectively. $\sqrt{K_x^+} \approx 1.7$. DNS data for $Re_\tau \approx 670$ and $Re_\theta \approx 2,000$ from Schlatter and Örlü (2010). (a) Mean velocity (u^+). (b) Streamwise velocity fluctuations (u_{rms}^+). (c) Wall-normal velocity fluctuations (v_{rms}^+). (d) Reynolds stress ($-\overline{u'v'}$).

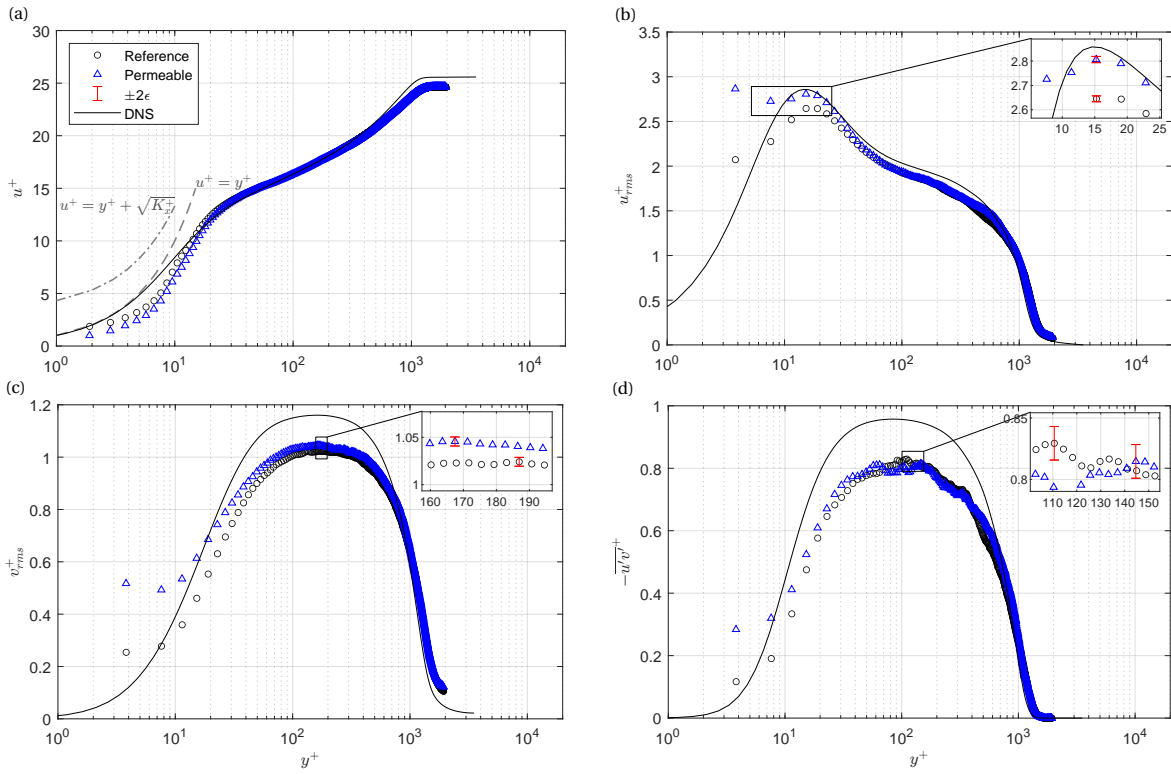


Figure 12.18: Boundary layer profiles for $U_\infty \approx 20$ m/s at Station 4. $Re_\tau \approx 1,220$ & $1,210$ and $Re_\theta \approx 3,400$ & $3,380$ for smooth wall and permeable surface respectively. $\sqrt{K_x^+} \approx 3.3$. DNS data for $Re_\tau \approx 1,150$ and $Re_\theta \approx 3,630$ from Schlatter and Örlü (2010). (a) Mean velocity (u^+). (b) Streamwise velocity fluctuations (u_{rms}^+). (c) Wall-normal velocity fluctuations (v_{rms}^+). (d) Reynolds stress ($-\overline{u'v'}$).

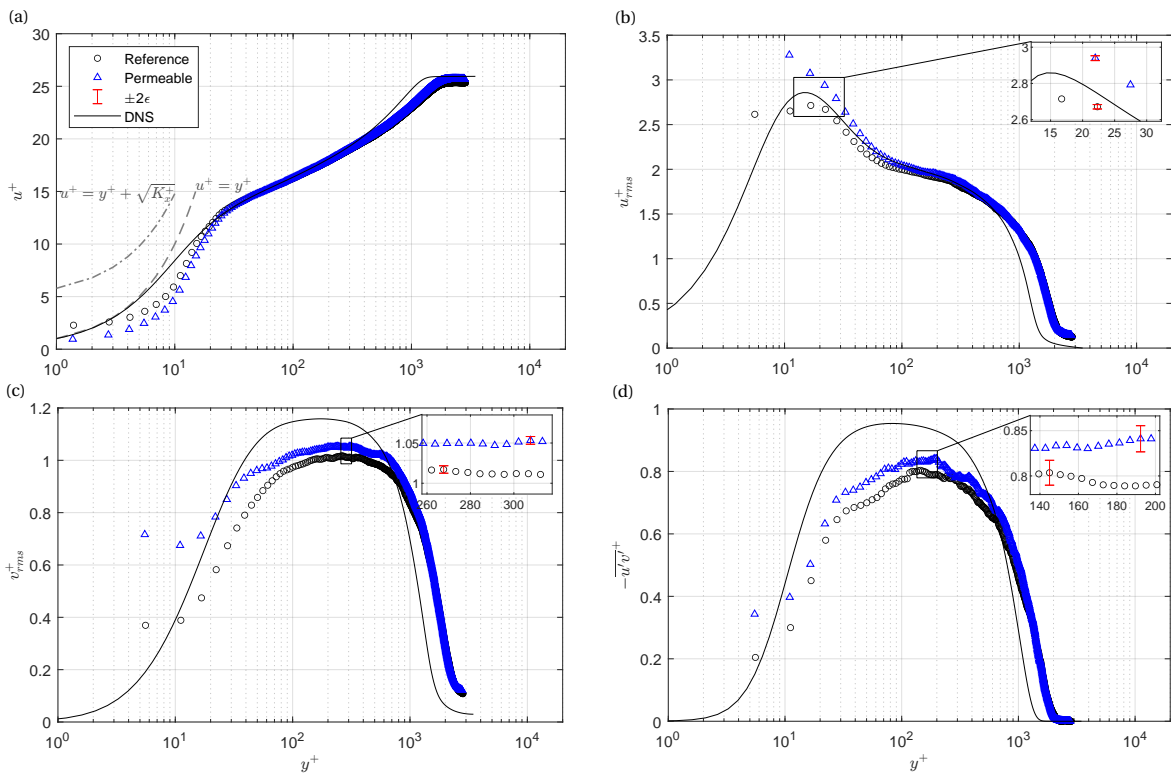


Figure 12.19: Boundary layer profiles for $U_\infty \approx 30$ m/s at Station 4. $Re_\tau \approx 1,740$ & $1,710$ and $Re_\theta \approx 4,890$ & $4,920$ for smooth wall and permeable surface respectively. $\sqrt{K_x^+} \approx 4.8$. (a) Mean velocity u^+ . (b) Streamwise velocity fluctuations u_{rms}^+ . (c) Wall-normal velocity fluctuations v_{rms}^+ . (d) Reynolds stress $-\overline{u'v'}$.

12.4. Quadrant analysis

A further breakdown of the turbulent fluctuations is performed via a quadrant analysis. All individual data points for the instantaneous velocity fluctuations are normalised with the root-mean-square values at their corresponding y -coordinate. This yields a set of approximately 378,000 data points per y -location, which are divided into 50×50 square bins in a domain of $[-5, 5]$. Analyses are performed at wall-normal heights of $y^+ = \{10, 30, 100, 300\}$, to investigate what happens in the buffer layer and wake region for the different cases of lower and higher peak Reynolds stresses at $U_\infty = 10$ & 30 m/s respectively. The quadrant analysis is divided into event probability (Section 12.4.1), individual event contribution to Reynolds stress (Section 12.4.2) and aggregated event contribution to Reynolds stress (Section 12.4.3). Section 2.3 explains the analysis methods.

12.4.1. Event probability

Figure 12.20 presents the Joint Probability Density Function (JPDF) for the smooth wall, and the difference of the permeable wall with respect to this reference smooth wall. Overall, it can be observed that for higher y^+ , the contour map has a higher degree of symmetry, aligned across the negative unity slope. This indicates that the boundary layer is in a more isotropic turbulent state further away from the wall. Furthermore, the contour is stretched to larger values inside Q2 and Q4 compared to Q1 and Q3, indicating a higher probability of stronger ejection and sweep events compared to inner and outer interaction. Also, the relative occurrence of these events, irrespective of strength, is higher (approximately 30 – 35% compared to 15 – 20%).

The differences in event probability between the two surfaces are relatively small. At low velocities ($U_\infty = 10$ m/s), there are somewhat more ejection (+1%) and slight less sweep events (–0.5%) near the wall ($y^+ = 10$), and also slightly less sweep events (–0.5%) further away from the wall ($y^+ = 100$). Also, a higher proportion of weak events (red colour around (0,0)) and lower proportion of strong events (blue colour further away from (0,0)) can be seen for $y^+ = 10, 30$ & 100 , while the opposite is true for $y^+ = 300$. At high velocities ($U_\infty = 30$ m/s), large differences seem present near the wall ($y^+ = 10$) at first sight. It should be noted however that the validity of data at this location is questionable, given that it falls within the first four data-points from the wall, which from the diagnostic plot are known to be biased (Section 12.1.3). This was also observed in the turbulent statistics profiles (Section 12.3). At the other wall-normal locations, overall a lower proportion of weak events and higher proportion of stronger events take place for the permeable wall.

12.4.2. Individual event contribution to Reynolds stress

Figure 12.21 presents the Weighted Joint Probability Density Function (WJPDF) for the smooth wall, and the difference of the permeable wall with respect to this reference smooth wall. Absolute values are plotted, such that the strength of events from Q1 and Q3 (which have positive values) can more easily be compared to those from Q2 and Q4 (which have negative values). The contours are empty (zero value) along the axes per definition. As previously mentioned, the data at $y^+ = 10$ for $U_\infty = 30$ m/s is thought not to be valid. Overall, it can be observed that Q2 and Q4 events contribute more to the Reynolds stress (darker shading) than Q1 and Q3 events, regardless of y -location or velocity. Furthermore, the largest contribution is mostly from medium-strength events, as the darkest regions are neither close to the axes nor far towards the corners of the plot. The near-wall location ($y^+ = 10$) forms an exception, where the strong sweep and ejection events with large wall-normal fluctuations (clear dark shading further away from the x -axis) also contribute significantly to the Reynolds stress. Note that the trend towards symmetry for larger wall-normal locations observed in the regular JPDF contours (Figure 12.20) is also observed here. A slightly larger variance in ejection event contribution remains present.

A few trends can be observed when comparing the two surfaces. Firstly, for low velocities ($U_\infty = 10$ m/s) and close to the wall ($y^+ = 10$), sweep events with larger wall-normal velocity fluctuations have a larger contribution (red shading further away from x -axis) to the Reynolds stress compared to sweep events with lower wall-normal velocity fluctuations (blue shading closer to x -axis). Furthermore, at $y^+ = 100$, an overall decrease in contribution to Reynolds stress can be observed (significantly more blue than red shading). The opposite is true for high velocities ($U_\infty = 30$ m/s), where the majority of the shading is red. For some cases, e.g. $y^+ = 30$ at $U_\infty = 10$ m/s, no clear pattern can be distinguished, as differences are distributed seemingly randomly in the plot, with approximately an equal proportion of increase and decrease.

12.4.3. Aggregated event contribution to Reynolds stress

Figure 12.22 presents the aggregated contribution of all events to the Reynolds stress after performing hole filter sampling. As previously mentioned, the data at $y^+ = 10$ for $U_\infty = 30$ m/s is thought not to be valid, which is evident from how the plotted trends (Figure 12.22b) heavily deviate from the other cases. Overall, it can be observed that near the wall ($y^+ = 10$), sweep events contribute more to the Reynolds stress (blue line above red line), whereas the opposite is true for all other wall-normal locations. Also, strong events have a larger contribution near the wall than further away from the wall: for $U_\infty = 10$ m/s, the combined contributions within $H = 8$ is approximately 80% for $y^+ = 300$, but only 70% for $y^+ = 10$. Similar observations hold for $U_\infty = 30$ m/s when comparing $y^+ = 30$ to $y^+ = 100$. For $y^+ = 300$, Q4-events have a larger contribution to the Reynolds stress for 30 m/s compared to 10 m/s. This could be explained by the fact that at lower velocities, $y^+ = 300$ is closer to the BL edge ($y/\delta \approx 0.3$ vs. $y/\delta \approx 0.1$). While the wall-normal location is the same in inner variables, which provides the relevant length scale for $y/\delta < 0.1$, it is different in outer variables, which is more relevant for $y^+ > 100$.

Differences between the two surfaces depend on both the wall-normal location and the freestream velocity. For $U_\infty = 10$ m/s, the Q2- and Q4-events result in a higher production of Reynolds stress close to the wall ($y^+ = 10$), but lower production close to the location of peak Reynolds stress ($y^+ = 100$). At the actual location of peak Reynolds stress ($y^+ = 50$), the strength of Q2- and Q4-events is also lower (not shown here). For $U_\infty = 30$ m/s, the Q2- and Q4-events result in a higher production of Reynolds stress for all wall-normal locations. This indicates a higher degree of turbulence in the entire boundary layer and corresponds to findings in both the JPDF and WJPDF (Figures 12.20 and 12.21). When normalising w.r.t. the plate's own value of the Reynolds stress (i.e. not normalising w.r.t. smooth case), the relative contribution of Q2- and Q4-events does not show a clear trend when comparing the two surfaces and is relatively similar at most wall-normal locations (not shown here). This indicates that although the strength of the events differs for certain wall-normal locations when comparing the two surfaces, there is no clear indication for a significant difference in the overall state of the boundary layer in terms of a changed relative contribution of the turbulent events.

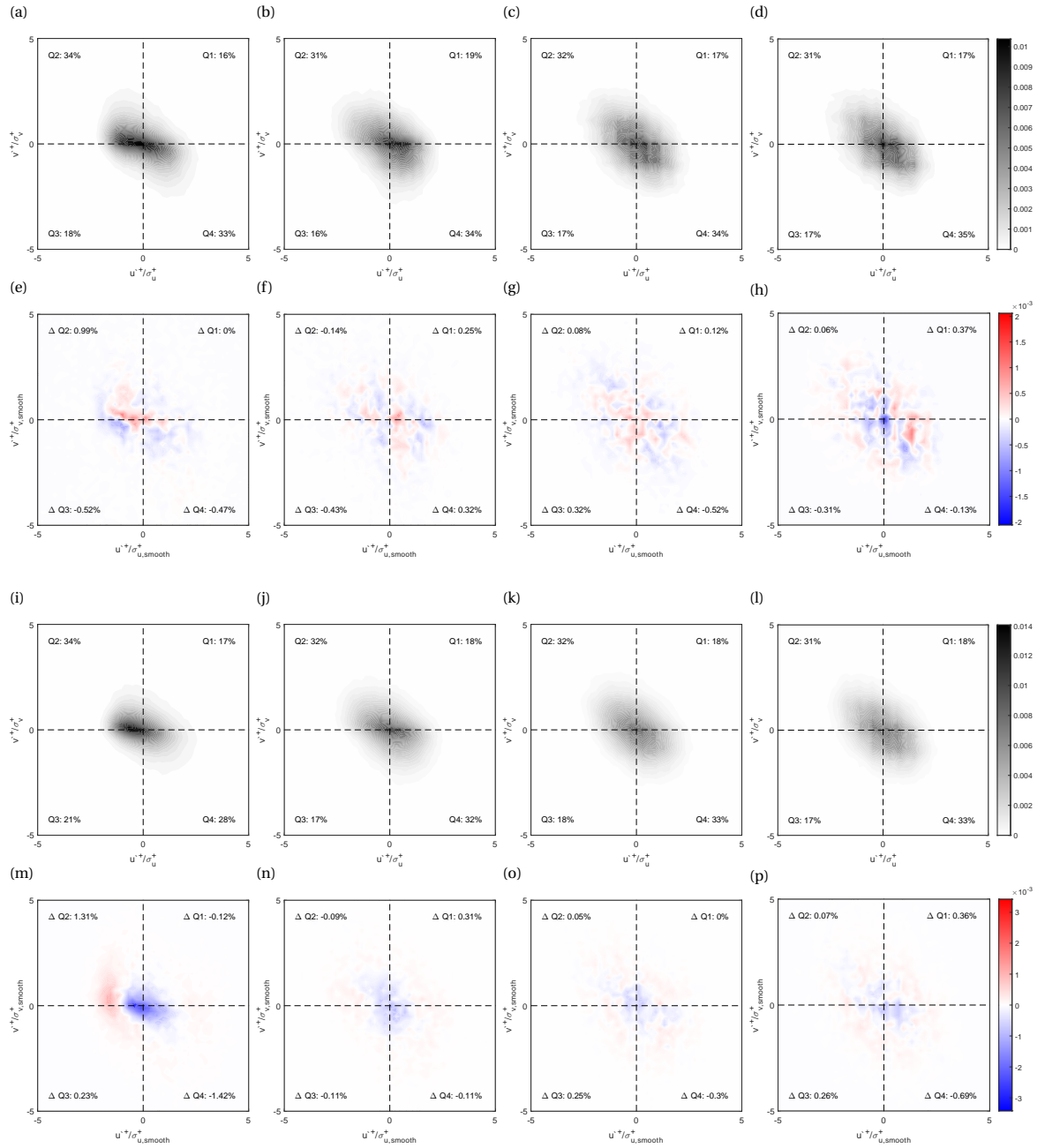


Figure 12.20: Joint probability density function for Station 4. (a-d, i-l) Reference smooth wall. (e-h, m-p) Difference of permeable wall w.r.t. reference smooth wall. (a-h) $U_\infty = 10$ m/s. (i-p) $U_\infty = 30$ m/s. (a, e, i, m) $y^+ = 10$. (b, f, j, n) $y^+ = 30$. (c, g, k, o) $y^+ = 100$. (d, h, l, p) $y^+ = 300$.

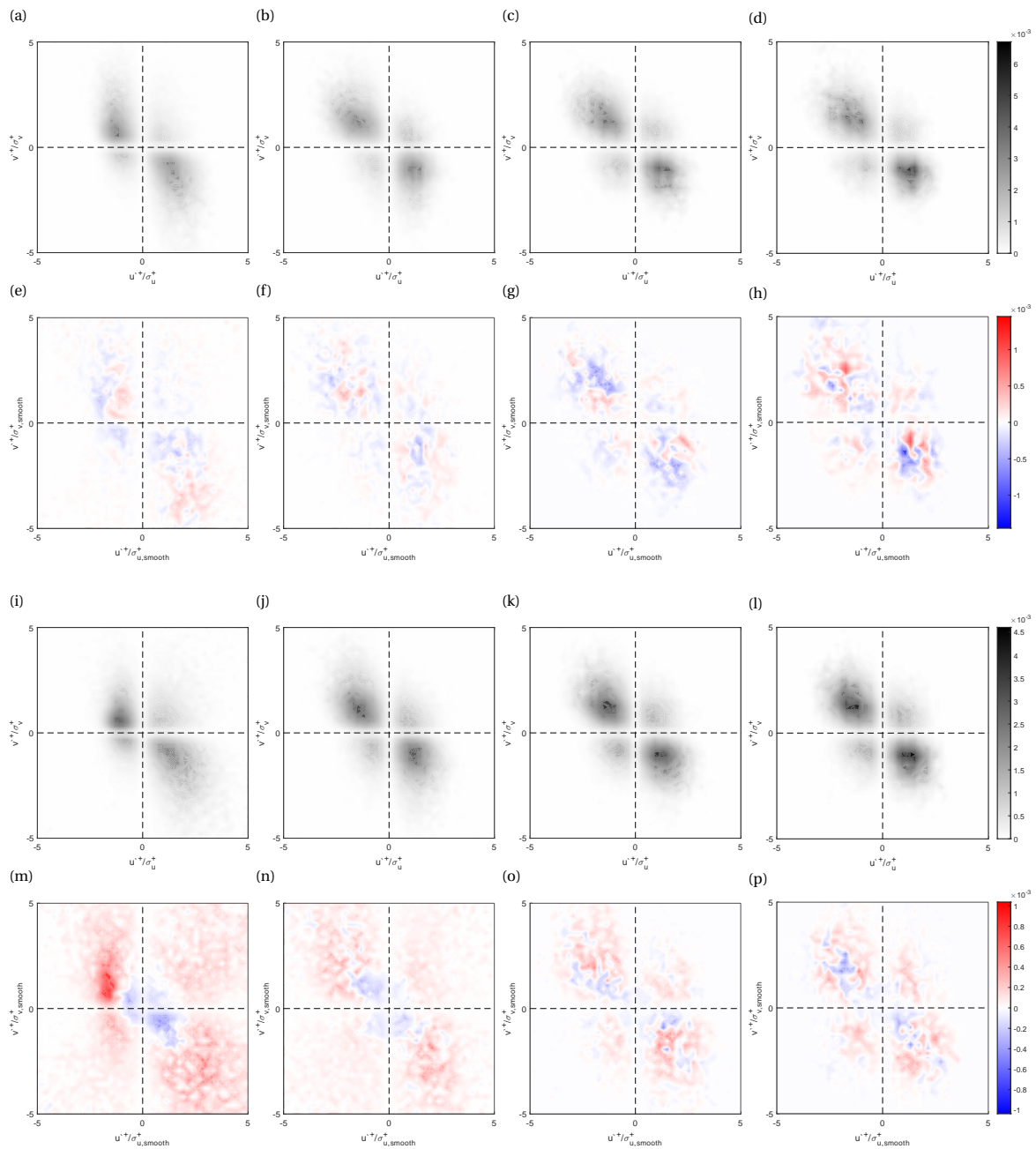


Figure 12.21: Weighted joint probability density function for Station 4. (a-d, i-l) Reference smooth wall. (e-h, m-p) Difference of permeable wall w.r.t. reference smooth wall. (a-h) $U_\infty = 10$ m/s. (i-p) $U_\infty = 30$ m/s. (a, e, i, m) $y^+ = 10$. (b, f, j, n) $y^+ = 30$. (c, g, k, o) $y^+ = 100$. (d, h, l, p) $y^+ = 300$.

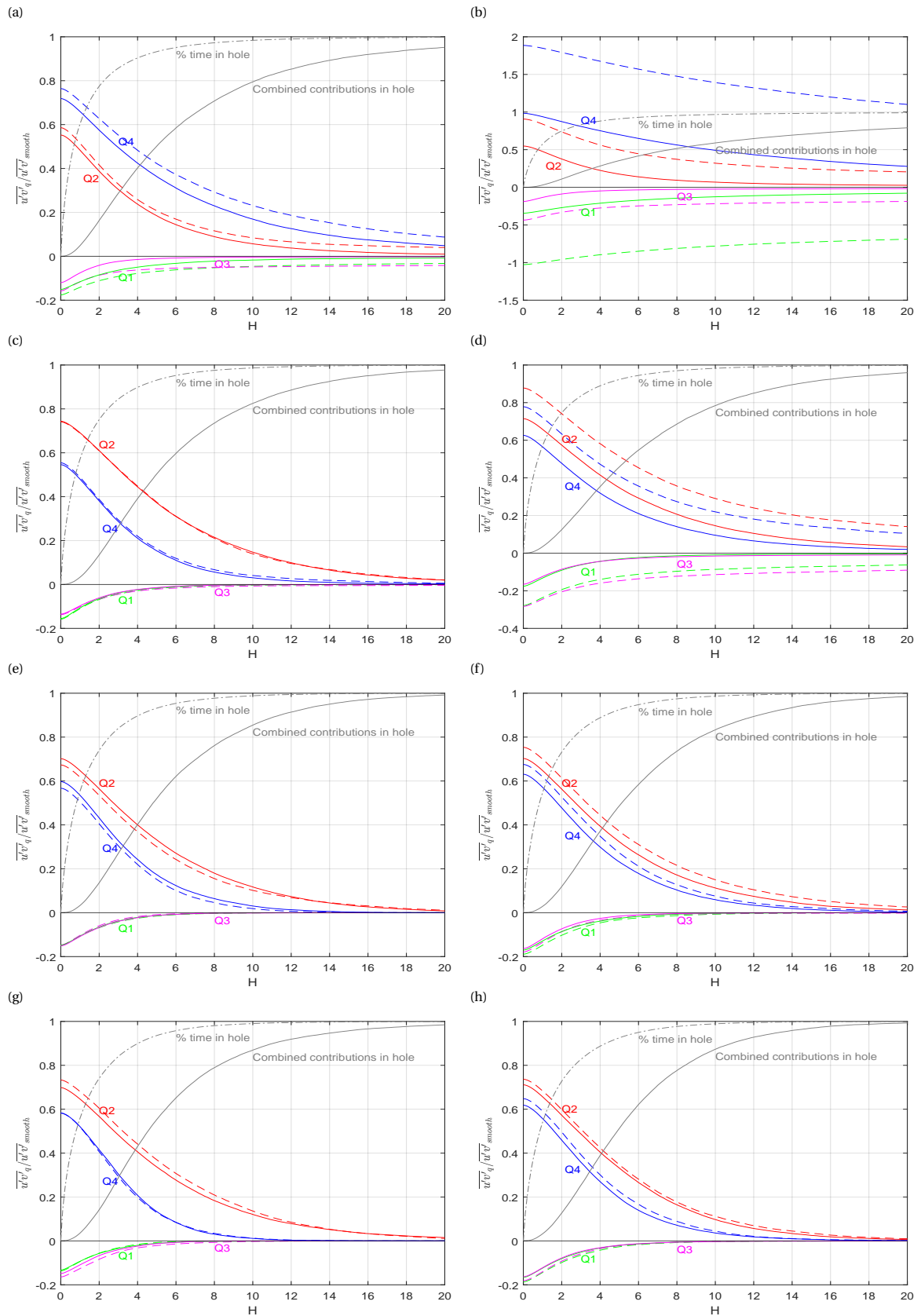


Figure 12.22: Reynolds stress contributions for Station 4. Solid lines represent reference smooth wall, dashed lines represent permeable surface. (a, c, e, g) $U_\infty = 10$ m/s. (b, d, f, h) $U_\infty = 30$ m/s. (a, b) $y^+ = 10$. (c, d) $y^+ = 30$. (e, f) $y^+ = 100$. (g, h) $y^+ = 300$.

12.5. Turbulent flow structures

A qualitative analysis was performed on the turbulent structures in the BL over the smooth and permeable surfaces. These structures were visualised by computing the vorticity on the velocity fluctuation vector fields (Equation (12.6)). Examples of the result are shared in Figure 12.23 for both surfaces at 10 and 30 m/s.

$$\omega'_z = \frac{du'}{dx} - \frac{dv'}{dy} \quad (12.6)$$

Typical structures for canonical wall-bounded turbulence can be observed over both surfaces at both velocities: high velocity sweeps moving towards the wall and low-speed ejections travelling away from the wall (rotating counterclockwise in the images). These ejections form the 'head' of hairpin vortices and can be observed to travel together in packets along a 'ramp'. The observed ramps correspond well to the dashed lines drawn at an angle of 12° , which was found to be the mean growth angle of such hairpin ramps (Adrian et al., 2000). The 'leg' of the hairpin vortices is visible in Figure 12.23b as an elongated pocket of lower momentum fluid being lifted away from the surface. Two of these instances can be observed in Figure 12.23c and the distance in between ($\approx 1,300\delta_v$) corresponds to the characteristic wavelength of the near-wall cycle of $1,000\delta_v$. The different structures are larger and easier to identify for the lower velocity since δ_v is approximately three times larger. Based on this qualitative assessment, no large differences in turbulent structures between the two surfaces are observed.

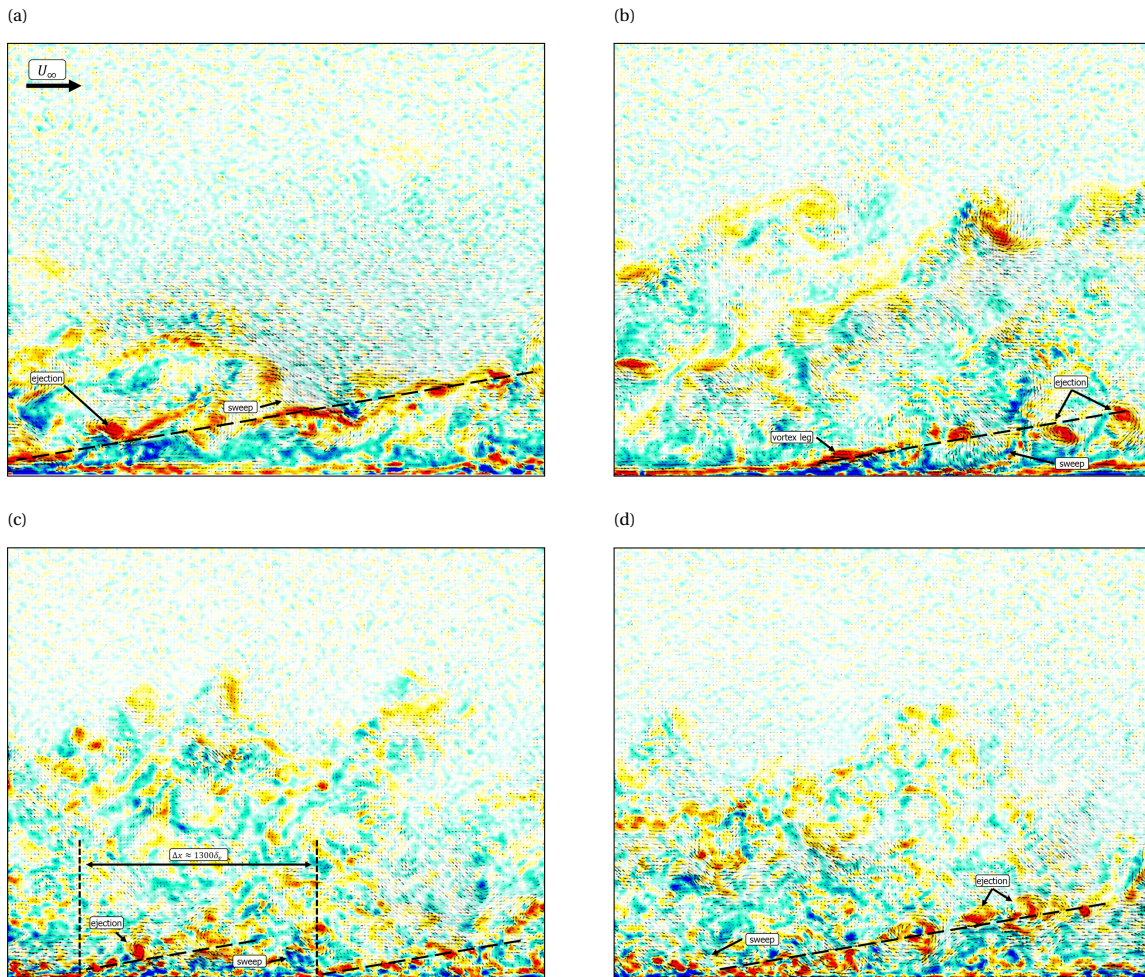


Figure 12.23: Visualisation of the instantaneous turbulent structures. Vorticity of the instantaneous minus mean flow velocity. Flow from left to right. Dashed lines indicate angle of 12° , which is the mean growth angle of inclined hairpin ramps (Adrian et al., 2000). (a,b) $U_\infty = 10$ m/s. (c,d) $U_\infty = 30$ m/s. (a,c) Reference smooth wall. (b,d) Permeable plate.

12.6. Discussion

Different analyses were performed on the experimental data from the PIV measurements: BL development of integral and friction parameters; BL profiles of the mean velocity, rms velocity fluctuations, and Reynolds stress; a decomposition of velocity fluctuations into turbulent events via quadrant analysis; and finally a qualitative assessment of turbulent structures. This section discusses the most relevant findings in terms of significance and relation to knowledge from literature. Topics covered are the occurrence of slip (Section 12.6.1), u_τ and C_f in (Section 12.6.2), turbulent activity (Section 12.6.3) and flow structures (Section 12.6.4).

12.6.1. Occurrence of slip

Gómez-de-Segura and García-Mayoral (2019) derived that a permeable surface provides a slip related to its permeability via $\ell_x^+ \approx \sqrt{K_x^+}$. It was verified with their own DNS results, and also experiments found an indication of streamwise slip that corresponded to this relation (Efstathiou and Luhar, 2020). Figure 12.24 shows the findings by Efstathiou and Luhar (2020) alongside a result from this study for similar $\sqrt{K_x^+}$. Even though the near-wall bias prohibited accurate determination of a potential slip length, no indications of a slip length were observed for the permeable wall in this research. This is likely caused by the low pore area relative to the entire surface area. Figure 12.25 shows three surface configurations and their ratio of non-solid wall area to total area at the surface plane. While the configuration of Efstathiou and Luhar (2020) has nearly 50% of the surface plane reserved for pores, this value is an order of magnitude lower (5%) for this research. The majority of the surface therefore imposes a strict no-slip condition on the flow. Although, in light of the averaged permeability on a macroscopic scale, this surface might provide slip in theory, in practice it physically does not allow for such slip over the majority of the surface.

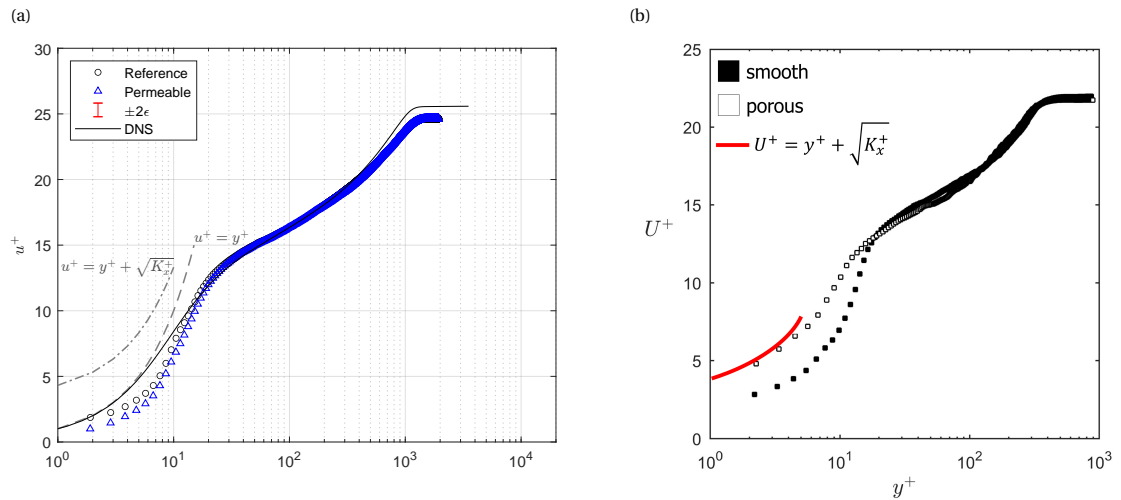


Figure 12.24: Comparison of velocity profiles for similar streamwise permeability. (a) This research, $\sqrt{K_x^+} = 3.3$. (b) Efstathiou and Luhar (2020), $\sqrt{K_x^+} = 3.0$.

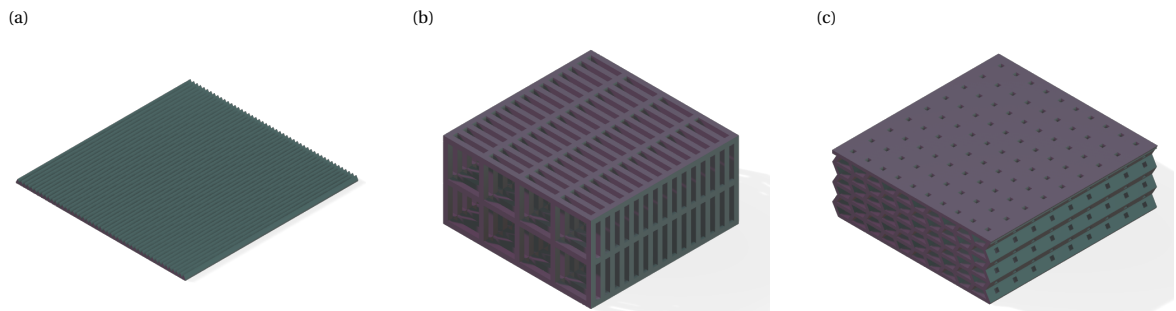


Figure 12.25: Isometric view renders of different surfaces. S_f = non-solid wall surface area at interface, expressed in %. (a) Riblets ($s = 225 \mu\text{m}$, $\alpha = 57^\circ$), $S_f \approx 100\%$. (b) Structure from Efstathiou and Luhar (2020), $S_f \approx 50\%$. (c) Structure from this research, $S_f \approx 5\%$. Renders approximately to scale, with $w \times l \approx 11 \text{ mm} \times 11 \text{ mm}$.

12.6.2. Friction velocity and coefficient

The found C_f values are not in line with predictions based on the theoretical model (Figure 12.14). At the velocities where a drag reduction is predicted, none is observed. In contrast: at the last station, for increasing velocity, the difference w.r.t. reference plate goes from positive ($\Delta C_f = +4\%$) towards negative ($\Delta C_f = -2\%$). One would expect that, after the predicted breakdown velocity (of approximately 8–9 m/s), the drag-reducing effects diminish and eventually turn into a drag increase. The friction velocity was computed using the BL fitting method by Rodríguez-López et al. (2015). As discussed in Appendix H.2, it was found that this method was sensitive to initial conditions, even though Rodríguez-López et al. (2015) argues that the optimisation problem is convex and yields a unique solution. The BL fitting parameters show a relatively large spread and sometimes reach the set bounds (Appendix I.2.2). It could be that the numerical implementation results in non-convexity and non-uniqueness. The uncertainty in u_τ originating from this issue is estimated to be within $\pm 2.5\%$, which translates into an uncertainty of C_f of $\pm 5\%$. This means that the uncertainty on ΔC_f can be as large as $\pm 10\%$ in the most extreme case. This is more than the difference between the computed ($+4\%C_f$) and predicted ($-4\%C_f$) values at $U_\infty = 5$ m/s, and therefore could in theory account for the discrepancy. This is only in the unlikely case that the estimated u_τ for the reference and permeable surfaces are both at opposite edges of the uncertainty bound. Using the original numerical implementation by Rodríguez-López et al. (2015) did remove the sensitivity to initial conditions, but was not completely robust and lead to even poorer fits in some cases, and therefore was not used in this research.

u_τ can also be estimated directly from the linear profile in the viscous sublayer. This method was discarded in this research because of the averaging effects that occurred over a wall-normal distance larger than the extent of the viscous sublayer for $U_\infty = 20$ & 30 m/s, which would result in underestimation of u_τ for these velocities (as discussed in Section 12.1.2 and appendix H.2). For sake of completeness, Table 12.3 shares the difference in C_f as calculated based on the direct fitting method for u_τ . Significant reductions in C_f arise, with the largest for 10 m/s, the velocity closest to the predicted point of breakdown. The trend in C_f thus agrees qualitatively with the theoretical model. However, the values are very far off from the predictions, at least twice as high. Furthermore, note that the values at station 4 deviate significantly for the measurements with different camera zoom settings. The large differences between permeable surface and smooth wall could arise if the averaging effect near the wall is larger for the permeable plate, for example if the wall is slightly higher at the back of the laser sheet compared to the front. This was also mentioned in Section 12.3 as a possible cause for the larger underestimation of the velocity profile in the inner layer for the permeable plate. All in all, there is little confidence in the results obtained with this method and no further weight is given to them.

Table 12.3: ΔC_f (%) of permeable surface w.r.t. smooth wall based on u_τ estimation from direct linear fitting in viscous sublayer.

U_∞ (m/s)	Station 2	Station 3	Station 4	Station 4 (zoom)
5	-3.3	-4.7	-8.1	-16.7
10	-20.2	-15.6	-15.2	-26.4
20	-8.8	-17.9	-9.8	-19.9
30	-5.9	-6.7	2.8	-13.5

12.6.3. Turbulent activity

The Reynolds stress profiles showed a decrease in peak value for 5 & 10 m/s (Figures 12.16d and 12.17d) and an increase in peak value for 30 m/s (Figure 12.19d). The latter is mainly caused by an increase in wall-normal velocity fluctuations (Figure 12.19c). This is in line with what is known from literature. Permeable surfaces, regardless of (an)isotropy, where the wall-normal permeability is too large, facilitate momentum exchange across the freestream - substrate interface and consequently strengthen wall-normal velocity fluctuations (Breugem et al., 2006; Pokrajac and Manes, 2009; Suga et al., 2010; Gómez-de-Segura and García-Mayoral, 2019). It was also observed in the experimental work into streamwise-preferential substrates by Efstathiou and Luhar (2020).

The observed decrease in Reynolds stress peak value originates from a less strong streamwise velocity fluctuations for 5 m/s, and a combination of less strong streamwise and wall-normal velocity fluctuations for 10 m/s. The differences are statistically significant, since they exceed the sum of twice the standard error of both profiles. Furthermore, the differences are not caused by normalising since the differences in u_τ are less than 2%. A check on the profiles in physical units yields the same trends and confirms the statistical significance of these observations (see Appendix I.2.1). As such, the findings qualitatively agree somewhat with the DNS results by Gómez-de-Segura and García-Mayoral (2019), who reported a slight decrease in peak Reynolds stress, albeit much smaller than the one observed in this research (Figure 12.26). Furthermore, also different from the findings here, is that this decrease was caused by a strong decrease in streamwise velocity fluctuations, which compensated for an almost equally strong increase in wall-normal velocity fluctuations.

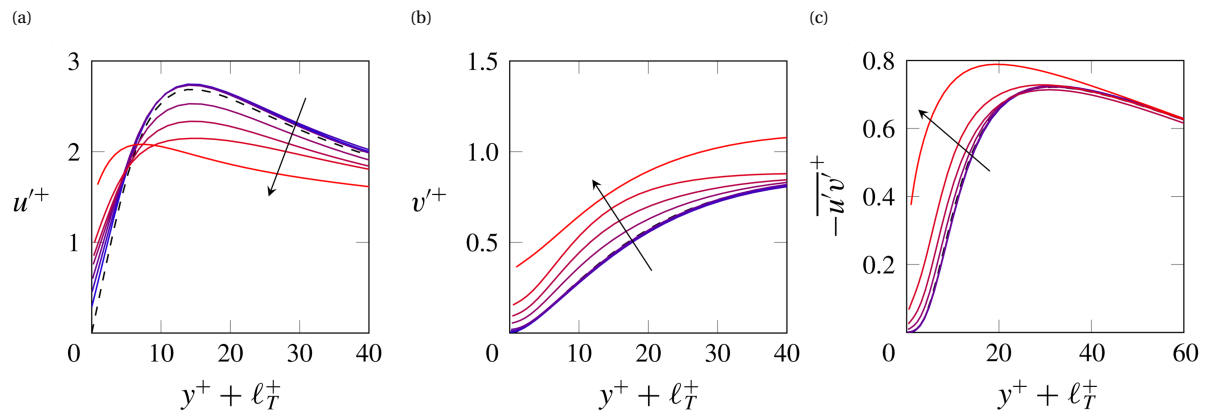


Figure 12.26: One-point turbulent statistics from Gómez-de-Segura and García-Mayoral (2019). Lines from blue to red (in the direction of the arrow) correspond to cases C1-C7. C6 and C7 (last two lines) have $\sqrt{K_y^+} > 0.38$ and are beyond the point of breakdown. $l_T^+ (= \sqrt{K_z^+})$ denotes the turbulence virtual origin. Black-dashed lines represent the smooth-wall case. (a) Rms streamwise velocity fluctuations. (b) Rms wall-normal velocity fluctuations. (c) Reynolds stress.

Further checking the Reynolds stress profiles (in physical units) for the zoomed-in measurement of station 4, shows that the decrease in Reynolds stress only occurs partially at 5 m/s, and not at 10 m/s. A similar check of station 3 shows that the Reynolds stress is higher for all velocities. See Appendix I.2.1 for these results. All in all, this weakens the significance of the decrease found at station 4 (regular zoom). Unfortunately, this measurement was not performed twice and thus repeatability cannot be guaranteed. The findings from the quadrant analyses (Section 12.4) do not provide any more insight into this decrease in Reynolds stress, other than the fact that it cannot be attributed to a change of a single, specific type of turbulent event. With the knowledge at hand, it is thought that this observation is a local effect, either caused by a local deviation in the permeability or an imperfection in the wall surface upstream. This would explain the fact that a similar but not identical observation was made at 5 m/s for the zoomed-in view measurement of station 4.

12.6.4. Turbulent flow structures

Only a qualitative analysis was performed on the turbulent flow structures above both surfaces. No significant differences were found as both surfaces showed typical wall-bounded turbulent structures, such as sweeps, ejections, hairpin vortex legs and inclined packets of hairpin vortices. No indications for the occurrence of spanwise coherent structures (KH-rollers) were found. This is to be expected as such rollers are very small and occur immediately near the wall ($y^+ < 30$). Unfortunately, the experimental data did not allow for quantitative analysis of the flow structures in the form of spectral analysis. Temporal spectra could not be computed since the collected data is not time-resolved. Spatial spectra could not be reliably computed for two reasons (the data is provided in Appendix I.2.3). At lower velocities, the field of view is too small (expressed in viscous units) to capture structures with wavelengths in the order of the near-wall cycle characteristic wavelength, hence a complete picture of the typical structures in the BL cannot be given. At higher velocities, the data close to the wall (specifically $y^+ = 15$, the location of peak energy for the near-wall cycle) is biased and shows up in the computed spectra as high-energy noise (at the wavelengths associated with the spanwise coherent structures). All in all, the occurrence of spanwise coherent structures associated with KH-instabilities, as found above surfaces with too high wall-normal permeabilities both in DNS (Gómez-de-Segura and García-Mayoral, 2019) and well as in experiments (Efstathiou and Luhar, 2020), could not be correctly examined.

This page has been intentionally left blank.

IV

Discussion, conclusions, and recommendations

In the foregoing parts, different building blocks of this research have been covered: the theoretical framework on the basis of which this research was designed in Part I, the manufactured test specimens with which results have been obtained in Part II, and the wind tunnel experimental methods, results and the subsequent discussion in Part III. This part synthesises the findings of this research. Chapter 13 shares an overarching discussion, correlating the direct force measurements and PIV results first, and subsequently scrutinising the theoretical framework. Finally, Chapter 14 sums up the conclusions and gives recommendations for future research.

This page has been intentionally left blank.

13

Discussion

Discussion of the results from the direct force measurements and PIV experiments have been provided in Sections 10.4 and 12.6 respectively. This chapter serves as an overarching discussion. Correlation between the results of the two experiments is discussed first, in Section 13.1. Then, the theoretical framework that formed the basis of this study is scrutinised in Section 13.2.

13.1. Correlation of experimental results

The main metric to correlate the experimental results on, is the drag or friction coefficient (C_D or C_f) and its difference between the smooth and permeable surfaces (ΔC_D or ΔC_f). After the performed corrections, the determined C_D from direct force measurements (DFM) should be equal or close to the true C_f integrated along the test plate. Therefore C_D and C_f are used interchangeably in the remainder of this section. For the PIV measurements, C_f was determined via the estimated friction velocity (referred to as u_τ -based estimates in this section). The results are presented in Figure 13.2. All three stations on the test plate (S2, S3 & S4) are shown for the PIV measurements, and hence represent the point-wise friction coefficient. As an extra means of comparison, C_f as estimated via the change in momentum thickness along the streamwise direction (via Equation (2.7)) is also given (referred to as θ -based estimates in this section). This is based on three possible streamwise intervals (S1-S3, S1-S2 and S2-S3). Table 13.1 summarises the different methods via which C_D and C_f were obtained. It should be noted upfront that, although the test plate mount for the PIV measurements was designed to resemble the Hill as closely as possible, differences in flow conditions and BL development along the surface between the different experiments could still be present and partially explain differences in the results.

Figure 13.2a presents C_D (or C_f) for the smooth wall obtained via the different methods. For the direct force measurements, the results are averaged across the four measurements. Also, a theoretical trend is shown. It is based on the power-law relation (Equation (2.23)) integrated in streamwise direction along the test plate. Black, open markers denote the results from the direct force measurements before applying pressure corrections. The direct force measurement results show the largest differences at lower velocities, but converge with increasing Re_1 , a result of the larger measurement uncertainty at lower velocities and hence absolute forces. The θ -based estimates show large deviations between the different reference intervals. Since C_f decreases along the streamwise direction, it comes as no surprise that the S3-S4 interval yields the lowest estimate and the S2-S3 interval the highest. All estimates are significantly lower than the results from the direct force measurements and u_τ -based estimates. This can be explained through the near-wall bias discussed in Section 12.1.2. The velocity underestimation near the wall translates into a lower estimated momentum loss, which is visualised in Figure 13.1b. A lower estimated momentum loss at all stations means a lower estimation of the momentum thickness derivative along the streamwise direction, and hence an underestimation of C_f as well. To summarise, the θ -based method for C_f suffers from the near-wall bias in the data and the corresponding results are considered inaccurate.

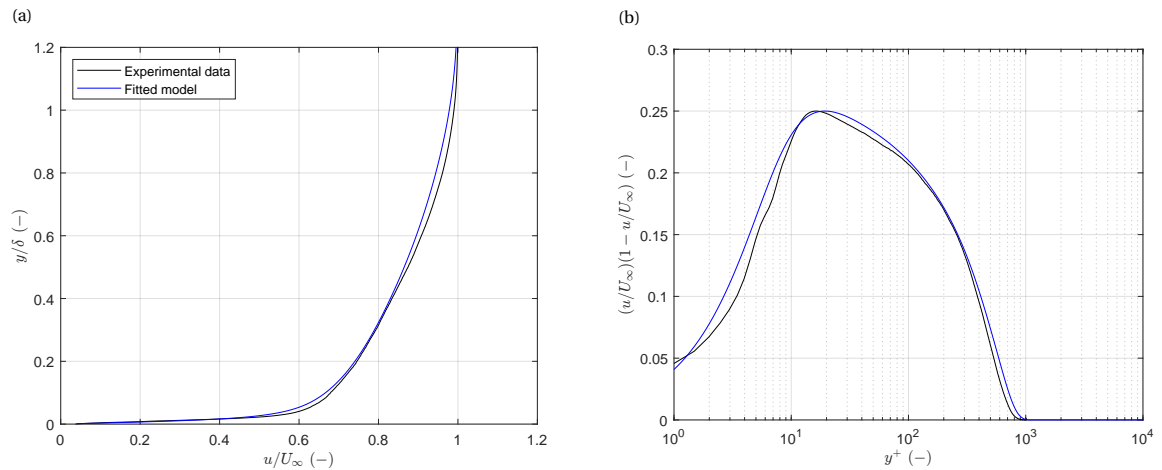


Figure 13.1: Visualisation of momentum loss. Data for smooth wall, $U_\infty = 10$ m/s at Station 4 (Figure 12.17a). $\Delta\theta = -8.8\%$ (experimental w.r.t. model). (a) Normalised velocity profile. (b) Normalised momentum loss profile.

The u_τ -based estimates lie relatively close to one another, with the lowest estimates for station 4. The estimates are in the same range as the direct force measurement results for low Re_1 , but significantly higher for high Re_1 . Especially the S3- and S4-estimates follow the theoretical curve well for $Re_1 > 0.6 \times 10^6$ ($U_\infty > 10$ m/s). The discrepancy between the u_τ -based estimates and the direct force measurement results can originate with either of the two methods. The uncertainty in the u_τ -based C_f was estimated to be approximately $\pm 5\%$. This is less than the difference between the values for C_f (u_τ -based) and C_D (DFM) at $Re \approx 2 \times 10^6$ ($\approx 11\%$). Therefore, it can only be explained if there is a consistent bias in u_τ due to the fitting method. If so, the most reasonable explanation would be that fitting on only the outer layer ($y^+ > 30$) skews the estimated u_τ to higher values. For the direct force measurements, a potential cause for the discrepancy could be that the pressure drag corrections are too large. The non-pressure drag corrected C_D shows a better correspondence with C_f , obtained from both the u_τ -based estimates and the theoretical relation. To the author's knowledge, the Hill measurement device and data-processing script have been validated using drag difference data (ΔC_D) only. A consistent bias in the pressure drag correction regardless of tested surface, hence would (partially) cancel out against one another when computing drag differences. Such bias thus would not affect the main purpose of the measurements, namely testing for drag differences. As such, this hypothesis does not invalidate the conclusions of this research based on the measured drag differences.

Figure 13.2b presents the drag difference (ΔC_D) between the reference smooth wall and permeable surface obtained via the different methods. The results for the θ -based method are seemingly all over the place. At $Re_1 \approx 0.6 \times 10^6$ (10 m/s), the points lie close to one another, and close to the predicted drag reduction. Furthermore, for the whole plate (S2-S4), and the beginning of the plate (S2-S3), the trends resemble what would be expected based on the theoretical framework: an increase in drag reduction up to a point of breakdown, after which the drag reduction diminishes and eventually turns into a drag increase. The clear deviation for S3-S4 casts doubts on the validity of the trend however. In addition, it was discussed that the permeable surface might suffer more heavily from the near-wall bias. As such, the momentum loss would be underestimated even more for these measurements, therefore translating into an artificial reduction in C_f compared to the reference plate. All in all, the results from the θ -based method are thought to be biased, and hence not valid enough to base conclusions on.

For the u_τ -based method, no significant differences between the two plates exist for the S3 and S4 measurements. The differences found in the S2 measurements are thought to be caused by the flow acceleration across the leading edge for the permeable plate. While the BL has not fully adapted to the surface and thus u_τ is similar to that of the smooth wall, the higher U_∞ translates into a lower C_f (via Equation (2.22)). At the highest velocity, all measurements yield a slight drag decrease. However, this is within the estimated uncertainty on C_f for the u_τ -based method. It is clear that ΔC_f for the u_τ -based method does not correspond to the direct force measurement results: not in absolute estimates, nor trend. The u_τ -based estimates (especially at higher velocities) are also not in line with the increase in turbulent activity for the permeable plate. In that sense, those observations qualitatively agree better with the direct force measurement results.

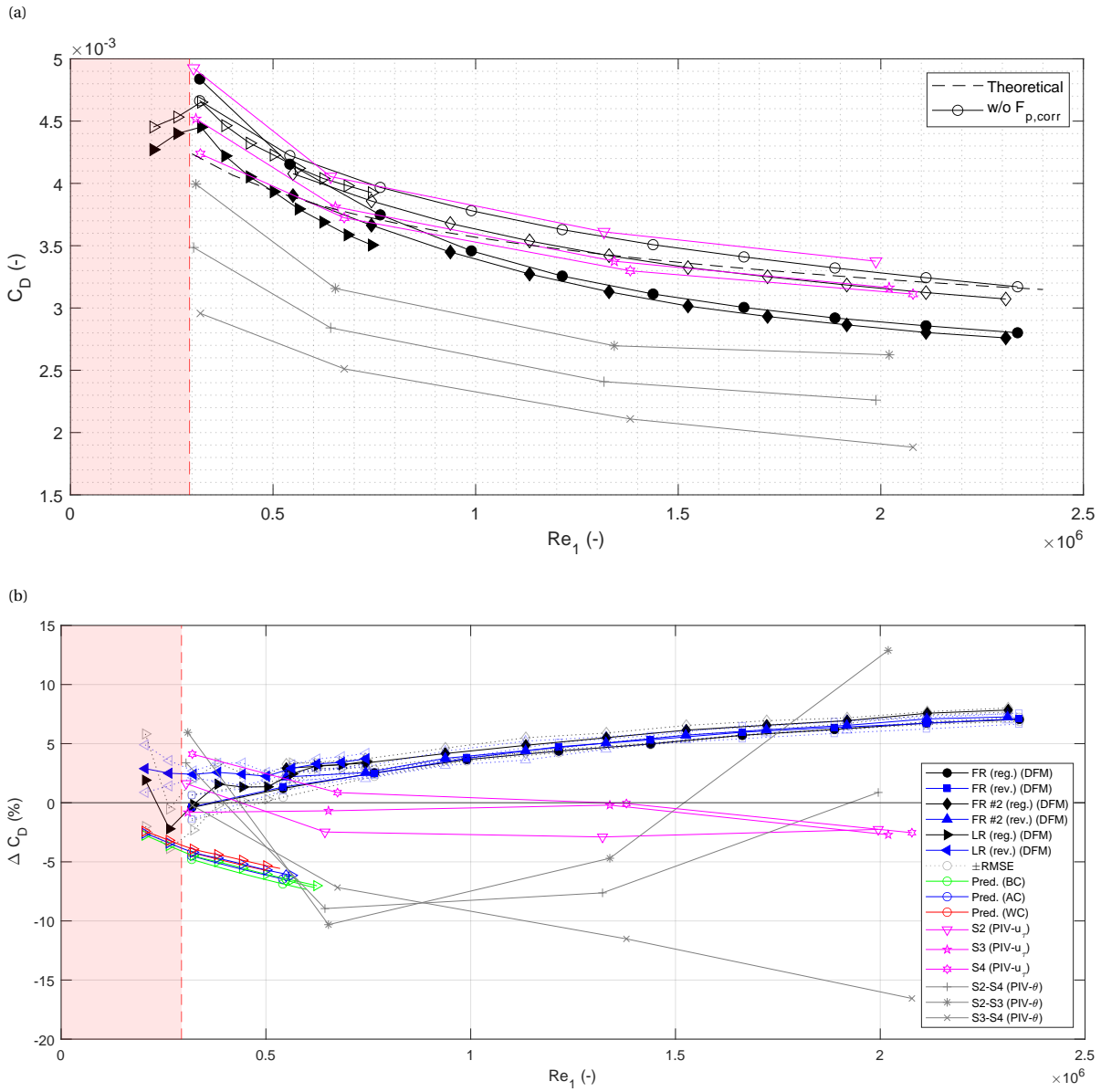


Figure 13.2: Correlation of results from direct force measurements and PIV experiments. Magenta: PIV estimation via u_T (Equation (2.22)). Grey: PIV estimation via θ (Equation (2.7)). (a, b) Results for reference plate. (a) Drag coefficient C_D . Values for direct force measurements averaged over four measurements within measurement set. Theoretical C_f calculated via Equation (2.23) and integrated over the streamwise location on the plate w.r.t. the tripping point ($x \approx 600 - 1500$ mm). (b) Drag change w.r.t. reference plate. Reg.: Regular orientation. Rev.: Reversed orientation. LR: Low-speed regime. Pred.: Prediction based on theoretical model. BC: Best case, AC: Average case, WC: Worst case. S2, S3 and S4 denote Stations 2, 3 and 4 from the PIV experiments.

Table 13.1: Overview of methods via which C_D and C_f were obtained.

Data source	Location	Method	Output
Direct force measurement	Entire plate	Regular C_D calculation	C_D & ΔC_D
Theoretical framework prediction	Entire plate	Slip lengths and virtual origin model	ΔC_f
PIV	Individual station (e.g. S2)	Friction velocity (u_T)	C_f & ΔC_f
PIV	Between stations (e.g. S2-S4)	Momentum thickness (θ)	C_f & ΔC_f

There could be several reasons for the discrepancies between ΔC_D from the direct force measurements and ΔC_f from the PIV measurements, besides the slightly different measurement setups. First, the estimates in ΔC_f could be faulty. The difference between the DFM-based ΔC_D and u_τ -based ΔC_f lies within the estimated uncertainty on ΔC_f ($\approx 10\%$). However, it would be reasonable to expect that even considering the uncertainty, a trend of increasing C_f for increasing Re_1 could be observed. Secondly, there could be other drag sources than pure surface friction that are measured with the direct force measurements but do not show up in the u_τ -based C_f . As discussed earlier in Section 10.4.4, this can be further broken down into three possibilities (Figure 13.3): (1) pressure drag within the permeable structure, this can happen with flow entering the surface through the pores and exerting a pressure force on the wall in the downstream direction, creating extra net drag, and at the TE where the permeable structure ends in a solid wall; (2) friction drag due to the flow within the permeable structure, especially at higher velocities when the 'channel' height in the printed structure allows the development of local BLs larger than only the viscous sublayer; and (3) pressure drag on the surface due to local plate imperfections. Neither of these three would show up in the u_τ -based C_f . While the θ -based C_f should account for all potential sources of drag (as it covers the total momentum loss in the flow), it might not be able to do so correctly due to the near-wall bias and thus the consequently inaccurate estimates.

All in all, it is challenging to make definitive conclusions on the difference in pure friction between the permeable and smooth surfaces. The u_τ -based C_f does not yield significant differences. However, it is likely that other drag sources play a role and show up in the DFM-based C_D . The structure used in this research consisted of long, continuous channels with pores spaced at 1.25 mm. To prevent friction drag within the surface, one would need to prohibit the formation of boundary layers within such channels, e.g. by having a smaller inter-pore distance or not having a channel-based structure. To prevent pressure drag within a permeable surface, one would need to be certain of slow, Stokes flow within the structure while minimising the frontal areas w.r.t. flow direction. These can be expected to be huge engineering challenges and thus it is thought that in real-world applications, it is highly likely that permeable surfaces would also encounter these other forms of drag. This is opposed to the assumption by Gómez-de-Segura and García-Mayoral (2019) that pressure drag within the substrate is negligible. Unfortunately, the potential occurrence of pressure drag within the substrate also makes it very challenging to experimentally test the validity of the theoretical framework.

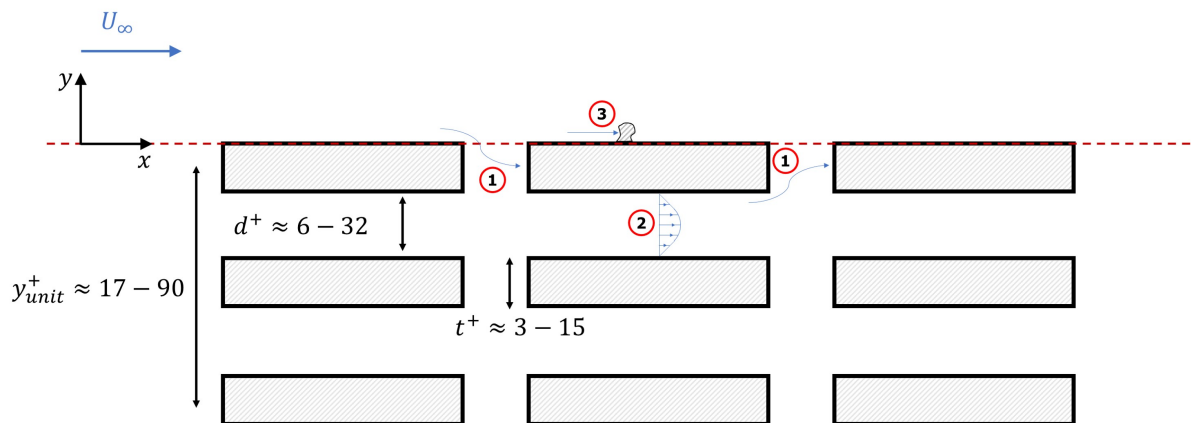


Figure 13.3: Schematic of potential extra drag sources in permeable substrate.

13.2. Theoretical framework discussed

The theoretical framework and DNS results by Gómez-de-Segura and García-Mayoral (2019) formed the foundation for this experimental research. No drag reductions were found in conditions where the model predicts a moderate drag reduction. In Section 13.1 it was posited that for experimental settings, testing the validity of the framework is challenging: the direct force measurements are susceptible to sources of drag other than pure friction, while the uncertainty in C_f determined via u_τ extracted from PIV data is such that it is not possible to do definitive conclusions on the friction drag based on these values. However, regardless of these uncertainties, the discrepancies between the predicted values based on the theoretical model, and the data obtained from different experimental methods, render it worthwhile to discuss this theoretical framework in more detail. Specifically, the assumptions used in the derivation of the model, and on the underlying drag reduction working principle, will be reviewed from three perspectives. Firstly, in light of the experiments conducted in this research and by Efstathiou and Luhar (2020); secondly, in two hypothetical practical applications; and lastly, in a general sense. The reader is referred to Section 3.4 for a concise overview of the most important assumptions and building blocks of the theoretical framework.

13.2.1. Experimental setting

To the author's knowledge, to date, only two experimental studies have been performed that test the theoretical model predictions: the work from Efstathiou and Luhar (2020) and this research. Moreover, this research is the only one where the permeability of the tested surface was such that drag reductions were predicted; the surface of Efstathiou and Luhar (2020) was a priori known to have a too large wall-normal permeability. The occurrence of slip in these two studies has already been covered in Section 12.6.1. This section covers the hypothesised physical working mechanism behind the drag reduction first, and subsequently the permeable surface discretisation and length scales at play.

Filtering of turbulence

The idea behind the drag reduction of streamwise-preferential permeable surfaces is that they function as a filter for turbulent structures that are responsible for a portion of the friction production. According to the theoretical framework, there is an offset between the virtual origins of the mean flow and turbulence, interpreted as the quasi-streamwise (QS) vortices, with that of the turbulence being less 'deep'. This working mechanism is similar to that which is thought to occur in riblets, namely that QS-vortices occur above the riblet tips and do not reach the exposed surface area, while the mean flow penetrates in between the individual riblets (see Figure 2.4). As such, less momentum transfer of these vortices reaches the wall and consequently, less friction is generated. This can be understood intuitively when noting that effective riblets have a spanwise spacing and height (s^+ & $h^+ \approx 5 - 20$) (García-Mayoral and Jiménez, 2011a) that is smaller than the diameter of most QS-vortices ($d^+ \approx 5 - 110$ with 73% having diameters of $d^+ \approx 10 - 40$ (Robinson, 1991) and an overall average diameter of $\bar{d}^+ \approx 30$ (Kim et al., 1971; Blackwelder and Eckelmann, 1979; Kim et al., 1987)). For the flat surface with small pores investigated in this research however, the large solid-wall surface area combined with the spanwise inter-pore distance ($d_p^+ \approx 15 - 70$ for $U_\infty = 5 - 30$ m/s) allows for QS-vortices to sweep across the surface and generate friction. Although the conceptual approximation of the permeable surface would filter out turbulence, the physical realisation cannot. This is in contrast with riblets, where the physical realisation can actually weaken the friction effect of turbulent structures.

Discretisation and length scales

Gómez-de-Segura and García-Mayoral (2019) focus on pores that are much smaller than any near-wall turbulent length scale and in their model assume infinitely small pores. It is therefore relevant to check the relative sizes of the pores and thicknesses of the printed structures on the one hand, and the expected slip lengths (and therefore velocity profile penetration depths) on the other hand. Figure 13.4 visualises these dimensions for Efstathiou and Luhar (2020) and this research. It is clear that in all cases, the expected penetration depth for the mean velocity profile (ℓ_x^+) is similar to, or smaller than, the thicknesses of the printed structures. Note that this penetration depth resembles the virtual origin of the profile, not the actual location where the flow velocity is zero. Since $\sqrt{K_y^+} < \sqrt{K_x^+}$ and $\sqrt{K_z^+} < \sqrt{K_x^+}$, the same is true for the penetration depth of the turbulent structures. Therefore, the pores are not much smaller than any near-wall turbulent length scale, and therefore these structures do not meet the set assumptions of the theoretical framework.

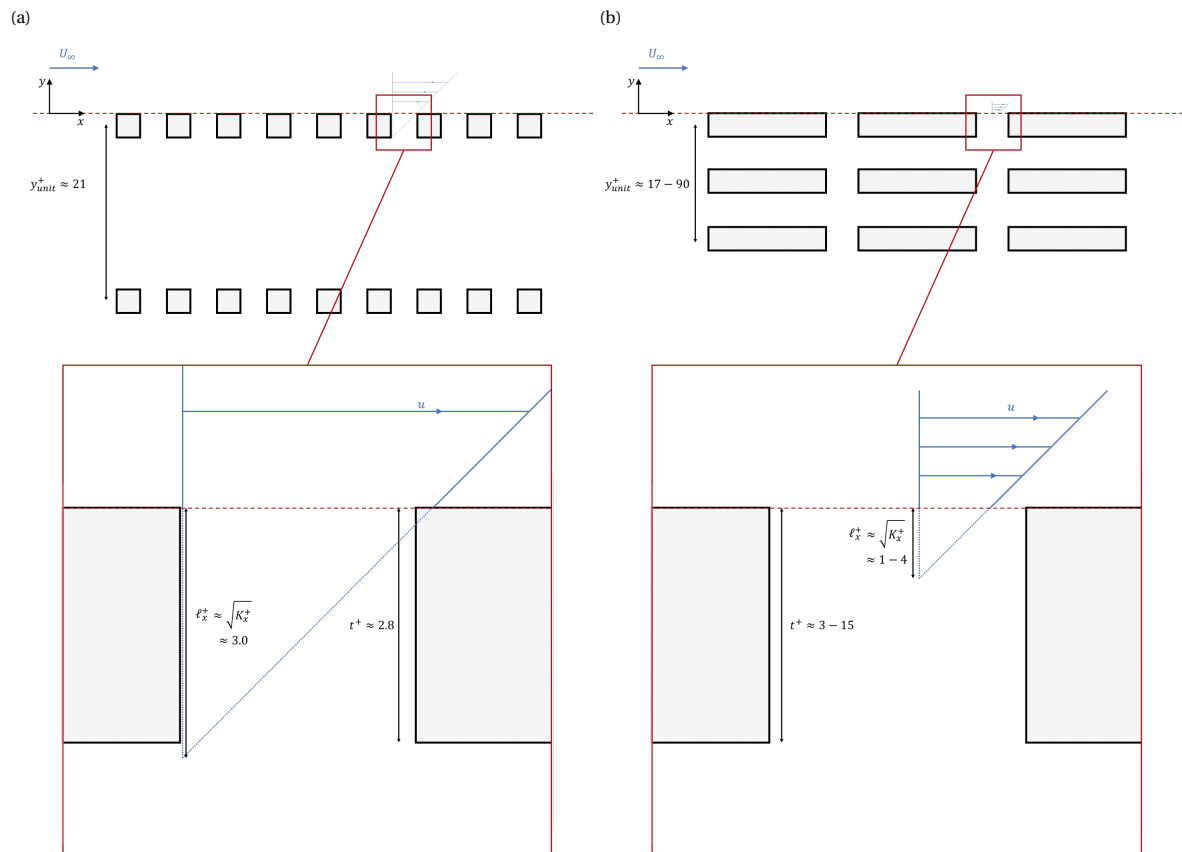


Figure 13.4: Schematic of expected profile penetration depth and structure length scales for the structures from Efstathiou and Luhar (2020) (a) and this research (b). Range in values in (b) to account for different tested freestream velocities ($U_\infty = 5 - 30$ m/s).

13.2.2. Practical applications

Unfortunately, the experimental conditions in this research, as well as in the work of Efstathiou and Luhar (2020), did not meet the set assumptions of the theoretical framework and also did not provide the physical conditions for the underlying working principle in terms of slip and preventing the QS-vortices to sweep across the surface. Nevertheless, it is interesting to assess whether this might be possible in practical applications. Gómez-de-Segura and García-Mayoral (2019) envision anisotropic permeable substrates to be used for external-flow applications as coatings on vehicle surfaces. Therefore, two cases will be discussed: large aircraft and ships. Turbulent drag is the largest source of fuel consumption in both these modes of transportation, and they serve as cases in two different media, namely air and water. For sake of the argument, material and fabrication constraints are omitted. Given the progress in material and manufacturing sciences, it is plausible that in ten years there will be wide-scale availability of (meta-)materials that are unheard of today. Also, other practical issues such as pore contamination, icing, etc. are not considered. BL properties are estimated via smooth-wall, flat-plate power-law methods as done in Section 4.1 and for which the equations are given in Section 2.1.

Aircraft

An Airbus A350-900 is taken as a reference aircraft. Assuming a fuselage length of 50 m, cruise speed of 900 km/h and flight altitude of 11 km (ISA conditions: $\rho = 0.364$ kg/m³, $p = 22.6$ kPa, $T = -56.5$ °C), the viscous length scale is of $O(5\mu\text{m})$. Closer examination reveals that a value of $O(4\mu\text{m})$ is reached after 1 m of development length, hence this length scale value also holds for shorter aircraft. Given a maximum allowable wall-normal permeability of $\sqrt{K_y^+} < 0.38$ for the linear drag reduction regime, this yields that the penetration depth will be not more than approximately $2\mu\text{m}$. Following Gómez-de-Segura and García-Mayoral (2019), we assume equal spanwise and wall-normal permeabilities, hence $\ell_{z,max} \approx 2\mu\text{m}$.

The crucial question here is: how small do the pores need to be such that the permeable substrate can be modelled as a continuum, meeting the assumptions set by Gómez-de-Segura and García-Mayoral (2019). Unfortunately, they do not provide any insight on the matter, apart from mentioning that they "focus on permeable materials where the pores are much smaller than any near-wall turbulent length scale". A reasonable assumption would be to set the repeating unit cell an order of magnitude smaller than the smallest penetration depth. A value of $0.2 \mu\text{m}$ means that the penetration depth covers ten repeating unit cells across which averaging takes place, and it is more than an order of magnitude smaller than the viscous length scale ($0.038\delta_\nu$). It furthermore is assumed that pores and solid objects in the flow are of similar size, i.e. $\approx 0.1 \mu\text{m}$ (Figure 13.5). For sake of simplicity in this argument, isotropic structures are assumed.

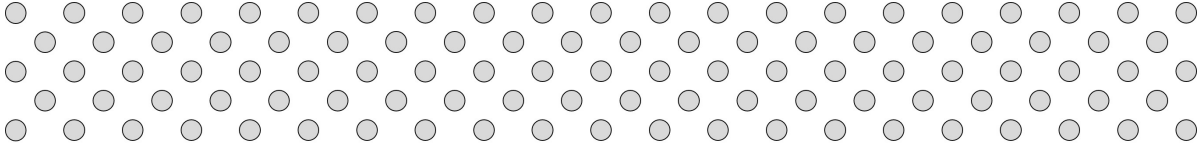


Figure 13.5: Schematic of permeable substrate with pores and solid objects of equal size ($\epsilon = 0.80$).

The very small required pore sizes bring such a surface into the realm of free molecular movement in gases. At standard sea-level atmospheric conditions, the mean free path for air is approximately 68 nm. For the flight conditions considered here, it can be calculated via Equation (13.1) (Vincenti and Kruger, 1965), where R is the universal gas constant and M the molecular weight, and is found to be approximately $0.2 \mu\text{m}$. This means that the Knudsen number is approximately 2, which brings the flow in the so-called transitional regime (Karniadakis et al., 2000). In this regime, the stochastic movement of individual gas (air) molecules is of the same size order as the pores are. Consequently, continuum flow assumptions do not hold anymore, and effects such as Knudsen diffusivity and Knudsen friction are expected to play a role. Summarised: in flight conditions, the framework as proposed by Gómez-de-Segura and García-Mayoral (2019) is not expected to be valid because the assumptions of continuum flow and sufficiently small pore size conflict.

$$\lambda = \frac{\mu}{p} \sqrt{\frac{\pi RT}{2M}} \quad K = \Phi_s^2 \frac{\epsilon^3 D_p^2}{150(1-\epsilon)^2} \quad (13.1, 13.2)$$

Ships

For water, Knudsen effects do not play a role since the mean free path of liquid molecules is generally smaller than their diameter. An ultra-large container ship is taken as a reference ship. These ships often have a length of 400 m. Assuming standard seawater conditions ($\rho = 1.025 \times 10^{-3} \text{ kg/m}^3$, $T = 17 \text{ }^\circ\text{C}$, $\mu = 1.17 \times 10^{-3} \text{ Ns/m}^2$), the viscous length scale is $O(4.5 \mu\text{m})$. A value of $O(3.5 \mu\text{m})$ is reached after 10 m of development length, hence this length scale value also holds for shorter container ships. The viscous length scale for these ships therefore is similar to aircraft, hence following the same reasoning as for the previously discussed case, similar permeabilities and required pore sizes can be expected, i.e. $K_z \approx 3.6 \times 10^{-12} \text{ m}^2$ and $D_p \sim O(0.1 \mu\text{m})$.

The next question is: are the required pore sizes in the right order of magnitude to yield the required permeability values? For this, the hypothetical structure of Figure 13.5 is considered: an isotropic porous medium consisting of spherical objects. The Kozeny-Carman permeability (obtained from combining the Kozeny-Carman (Carman, 1956) and Darcy equations) is an often-used estimate of the permeability of a packed bed of solids, and given in Equation (13.2), where Φ_s is the particle sphericity and D_p is the average particle diameter. Assuming perfect spherical particles ($\Phi_s = 1$), and a pore and particle size of $0.1 \mu\text{m}$ (and consequently porosity of $\epsilon = 0.80$), then yields a permeability of $9.0 \times 10^{-14} \text{ m}^2$. This is approximately two orders of magnitude smaller than what would be expected for K_z , which is not a problem since one wants to limit the permeability in this direction. However, it is almost three orders of magnitude smaller than K_x , hence the substrate would not be permeable enough to provide streamwise slip. In fact, to achieve this required permeability in streamwise direction, Equation (13.2) yields a required particle diameter (and hence pore diameter in this hypothetical case) of approximately $50 \mu\text{m}$ or $10\delta_\nu$, also more than two orders of magnitude larger than the required length scales of the pore and particle diameters. Summarised: in ship conditions, the model as proposed by Gómez-de-Segura and García-Mayoral (2019) is not expected to be valid because there is a mismatch between the expected permeability length scales and the required pore sizes such that the model assumptions hold.

13.2.3. Generalised case

The conditions in both the experiments of this research and the work by Efstathiou and Luhar (2020) as well as the two hypothetical practical applications discussed, do not allow for applying the theoretical framework. A last question remains: is there a set of conditions that does allow for validly using the proposed framework? Continuing the line of reasoning from the previous practical application example, one can rewrite Equation (13.2) to obtain a direct relationship between slip length and pore diameter:

$$\ell = \sqrt{\frac{\epsilon^3}{150(1-\epsilon)^2}} D_p \quad (13.3)$$

Still assuming that the pore and particle sizes should be at least an order of magnitude smaller than the slip length (or penetration depth), i.e. $\ell > 10D_p$, this can be further rewritten to:

$$\sqrt{\frac{\epsilon^3}{150(1-\epsilon)^2}} > 10 \quad (13.4)$$

Solving this for ϵ yields a real solution for $0.99967 < \epsilon < 1$. According to the Kozeny-Carman relation, the match between particle/pore size and resultant permeability can only be achieved by a porosity of at least 99.967%, a value at which it is highly questionable whether the relationship remains valid. Nevertheless, it indicates that a mismatch between pore/particle size and required permeability exists. For a reasonable porosity (e.g. $\epsilon = 0.5$), $\ell \approx 0.06D_p$, i.e. the permeability translates into a slip length and penetration depth that is significantly smaller than the pore/particle size responsible for this permeability. This inherently violates the main assumption of the theoretical framework.

To ensure that this finding is not solely dependent on the permeability model used, a similar calculation is made using the permeability models for unidirectional fibres as given in Equations (6.1) and (6.2). Again, for $\epsilon = 0.5$, $\ell_{\parallel} \approx 0.15D_p$ and $\ell_{\perp} \approx 0.013D_p$. All things considered, it is thought that the characteristic length scales that yield permeability values required for a proper functioning of the drag-reducing working mechanism, are too large for the small pore assumption of the theoretical framework to be valid, regardless of flow conditions.

Conclusions and recommendations for further research

This chapter forms the closing of this report. Conclusions are shared in Section 14.1, after which recommendations for further research are given in Section 14.2.

14.1. Conclusions

Turbulent boundary layers over streamwise-preferential permeable surfaces is a novel academic topic. DNS studies hint at drag reductions of up to 25% (Gómez-de-Segura and García-Mayoral, 2019; Li et al., 2020). A theoretical framework relates the permeability to drag reduction via slip lengths and virtual origins and it is hypothesised that the drag reduction originates from a lower contribution of quasi-streamwise (QS) vortices to the skin friction (Gómez-de-Segura and García-Mayoral, 2019). The only experimental study to date (Efstathiou and Luhar, 2020) lacked samples with the required permeability to test the drag reduction hypotheses and did not discuss the framework assumptions. This research project aimed to capture the entire picture, experimentally exploring the potential of the concept while simultaneously testing the theoretical framework hypotheses and ultimately assessing the framework's validity in experimental settings.

This thesis is the first experimental study that meets the permeability requirements to test the drag reduction predictions from the theoretical framework. Unfortunately, no drag reduction was measured. Also, none of the hypothesised flow modulation effects were observed. Scrutinising the theoretical framework reveals that the made assumptions conflict with the physical link between characteristic length scales (pore size) and permeability. All things considered, it is deemed unlikely that turbulent drag reduction by means of streamwise-preferential surfaces is feasible in experimental settings.

Listed below are the conclusions related to the different research (sub-)objectives and -questions. For sake of brevity, answers to multiple (sub-)questions are sometimes merged into a single, coherent conclusion.

- **3D-printed structures are the most viable physical realisation of streamwise-preferential substrates for aerodynamic research into turbulent boundary layers and friction drag.**

Test plates using three types of substrates were produced: seal fur, continuous fibres, and 3D-printed, of which the latter method is deemed the best. It has a large design space, allows for experimental permeability characterisation and rapid prototyping, and has the least amount of imperfections that have a negative influence on the quality of the results obtained with wind tunnel measurements. The design was limited in terms of the level of detail by the available printer resources (Prusa SL1) with 250 μm as the smallest achievable pore size. The permeabilities were in the required range, outperforming the 3D-printed design by Efstathiou and Luhar (2020).

- **The tested streamwise-preferential substrates increase drag and hence disagree with the theoretical model drag reduction predictions.**

In direct force measurements, the seal furs, continuous fibres, and 3D-printed surface increased drag with 20 – 320%, 30 – 90% and 0 – 8% respectively, where all values grow with increasing Re . For the latter, the data at low velocities ($0.3 \times 10^6 < Re_1 < 0.5 \times 10^6$) was inconclusive, albeit hinting at a slight drag increase. PIV experiments yielded u_τ -based friction estimates of $-2.5\% < \Delta C_f < 4\%$, with a decreasing trend for increasing velocity. These values are smaller than the estimated uncertainty bound of $\pm 10\%$ and thus no solid conclusions on the pure skin friction can be done. The change in drag for both methods does not agree with the theoretical framework predictions, neither in values (predicted DR $\approx 6 - 7\%$ at 8 – 9 m/s) nor in trend.

- **Other sources than surface friction are non-negligible and contribute to the measured drag.**

The discrepancy between the direct force measurement-based ΔC_D and PIV- u_τ -based ΔC_f points to other sources of drag. These were not quantified but are thought to be (a combination of) pressure drag and friction drag within the permeable structure, and pressure drag on the surface due to local plate imperfections. This would be at odds with the statement by Gómez-de-Segura and García-Mayoral (2019) that for external flows, the effect of the mean pressure gradient within the permeable substrate is negligible.

- **Differences in turbulent activity are not attributable to changes in turbulent events or coherent structures.**

One-point turbulent statistics show an increase in turbulence at the plate trailing edge (most fully developed BL) for $U_\infty = 20$ & 30 m/s, and a decrease in Reynolds stress for 5 & 10 m/s. The observed increase is due to the high wall-normal permeability enabling an increase in wall-normal velocity fluctuations, which agrees with literature. The observed decrease is statistically significant, but different measurements at the same location (with different camera zoom settings) only showed a minor decrease in Reynolds stress for 5 m/s, while measurements at other locations showed an increase in Reynolds stress for all velocities. Based on quadrant analysis and qualitative analysis of instantaneous flow fields, the decrease cannot be attributed to the attenuation of a specific type of turbulent event nor a change in coherent structures. It is thought that the observed decrease in Reynolds stress is a local effect, caused by a local deviation in permeability or an imperfection in the surface upstream.

- **None of the hypothesised flow modulation effects are observed.**

No slip velocity at the substrate-flow interface was measured. This is likely caused by the low pore area relative to the entire surface area (5%), meaning that the majority of the surface imposes a strict no-slip condition on the overlying flow. The measurement data did not allow for identification of spanwise-coherent structures related to KH-instabilities ("rollers").

- **The tested surface does not physically allow for the hypothesised drag reduction mechanism.**

In an abstracted sense, the permeability values translate into a difference in virtual origins for the mean flow and turbulence, and consequently should lower the contribution of QS-vortices to the friction drag. In practice however, such filtering does not happen as the flat surface is still exposed to the QS-vortices. This is in contrast with e.g. riblets, for which it has been demonstrated that they physically prohibit QS-vortices to penetrate and thus reduce the consequential skin friction.

- **The validity of the theoretical framework is questionable for physical realisations.**

Based on analytical derivations, regardless of environmental circumstances, pores of a given size are expected to always lead to permeabilities that yield virtual origins that are between one and three orders of magnitude smaller than the pore size. The theoretical model does not consider this physical relationship between pore size and permeability. As such, it is believed that there is an inherent mismatch between the pore size assumption and the virtual origin model.

14.2. Recommendations for further research

This research was a first of its kind, with valuable lessons learnt and ample areas for improvement. Simultaneously, it casts serious doubts on the validity of the theoretical framework, as proposed by Gómez-de-Segura and García-Mayoral (2019), in experimental settings. Both aspects provide the case that it is academically relevant to further study this topic. If shortcomings in this research lead to false doubts on this concept, then one would discard a potentially very promising method for turbulent drag reduction. However, if the findings from this research do point in the right direction, then that should be quickly confirmed by repeated studies and communicated within the academic community, such that resources can be directed towards other methods for turbulent drag reduction, which is still deemed one of the most important topics in the field of aerodynamics to move towards a more sustainable future. Although not the focus of this study, it should be noted that, given the relatively small increase in drag, streamwise-preferential surfaces might be interesting for other (flow control) purposes involving turbulent boundary layers.

Further research is recommended in the following sequential manner:

- **Better in-depth understanding of flow through permeable substrates.**

The literature study preceding this research extensively explored biomimetics for turbulent drag reduction and turbulent boundary layers over permeable substrates, and covered the basics of flow through permeable substrates. The largest uncertainty on the validity of the theoretical model is inherently linked to this latter subject. A better, in-depth understanding would be highly valuable for an improved assessment of the validity of the theoretical model in experimental settings. Topics should include the minimum required extent of the volume averaging region, and how macroscopic permeability values translate down to the level of individual unit cells. This recommendation would fit well within the scope of a new literature study.

- **Repeated experimental study with improvements in 3D-printed test plate, WT facilities and PIV methodology.**

This experimental research should be repeated using the lessons learnt. It would fit well within the scope of a new MSc thesis. Improvements are recommended on the following three aspects:

- **Design parameter sweep with 3D-printed test plates using salt-infused resin printing.**

An iteration in the design and production of the 3D-printed test plates can be done. Producing multiple test plates of the same type but with different design parameters provides more insight into the relationship between permeability and the measured quantities such as drag and turbulent activity. Smaller pores are necessary to reach permeability values that correspond to higher predicted breakdown velocities, where uncertainty in the direct force measurements is lower. Also, a more homogeneous distribution of pores with less solid surface area at the flow-substrate interface should be aimed at. Since the printer resolution was the limiting factor in this research, a different method has to be pursued. A possible solution could be to use salt-infused resin printing (Mu et al., 2017). The large-scale primary structure (for streamwise permeability) is designed and printed, after which the salt particles are washed out of the print, revealing the small-scale secondary structure (for spanwise and wall-normal permeabilities). The additional benefit is that this might allow for printing test plates in one piece given that access to a printer with a large enough build volume is within the project resource budget.

- **Adjust WT facilities to obtain a canonical ZPG TBL.**

Three changes to the WT facilities could improve the quality of the turbulent boundary layer, bringing it closer to a canonical ZPG TBL. Firstly, an auxiliary test section with a longer development length (> 3 m) ensures smaller relative changes in BL parameters (e.g. δ and Re_τ) along the test plate and the possibility of measurements at higher Re_τ . Secondly, a more stable freestream inflow at lower velocities would give the possibility of measurements at lower Re_τ . Although higher values are more interesting for industrial applications, it is often easier to test the fundamentals of novel concepts at lower values, such as in this research. Lastly, the addition of a variable top wall could aid in ensuring a ZPG TBL and also gives the ability to create adverse- or favourable pressure gradients as needed.

- **Optimise PIV setup for TBL capturing and improve on BL fitting methods.**

The measurement setup can be further optimised for capturing the TBL. Near-wall bias should be mitigated, either by having the camera optical axis aligned with the wall plane, or by using a special lens. Furthermore, two coupled cameras above each other recording simultaneously can capture the entire BL while simultaneously getting the highest level of detail possible. In data processing, efforts should be aimed at improving the BL fitting methods. If the above-mentioned setup improvements result in data that allows for direct linear fitting in the viscous sublayer, then this method is preferred for determining u_T . The optimiser based on Rodríguez-López et al. (2015) still remains valuable for determining the other parameters and therefore should be scrutinised in terms of solution uniqueness, convergence and robustness.

- **DNS study on geometrically resolved permeable structures.**

Previous DNS studies have been performed on idealised permeable substrates that were modelled analytically and therefore did not accurately reflect physical reality. On the other side, this experimental study was limited in the analysis capabilities, specifically the flow behaviour directly at the surface and within the substrate. Especially the latter remains challenging within an experimental setting. DNS studies in which the permeable substrate is geometrically resolved would solve both issues: the data reflects physical reality and can be used to perform a more detailed analysis of the flow behaviour. Due to the large scope and required computational resources, such a project would fit best within a PhD thesis.

Bibliography

- Abderrahaman-Elena, N., & García-Mayoral, R. (2017). Analysis of anisotropically permeable surfaces for turbulent drag reduction. *Physical Review Fluids*, 2(11). doi:[10.1103/PhysRevFluids.2.114609](https://doi.org/10.1103/PhysRevFluids.2.114609)
- Adrian, R. J., Meinhart, C. D., & Tomkins, C. D. (2000). Vortex organization in the outer region of the turbulent boundary layer. *Journal of Fluid Mechanics*, 422, 1–54.
- Airbus. (2019). *Global Market Forecast Cities, Airports & Aircraft 2019-2038*.
- Alfredsson, P. H., & Örlü, R. (2010). The diagnostic plot — a litmus test for wall bounded turbulence data. *European Journal of Mechanics - B/Fluids*, 29(6), 403–406. doi:[10.1016/j.euromechflu.2010.07.006](https://doi.org/10.1016/j.euromechflu.2010.07.006)
- ASTM. (2014). F2952-14 Standard Guide for Determining the Mean Darcy Permeability Coefficient for a Porous Tissue Scaffold. Standard. doi:[10.1520/F2952-14](https://doi.org/10.1520/F2952-14)
- Åström, B. T., Pipes, R. B., & Advani, S. G. (1992). On flow through aligned fiber beds and its application to composites processing. *Journal of Composite Materials*, 26(9), 1351–1373.
- Beavers, G. S., & Joseph, D. D. (1967). Boundary conditions at a naturally permeable wall. *Journal of Fluid Mechanics*, 30(1), 197–207. doi:[10.1017/s0022112067001375](https://doi.org/10.1017/s0022112067001375)
- Bechert, D. W., & Bartenwerfer, M. (1989). The viscous flow on surfaces with longitudinal ribs. *Journal of fluid mechanics*, 206, 105–129.
- Bechert, D. W., Bartenwerfer, M., Hoppe, G., & Reif, W. E. (1986). Drag Reduction Mechanisms Derived From Shark Skin. In *Congress of the international council of the aeronautical sciences* (Vol. 2, pp. 1044–1068). Retrieved from <http://www.scopus.com/inward/record.url?eid=2-s2.0-0022933470%7B%5C%7DpartnerID=40%7B%5C%7Dmd5=f04b3e229423dd25a74467b71c8d1940>
- Bechert, D. W., Bruse, M., Hage, W., Van Der Hoeven, J. G. T., & Hoppe, G. (1997). Experiments on drag-reducing surfaces and their optimization with an adjustable geometry. *Journal of Fluid Mechanics*, 338, 59–87. doi:[10.1017/S0022112096004673](https://doi.org/10.1017/S0022112096004673)
- Bechtold, G., & Ye, L. (2003). Influence of fibre distribution on the transverse flow permeability in fibre bundles. *Composites Science and Technology*, 63(14), 2069–2079. doi:[10.1016/s0266-3538\(03\)00112-x](https://doi.org/10.1016/s0266-3538(03)00112-x)
- Berdichevsky, A. L., & Cai, Z. (1993). Preform permeability predictions by self-consistent method and finite element simulation. *Polymer Composites*, 14(2), 132–143.
- Blackwelder, R. F., & Eckelmann, H. (1979). Streamwise vortices associated with the bursting phenomenon. *Journal of Fluid Mechanics*, 94(3), 577–594. doi:[10.1017/s0022112079001191](https://doi.org/10.1017/s0022112079001191)
- Breugem, W. P., Boersma, B. J., & Uittenbogaard, R. E. (2006). The influence of wall permeability on turbulent channel flow. *Journal of Fluid Mechanics*, 562. doi:[10.1017/s0022112006000887](https://doi.org/10.1017/s0022112006000887)
- Brinkman, H. C. (1949). A calculation of the viscous force exerted by a flowing fluid on a dense swarm of particles. *Flow, Turbulence and Combustion*, 1(1), 27.
- Bruschke, M. V., & Advani, S. G. (1993). Flow of generalized Newtonian fluids across a periodic array of cylinders. *Journal of Rheology*, 37(3), 479–498. doi:[10.1122/1.550455](https://doi.org/10.1122/1.550455)
- Buck, A. L. (1981). New Equations for Computing Vapor Pressure and Enhancement Factor. *Journal of Applied Meteorology and Climatology*, 20(12), 1527–1532. doi:[10.1175/1520-0450\(1981\)020<1527:Nefcvp>2.0.Co;2](https://doi.org/10.1175/1520-0450(1981)020<1527:Nefcvp>2.0.Co;2)
- Bushnell, D. M. (2003). Aircraft drag reduction—a review. *Proceedings of the Institution of Mechanical Engineers, Part G: Journal of Aerospace Engineering*, 217(1), 1–18.
- Busse, A., & Sandham, N. D. (2012). Influence of an anisotropic slip-length boundary condition on turbulent channel flow. *Physics of Fluids*, 24(5). doi:[10.1063/1.4719780](https://doi.org/10.1063/1.4719780)
- Cai, Z., & Berdichevsky, A. L. (1993). An improved self-consistent method for estimating the permeability of a fiber assembly. *Polymer composites*, 14(4), 314–323.
- Carman, P. C. (1956). Flow of Gases through Porous Media. Retrieved from <https://ci.nii.ac.jp/naid/10003529006/en/>
- Chauhan, K. A., Monkewitz, P. A., & Nagib, H. M. (2009). Criteria for assessing experiments in zero pressure gradient boundary layers. *Fluid Dynamics Research*, 41(2), 21404.
- Chen, X., & Papathanasiou, T. (2007). Micro-scale modeling of axial flow through unidirectional disordered fiber arrays. *Composites Science and Technology*, 67(7-8), 1286–1293. doi:[10.1016/j.compscitech.2006.10.011](https://doi.org/10.1016/j.compscitech.2006.10.011)

- Chen, X., & Papathanasiou, T. D. (2008). The transverse permeability of disordered fiber arrays: a statistical correlation in terms of the mean nearest interfiber spacing. *Transport in Porous Media*, 71(2), 233–251. doi:10.1007/s11242-007-9123-6
- Choi, H., Moin, P., & Kim, J. (1994). Active turbulence control for drag reduction in wall-bounded flows. *Journal of Fluid Mechanics*, 262, 75–110.
- Choi, K.-S. (1989). Near-wall structure of a turbulent boundary layer with riblets. *Journal of Fluid Mechanics*, 208, 417–458. doi:10.1017/s0022112089002892
- Choi, K.-S. (2000). European drag-reduction research—recent developments and current status. *Fluid Dynamics Research*, 26(5), 325.
- Chor, M. V., & Li, W. (2007). A permeability measurement system for tissue engineering scaffolds. *Measurement Science and Technology*, 18(1), 208–216. doi:10.1088/0957-0233/18/1/026
- Clauser, F. H. (1956). The turbulent boundary layer. In *Advances in applied mechanics* (Vol. 4, pp. 1–51). Elsevier.
- Coles, D. (1956). The law of the wake in the turbulent boundary layer. *Journal of Fluid Mechanics*, 1(2), 191–226.
- Darcy, H. P. G. (1856). *Les Fontaines publiques de la ville de Dijon. Exposition et application des principes à suivre et des formules à employer dans les questions de distribution d'eau, etc.* V. Dalamont.
- Davis, R. W., Williams, T. M., & Kooyman, G. L. (1985). Swimming metabolism of yearling and adult harbor seals *Phoca vitulina*. *Physiological Zoology*, 58(5), 590–596.
- Davit, Y., Bell, C. G., Byrne, H. M., Chapman, L. A. C., Kimpton, L. S., Lang, G. E., ... Shipley, R. J. (2013). Homogenization via formal multiscale asymptotics and volume averaging: How do the two techniques compare? *Advances in Water Resources*, 62, 178–206.
- der Westhuizen, J., & Du Plessis, J. P. (1996). An attempt to quantify fibre bed permeability utilizing the phase average Navier-Stokes equation. *Composites Part A: Applied Science and Manufacturing*, 27(4), 263–269.
- Ding, L., Shih, C., Liang, Z., Zhang, C., & Wang, B. (2003). In situ measurement and monitoring of whole-field permeability profile of fiber preform for liquid composite molding processes. *Composites Part A: Applied Science and Manufacturing*, 34(8), 779–789. doi:10.1016/s1359-835x(03)00121-0
- Drummond, J. E., & Tahir, M. I. (1984). Laminar viscous flow through regular arrays of parallel solid cylinders. *International Journal of Multiphase Flow*, 10(5), 515–540.
- Efstathiou, C., & Luhar, M. (2020). Turbulent boundary layers over streamwise-preferential porous materials. Online Database. Retrieved from <https://arxiv.org/abs/2006.00182>
- Efstathiou, C., & Luhar, M. (2018). Mean turbulence statistics in boundary layers over high-porosity foams. *Journal of Fluid Mechanics*, 841, 351–379. doi:10.1017/jfm.2018.57
- EIA. (2015). Passenger travel accounts for most of world transportation energy use. Web Page. Retrieved from <https://www.eia.gov/todayinenergy/detail.php?id=23832>
- Endruweit, A., Gommer, F., & Long, A. C. (2013). Stochastic analysis of fibre volume fraction and permeability in fibre bundles with random filament arrangement. *Composites Part A: Applied Science and Manufacturing*, 49, 109–118. doi:10.1016/j.compositesa.2013.02.012
- Erdsack, N., Dehnhardt, G., Witt, M., Wree, A., Siebert, U., & Hanke, W. (2015). Unique fur and skin structure in harbour seals (*Phoca vitulina*)—thermal insulation, drag reduction, or both? *J R Soc Interface*, 12(104), 20141206. doi:10.1098/rsif.2014.1206
- Favier, J., Dauptain, A., Basso, D., & Bottaro, A. (2009). Passive separation control using a self-adaptive hairy coating. *Journal of Fluid Mechanics*, 627, 451–483. doi:10.1017/s0022112009006119
- Fischer, M. C., & Ash, R. L. (1974). A general review of concepts for reducing skin friction, including recommendations for future studies.
- Forchheimer, P. (1901). Wasserbewegung durch boden. *Z. Ver. Deutsch, Ing.* 45, 1782–1788.
- Formlabs. (2017). SLA vs. DLP: Guide to Resin 3D Printers. Web Page. Retrieved from <https://formlabs.com/blog/resin-3d-printer-comparison-sla-vs-dlp/>
- Gad-el-Hak, M. (2000). *Flow control: passive, active, and reactive flow management*. Cambridge university press.
- García-Mayoral, R., Gómez-de-Segura, G., & Fairhall, C. T. (2019). The control of near-wall turbulence through surface texturing. *Fluid Dynamics Research*, 51(1). doi:10.1088/1873-7005/aadfcc
- García-Mayoral, R., & Jiménez, J. (2011a). Drag reduction by riblets. *Philos Trans A Math Phys Eng Sci*, 369(1940), 1412–1427. doi:10.1098/rsta.2010.0359

- García-Mayoral, R., & Jiménez, J. (2011b). Hydrodynamic stability and breakdown of the viscous regime over riblets. *Journal of Fluid Mechanics*, 678, 317–347. doi:[10.1017/jfm.2011.114](https://doi.org/10.1017/jfm.2011.114)
- Gatti, D., & Quadrio, M. (2016). Reynolds-number dependence of turbulent skin-friction drag reduction induced by spanwise forcing. *Journal of Fluid Mechanics*, 802, 553–582.
- Gebart, B. R. (1992). Permeability of unidirectional reinforcements for RTM. *Journal of composite materials*, 26(8), 1100–1133.
- Gibson, I., Rosen, D. W., & Stucker, B. (2010). *Additive Manufacturing Technologies*. doi:[10.1007/978-1-4419-1120-9](https://doi.org/10.1007/978-1-4419-1120-9)
- Gómez-de-Segura, G., Fairhall, C. T., MacDonald, M., Chung, D., & García-Mayoral, R. (2018a). Manipulation of near-wall turbulence by surface slip and permeability. *Journal of Physics: Conference Series*, 1001. doi:[10.1088/1742-6596/1001/1/012011](https://doi.org/10.1088/1742-6596/1001/1/012011)
- Gómez-de-Segura, G., & García-Mayoral, R. (2019). Turbulent drag reduction by anisotropic permeable substrates – analysis and direct numerical simulations. *Journal of Fluid Mechanics*, 875, 124–172. doi:[10.1017/jfm.2019.482](https://doi.org/10.1017/jfm.2019.482)
- Gómez-de-Segura, G., Sharma, A., & García-Mayoral, R. (2018b). Turbulent Drag Reduction Using Anisotropic Permeable Substrates. *Flow Turbul Combust*, 100(4), 995–1014. doi:[10.1007/s10494-018-9916-4](https://doi.org/10.1007/s10494-018-9916-4)
- Gong, H., Beauchamp, M., Perry, S., Woolley, A. T., & Nordin, G. P. (2015). Optical Approach to Resin Formulation for 3D Printed Microfluidics. *RSC Adv*, 5(129), 106621–106632. doi:[10.1039/C5RA23855B](https://doi.org/10.1039/C5RA23855B)
- Gong, H., Bickham, B. P., Woolley, A. T., & Nordin, G. P. (2017). Custom 3D printer and resin for 18 μm x 20 μm microfluidic flow channels. *Lab Chip*, 17(17), 2899–2909. doi:[10.1039/c7lc00644f](https://doi.org/10.1039/c7lc00644f)
- Graver, B., Zhang, K., & Rutherford, D. (2019). CO2 emissions from commercial aviation. *International Council on Clean Transportation Working Paper*.
- Greidanus, A., Delfos, R., Tokgoz, S., & Westerweel, J. (2015). Turbulent Taylor-Couette flow over riblets: drag reduction and the effect of bulk fluid rotation. *Experiments in Fluids*, 56(5), 1–13.
- Hahn, S., Je, J., & Choi, H. (2002). Direct numerical simulation of turbulent channel flow with permeable walls. *Journal of Fluid Mechanics*, 450, 259–285. doi:[10.1017/s0022112001006437](https://doi.org/10.1017/s0022112001006437)
- Happel, J. (1959). Viscous flow relative to arrays of cylinders. *AIChE Journal*, 5(2), 174–177.
- Hasimoto, H. (2006). On the periodic fundamental solutions of the Stokes equations and their application to viscous flow past a cubic array of spheres. *Journal of Fluid Mechanics*, 5(02). doi:[10.1017/s0022112059000222](https://doi.org/10.1017/s0022112059000222)
- Head, M. R., & Bandyopadhyay, P. (1981). New aspects of turbulent boundary-layer structure. *Journal of Fluid Mechanics*, 107(-1). doi:[10.1017/s0022112081001791](https://doi.org/10.1017/s0022112081001791)
- Hemmen, P. (2018). *Towards Practical Hybrid Laminar Flow Control*.
- Ho, R. T., & Gelhar, L. W. (1973). Turbulent flow with wavy permeable boundaries. *J. Fluid Mech*, 58(2), 403–414.
- IATA. (2013). *Aircraft Technology Roadmap to 2050*.
- IATA. (2019). Fuel fact sheet. Dataset.
- Innocentini, M. D. M., & Pandolfelli, V. C. (2001). Permeability of Porous Ceramics Considering the Klinkenberg and Inertial Effects. *Journal of the American Ceramic Society*, 84(5), 941–944. doi:[10.1111/j.1151-2916.2001.tb00772.x](https://doi.org/10.1111/j.1151-2916.2001.tb00772.x)
- Innocentini, M. D. M., Pardo, A. R. F., & Pandolfelli, V. C. (2000). Influence of Air Compressibility on the Permeability Evaluation of Refractory Castables. *Journal of the American Ceramic Society*, 83(6), 1536–1538. doi:[10.1111/j.1151-2916.2000.tb01426.x](https://doi.org/10.1111/j.1151-2916.2000.tb01426.x)
- Itoh, M., Tamano, S., Iguchi, R., Yokota, K., Akino, N., Hino, R., & Kubo, S. (2006). Turbulent drag reduction by the seal fur surface. *Physics of Fluids*, 18(6), 65102.
- ITTC. (2011). Recommended Procedures Fresh Water and Seawater Properties, IITC Specialist Committee.
- Jackson, G. W., & James, D. F. (1986). The permeability of fibrous porous media. *The Canadian Journal of Chemical Engineering*, 64(3), 364–374.
- Jennings, S. G. (1988). The mean free path in air. *Journal of Aerosol Science*, 19(2), 159–166.
- Jiménez, J. (1994). On the structure and control of near wall turbulence. *Physics of Fluids*, 6(2), 944–953. doi:[10.1063/1.868327](https://doi.org/10.1063/1.868327)
- Jimenez, J., Uhlmann, M., Pinelli, A., & Kawahara, G. (2001). Turbulent shear flow over active and passive porous surfaces. *Journal of Fluid Mechanics*, 442, 89.
- Kähler, C. J., Scharnowski, S., & Cierpka, C. (2012). On the uncertainty of digital PIV and PTV near walls. *Experiments in Fluids*, 52(6), 1641–1656. doi:[10.1007/s00348-012-1307-3](https://doi.org/10.1007/s00348-012-1307-3)
- Karniadakis, G. E., Beskok, A., & Aluru, N. (2000). *Microflows and Nanoflows: fundamentals and simulation*. Interdisciplinary Applied Mathematics. doi:[10.1007/0-387-28676-4](https://doi.org/10.1007/0-387-28676-4)

- Kim, H. T., Kline, S. J., & Reynolds, W. C. (1971). The production of turbulence near a smooth wall in a turbulent boundary layer. *Journal of Fluid Mechanics*, 50(1), 133–160. doi:[10.1017/s0022112071002490](https://doi.org/10.1017/s0022112071002490)
- Kim, J., Moin, P., & Moser, R. (1987). Turbulence statistics in fully developed channel flow at low Reynolds number. *Journal of Fluid Mechanics*, 177, 133–166. doi:[10.1017/s0022112087000892](https://doi.org/10.1017/s0022112087000892)
- Klän, S., Burgmann, S., Bachmann, T., Klaas, M., Wagner, H., & Schröder, W. (2012). Surface structure and dimensional effects on the aerodynamics of an owl-based wing model. *European Journal of Mechanics - B/Fluids*, 33, 58–73. doi:[10.1016/j.euromechflu.2011.12.006](https://doi.org/10.1016/j.euromechflu.2011.12.006)
- Klän, S., Bachmann, T., Klaas, M., Wagner, H., & Schröder, W. (2008). Experimental analysis of the flow field over a novel owl based airfoil. *Experiments in Fluids*, 46(5), 975–989. doi:[10.1007/s00348-008-0600-7](https://doi.org/10.1007/s00348-008-0600-7)
- Kline, S. J., Reynolds, W. C., Schraub, F. A., & Runstadler, P. W. (1967). The structure of turbulent boundary layers. *J. Fluid Mech*, 30(4), 741–773.
- Kong, F., & Schetz, J. (1982). Turbulent boundary layer over porous surfaces with different surface geometries. In *20th aerospace sciences meeting*. doi:[10.2514/6.1982-30](https://doi.org/10.2514/6.1982-30)
- Kuwabara, S. (1959). The forces experienced by randomly distributed parallel circular cylinders or spheres in a viscous flow at small Reynolds numbers. *Journal of the physical society of Japan*, 14(4), 527–532.
- Kuwata, Y., & Suga, K. (2016). Lattice Boltzmann direct numerical simulation of interface turbulence over porous and rough walls. *International Journal of Heat and Fluid Flow*, 61, 145–157. doi:[10.1016/j.ijheatfluidflow.2016.03.006](https://doi.org/10.1016/j.ijheatfluidflow.2016.03.006)
- Kuwata, Y., & Suga, K. (2017). Direct numerical simulation of turbulence over anisotropic porous media. *Journal of Fluid Mechanics*, 831, 41–71. doi:[10.1017/jfm.2017.619](https://doi.org/10.1017/jfm.2017.619)
- Kuwata, Y., & Suga, K. (2019). Extensive investigation of the influence of wall permeability on turbulence. *International Journal of Heat and Fluid Flow*, 80. doi:[10.1016/j.ijheatfluidflow.2019.108465](https://doi.org/10.1016/j.ijheatfluidflow.2019.108465)
- Lai, Y.-J. (2021). *Turbulent Viscous Drag Reduction in Air by Compliant Surfaces*.
- Lesage, V., Hammill, M. O., & Kovacs, K. M. (1999). Functional classification of harbor seal (*Phoca vitulina*) dives using depth profiles, swimming velocity, and an index of foraging success. *Canadian Journal of Zoology*, 77(1), 74–87.
- Li, Q., Pan, M., Zhou, Q., & Dong, Y. (2020). Turbulent drag modification in open channel flow over an anisotropic porous wall. *Physics of Fluids*, 32(1). doi:[10.1063/1.5130647](https://doi.org/10.1063/1.5130647)
- Lovera, F., & Kennedy, J. F. (1969). Friction-factors for flat-bed flows in sand channels. *Journal of the Hydraulics Division*.
- Luchini, P. (1996). Reducing the turbulent skin friction. In *Computational methods in applied sciences' 96 (paris, 9-13 september 1996)* (pp. 465–470).
- Luchini, P. (2015). The relevance of longitudinal and transverse protrusion heights for drag reduction by a superhydrophobic surface. In *Proc. european drag reduction and flow control meeting—edrfmc 2015; march 23–26* (pp. 81–82).
- Luchini, P., Manzo, F., & Pozzi, A. (1991). Resistance of a grooved surface to parallel flow and cross-flow. *Journal of Fluid Mechanics*, 228. doi:[10.1017/s0022112091002641](https://doi.org/10.1017/s0022112091002641)
- Lundström, T. S., & Gebart, B. R. (1995). Effect of perturbation of fibre architecture on permeability inside fibre tows. *Journal of composite materials*, 29(4), 424–443.
- Mei, C. C., & Vernescu, B. (2010). *Homogenization methods for multiscale mechanics*. World scientific.
- Min, T., & Kim, J. (2004). Effects of hydrophobic surface on skin-friction drag. *Physics of Fluids*, 16(7), L55–L58. doi:[10.1063/1.1755723](https://doi.org/10.1063/1.1755723)
- Monkewitz, P. A., Chauhan, K. A., & Nagib, H. M. (2007). Self-consistent high-Reynolds-number asymptotics for zero-pressure-gradient turbulent boundary layers. *Physics of Fluids*, 19(11), 115101.
- Mu, X., Bertron, T., Dunn, C., Qiao, H., Wu, J., Zhao, Z., ... Qi, H. J. (2017). Porous polymeric materials by 3D printing of photocurable resin. *Materials Horizons*, 4(3), 442–449. doi:[10.1039/c7mh00084g](https://doi.org/10.1039/c7mh00084g)
- Musker, A. J. (1979). Explicit expression for the smooth wall velocity distribution in a turbulent boundary layer. *AIAA Journal*, 17(6), 655–657.
- Nagib, H. M., Chauhan, K. A., & Monkewitz, P. A. (2007). Approach to an asymptotic state for zero pressure gradient turbulent boundary layers. *Philos Trans A Math Phys Eng Sci*, 365(1852), 755–770. doi:[10.1098/rsta.2006.1948](https://doi.org/10.1098/rsta.2006.1948)
- Nelson, G. (2018). Contribution of the Global Aviation Sector to Achieving Paris Agreement Climate Objectives. In *Climate action network (can), bonn, germany, 2nd april*.
- Nguyen, T. T., & Indraratna, B. (2016). Hydraulic behaviour of parallel fibres under longitudinal flow: a numerical treatment. *Canadian Geotechnical Journal*, 53(7), 1081–1092. doi:[10.1139/cgj-2015-0213](https://doi.org/10.1139/cgj-2015-0213)
- Nieuwstadt, F. T., Westerweel, J., & Boersma, B. J. (2016). *Turbulence*. doi:[10.1007/978-3-319-31599-7](https://doi.org/10.1007/978-3-319-31599-7)

- Nikuradse, J. (1950). *Laws of flow in rough pipes*. National Advisory Committee for Aeronautics.
- Niu, J., & Hu, D. L. (2011). Drag reduction of a hairy disk. *Physics of Fluids*, 23(10). doi:10.1063/1.3639133
- Ochoa-Tapia, J. A., & Whitaker, S. (1995). Momentum transfer at the boundary between a porous medium and a homogeneous fluid—I. Theoretical development. *International Journal of Heat and Mass Transfer*, 38(14), 2635–2646.
- Pennella, F., Cerino, G., Massai, D., Gallo, D., Falvo D'Urso Labate, G., Schiavi, A., ... Morbiducci, U. (2013). A survey of methods for the evaluation of tissue engineering scaffold permeability. *Ann Biomed Eng*, 41(10), 2027–2041. doi:10.1007/s10439-013-0815-5
- Pokrajac, D., & Manes, C. (2009). Velocity Measurements of a Free-Surface Turbulent Flow Penetrating a Porous Medium Composed of Uniform-Size Spheres. *Transport in Porous Media*, 78(3), 367–383. doi:10.1007/s11242-009-9339-8
- Prandtl, L. (1904). Über Flüssigkeitsbewegung bei sehr kleiner Reibung. *Verhandl. III, Internat. Math.-Kong., Heidelberg, Teubner, Leipzig, 1904*, 484–491.
- Raffel, M., Willert, C. E., & Kompenhans, J. (1998). *Particle Image Velocimetry: A Practical Guide*. Springer. Retrieved from <https://books.google.nl/books?id=enOLTmfYVPQC>
- Raffel, M., Willert, C. E., Scarano, F., Kähler, C. J., Wereley, S. T., & Kompenhans, J. (2018). *Particle image velocimetry: a practical guide*. Springer.
- Raupach, M. R., Antonia, R. A., & Rajagopalan, S. (1991). Rough-wall turbulent boundary layers. *Applied Mechanics Reviews*, 44(1), 1–25. doi:10.1115/1.3119492
- Robinson, S. K. (1991). Coherent motions in the turbulent boundary layer. *Annual Review of Fluid Mechanics*, 23(1), 601–639.
- Rodríguez-López, E., Bruce, P. J. K., & Buxton, O. R. H. (2015). A robust post-processing method to determine skin friction in turbulent boundary layers from the velocity profile. *Experiments in Fluids*, 56. doi:10.1007/s00348-015-1935-5
- Rosti, M. E., Brandt, L., & Pinelli, A. (2018). Turbulent channel flow over an anisotropic porous wall – drag increase and reduction. *Journal of Fluid Mechanics*, 842, 381–394. doi:10.1017/jfm.2018.152
- Rosti, M. E., Cortelezzi, L., & Quadrio, M. (2015). Direct numerical simulation of turbulent channel flow over porous walls. *Journal of Fluid Mechanics*, 784, 396–442. doi:10.1017/jfm.2015.566
- Rowin, W. A., Hou, J., & Ghaemi, S. (2018). Turbulent channel flow over riblets with superhydrophobic coating. *Experimental Thermal and Fluid Science*, 94, 192–204. doi:10.1016/j.expthermflusci.2018.02.001
- Rubio Carpio, A., Merino Martínez, R., Avallone, F., Ragni, D., Snellen, M., & van der Zwaag, S. (2019). Experimental characterization of the turbulent boundary layer over a porous trailing edge for noise abatement. *Journal of Sound and Vibration*, 443, 537–558. doi:10.1016/j.jsv.2018.12.010
- Ruff, J. F., & Gelhar, L. W. (1972). Turbulent shear flow in porous boundary. *J. Engrg. Mech*, 504(98), 975.
- Sangani, A. S., & Yao, C. (1988). Transport processes in random arrays of cylinders. II. Viscous flow. *The Physics of fluids*, 31(9), 2435–2444.
- Sangani, A. S., & Acrivos, A. (1982). Slow flow past periodic arrays of cylinders with application to heat transfer. *International journal of Multiphase flow*, 8(3), 193–206.
- Schlatter, P., & Örlü, R. (2010). Assessment of direct numerical simulation data of turbulent boundary layers. *Journal of Fluid Mechanics*, 659, 116–126. doi:10.1017/s0022112010003113
- Scholander, P. F., Walters, V., Hock, R., & Irving, L. (1950). Body insulation of some arctic and tropical mammals and birds. *The Biological Bulletin*, 99(2), 225–236.
- Scholz, S., Gillespie, J. W., & Heider, D. (2007). Measurement of transverse permeability using gaseous and liquid flow. *Composites Part A: Applied Science and Manufacturing*, 38(9), 2034–2040. doi:10.1016/j.compositesa.2007.05.002
- Sciacchitano, A., & Wieneke, B. (2016). PIV uncertainty propagation. *Measurement Science and Technology*, 27(8). doi:10.1088/0957-0233/27/8/084006
- Sharma, S., & Siginer, D. A. (2010). Permeability Measurement Methods in Porous Media of Fiber Reinforced Composites. *Applied Mechanics Reviews*, 63(2). doi:10.1115/1.4001047
- Shimizu, Y., Tsujimoto, T., & Nakagawa, H. (1990). Experiment and macroscopic modelling of flow in highly permeable porous medium under free-surface flow. *J. Hydrosoci. Hydraul. Eng*, 8(1), 69–78.
- Shou, D., Fan, J., & Ding, F. (2011). Hydraulic permeability of fibrous porous media. *International Journal of Heat and Mass Transfer*, 54(17-18), 4009–4018. doi:10.1016/j.ijheatmasstransfer.2011.04.022
- Smith, & Metzler. (1983). The characteristics of low-speed streaks in the near-wall region of a turbulent boundary layer.

- Sobera, M. P., & Kleijn, C. R. (2006). Hydraulic permeability of ordered and disordered single-layer arrays of cylinders. *Phys Rev E Stat Nonlin Soft Matter Phys*, 74(3 Pt 2), 36301. doi:[10.1103/PhysRevE.74.036301](https://doi.org/10.1103/PhysRevE.74.036301)
- Spalart, P. R., & McLean, J. D. (2011). Drag reduction: enticing turbulence, and then an industry. *Philosophical Transactions of the Royal Society A: Mathematical, Physical and Engineering Sciences*, 369(1940), 1556–1569.
- Sparrow, E. M., & Loeffler Jr, A. L. (1959). Longitudinal laminar flow between cylinders arranged in regular array. *AIChE Journal*, 5(3), 325–330.
- Suga, K., Matsumura, Y., Ashitaka, Y., Tominaga, S., & Kaneda, M. (2010). Effects of wall permeability on turbulence. *International Journal of Heat and Fluid Flow*, 31(6), 974–984. doi:[10.1016/j.ijheatfluidflow.2010.02.023](https://doi.org/10.1016/j.ijheatfluidflow.2010.02.023)
- Suga, K., Nakagawa, Y., & Kaneda, M. (2017). Spanwise turbulence structure over permeable walls. *Journal of Fluid Mechanics*, 822, 186–201. doi:[10.1017/jfm.2017.278](https://doi.org/10.1017/jfm.2017.278)
- Suga, K., Okazaki, Y., Ho, U., & Kuwata, Y. (2018). Anisotropic wall permeability effects on turbulent channel flows. *Journal of Fluid Mechanics*, 855, 983–1016.
- Szodruch, J. (1991). Viscous drag reduction on transport aircraft. In *29th aerospace sciences meeting*. doi:[10.2514/6.1991-685](https://doi.org/10.2514/6.1991-685)
- Takamura, K., Fischer, H., & Morrow, N. R. (2012). Physical properties of aqueous glycerol solutions. *Journal of Petroleum Science and Engineering*, 98, 50–60.
- Tamayol, A., & Bahrami, M. (2009). Analytical determination of viscous permeability of fibrous porous media. *International Journal of Heat and Mass Transfer*, 52(9-10), 2407–2414. doi:[10.1016/j.ijheatmasstransfer.2008.09.032](https://doi.org/10.1016/j.ijheatmasstransfer.2008.09.032)
- Tamayol, A., & Bahrami, M. (2010). Parallel Flow Through Ordered Fibers: An Analytical Approach. *Journal of Fluids Engineering*, 132(11). doi:[10.1115/1.4002169](https://doi.org/10.1115/1.4002169)
- Tamayol, A., & Bahrami, M. (2011). Transverse permeability of fibrous porous media. *Phys Rev E Stat Nonlin Soft Matter Phys*, 83(4 Pt 2), 46314. doi:[10.1103/PhysRevE.83.046314](https://doi.org/10.1103/PhysRevE.83.046314)
- Tamayol, A., Wong, K. W., & Bahrami, M. (2012). Effects of microstructure on flow properties of fibrous porous media at moderate Reynolds number. *Phys Rev E Stat Nonlin Soft Matter Phys*, 85(2 Pt 2), 26318. doi:[10.1103/PhysRevE.85.026318](https://doi.org/10.1103/PhysRevE.85.026318)
- Theodorsen, T. (1952). Mechanism of turbulence. In *Proceedings of the second midwestern conference on fluid mechanics* (pp. 1–18). Ohio State University.
- Tomadakis, M. M., & Robertson, T. J. (2005). Viscous Permeability of Random Fiber Structures: Comparison of Electrical and Diffusional Estimates with Experimental and Analytical Results. *Journal of Composite Materials*, 39(2), 163–188. doi:[10.1177/0021998305046438](https://doi.org/10.1177/0021998305046438)
- Van Campenhout, O. W. G. (2016). *Going against the flow: An experimental investigation into the flow mechanics of dimpled surfaces in turbulent boundary layers*.
- Van Nesselrooij, M. (2015). *On the drag reduction of dimpled surfaces in turbulent boundary layers*.
- Van Oudheusden, B. W. (2020). Viscous Flows - Incompressible Turbulent Flow. Generic.
- van Nesselrooij, M., van Campenhout, O. W. G., van Oudheusden, B. W., Schrijer, F. F. J., & Veldhuis, L. L. M. (2021). *Development of an experimental apparatus for flat plate drag measurements and considerations for such measurements*.
- Venkataraman, D., & Bottaro, A. (2012). Numerical modeling of flow control on a symmetric aerofoil via a porous, compliant coating. *Physics of Fluids*, 24(9). doi:[10.1063/1.4748962](https://doi.org/10.1063/1.4748962)
- Vincenti, W. G., & Kruger, C. H. (1965). *Introduction to physical gas dynamics*.
- Wadkanovaren. (2011). Gemiddelde watertemperatuur op het Wad. Web Page. Retrieved from <https://www.wadkanovaren.nl/pub/watertemperatuur.pdf>
- Wallace, J. M. (2016). Quadrant Analysis in Turbulence Research: History and Evolution. *Annual Review of Fluid Mechanics*, 48(1), 131–158. doi:[10.1146/annurev-fluid-122414-034550](https://doi.org/10.1146/annurev-fluid-122414-034550)
- Wallace, J. M., & Brodkey, R. S. (1977). Reynolds stress and joint probability density distributions in the u-v plane of a turbulent channel flow. *The Physics of Fluids*, 20(3), 351–355.
- Whitaker, S. (1999). *The method of volume averaging*. Springer Science & Business Media.
- White, F. M., & Corfield, I. (2006). *Viscous fluid flow*. McGraw-Hill New York.
- Wilson, D. E., & Burnie, D. (2001). *Animal: the definitive visual guide to the world's wildlife*. Dorling Kindersley, London, UK.
- Winzen, A., Klaas, M., & Schröder, W. (2013). High-speed PIV measurements of the near-wall flow field over hairy surfaces. *Experiments in Fluids*, 54(3). doi:[10.1007/s00348-013-1472-z](https://doi.org/10.1007/s00348-013-1472-z)

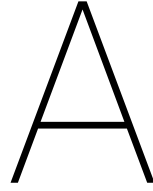
- Wood, B. D., He, X., & Apte, S. V. (2020). Modeling turbulent flows in porous media. *Annual Review of Fluid Mechanics*, 52, 171–203.
- Woudberg, S. (2017). Permeability prediction of an analytical pore-scale model for layered and isotropic fibrous porous media. *Chemical Engineering Science*, 164, 232–245. doi:[10.1016/j.ces.2017.01.061](https://doi.org/10.1016/j.ces.2017.01.061)
- Zagni, A. F. E., & Smith, K. V. H. (1976). Channel flow over permeable beds of graded spheres. *Journal of the hydraulics division*, 102(2), 207–222.
- Zampogna, G. A., & Bottaro, A. (2016). Fluid flow over and through a regular bundle of rigid fibres. *Journal of Fluid Mechanics*, 792, 5–35. doi:[10.1017/jfm.2016.66](https://doi.org/10.1017/jfm.2016.66)
- Zarandi, M. A. E., Arroyo, S., & Pillai, K. M. (2019). Longitudinal and transverse flows in fiber tows: Evaluation of theoretical permeability models through numerical predictions and experimental measurements. *Composites Part A: Applied Science and Manufacturing*, 119, 73–87. doi:[10.1016/j.compositesa.2018.12.032](https://doi.org/10.1016/j.compositesa.2018.12.032)
- Zippe, H. J., & Graf, W. H. (1983). Turbulent boundary-layer flow over permeable and non-permeable rough surfaces. *Journal of Hydraulic research*, 21(1), 51–65.

This page has been intentionally left blank.

V

Appendices

This page has been intentionally left blank.



Statistical methods

Root-mean-square error (RMSE)

The root-mean-square error (RMSE) is a metric that can be used to assess the spread in measurement data. For any variable x in sample of size n , it is defined as

$$\text{RMSE} = \sqrt{\frac{\sum_{i=1}^n (x_i - \bar{x})^2}{n}}. \quad (\text{A.1})$$

Coefficient of determination (R^2)

The coefficient of determination (R^2) indicates the quality of a fitted predictor (f_i) to measurement data (y_i). Strictly speaking, it is a measure of the variation in the dependent variable that is predictable from the independent variables. It is defined as

$$R^2 = 1 - \frac{\sum_{i=1} (y_i - f_i)^2}{\sum_{i=1} (y_i - \bar{y})^2}. \quad (\text{A.2})$$

One-sample t -test

A one-sample t -test is used to determine whether the mean of a sample or signal (\bar{x}) is equal to a value specified in a null hypothesis (μ_0). First, the t -statistic is computed as follows:

$$t = \frac{\bar{x} - \mu_0}{\sqrt{\frac{\sigma^2}{n}}}, \quad (\text{A.3})$$

where σ^2 is the sample variance. With $n-1$ degrees of freedom, a p -value corresponding to the t -statistic can be looked up in a standard table. If it lies below the chosen threshold for statistical significance (α), the null hypothesis is rejected.

Welch's two-sample t -test

Welch's two-sample t -test is a general case of the one-sample t -test and used to determine whether two different samples or signals have equal means. First, the t -statistic is computed as follows:

$$t = \frac{\mu_1 - \mu_2}{\sqrt{\frac{\sigma_1^2}{n_1} + \frac{\sigma_2^2}{n_2}}}. \quad (\text{A.4})$$

The degrees of freedom is computed using the Welch-Satterthwaite equation:

$$d.o.f. \approx \frac{\left(\frac{\sigma_1^2}{n_1} + \frac{\sigma_2^2}{n_2}\right)^2}{\frac{1}{n_1-1} \left(\frac{\sigma_1^2}{n_1}\right)^2 + \frac{1}{n_2-1} \left(\frac{\sigma_2^2}{n_2}\right)^2}. \quad (\text{A.5})$$

The null hypothesis (both samples have equal means) can be rejected if the p -value corresponding to the t -statistic lies below the chosen threshold for statistical significance.

This page has been intentionally left blank.

B

Permeability of fibrous substrates

Permeability of fibrous substrates is a well-covered topic due to its importance in the manufacturing of fibre-reinforced polymer composites (FRC). One of the main production techniques, liquid composite moulding (LCM), consists of a fluid resin being injected in or drawn through a mould with dry fibres. The development of effective production processes requires adequate knowledge of the permeability of the fibrous substrate at hand. It has led to a wide body of literature, including analytical models and experimental and numerical studies. This appendix focuses on the literature covering unidirectional parallel (1D) fibrous substrates. A comprehensive historical review is omitted since the purpose of this section is to establish the set of parameters of fibrous substrates that govern their permeability.

B.1. Flow modelling

The majority of literature deals with Darcy flow where inertial effects do not play a role. This is a safe assumption given that LCM occurs at low Reynolds numbers. Taking inertial effects into account via a Forchheimer term adds complexity to the problem, and therefore no analytical models exist for permeability through fibrous substrates at moderate Reynolds number, although the topic has been studied by Tamayol et al. (2012). Another widely accepted assumption is that of no-slip conditions at the interface between fluid and fibres, mainly due to the majority of studies relating to liquid flow. Shou et al. (2011) does take the slip effect into account via the Knudsen number to have a valid model for superfine fibres (50 nm to 5 μm). Based on the dimensions of interest ($> 25 \mu\text{m}$), it is considered that most studies assuming Darcy flow and no-slip conditions in the fibrous medium suffice.

B.2. Topology types for permeability expressions

Fibrous substrates can have fibres oriented in one direction (1D), such as in FRCs, within a plane (2D), such as woven fibre mats, or in all directions (3D), such as glass wool insulation. All cases are covered in literature for different applications. The seal fur discussed in Itoh et al. (2006) has hairs aligned in one direction, and Gómez-de-Segura and García-Mayoral (2019) suggest unidirectional rods as a practical implementation for useful anisotropic permeable substrates. Consequently, the focus here lies on 1D oriented fibres.

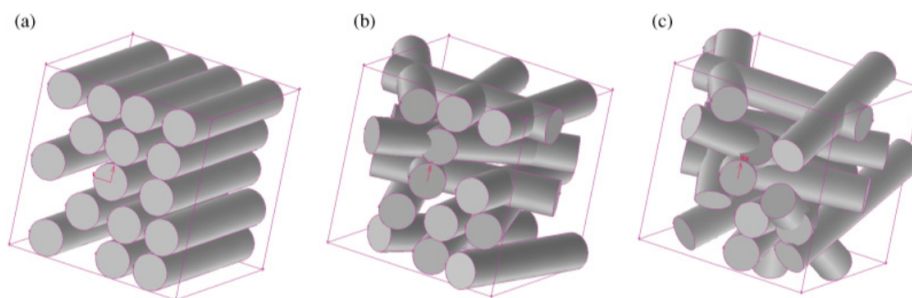


Figure B.1: Difference in fibre orientation within fibrous substrates: (a) 1D, (b) 2D, and (c) 3D (Tamayol and Bahrami, 2011).

The majority of analytical models simplify the topology to a geometry of regularly spaced (ordered) fibres with a circular cross-section. In this simplification, the 'unit cell' is the smallest volume which can represent the characteristics of the whole structure. The fibrous substrate is assumed to be periodic with the unit cells repeating themselves throughout the structure. For 1D oriented fibres, this means that, given a unit cell of unity aspect ratio, two distinct permeabilities exist: an axial (or parallel) permeability (K_{\parallel}) along the fibres, and a normal (or transverse) permeability (K_{\perp}) perpendicular to the fibres. With the unit-cell approach, the spacing and pattern of the fibres can be translated into the porosity parameter (ϵ), which represents the volume fraction of void filled by the fluid to the total volume of the substrate. Literature also often mentions the fibre volume ratio, $\phi = 1 - \epsilon$.

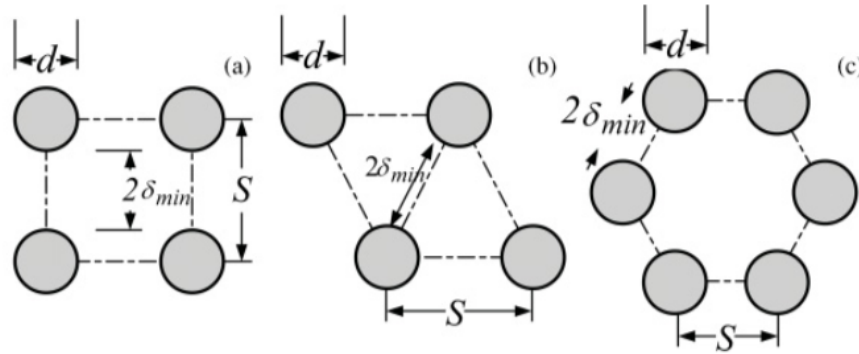


Figure B.2: Examples of different unit cells for 1D ordered fibrous substrates: (a) square, (b) staggered, and (c) hexagonal (Tamayol and Bahrami, 2011).

The permeability of the fibrous substrate can be expressed as a function of two governing parameters:

$$K = D_f^2 f(\epsilon), \quad (\text{B.1})$$

where D_f represents the fibre diameter. In literature, permeability is also often expressed as dimensionless quantity (K/D_f^2) rendering it a function of porosity only. Analytical models differ in their representation of $f(\epsilon)$. For experimental studies, often K/D_f^2 is plotted against a measured ϵ , a necessary simplification as it is complex to capture the exact microstructure of the entire substrate. This explains the spread in experimentally obtained results summarised in several review papers such as Jackson and James (1986).

B.3. The effect of irregularity in fibre spacing on permeability

Another relevant aspect of fibrous substrates is that in reality, the fibres will have a certain degree of randomness in their spacing. This is an important reason for discrepancies between analytically and experimentally obtained permeability values. In general, there is quite good agreement about the effect of randomness on the permeability of 1D fibrous substrates. For a fixed porosity, a higher degree of non-uniformity in the fibre distribution leads to a higher parallel permeability (Sangani and Yao, 1988; Cai and Berdichevsky, 1993; Chen and Papathanasiou, 2007). This is because zones with low fibre density become the main flow channels, dominating the effective (overall) permeability. The exact opposite is true for transverse permeability, for which the flow is dominated by zones with high fibre density and low spacing (Cai and Berdichevsky, 1993; Lundström and Gebart, 1995; Bechtold and Ye, 2003; Chen and Papathanasiou, 2008). Consequently, the anisotropic permeability ratio (parallel-to-transverse) will be higher in practice than for analytical models based on regularity assumptions.

Taking irregularity into account in modelling permeability has been done by Endruweit et al. (2013). They estimated probabilities for the occurrence of certain local filament arrangements (such as square or hexagonal, similar to the unit-cell approach) as a function of fibre compaction level (the opposite of porosity). With this estimated probability distribution, an equivalent permeability was calculated based on a weighted average of permeabilities of local filament arrangements (unit cells). They calculated anisotropy ratios (K_{\parallel}/K_{\perp}) of approximately 100, which is close to the ratio $\sqrt{K_x^+}/\sqrt{K_z^+} = 11.4$ for the substrates with which Gómez-de-Segura and García-Mayoral (2019) obtained a drag reduction of 25%. Unfortunately, no extensive validation of this method was performed. A comparison to numerical results obtained via CFD simulations is briefly

made, mentioning that although values differ by a factor two, the trend and order of magnitude are similar (Endruweit et al., 2013). A last important note on most analytical models is the assumption that fibres stay fixed, and that no fluid-fibre interaction takes place. This holds at low Reynolds number when inertial effects do not play a role. For a more extensive numerical model which also includes this mutual interaction, the reader is referred to Nguyen and Indraratna (2016).

B.4. Analytical models for permeability

For 1D fibrous substrates alone, a large number of analytical models have been developed. It is out of the scope of this study to thoroughly present and evaluate all of them. This section aims to give an overview of which models exist, how they have been evaluated previously, and what the main similarities and differences are. There are several publications that describe the historical development of the field (Jackson and James, 1986; Åström et al., 1992; Tomadakis and Robertson, 2005; Tamayol and Bahrami, 2010; Woudberg, 2017). A few review papers have also compared analytical models against numerical and/or experimental results (Jackson and James, 1986; Åström et al., 1992; Zarandi et al., 2019). Jackson and James (1986) mainly covered high porosity ($\epsilon > 0.7$) substrates. Zarandi et al. (2019) performed both numerical simulations and experimental tests into the permeability of substrates with moderate porosity ($\epsilon = 0.4 - 0.5$) and small fibres ($30\mu m$) and compared the results to predictions by several analytical models. They found that the models by der Westhuizen and Du Plessis (1996) (Equation (6.1)) and Brusckke and Advani (1993) (Equation (6.2)) had the most accurate predictions for parallel and transverse permeabilities respectively. Table B.1 presents an overview of the analytical permeability models found in literature.

$$\frac{K_{\parallel}}{D_f^2} = \frac{(5.299 - 2.157\epsilon)\epsilon^2}{192(1 - \epsilon)^2} \quad (\text{B.2})$$

$$\frac{K_{\perp}}{D_f^2} = \frac{1}{3\sqrt{3}} \frac{(1 - l_h^2)^2}{l_h} \left(\frac{3 \tan^{-1}(\sqrt{(1 + l_h)/(1 - l_h)})}{\sqrt{1 - l_h^2}} + \frac{1}{2} l_h^2 + 1 \right)^{-1}, \quad (\text{B.3})$$

where $l_h^2 = \frac{2\sqrt{3}}{\pi}(1 - \epsilon)$.

Nearly all models include dependency of the dimensionless permeability on the fibre volume fraction or porosity. Models that yield other parameters, such as drag coefficients, are often rewritten into a relation such as Equation (B.1). Except for the earliest models, most of them also cover the entire range of fibre volume fraction, from 0.05 to 0.8 (which is the approximate upper limit for different theoretical fibre packing layouts). Not all models are validated in the same way: some are compared against numerical (CFD) results, others against data from literature, and only a few authors actually performed their own experiments to obtain validation data.

Validation of analytical models is challenging because there is a wide spread in experimental results. There are numerous reasons for experimental data scattering: fibre arrangement and misalignment, structure inhomogeneity, fibre mobility and deformation, fibre surface slip, nonviscous flow and inertia effects, tube wall friction, wetting and capillary effects, surface tension, gas compressibility, nonisothermal flow, fibre shape and size distribution, and fibre aspect ratio. Comparison between analytical predictions and experimental results are often made on a logarithmic scale as the permeability spans several orders of magnitude. These plots can be misleading as differences less than an order of magnitude become barely visible. Even the best performing models predict permeabilities that differ a factor 2 compared to experimental or numerical results (Zarandi et al., 2019). The mentioned challenges on model validation could explain why currently no consensus exists on one 'best' analytical permeability model.

Table B.1: Overview of (semi-)analytical permeability models for unidirectional fibrous substrates.

Study	Orientation	Method	Numerical validation	Experimental validation	Discussed in review paper
Kuwabara (1959)	Parallel & transverse	Stokes equation for circular unit cell, zero vorticity at boundary. Randomly arranged fibres.	No	No	Jackson and James (1986), Åström et al. (1992), and Zarandi et al. (2019)
Happel (1959)	Parallel & transverse	Stokes equation for circular unit cell, zero shear stress at boundary.	No	No	Jackson and James (1986) and Åström et al. (1992)
Hasimoto (2006)	Transverse	Fourier series to solve Stokes equation for square array.	No	No	Jackson and James (1986) and Åström et al. (1992)
Sparrow and Loeffler Jr (1959)	Parallel	Square and triangular unit cell, solved Stokes equation by power series technique, requiring zero shear stress at discrete points on boundary.	No	No	Jackson and James (1986) and Åström et al. (1992)
Sangani and Acrivos (1982)	Transverse	Stokes equation for unit cell, least-squares techniques through square and hexagonal arrays.	Yes	No	Jackson and James (1986) and Åström et al. (1992)
Drummond and Tahir (1984)	Parallel & transverse	Distributed singularities to find flow field in square, triangular, hexagonal and rectangular arrays.	No	No	Jackson and James (1986) and Åström et al. (1992)
Gebart (1992)	Parallel & transverse	Simplified and reduced general form of NS-equation, square and hexagonal arrays.	Yes	Unidirectional fabric in experiments in presence of dual-scale effects	Zarandi et al. (2019)
Berdichevsky and Cai (1993)	Parallel & transverse	Self-consistent method where Stokes flow in fiber-sized gap is matched with Darcy flow in surrounding porous medium. Flow and dissipation-energy consistency conditions were applied.	Yes	No	Zarandi et al. (2019)
Bruschke and Advani (1993)	Transverse	Matching of analytic solution using Lubrication approach for low porosities and analytic cell model solution for high porosities.	Yes	No	Zarandi et al. (2019)
der Westhuizen and Du Plessis (1996)	Parallel & transverse	Representative unit cell (RUC) approach. Mathematically related micro-scale surface-integral term of the phase averaged NS-equation and Darcy permeability.	No	Results from literature	Zarandi et al. (2019)
Tomadakis and Robertson (2005)	Parallel & transverse	Permeability calculations based on electrical conduction principles and numerical fitting of tortuosity	No	Results from literature	
Sobera and Kleijn (2006)	Parallel & transverse	Geometric scale analysis method on orderly and disorderly lay-out	Yes	No	
Tamayol and Bahrami (2009)	Parallel & transverse	Unit cell with square and hexagonal arrays, integral technique, parabolic velocity profile	No	Results from literature	
Tamayol and Bahrami (2010)	Parallel	Unit cell with square, hexagonal and staggered arrays, integral technique, solve Poisson for velocity distribution	Yes	Results from literature	
Tamayol and Bahrami (2011)	Transverse	Unit cell with square array, scale analysis, fitted parameter as estimation of tortuosity	No	Gravity-driven tubes-test bed & results from literature	Zarandi et al. (2019)
Shou et al. (2011)	Parallel & transverse	Unit cell, randomness via Voronoi tessalation, slip effect via Knudsen number	No	Results from literature	
Endruweit et al. (2013)	Parallel & transverse	Local fibre arrangements as function of local fibre volume fraction via statistical analysis, these arrangements are input for permeability calculations based on Gebart	No	No	
Woudberg (2017)	Parallel & transverse	Rectangular RUC model approach, similar to Westhuizen & Du Plessis	No	Results from literature	

C

3D-printing prototyping phase

A long prototyping phase preceded the production of the 3D-printed wind tunnel test plate. This was necessary due to the challenging nature of the objective, namely reliably printing porous structures with very small pores (< 1 mm), but with a large total size. This appendix covers the different stages of the prototyping phase in chronological order. The main findings are presented along with supporting results (pictures, scans and dimension measurements). For sake of brevity and readability, not all results are shared.

C.1. Printer comparison: Prusa SL1 vs. Formlabs Form 3

Very small test prints were performed on two printers to assess their capabilities: the Prusa SL1 and the Formlabs Form 3. Printing similar designs showed that the Prusa SL1 was superior in terms of detail (Figure C.1). The prints from the Formlabs Form 3 had clogged small pores. Furthermore, the Prusa SL1 prints faster due to a different working principle, using an LCD-mask on a UV-LED, while the Formlabs Form 3 deploys a travelling laser beam. Lastly, the Prusa SL1 offers more flexibility in print settings (such as exposure time and usable resin) and is cheaper in usage (spare parts and resin). The drawback is that it has a smaller build volume. Based on this preliminary test, the Prusa SL1 was chosen for the remainder of the research.

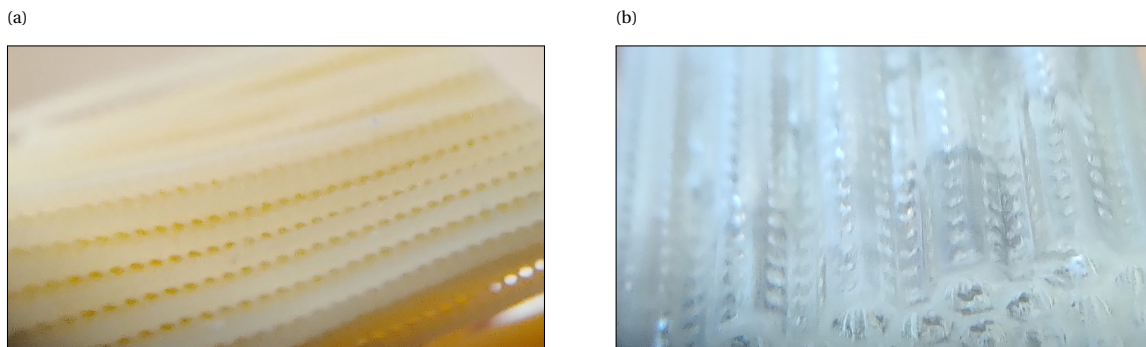


Figure C.1: Comparison of prints for Prusa SL1 (a) and Formlabs Form 3 (b).

C.2. First iteration: hexagon design

The first design was a honeycomb (hexagon), similar to the final design presented in Section 7.1.1, albeit without the solid wall halfway the hexagon and with rectangular (but not necessarily square) pores. Three samples with a hexagon diameter of 1.25 mm and wall thickness of 0.2 mm, but variations of the other design parameters, were printed and characterised in terms of permeability. The parameters and resulting permeabilities are shown in Table C.1. The takeaway was that even at the smallest possible pores (without clogging), this design yielded spanwise and wall-normal permeabilities that were too large.

Table C.1: Design parameters and permeability results of first design iteration. W_p = pore width, L_p = pore height, D_p = pore spacing, all in mm. For all designs, hexagon diameter = 1.25 mm and wall thickness = 0.2 mm. Permeabilities (K_x , K_y & K_z) all in m^2 .

Design	W_p	L_p	D_p	K_x	K_y	K_z	Comments
1-1	0.25	0.25	0.2	1.7×10^{-8}	7.1×10^{-10}	1.9×10^{-9}	
1-2	0.15	0.15	1	-	1.3×10^{-13}	1.6×10^{-12}	Results inconsistent and unreliable
1-3	0.2	0.4	1	-	6.9×10^{-10}	6.5×10^{-10}	
Target				1.5×10^{-9}	1.5×10^{-10}	1.5×10^{-10}	K_x is a minimum, K_y a maximum target

C.3. Second iteration: half-hexagon design

The second design was the half-hexagon design, which was ultimately used for the wind tunnel test plate. This section covers the different stages of the second iteration, on the basis of which the final set of design parameters and print settings was determined (these are shared in Sections 7.1.1 and 7.2.2 respectively).

C.3.1. Small sample parameter sweep

The goal of the small sample parameter sweep was to quickly assess the optimal parameter set (pore size and exposure time) for obtaining the smallest possible reliable pores. Furthermore, a different resin (AmeraLabs AMD-3 LED Black) was benchmarked against the stock resin (Prusa Tough Black). Four different pore sizes (l (μm) \times w (μm) = 100×100 , 150×150 , 200×200 and 150×200) and exposure times (2.5, 3.0, 3.5 and 4.0 seconds) were printed and examined, for three samples (approximately 1 cm \times 1 cm) per design variation. All design variations had a hexagon diameter of 1.25 mm, wall thickness of 0.2 mm and inter-pore distance of 1.0 mm. The main takeaways of this analysis were as follows:

- A minimum exposure time of 4.0 seconds is required. At lower values, the resin does not cure enough and the pores become ellipses, deviating from the design of square pores (Figure C.2).
- The minimum pore width is 200 μm . At lower values, the pores are either completely closed (100×100), or locally closed (150×150) (Figure C.3).
- The measured pore length is very close to the target, but the width is significantly wider. This is true for both the 150×200 and 200×200 designs (Table C.2). A more in-depth pore size analysis is provided in Section 7.3.1.
- No significant improvement was observed when using the AmeraLabs resin compared to the Prusa Tough Black resin, showing that for this design case, the pore size limitation is due to the printer and not the resin.

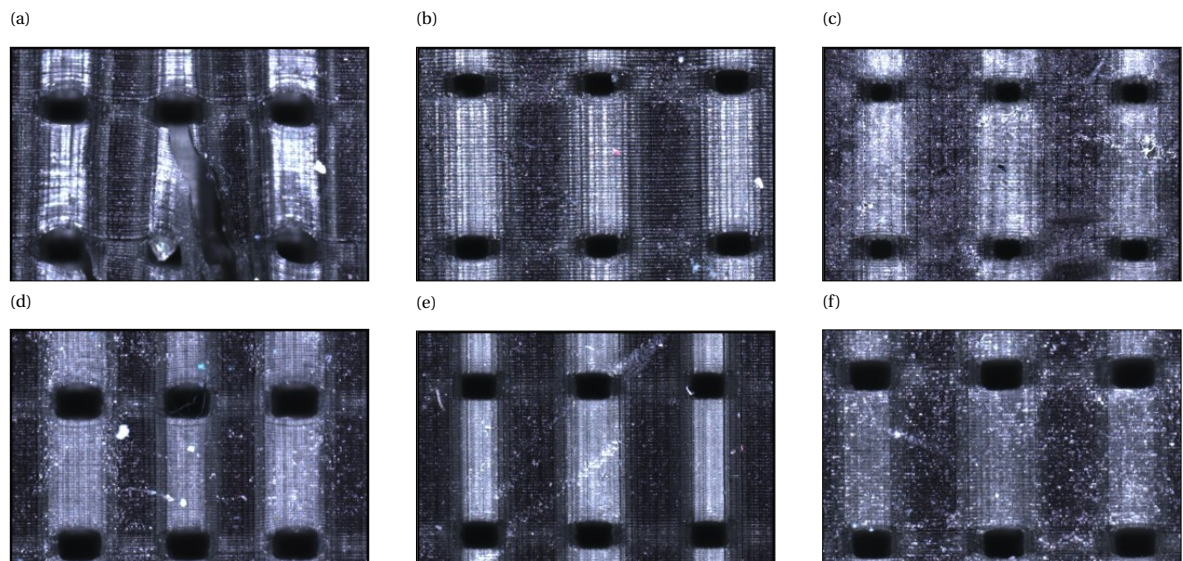


Figure C.2: Microscope scans of small samples for exposure time assessment. Pore sizes of 150×150 (a - c) and 200×200 (d - f) ($\mu m \times \mu m$). Exposure times of 3.0 (a, d), 3.5 (b, e) and 4.0 (c, f) seconds.

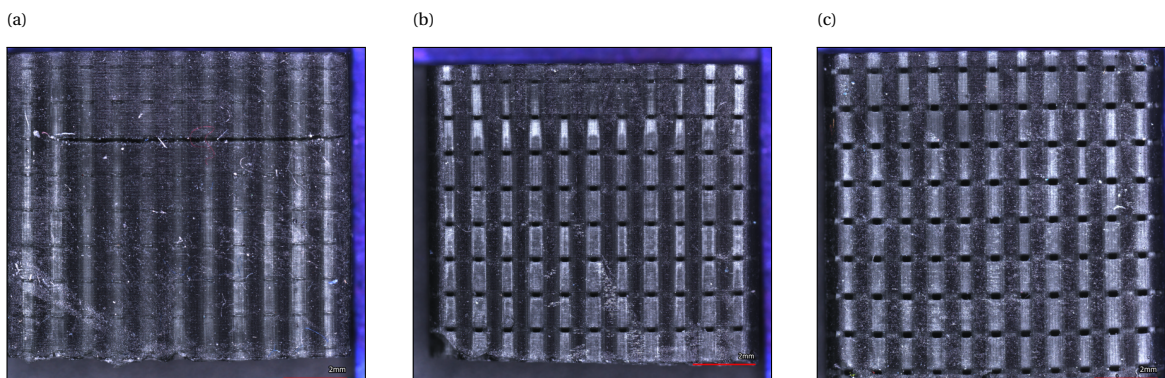


Figure C.3: Microscope scans of small samples for pore quality assessment. Pore sizes of 100×100 (a), 150×150 (b) and 200×200 (c) ($\mu\text{m} \times \mu\text{m}$). Exposure time is 4.0 seconds in all images.

Table C.2: Statistics on dimensions of wall-normal pores. Mean (μ), different w.r.t. target (Δ) and standard deviation (σ). Δ in %, length (L) and width (W) in μm , area (A) in $10^4 \mu\text{m}^2$.

Sample	Data points (#)	μ_L	Δ_L	σ_L	μ_W	Δ_W	σ_W	μ_A	Δ_A	σ_A
150×200	60	152	+1.3	15	272	+36.0	26	4.2	+38.3	0.7
200×200	67	199	+0.5	10	259	+29.5	28	5.2	+29.5	0.7

C.3.2. First full-size wind tunnel test plate parts

Based on the small sample parameter sweep, a few full-size wind tunnel test plate parts were printed (200×200 design). Unfortunately, they were not successful. Prints were assessed qualitatively by holding them against the light and observing the possibility of seeing through the prints. A large portion of pores was clogged at the sides of the parts, printed at the edge of the build plate (see Figure C.4a). It was not caused by bending of the somewhat flexible parts during printing, since adding supports did not solve the issue. Printing parts less wide at the same locations revealed that the issue was related to the location on the build plate (or location w.r.t. print display), and not related to the design or part itself. This was deduced from comparing thin samples printed at the side of the build plate (see Figure C.4b) and in the middle of the build plate (see Figure C.5). Recalibrating and even replacing the print display did not solve the issue either. Hence, it was concluded that the practical smallest achievable pore size for the wind tunnel test plate parts, was not the same as the value found in the small sample parameter sweep.

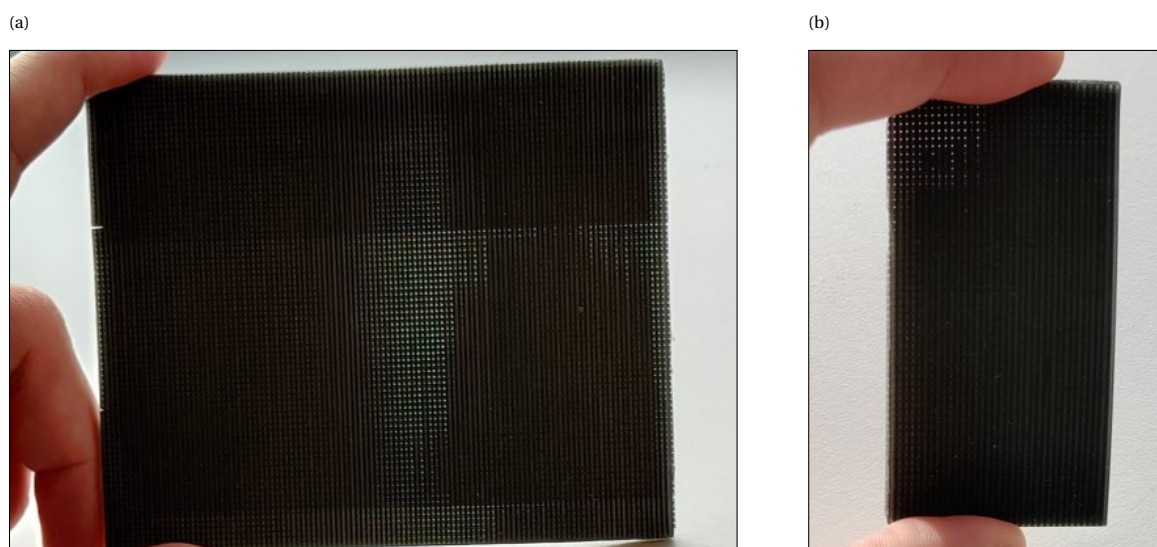


Figure C.4: Partially clogged wind tunnel test plate parts. (a) Full width sample. (b) Thin sample, printed at side of build plate.

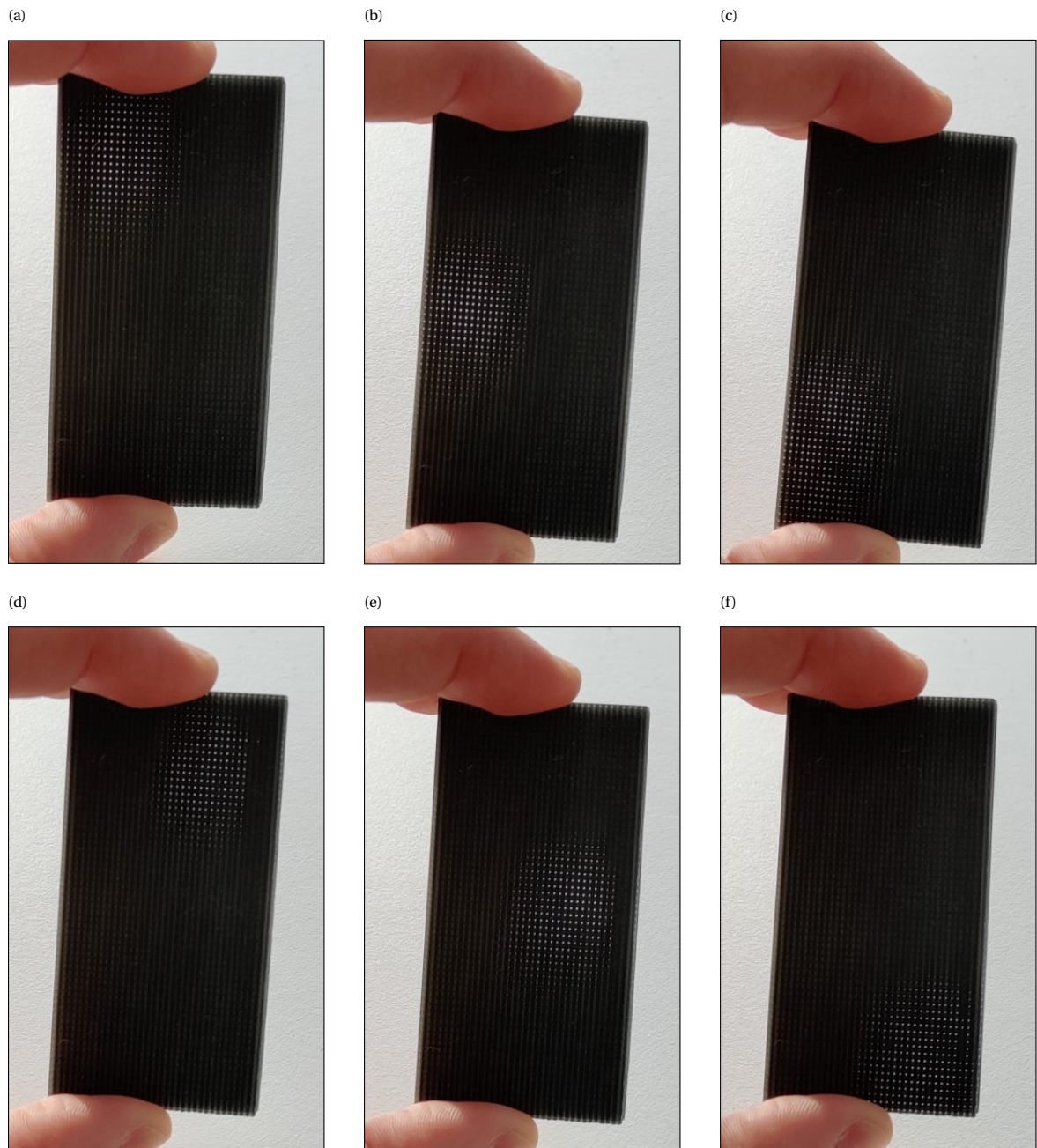


Figure C.5: Non-clogged wind tunnel test plate part. Thin sample. All subfigures are for the same sample, but slightly tilted to let light through different pores

C.3.3. Large sample parameter sweep

After the findings mentioned in Appendix C.3.2, a new parameter sweep was performed using large samples, i.e. wind tunnel test plate parts with the full width, but smaller length (to save time and resin). This was done since the sides of the print were the most challenging regions for obtaining reliable pores. Print reliability was assessed in the same qualitative manner as previously mentioned. All prints were scored in terms of quality on a scale from 1 (extremely poor) to 7 (perfect). Hexagon diameter, wall thickness, pore dimensions, exposure time and anti-aliasing settings (the degree to which the print display partially turns pixels on/off to selectively let light through, see Figure C.6) were varied. All prints had an inter-pore distance of 1.0 mm. The printed samples and assessment are shown in Table C.3. Turning off anti-aliasing decreased the quality in nearly all prints. Based on this assessment, the final design was chosen to be $D_h = 1350$, $t_w = 200$, $l_p = 250$ and $w_p = 250$ (all in μm), printed with anti-aliasing 'on', at an exposure time of 4.0 seconds.

Table C.3: Large sample parameter sweep results. Print quality assessed in terms of degree of clogged pores, rated on a scale from 1 to 7. D_h = hexagon diameter, t_w = wall thickness, l_p = pore length, w_p = pore width (all in μm). Exp. = exposure.

D_h	t_w	l_p	w_p	Exp. time (s)	Anti-aliasing	Score	Comments
1350	250	200	200	3.0	On	3	
1350	250	200	200	4.0	On	1	
1350	250	200	200	3.0	Off	2	Tried twice, same result
1350	200	200	200	3.0	On	5	
1350	200	200	200	4.0	On	2	
1350	200	200	200	3.0	Off	2	
1350	200	250	250	3.0	On	7	Soft
1350	200	250	250	4.0	On	7	Sturdy, best design and print settings
1350	200	250	250	3.0	Off	6	
1450	250	200	200	3.0	On	4	
1450	250	200	200	4.0	On	1	
1450	250	200	200	3.0	Off	2	
1450	250	250	250	3.0	On	5	
1450	250	250	250	4.0	On	4	
1450	250	250	250	3.0	Off	3	
1344	240	200	192	3.0	Off	2	
1450	200	200	200	3.0	On	7	
1450	200	200	200	3.5	On	5	A bit soft
1450	200	200	200	4.0	On	4	
1350	200	225	225	3.0	On	6	
1350	200	225	225	3.5	On	6	A bit soft

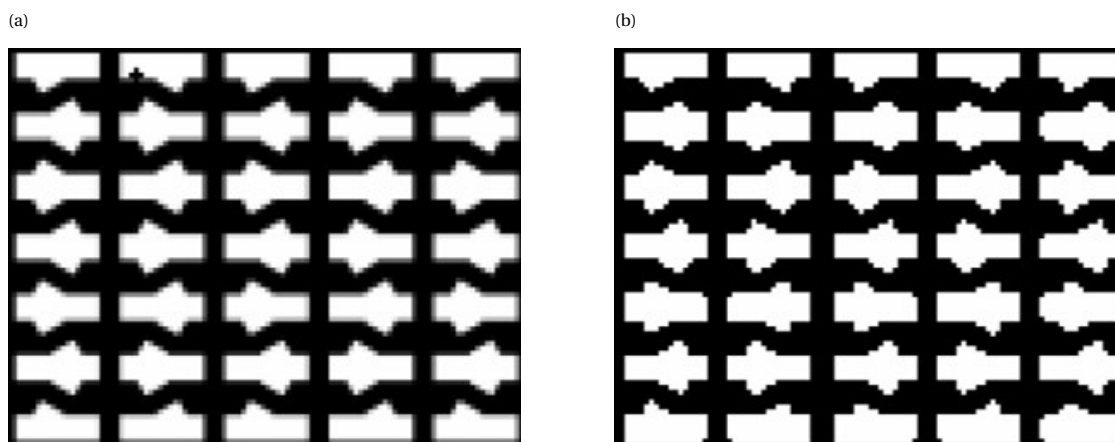
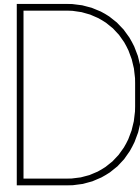


Figure C.6: Anti-aliasing feature of Prusa SL1, turned on (a) and off (b). Images show cross-section of wind tunnel test plate part (stream-wise direction in/out of image plane, wall-normal direction vertical, and spanwise direction horizontal). White indicates where light is let through (i.e. where solid walls are created).

This page has been intentionally left blank.



Permeability characterisation

This appendix serves as support material for the methodology and results sections of the permeability characterisation, discussed in Sections 7.4.1 and 7.4.2 respectively. It shares background information on the experimental technique from literature in Appendix D.1, findings from the preliminary measurements in Appendix D.2 and the final measurement results in Appendix D.3.

D.1. Background information on experimental technique

Permeability characterisation is a topic studied in many fields. This section is limited to literature dealing with porous scaffolds and fibrous substrates. Relevant review papers are written by Pennella et al. (2013) and Sharma and Siginer (2010) for the former and latter substrate category respectively, while ASTM (2014) provides a standard guide for permeability determination of porous scaffolds. Focus is laid on experimental methods, as numerical methods are expected to be relatively straightforward given the knowledge of experimental methods. The reader is encouraged to get acquainted with fluid flow modelling through permeable substrates first and referred to Section 3.1, before continuing with this section.

D.1.1. Assumptions and limitations

For permeability measurements, the fluid should obey Newton's law of viscosity and be chemically inert. The porous material through which the fluid flows should be rigid and stationary. Direct methods can be used to determine the permeability and are based on assumption that the flow rate through a given sample subjected to an applied pressure differential is constant with time. Consequently, there are two measurement approaches: measure the pressure differential across a sample for both increasing and decreasing flow rates, or measure the flow rate across a sample for changing pressure differentials.

From the pressure drop - flow rate measurements, the permeability can be calculated. In general, Darcy flow is assumed and hence the simple Darcy equation can be used. If inertial effects play a role a Forchheimer term can be included, e.g. via the Ergun-Forchheimer equation. More details on performing measurements dealing with inertial effects are given by Innocentini et al. (2000), Innocentini and Pandolfelli (2001), and Chor and Li (2007). Amongst other findings, it was shown that at a pore-size based Reynolds number of $Re_p \approx 8.6$, not using the Forchheimer term would result in a linearity error of approximately 10%. Most literature uses $Re < 1$ as the preferred condition for Darcy flow and $Re < 10$ as an absolute limit for using the Darcy assumption in permeability measurements. This assumption can be checked by plotting differential pressure drop for different flow rates. For Darcy flow, the result should be linear and pass through the origin.

D.1.2. Classification of methods

There are several ways in which permeability measurement setups can be classified: the type of flow (unidirectional (UD) or radial), type of fluid used (gas or liquid), in-plane or out-of-plane measurements, and the type of setup (pump-based or gravity-based). For fibrous substrates, rectilinear (UD) flow has less variability and is a better option than radial flow, which is mostly used for determining the principal permeability direction (Sharma and Siginer, 2010). For porous scaffolds, UD flow measurements are also the conventional method. In pump-based methods, the fluid motion is generated by a pump. The permeability chamber (per-

meameter) holds the test material through which the fluid is pumped at a continuous flow rate. Corrections for the pressure drop measured in an empty chamber should be taken into account. Pump-based methods can be used for both gases (often air) and liquids (often water). In gravity-based methods, gravity draws liquid through the test material in a vertical setup, such as in Figures D.1a and D.1b. Either a constant head or a falling head method can be deployed.

D.1.3. Liquid-based vs. gas-based methods

Working with liquids, especially in gravity-based methods, has a few drawbacks commonly acknowledged (Chor and Li, 2007; Pennella et al., 2013; ASTM, 2014). Firstly, the surface tension of the fluid could block small pores, causing lower permeability readings. Furthermore, a relatively high pressure differential is required to force the liquid through the test material, which can result in a structural deformation. This can be solved by using a lower pressure differential but at the cost of very long testing time intervals. Lastly, in the case materials are hydrophobic, and the test fluid is water, wetting agents such as ethanol have to be added to ensure the entire structure is wetted before performing the measurements.

Gas-based methods have been successfully used for both porous scaffolds (Chor and Li, 2007) (see Figure D.1c) and fibrous substrates (Ding et al., 2003; Scholz et al., 2007). Chor and Li (2007) were able to measure a wide range of permeability values ($4.66 \times 10^{-18} \text{ m}^2 - 2.36 \times 10^{-8} \text{ m}^2$) using two different sets of air pressure regulators and flow meters. Their setup was convenient to use as it typically took less than five seconds to reach a steady flow rate after the pressure regulator was adjusted. They validated their setup using permeability data provided by the manufacturers of the tested materials. Scholz et al. (2007) assessed the effect of gas compressibility on permeability measurements since a non-constant density would yield a non-constant fluid flow rate. If the pressure drop is less than 10 kPa, the deviation between Darcy and modified gas permeability stays below 5%. They furthermore found that fluid and gas permeabilities were comparable with an average difference of 5% across the tested fibre volume range. In the gas flow experiments of Ding et al. (2003), the Reynolds number was found to be in the range of 0.015–0.06, satisfying the assumptions for Darcy flow.

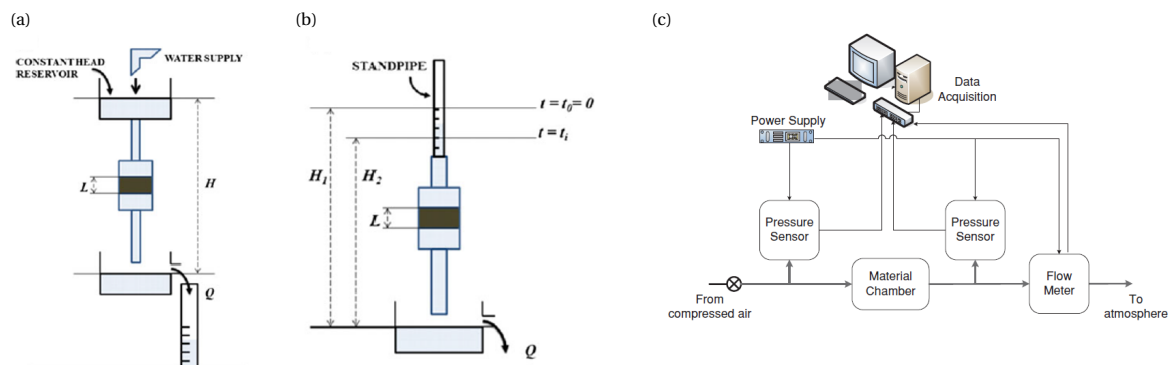


Figure D.1: Schematics of permeability measurement systems. (a, b) Gravity-based permeability measurement systems for liquids (Pennella et al., 2013), specifically constant head (a) and falling head (b). (c) Gas permeability measurement system (Chor and Li, 2007).

D.1.4. Practical tips

Lastly, listed below are a few practical tips on how to conduct good permeability measurements based on findings in literature.

- High accuracy and sensitivity of the used sensors is crucial. Permeability evaluation is based on simultaneous measurement of multiple quantities, namely the flow rate and up- and downstream pressure.
- Allow enough time for the system to reach steady-state after changing the pressure differential or flow rate.
- Perform cyclical measurements, i.e. first increasing the pressure differential, and then progressively decrease it back to the starting point.
- Ensure a ratio between measured sample thickness and mean pore diameter of at least 10, to ensure the obtained Darcy coefficient is representative of the structure as a whole.

- In rectilinear (UD) flow setups, use a flow inlet of the same dimensions as the permeability chamber to have proper one-dimensional flow and boundary conditions.
- Accurately measure the test sample dimensions (thickness and area), as errors in dimensional measurements will influence the calculated permeability.
- Non-linear plots (of pressure differential vs. flow rate) may indicate that the flow does not obey Darcy's law and inertial effects play a role. Forchheimer terms should be used to correct for this.

D.2. Preliminary measurement results

Several preliminary measurements were performed before the final measurements were conducted. These provided several learnings on the effects of using a two-piece sample, sample thickness and measuring at high pressure drops, which are discussed in Appendices D.2.1 to D.2.3 respectively.

D.2.1. Effect of two-piece sample

For material saving, it would be best to have a two-piece permeability sample, where only the inner, circular ring has to be replaced (see Figures D.2a and D.2b). Unfortunately, due to deformation of the inner piece during printing, no proper sealing between the two pieces could be ensured. This resulted in leakage and hence a lower measured pressure drop across the sample as visible in Figure D.2c. Based on this preliminary test, it was concluded that samples should be made out of one piece.

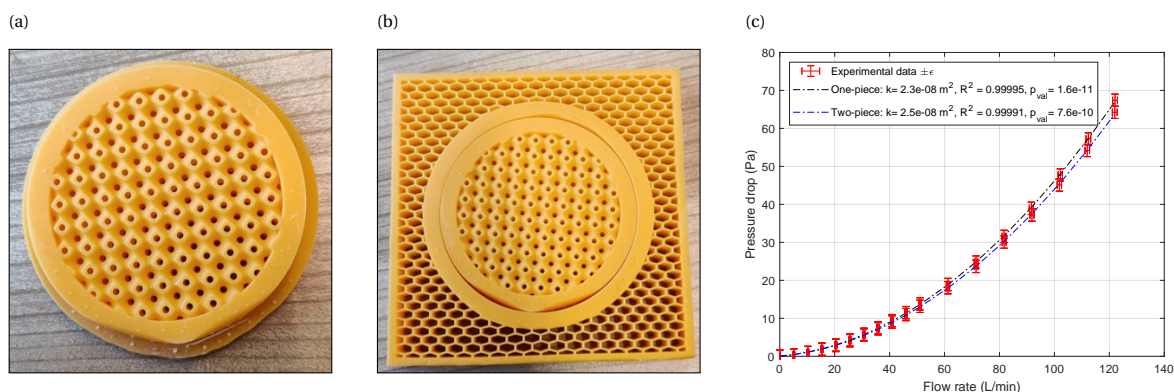


Figure D.2: Two-piece permeability sample (a, b) and pressure drop compared to one-piece sample (c).

D.2.2. Thickness effect

Measuring two samples of the same design but with different thicknesses, yields the same permeability if the fitting is independent of sample thickness (i.e. permeability is an intrinsic property of the permeable structure design). This requires measurement samples with a thickness such that there are enough repeating unit cells in the sample thickness direction. In Section 7.4.2 it was shown that the permeability values were independent of sample thickness for samples of approximately 10 & 12.5 mm. For thinner samples, the fitting is not independent of thickness. See Figure D.3 for measurements of two z -permeability samples with identical designs, but different thicknesses of 7.1 & 10.9 mm respectively. Although it is expected that the thicker sample results in a higher pressure drop at similar flow rates, the fitted Forchheimer equation (Equation (3.4)) should yield the same permeability as it accounts for sample thickness. Nevertheless, the extracted permeability is approximately 2 to 2.5 times lower for the thicker sample. It could be that the thick sample is more clogged internally, reducing its permeability. However, no resin leaked out during testing, and through visual inspection it was confirmed that one could see through the sample sufficiently. Hence it was concluded that with samples of 7.1 mm thickness, there were not enough repeating unit cells in the sample thickness direction for a reliable permeability estimate.

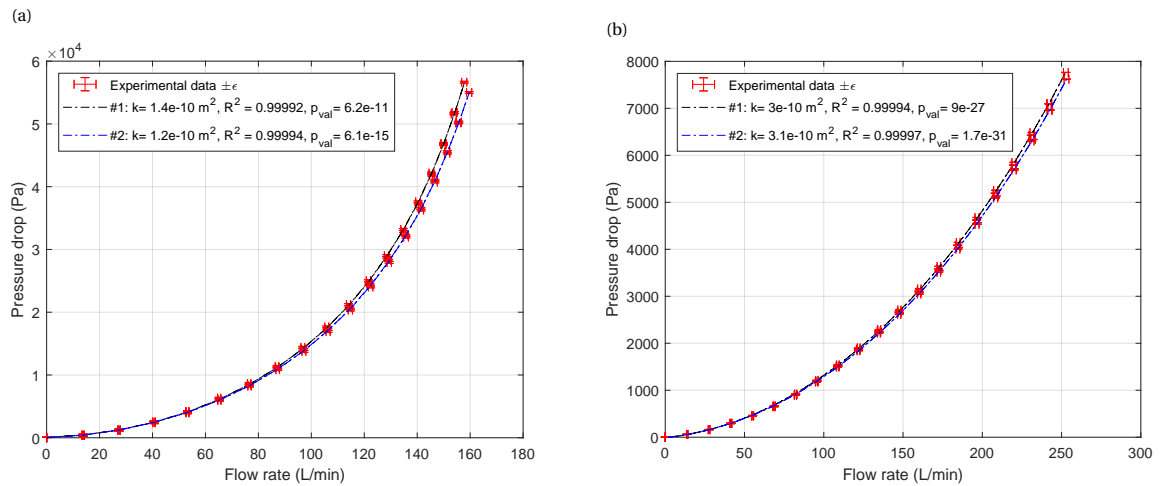


Figure D.3: Occurrence of thickness effect in permeability characterisation. z -permeability of design in 3D-printing prototyping phase. (a) Thin sample: 7.1 mm. (b) Thick sample: 10.9 mm. All samples are measured twice (yielding two separate fits per graph).

D.2.3. High pressure drop effect

Preliminary measurements showed that for certain samples, higher flow rates (and thus higher pressure drops) yielded inconsistent and sometimes non-physical (negative) permeability values. Overall, the setup and data fitting are capable of dealing with high flow rates. It was validated using data from Rubio Carpio et al. (2019), who measured up until the maximum flow rate, giving a maximum pressure drop of approximately 2 kPa. Also, measuring at very high pressure drops ($O(10\text{kPa})$) yields high quality fits and physical (positive) values for the z -permeability (Figure D.3b). However, for the y -permeability samples, measuring at high flow rates and pressure drops yields non-physical (negative) permeability values (Figure D.4). It could be that the sample is not rigid enough and slightly compresses at higher pressure drops. Consequently, in the final measurements, the flow rate was set at 30% of the maximum achievable value, such that pressure drops were generally below 2 kPa.

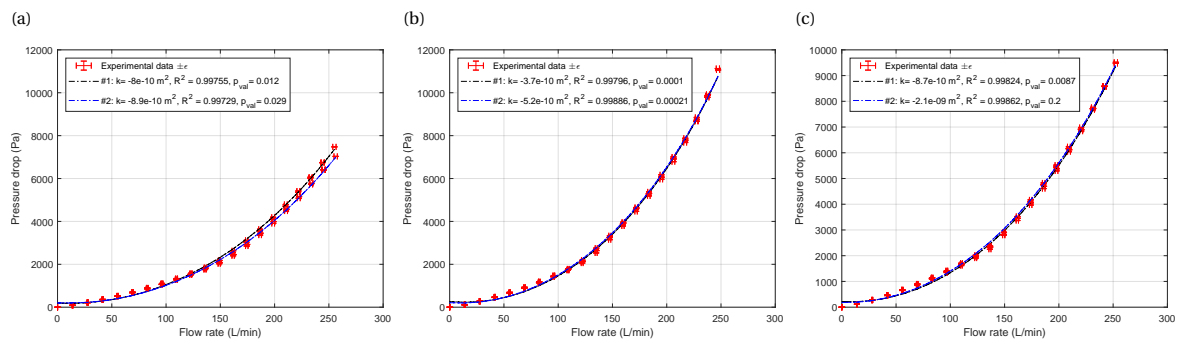


Figure D.4: Negative y -permeability at high pressure drops. Thin (10.7 mm) samples (a) #1 and (b) #2. (c) Thick (13.1 mm) sample. All samples are measured twice (yielding two separate fits per graph).

D.3. Final measurement results

Figure D.5 shows all the results of the final measurements, of which the permeabilities are summarised in Table 7.5.

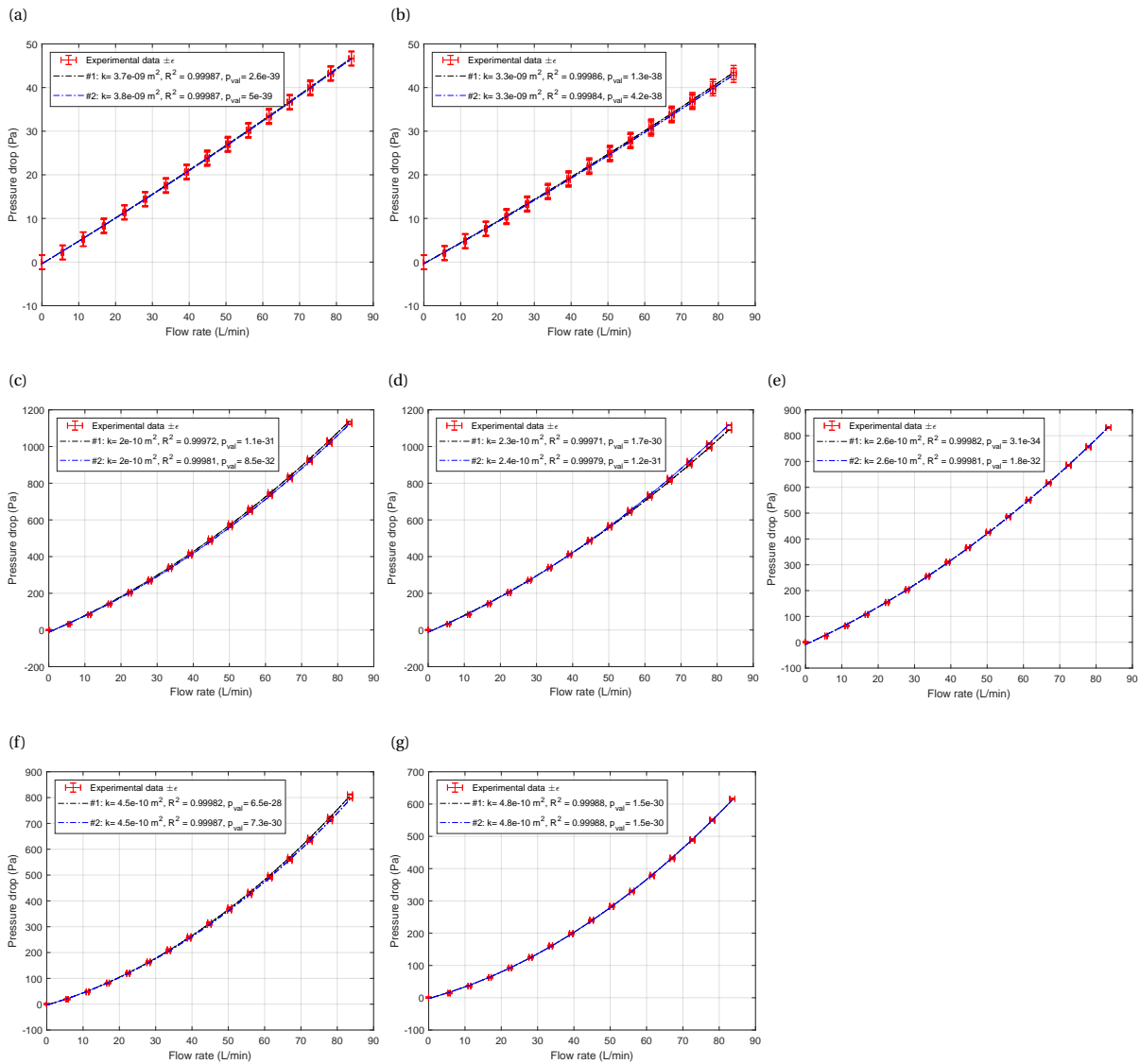
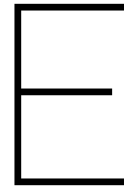


Figure D.5: Complete results for final permeability measurements. (a, b) x -permeability samples, with 10 (a) and 12.5 mm (b) thickness. (c, d, e) y -permeability samples, with 10.7 (c, d) and 13.1 mm (e) thickness. (f, g) z -permeability samples, with 9.7 (f) and 11.7 mm (g) thickness. All samples are measured twice (yielding two separate fits per graph).

This page has been intentionally left blank.



Taylor-Couette flow measurements with seal fur

This appendix shares the results of the drag measurements with the harbour seal fur in the Taylor-Couette flow setup. They were conducted and further analysed by Bastiaan Koot, an intern and prospective Master thesis student at Dimple Aerospace B.V., in collaboration with the Fluid Mechanics section from the Laboratory for Aero & Hydrodynamics (part of the Process & Energy department, 3ME faculty, TU Delft). The reader is referred to Greidanus et al. (2015) for a description of the experimental methodology.

Figure E.1 shows that the flat reference cylinder has a slightly higher drag than the data from literature. This is due to drift in the experimental setup that occurs over time. Decreasing the gap in the setup (by adding the 2 mm flat coating) results in a decrease of the drag, such that the data with 2 mm flat coating overlaps with the original reference data. Comparing the harbour seal fur to the reference cylinder (Figure E.2) shows a significant increase in friction coefficient, which grows with increasing Re . The increase is much larger if the flow is opposite to the preferred direction of the seal fur. Note that for this orientation, the drag increase reaches a maximum after which it slightly decreases again with increasing Re . It is thought that at this point, the fluid momentum is high enough to completely fold the hairs in the fur backwards, decreasing the drag compared to when they stand up nearly straight. Although the setup is different from the one used by Itoh et al. (2006), the difference in measured drag difference is remarkable. It will be further investigated in Bastiaan Koot in his Master thesis.

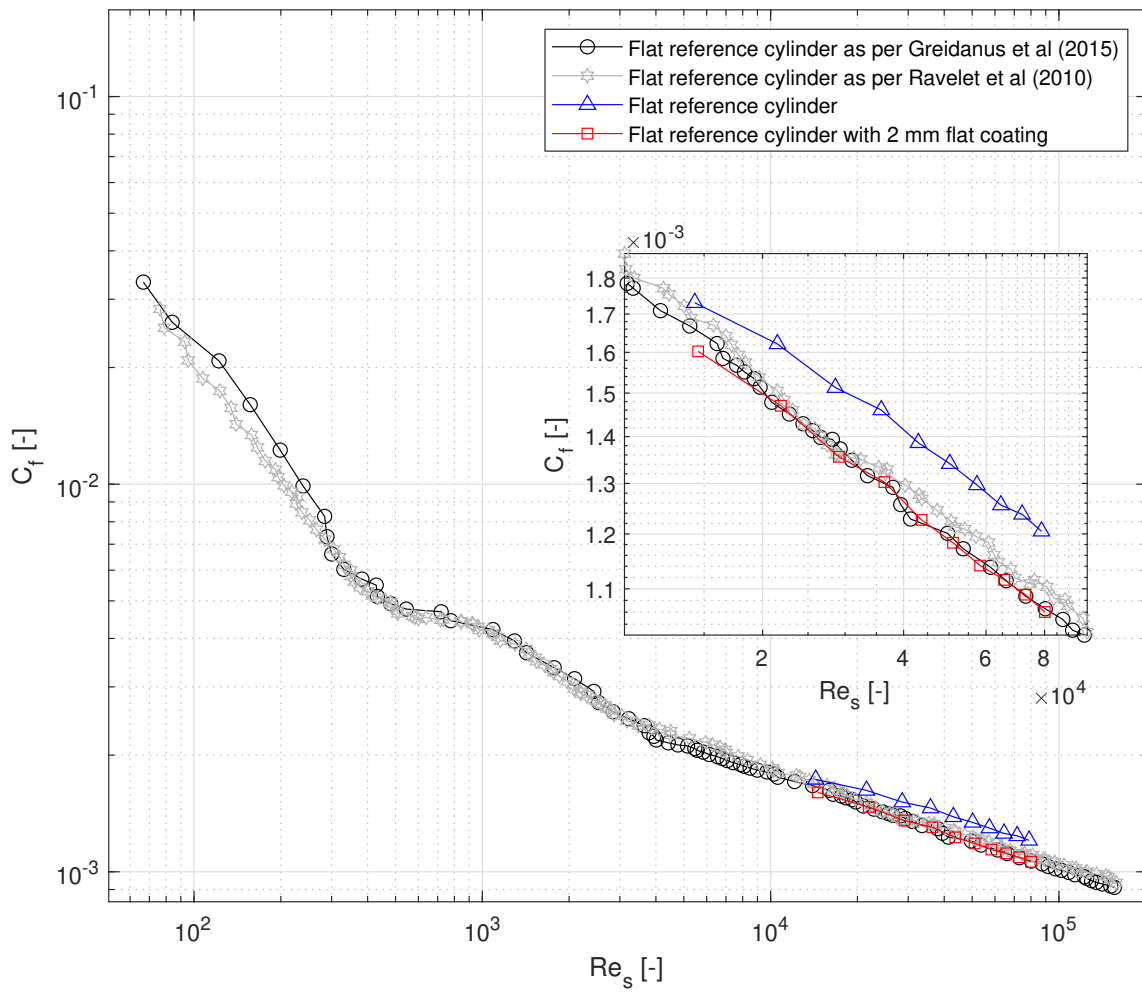


Figure E.1: Friction coefficient for reference cylinder in Taylor-Couette flow setup. Re_s = shear Reynolds number. Image by courtesy of Bastiaan Koot.

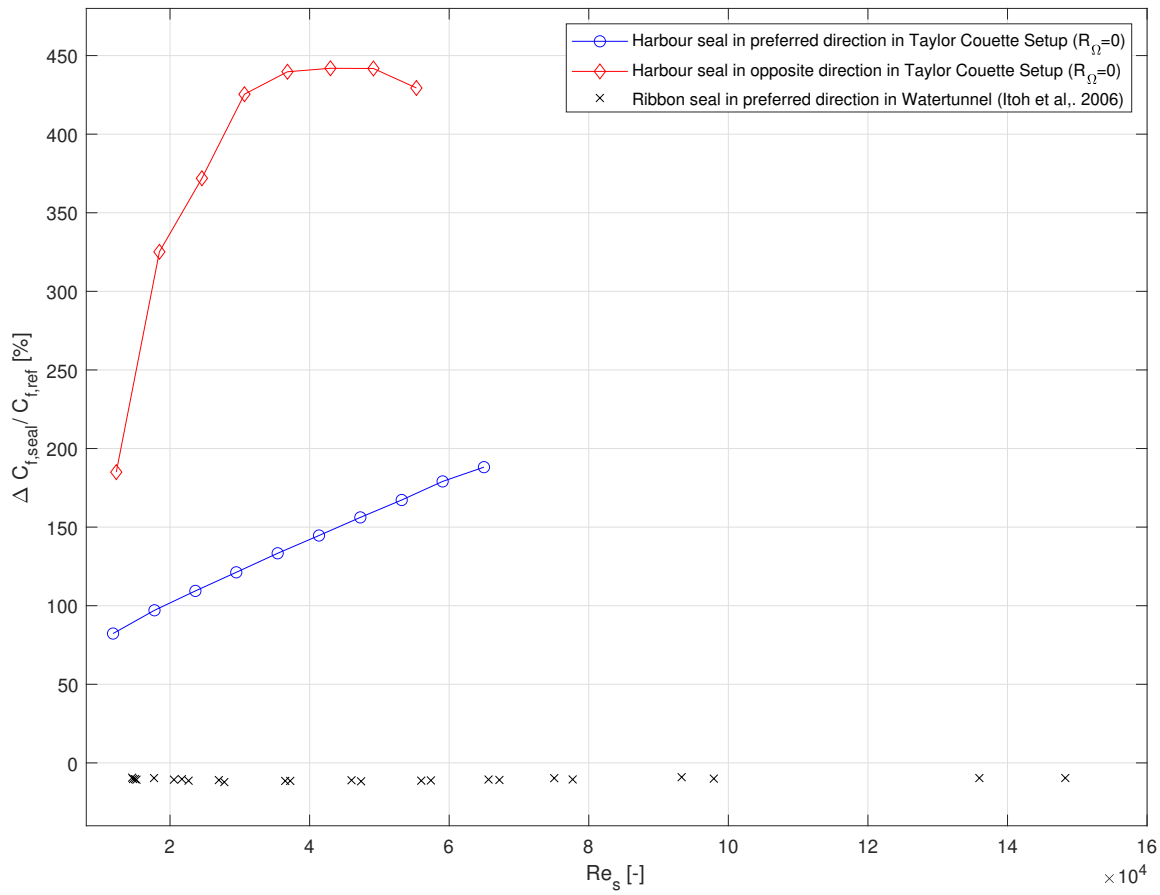
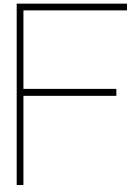


Figure E.2: Drag difference for seal fur compared to smooth reference cylinder in Taylor-Couette flow setup. Image by courtesy of Bastiaan Koot.

This page has been intentionally left blank.



Pressure probe measurements

Pressure probe measurements were performed to obtain an indication of the flow velocity within the continuous fibre plate. The results serve as supporting material for the discussion on the increase in C_D observed in the direct force measurements, as presented in Section 10.4.3.

F.1. Methodology

Measurements were performed with a traversable pressure probe guided through the top wall of the auxiliary test section of the M-tunnel, as shown in Figure F.1. The probe was connected to a Mensor DPG-2400, which measured the pressure differential between the probe (total pressure) and ambient (absolute pressure) at a rate of 10 Hz. This difference was used as an estimate for the dynamic pressure and hence flow velocity, since the pressure probe did not allow for measuring the local static pressure. The pressure probe was traversed to the solid bottom of the mould in which the fibres were laid, i.e. the starting position of the measurement. Measurement points were spaced at 0.1 mm until a wall-normal displacement of 7.0 mm, and steps of 1.0 mm between 7.0 mm and 30.0 mm. Hydrostatic effects were negligible ($dp = \rho g dz \approx 0.36$ Pa). An individual measurement took 5 seconds, yielding a signal of 50 data points of which the mean value was taken. Measurements were performed for the continuous fibre plate and an empty reference mould. Figure F.2 shows the locations on the plate at which measurements were taken.

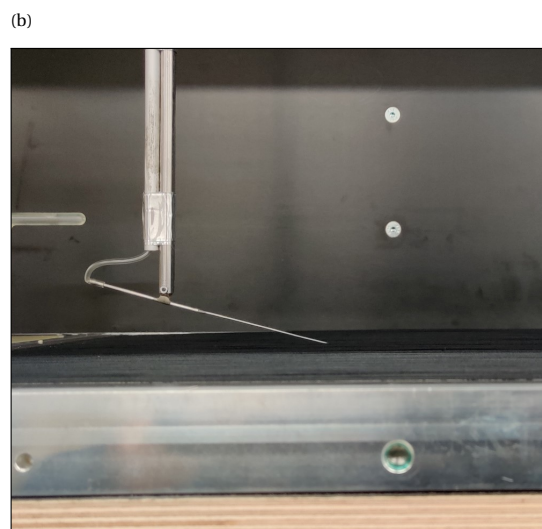


Figure F.1: Setup for pressure probe measurements. (a) Top view including traverse. (b) Side view, pressure probe and tubing above fibre test plate.

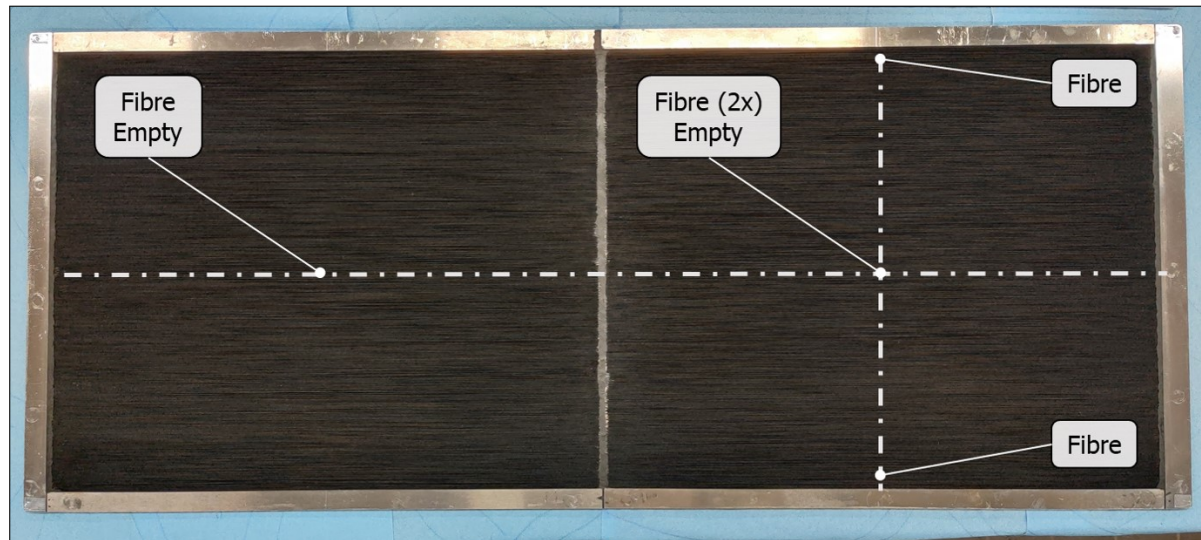


Figure E2: Pressure probe measurement locations. Flow from right to left.

E.2. Results

Figure E3 show the results of the pressure probe measurements. The fibre sheet edge is indicated, since it bulged at the measured locations as discussed in Section 6.3. The main observations are as follows:

- The flow velocity near the bottom of the mould in the continuous fibre substrate is very low. Compared to the empty mould, the flow experiencing the forward-facing steps halfway and at the TE of the mould, will carry less momentum and thus exert a lower pressure force on the test plate.
- The flow velocity in the top region of the continuous fibre substrate is significant and penetrates until it reaches approximately a depth that is flush with the WT wall. This likely causes significant extra friction drag, due to the increased wetted surface area of the fibres.
- The velocity profiles at the back-mid locations are less 'full' than at the front-mid locations for both test plates. This indicates that the step (solid strip halfway) in both plates causes an extra loss of momentum.
- The 'slip velocity' at the fibre sheet edge is between 7.6 and 8.7 m/s. Taking into account the uncertainty in the fibre sheet edge (± 0.25 mm) gives a range of 6.1 – 9.4 m/s. Based on an estimated streamwise permeability of 7.3×10^{-9} m² (Section 6.3), viscous length scale of 11 μ m and friction velocity of 1.3 m/s (Section 4.1), the theoretical slip velocity would be approximately 9.8 m/s, and theoretical penetration depth approximately 86 μ m. While the former is close to the observed values, the latter is clearly far off from how deep a significant flow velocity can be found.

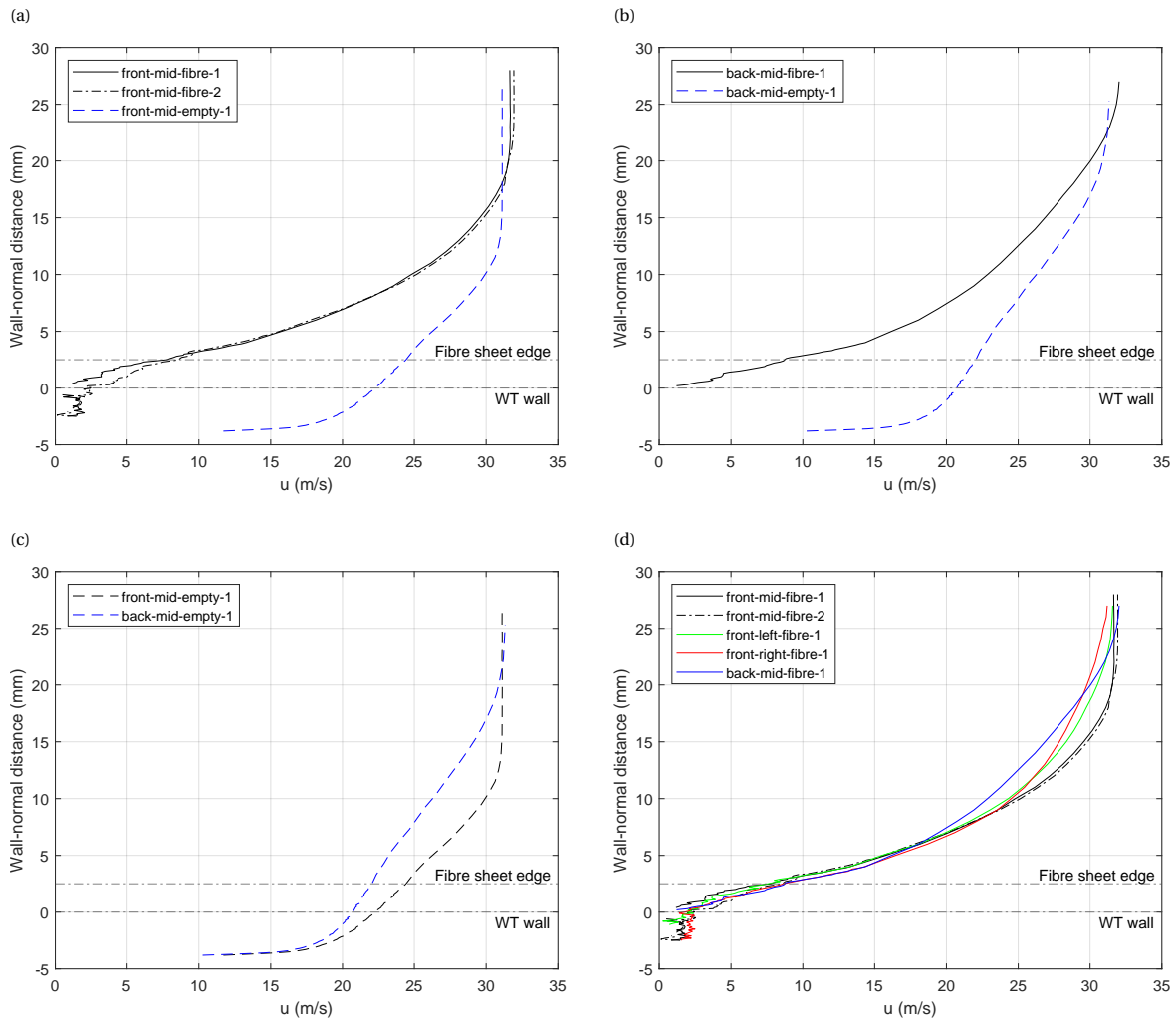


Figure E3: Results of pressure probe measurements, sorted by location (a, b) and test plate (c, d). (a) Mid-front. (b) Mid-back. (c) Empty mould. (d) Continuous fibre plate.

This page has been intentionally left blank.



PIV cross-correlation benchmark test

This appendix shows the results of the PIV cross-correlation benchmark test. It was done to settle on appropriate interrogation window settings, balancing achievable detail and data quality (low noise). The settings ultimately used in this research correspond to case a of Table G.1. Figure G.1 shows example images of instantaneous velocity magnitude fields for all thirteen different cases. Larger window sizes lead to less detail, but using window sizes that are too small leads to images that suffer from noise, i.e. the images are too grainy.

Table G.1: Overview of interrogation window settings in cross-correlation benchmark test. Cases correspond to subfigures in Figure G.1.

Case	Initial pass			Final passes		
	Size (px × px)	Shape	Overlap (%)	Size (px × px)	Shape	Overlap (%)
a	96 × 96	elliptical, 2:1	75	16 × 16	elliptical, 2:1	75
b	96 × 96	elliptical, 2:1	75	16 × 16	elliptical, 4:1	75
c	96 × 96	elliptical, 2:1	75	24 × 24	elliptical, 2:1	75
d	96 × 96	elliptical, 2:1	75	24 × 24	elliptical, 4:1	75
e	96 × 96	elliptical, 2:1	75	12 × 12	elliptical, 2:1	75
f	96 × 96	elliptical, 2:1	75	12 × 12	elliptical, 4:1	75
g	96 × 96	elliptical, 2:1	75	8 × 8	elliptical, 2:1	75
h	96 × 96	elliptical, 2:1	75	8 × 8	elliptical, 4:1	75
i	96 × 96	square, 1:1	50	16 × 16	elliptical, 2:1	75
j	96 × 96	circular, 1:1	50	16 × 16	elliptical, 2:1	75
k	64 × 64	elliptical, 2:1	75	16 × 16	elliptical, 2:1	75
l	64 × 64	square, 1:1	50	16 × 16	elliptical, 2:1	75
m	64 × 64	circular, 1:1	50	16 × 16	elliptical, 2:1	75

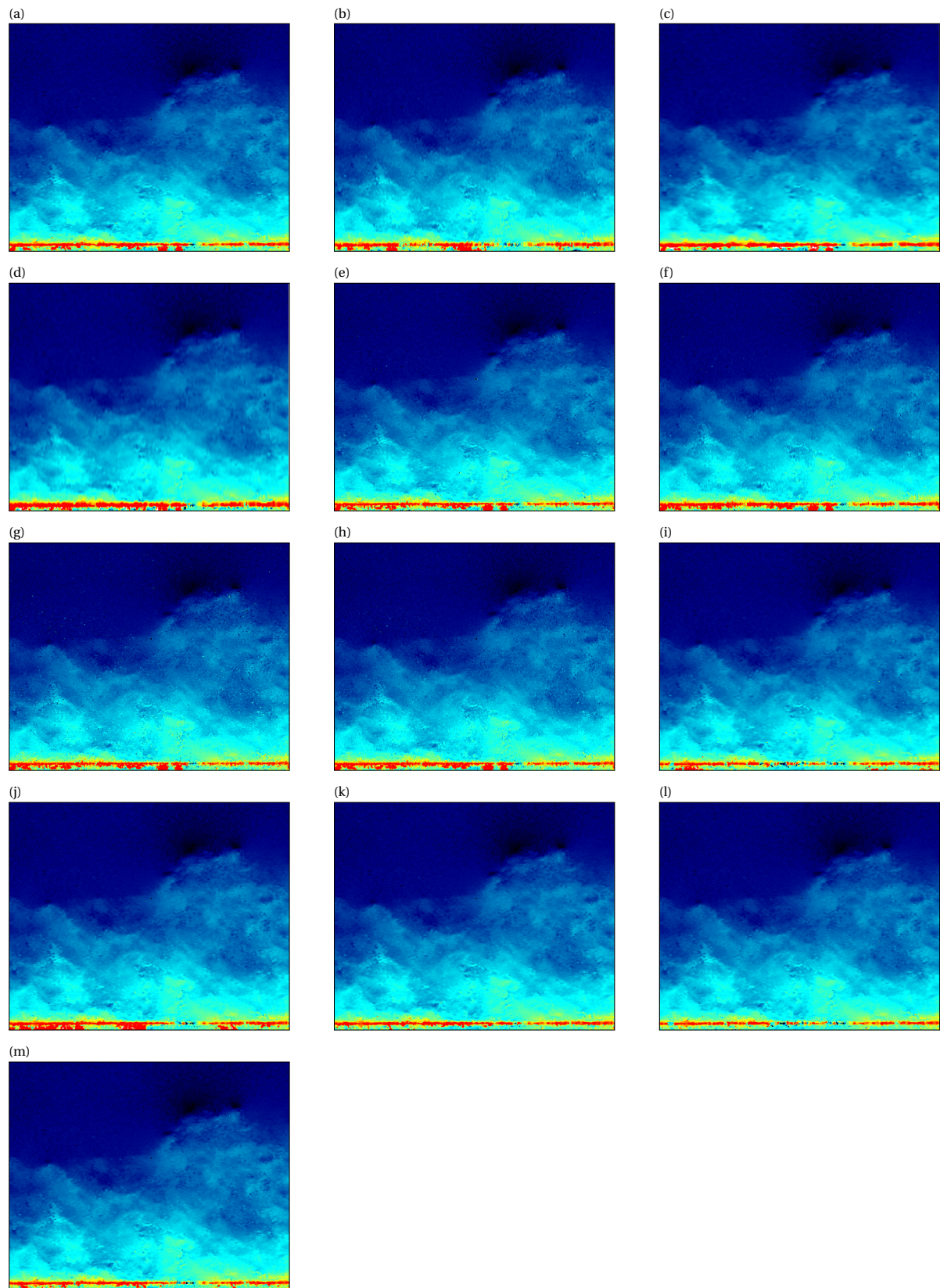
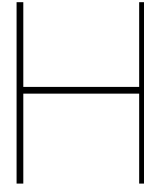


Figure G.1: Instantaneous velocity magnitude fields for the cross-correlation benchmark test. Subfigures (a - m) correspond to the cases as presented in Table G.1.



PIV data processing routine

This appendix covers two components of the PIV data processing routine in more detail: the wall estimation and BL profile correction in Appendix H.1 and the friction velocity estimation in Appendix H.2.

H.1. Wall estimation and BL profile correction

Having an accurate estimate of the wall location is important for reliable BL profiles. Typically the wall is not captured perfectly horizontally in the raw PIV images. A difference in y_{wall} at the beginning and end of the FOV (in streamwise direction) as small as 0.1 mm ($\approx 8\delta_\nu$ at $U_\infty = 30$ m/s) can cause significant issues with spatially averaging velocity profiles along the streamwise direction. As such, estimating the wall should be done along the streamwise direction of the entire FOV.

Figure H.1 visualises the wall estimation procedure. It consists of two main steps. First, the y -coordinate corresponding to the point of minimum mean velocity is determined for every streamwise coordinate (x). Figure H.1a shows this for two different x . The minimum point is found on a curve fitted to the experimental data points, allowing for estimating the wall location with a higher resolution than the vector pitch. To ensure robustness, searching the minimum point is only done within a "slice", i.e. a region bounded in y based on optical estimation of the wall region in DaVis. The resulting raw wall estimate profile is then smoothed (Figure H.1b), by first applying a double sliding median filter (window = 5% of image width, removing outliers > 3 times the mean residual (raw minus median)), and subsequently fitting a third-degree polynomial (cubic fit) to the sliding median profile.

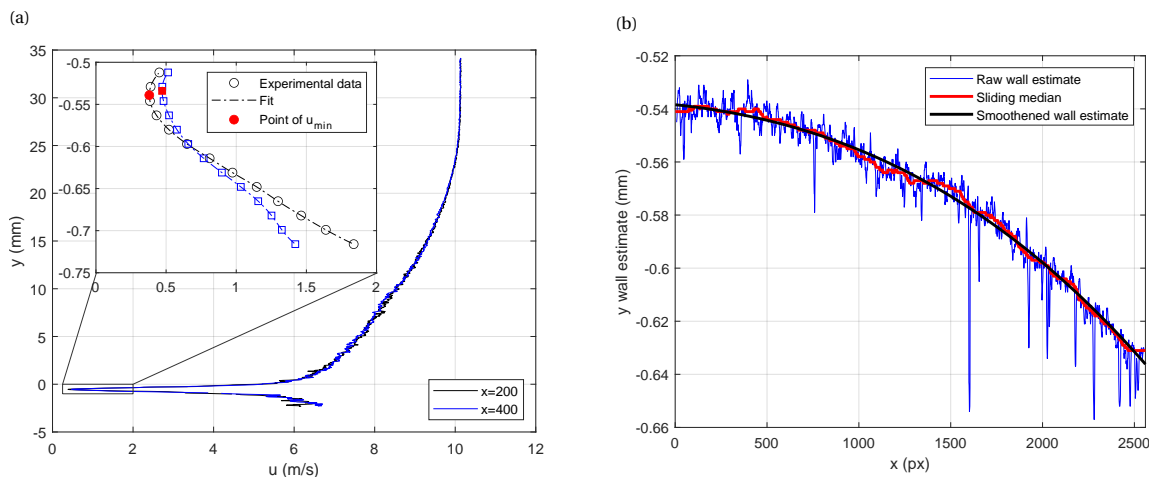


Figure H.1: Visualisation of wall estimation procedure. (a) Velocity profiles for two streamwise locations (in px) in FOV. (b) Wall estimate along streamwise direction in FOV.

With the smoothed wall estimate, the BL profiles can be corrected before performing spatial averaging. For every x -coordinate in the FOV, the BL profiles are shifted using the corresponding $y_{wall}(x)$ estimate, projecting it onto a new y -vector (starting at $y = 0$ and with the same vector pitch as the original data) using spline interpolation. Figure H.2 confirms that this step is especially important near the wall, where the velocity gradient is largest. The raw data shows an increasing u for constant y (in the image, expressed in px) and increasing x . This is because the wall gets slightly lower in the image for increasing x , and as such the local wall-normal distance and thus u increases with increasing x . Correcting using $y_{wall}(x)$ yields a constant u (including noise, which provides an argument for performing spatial averaging).

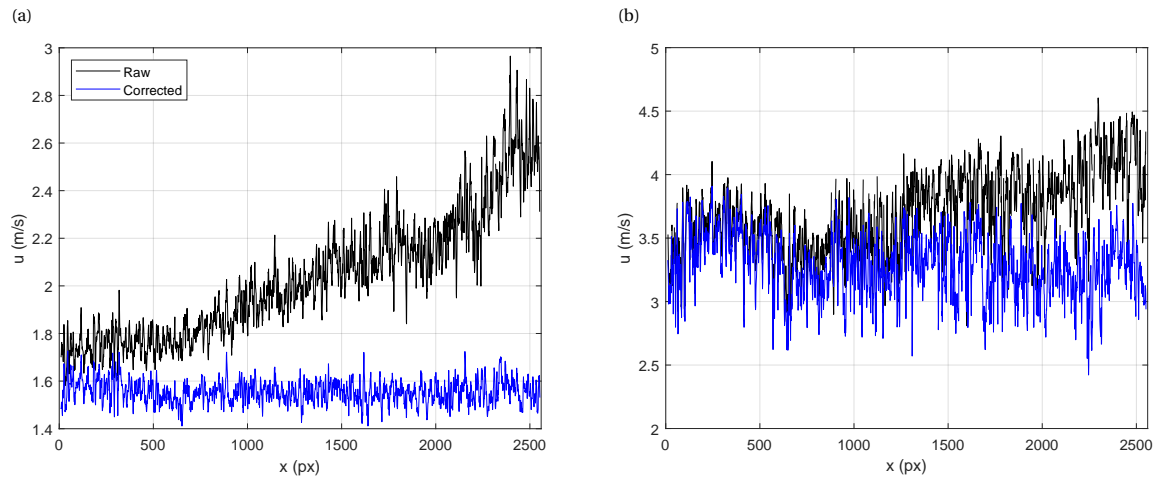


Figure H.2: Effect of BL profile correction using smoothed wall estimate along streamwise direction in FOV for (a) 10 px and (b) 20 px wall-normal distance from point of minimum velocity.

H.2. Friction velocity estimation

Different methods for estimating u_τ were tested. This section covers the assessment of these methods. First, the different methods will be discussed in detail in Appendix H.2.1. Then, a comparison between the methods will be shown in Appendix H.2.2

H.2.1. Assessment of individual methods

Four different methods were used for estimating u_τ : a direct linear fit in the viscous sublayer, Clauser's indirect method on the overlap layer, Spalding's Law of the Wall on the inner layer, and a composite profile on the outer layer, adjusted from Rodríguez-López et al. (2015). The methods will be discussed in this order using PIV data of the reference smooth plate recorded at the TE location (Station 4), with regular zoom at 10 m/s and 30 m/s (see Section 11.1 for more details on the measurements).

Linear fit in viscous sublayer

The friction velocity per definition is directly related to the slope of the velocity profile at the wall via Equations (2.9) and (2.20):

$$u_\tau = \sqrt{\nu \left. \frac{du}{dy} \right|_{y=0}}. \quad (\text{H.1})$$

The velocity profile in the viscous sublayer, strictly speaking $y^+ < 5$, is linear, hence the slope is constant. Consequently, it is possible to directly extract u_τ by determining the slope of the velocity profile in the near-wall region.

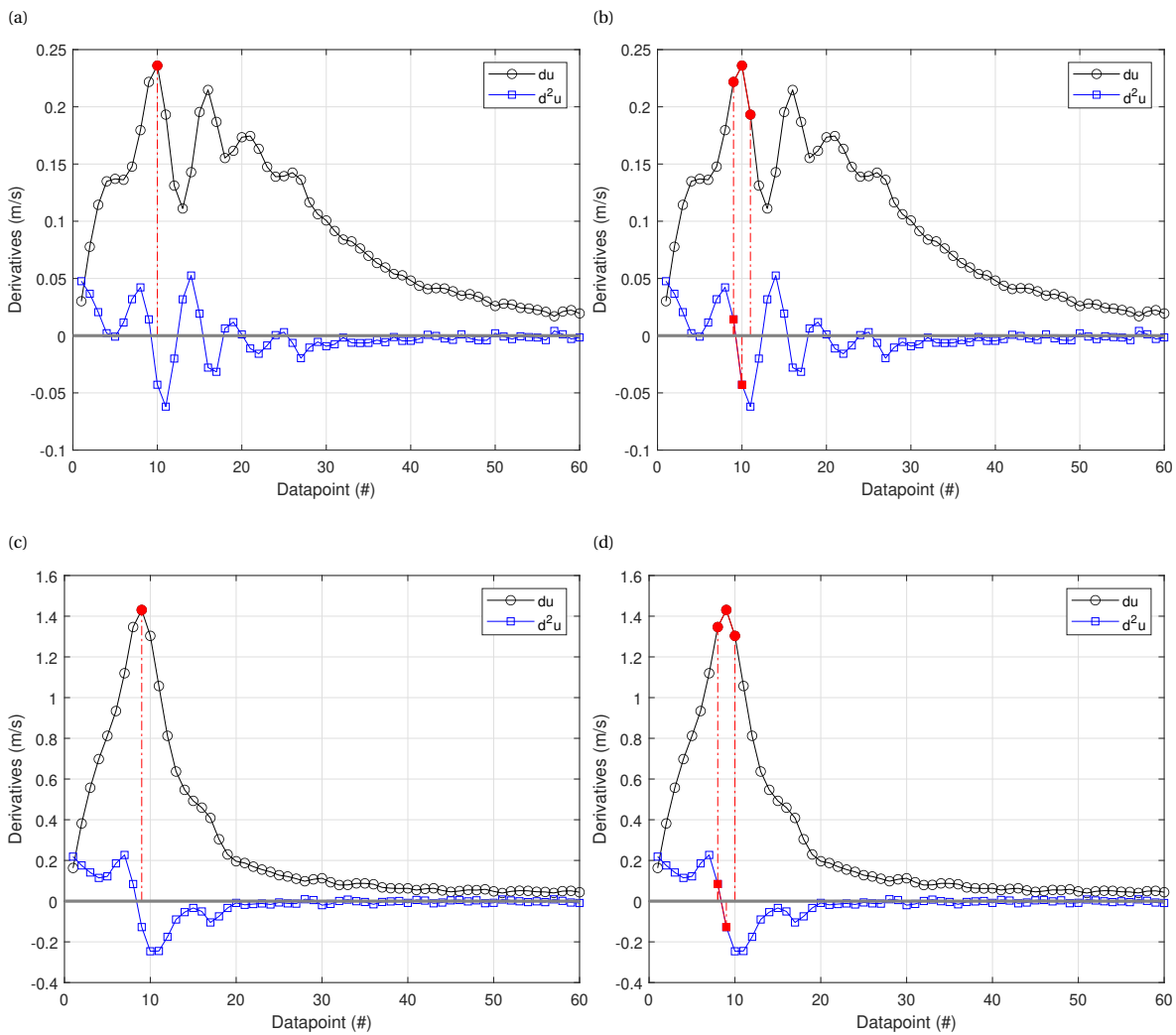


Figure H.3: Velocity profile first and second unit derivatives. (a, b) 10 m/s. (c, d) 30 m/s. (a, c) Fitting on two data points. (b, d) Fitting on four data points.

Figure H.3 shows the first and second unity derivatives of the velocity profile near the wall. The first few data points show an increase in the derivative, corresponding to the biased profile near the wall as explained in Section 12.1.2. Then, a peak occurs, which is broader for lower velocities (Figures H.3a and H.3b) than for higher velocities (Figures H.3c and H.3d). This is because the viscous sublayer is longer for lower velocities, when expressed in physical units and hence data points. Consequently, the slope of the velocity profile in the viscous sublayer as taken from the biased experimental data will be approximately constant for more data points. Furthermore, for the lower velocity, an oscillatory pattern can be observed in the peak region. It is thought that this has a numerical origin, most likely because the SOC output from DaVis has not completely converged.

Strictly speaking, fitting a linear profile in the viscous sublayer yields valid estimates of u_τ if at least two subsequent data points, including the heights over which averaging has occurred, lie in the viscous sublayer. This presents the case for using only two data points, for which the slope is highest, when performing the linear fit. This is especially true at higher velocities, where chances are higher that the slope as extracted from the experimental data is more biased due to the averaging effects. However, for lower velocities, taking into consideration the observed oscillatory pattern, the peak in the slope might be a numerical overshoot. Hence taking a few data points around this peak could provide a more reliable estimate, especially with the knowledge that the viscous sublayer can include more data points at lower velocities. Figure H.4 shows the linear fits for the different cases discussed here.

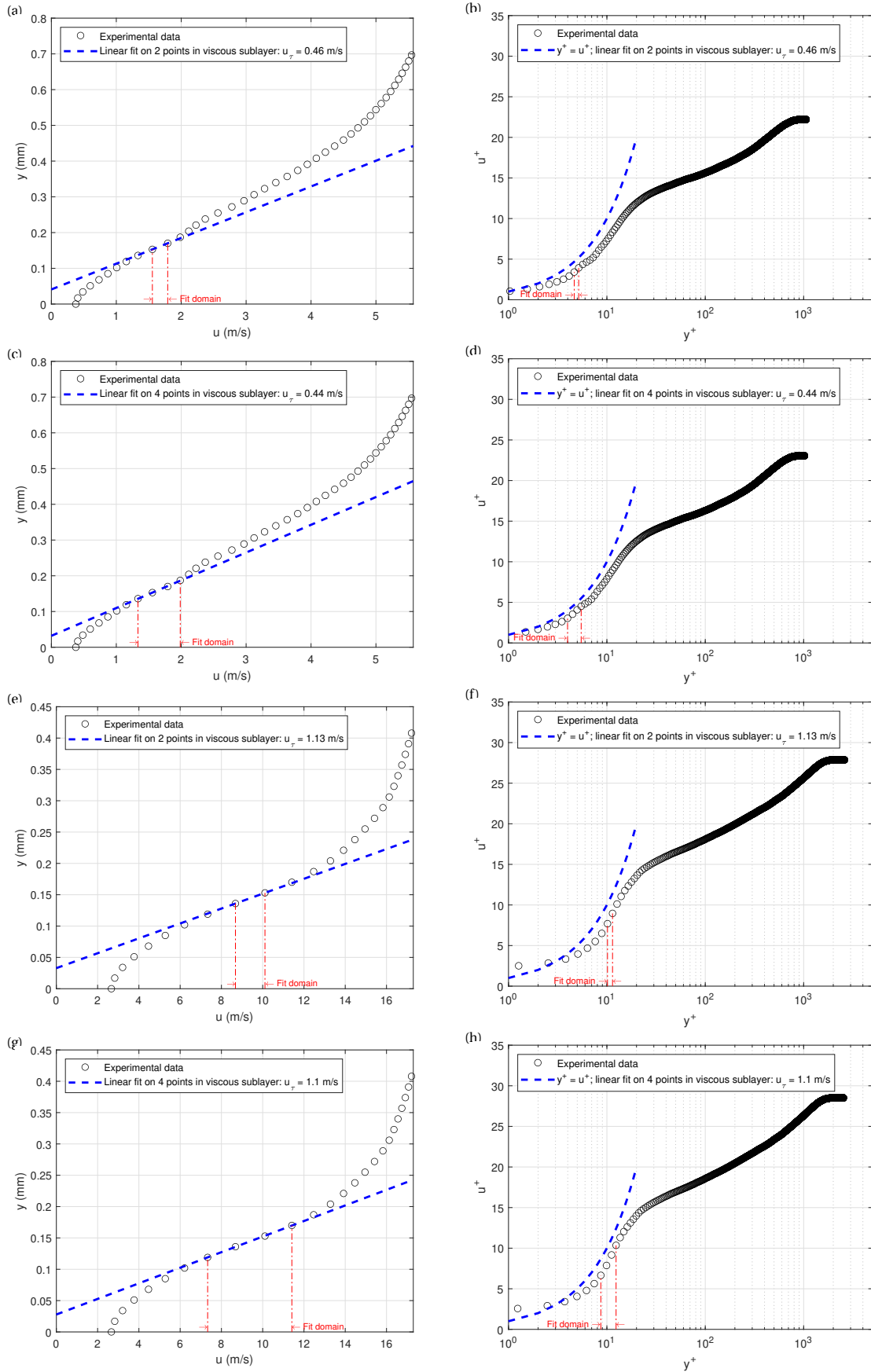


Figure H.4: Assessment of linear fitting in viscous sublayer for friction velocity estimation. (a, c, e, g) Physical units. (b, d, f, h) Viscous units. (a, b, c, d) 10 m/s. (e, f, g, h) 30 m/s. (a, b, e, f) Fitted on two data points. (c, d, g, h) Fitted on four data points.

Clauser's indirect method

When the velocity gradient cannot be determined accurately directly at the wall, indirect methods can be used. An example is by fitting the log-law to the overlap layer (the Clauser-plot). Since u_τ is unknown, a variable substitution can be made using Equation (2.22), yielding Equation (H.2). A best fit can be found by varying C_f for assumed constants B and κ , or by varying all parameters, which was done in this study with a least-squares optimization. u_τ can then be extracted from the estimated C_f . Figure H.5 shows the Clauser-plots obtained by the above-mentioned method. It can be seen that the overlap layer and consequently the fitting domain is smaller at lower velocities than at higher velocities.

$$\frac{u}{U_\infty} = \sqrt{\frac{C_f}{2}} \left(\frac{1}{\kappa} \ln \left(\frac{y U_\infty}{\nu} \sqrt{\frac{C_f}{2}} \right) + B \right) \tag{H.2}$$

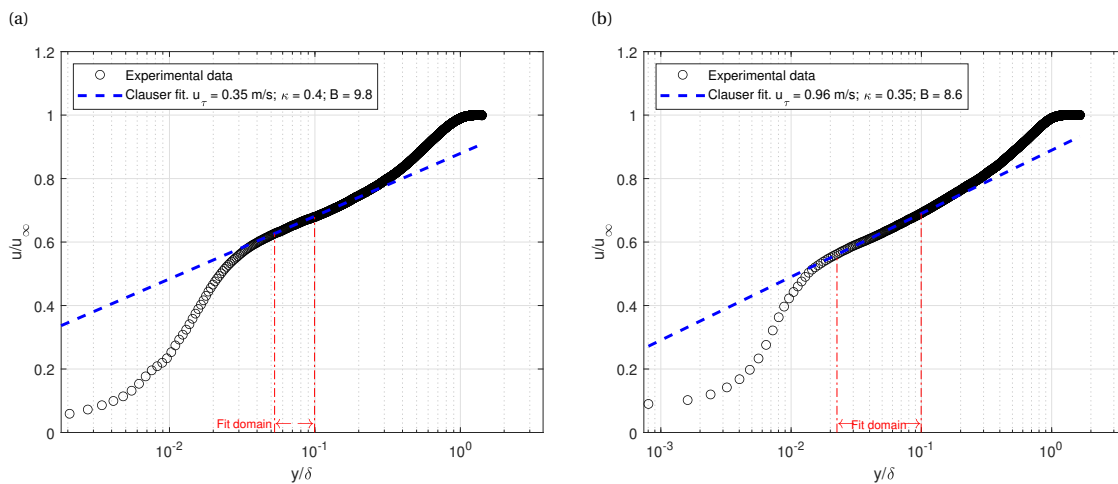


Figure H.5: Assessment of Clauser's indirect fitting for friction velocity estimation. (a) 10 m/s. (b) 30 m/s.

Spalding's Law of the Wall

Fitting on the entire inner layer, i.e. viscous sublayer, buffer layer and overlap layer, can be done with Spalding's Law of the Wall (Equation (2.14)). A least-squares optimization was done with u_τ , κ and B as parameters. Two observations can be made in Figure H.6. First, similar to Clauser's indirect method, the fit domain is larger for higher velocities. Furthermore, the experimental data lies below the fitted trend for $y^+ < 30$. These data points are underestimated because of the averaging effect at high velocity gradients. Consequently, the effect is visible more strongly for higher velocities.

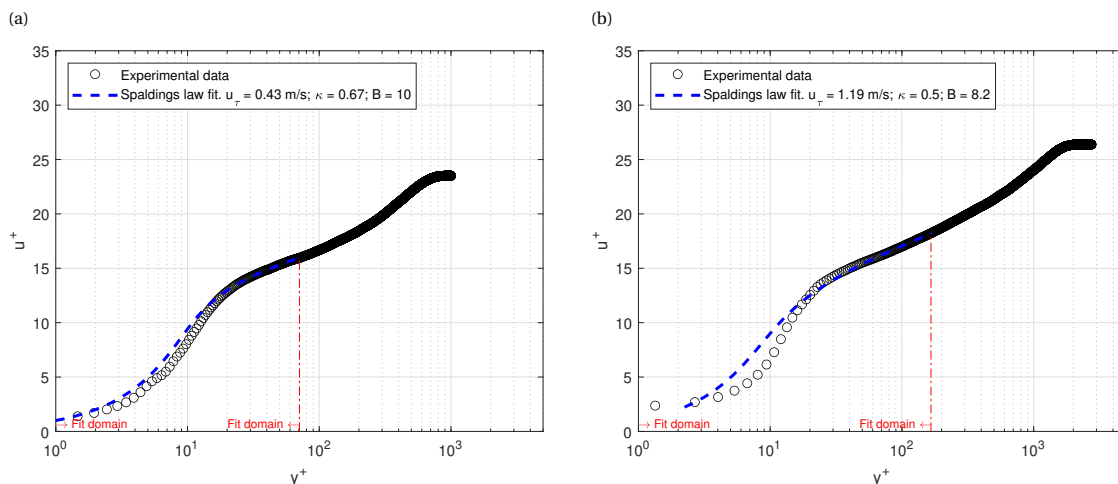


Figure H.6: Assessment of Spalding's law of the wall fitting for friction velocity estimation. (a) 10 m/s. (b) 30 m/s.

Composite profile

Rodríguez-López et al. (2015) presents a method for fitting to the entire BL profile, ranging from the viscous sublayer to the outer layer including the wake. This is done by combining Musker (Musker, 1979), bump (Monkewitz et al., 2007) and wake (Coles, 1956; Chauhan et al., 2009) profiles. The profile $u^+_{canonical}$ depends on $\{u_\tau, \Delta y, \kappa, \Pi, \delta\}$, where Δy is the potential wall offset in the measurement. The fitting parameters are found by minimising the residual error of the optimisation, either with a sum-of-squares error or mean absolute percentage error. He argues that the optimization problem is convex, hence insensitive to initial conditions, and robust in different cases such as flows subject to pressure gradients, poor data convergence and fewer data points.

The method was slightly adjusted in this study. Fitting was performed on only the outer layer, i.e. $y^+ > 30$ for two reasons. Firstly, the flow near the wall might be non-canonical across permeable surfaces while outer layer similarity generally holds. This is also the approach taken by Efstathiou and Luhar (2020) in their experimental work on turbulent boundary layers over streamwise-preferential porous materials. Secondly, the biased data points for $y^+ < 30$ might affect the fit and consequently yield inaccurate estimations of u_τ . The wall offset was assumed zero, i.e. $\Delta y = 0$. The wall-estimation method described in Appendix H.1 is performed before determining u_τ and is expected to be fairly accurate. Furthermore, letting the wall offset free in this optimization resulted in unrealistic fits with $\Delta y \sim O(10\delta_\nu)$. The experimental data was projected onto an evenly spaced logarithmic grid to prevent unintentionally giving high weight to the region near the edge of the boundary layer, where most of the data points lie.

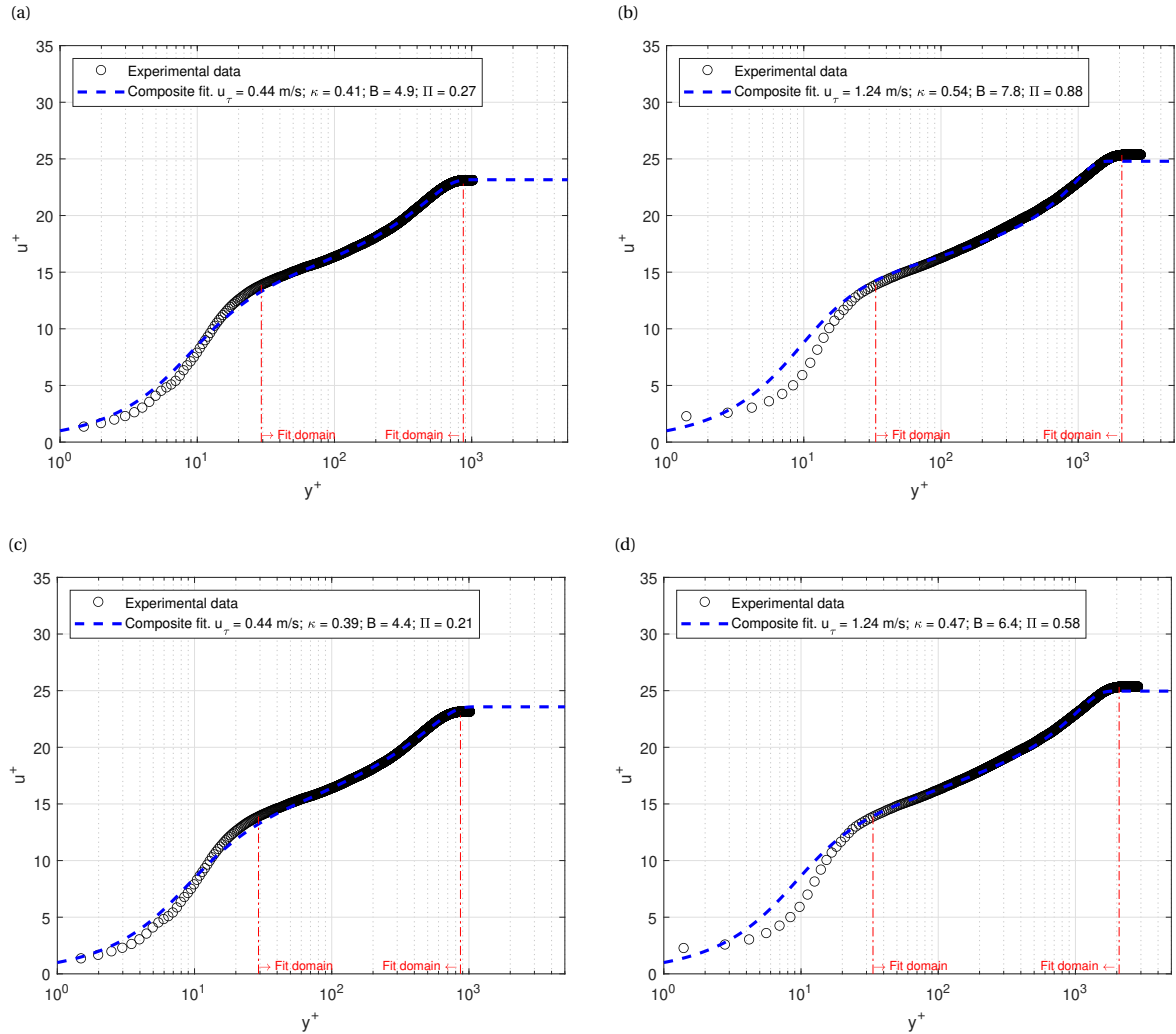


Figure H.7: Assessment of composite fitting (adapted from Rodríguez-López et al. (2015)) for friction velocity estimation. (a, b) Loose bounds, $0.2 < \kappa < 0.8$ and $0.1 < \Pi < 5$. (c, d) Tight bounds, $0.3 < \kappa < 0.6$ and $0.15 < \Pi < 0.6$. (a, c) 10 m/s . (b, d) 30 m/s .

Figure H.7 shows the results of this method. In general, the fit follows the experimental data well in the entire fitting region. For $y^+ < 30$, similar observations can be made as with fitting of Spalding's Law of the Wall; the experimental data lies below the fit. u_τ is fairly robust to a change in bounds of the fitting parameters κ and Π , but these fitting parameters themselves are not. The 10 m/s with tight bounds case (Figure H.7c) still allows for the optimal parameter set found in the loose bounds case (Figure H.7a). This implies that the solver is not convex and has multiple local optima. A lower estimation of κ , i.e. a less steep overlap layer fit, is accompanied by a higher estimation of Π , i.e. a larger wake contribution (Figure H.7b), and vice versa (Figure H.7c). Using the original numerical implementation by Rodríguez-López et al. (2015) (fitted to the entire profile with all data points on an evenly spaced linear grid) did remove the sensitivity to initial conditions, but it was not completely robust and even lead to poorer fits in some cases. Fixing these issues was deemed out of the scope of this research and as such, the adjusted method outlined in this appendix was used instead of the original implementation by Rodríguez-López et al. (2015).

H.2.2. Overall comparison

This section compares the different methods for estimating u_τ . For the linear method, results are taken from fitting on two data points. First, general observations in the estimated u_τ for the different methods, velocities and stations are discussed. Then, a robustness assessment is performed and the choice for the best method is defended. Finally, the different methods are compared to this choice of the best method, for all the different stations, velocities and test plates.

General observations

Figure H.8 shows the u_τ estimates for different estimation methods, velocities and locations for the reference test plate. A few observations can be made. First, the Clauser method consistently yields the lowest estimate. It is to be expected that this method is not accurate since the extent of the overlap layer is relatively small at low Reynolds numbers. Also noteworthy is the change of slope for the linear fit between 20 m/s and 30 m/s, going from yielding the largest estimates to estimates lower than with the Spalding and composite methods. This is most likely because of the averaging effect near the wall which is more pronounced at higher velocities as mentioned in Appendix H.2.1. At 30 m/s, the Spalding method yields estimates between the composite and linear methods. It takes a larger region for the data than the linear method, but might still be biased by the lower data points included in the fitting procedure, yielding an underestimation of u_τ .

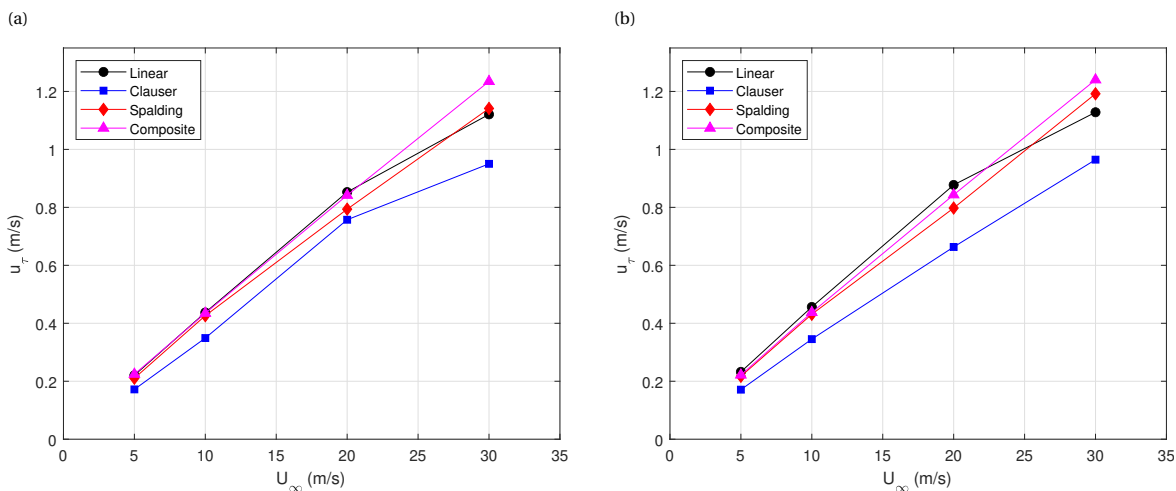


Figure H.8: Friction velocity (u_τ) for different velocities and estimation methods. (a) Station 3. (b) Station 4.

Robustness assessment

Assessing the robustness of the estimation methods is done using the data of Station 1. PIV measurements for both the permeable and reference plate were performed here, but the field of view is completely in front of the test plate leading edge. As such, an estimation method should yield the same u_τ for the permeable plate as for the reference plate, under the assumption that flow similarity also holds across the measurements. Figure H.9a shows the u_τ estimates for different estimation methods and velocities for the reference test plate. In general, similar observations can be made as with the other stations in Figure H.8: a consistently lower estimate from the Clauser method at the lower velocities, a change of slope for the linear fit at 20 m/s and 30 m/s and often an estimate from the Spalding method between the composite and linear methods at 30 m/s.

Figure H.9b shows the percentage difference in the normalised u_τ of the permeable measurement with respect to the reference measurement. The linear method is the most sensitive, with an absolute mean of 3.1% and a maximum of nearly 6% at the highest velocity. The composite method yields the lowest differences, all under 1% with an absolute mean of 0.4%. This serves as an indication that the composite method is the most robust for determining u_τ . Other arguments that support this finding are the fact that it uses the largest region of the velocity profile and is not influenced by the biased data points near the wall, a drawback that the linear and Spalding methods suffer from.

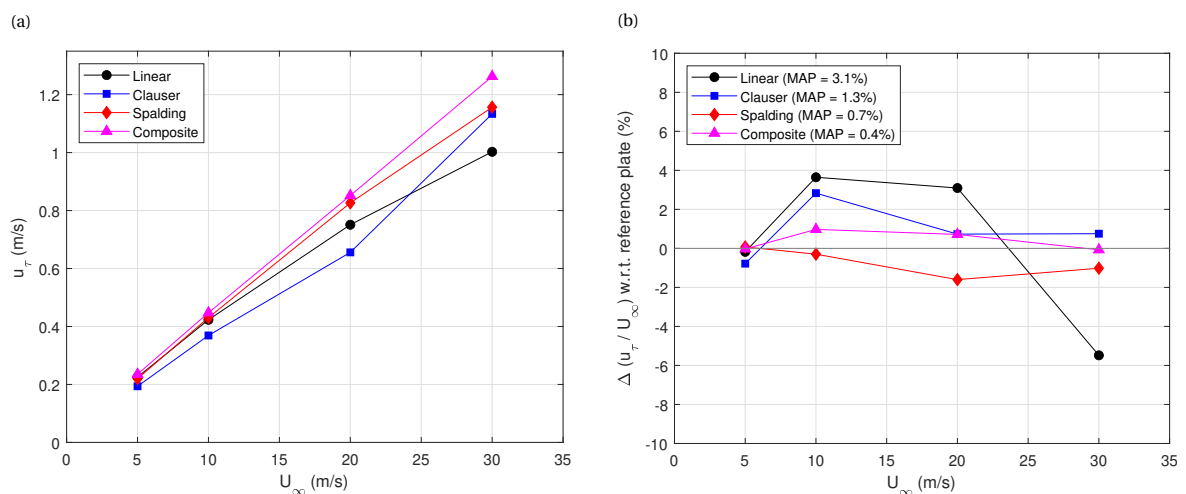


Figure H.9: Assessment of method similarity across measurements at Station 1 (in front of test plate LE), for different velocities and estimation methods. (a) Friction velocity (u_τ) for reference plate. (b) Percentage difference in normalised friction velocity (u_τ/U_∞) between permeable and reference plate measurements. MAP = Mean Absolute Percentage.

Full comparison

Figure H.10 shows the percentage difference in the normalised friction velocity of the linear, Clauser and Spalding methods with respect to the composite method, for both the permeable and reference plate at different stations and velocities. In general, similar insights can be extracted as with the absolute friction velocity data: a consistently lower estimate from the Clauser method at the lower velocities, a change of slope for the linear fit at 20 m/s and 30 m/s and often an estimate from the Spalding method between the composite and linear methods at 30 m/s.

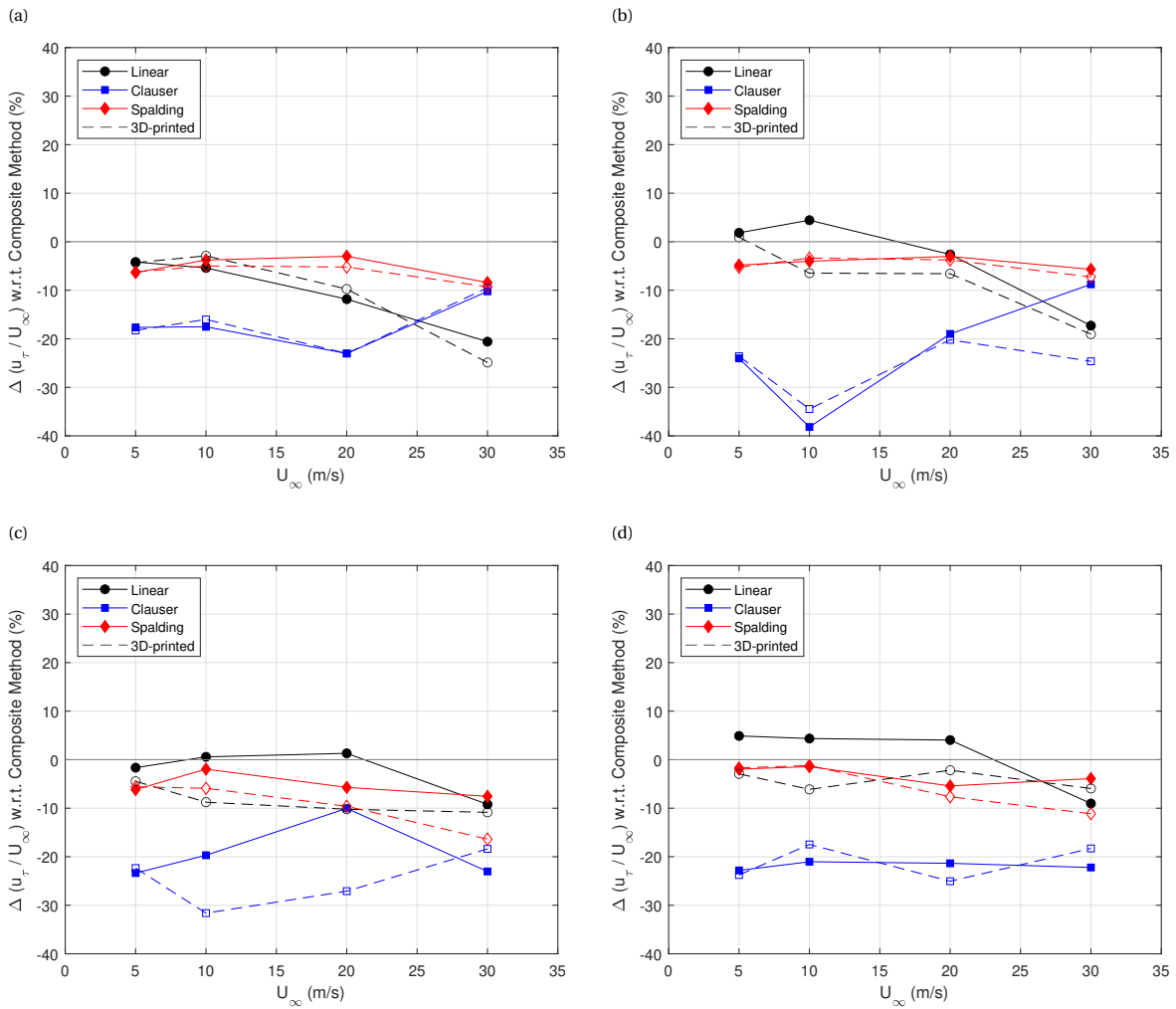


Figure H.10: Percentage difference in normalised friction velocity (u_τ/U_∞) between different estimation methods, with composite method as reference, for different velocities. (a) Station 1. (b) Station 2. (c) Station 3. (d) Station 4.

This page has been intentionally left blank.

PIV results

This appendix shares an extensive set of PIV results to support the analysis and discussion as shared in Chapter 12. Appendix I.1 covers the seal fur, and Appendix I.2 the 3D-printed surface. For sake of brevity and readability, not all results are shared.

I.1. Seal fur

Figure I.2 shows a comparison between the BL profiles (mean velocity and one-point turbulent statistics) for the grey seal and reference smooth wall, for all velocities for station 4 (regular view). They are expressed in outer variables. For the seal fur, it was not possible to accurately determine the effective wall location, due to heterogeneity of the surface (hairs of the fur). It was estimated to lie 1.5 mm below the laser sheet cut-off height, above which the data points were taken and processed (Figure I.1). As such, the profiles for the seal fur start at 1.5 mm in Figure I.2. The uncertainty in the exact effective wall location does not affect the interpretation of the results. The two following observations can be made:

- The turbulent activity is higher above the seal fur. The stronger streamwise and wall-normal velocity fluctuations indicate more turbulent mixing, which results in a higher Reynolds stress.
- The velocity profile is less 'full'. This indicates more momentum loss in the flow above the seal fur compared to the smooth wall. It is in line with the high drag increase observed in the direct force measurements.

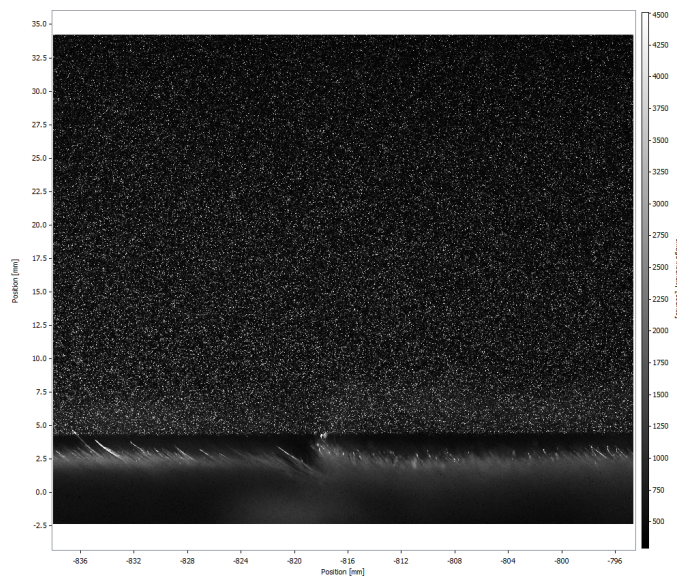


Figure I.1: Example of raw image from PIV measurement of the seal fur. Flow from right to left.

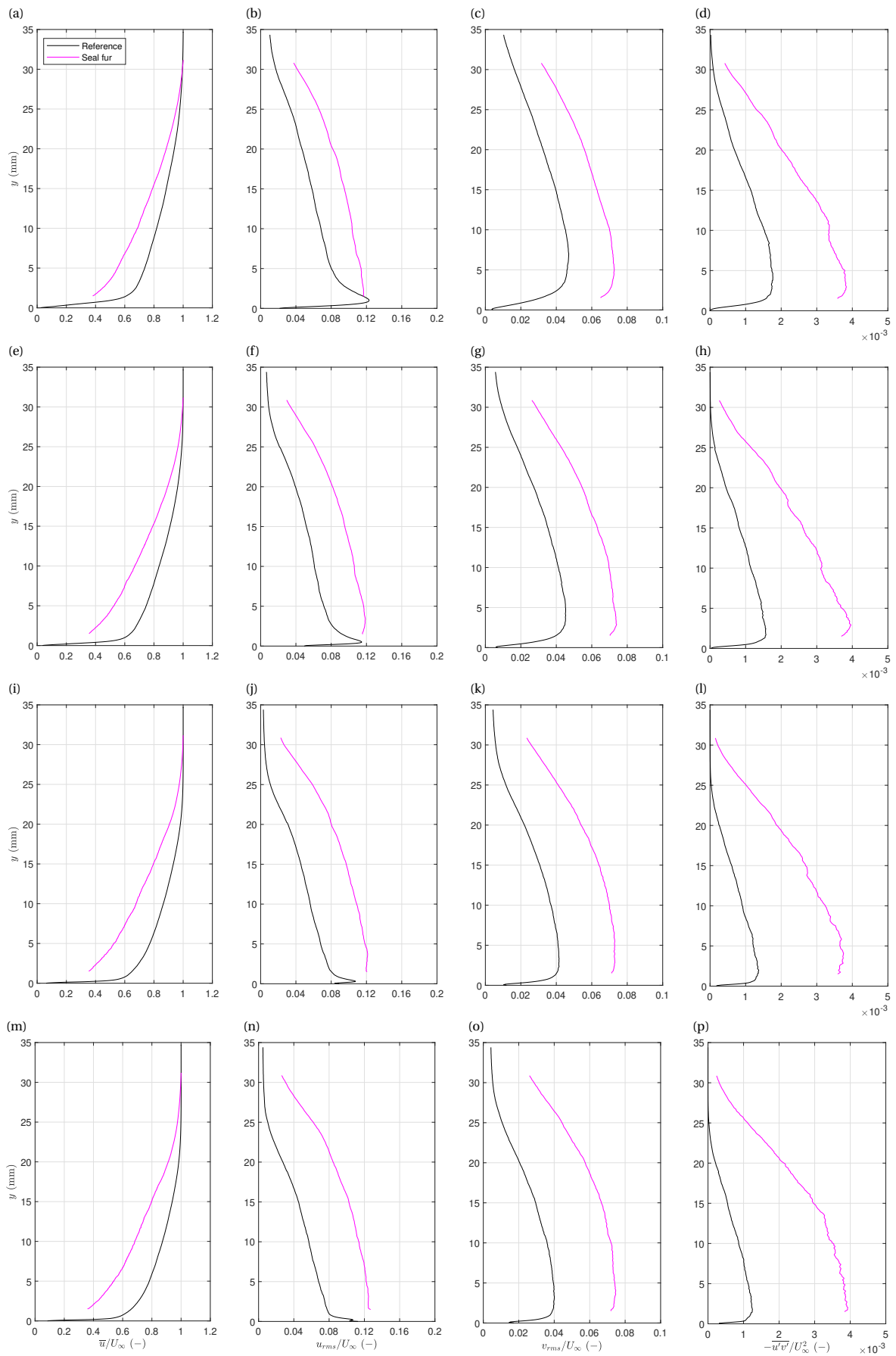


Figure 1.2: Boundary layer profiles for Station 4. $U_\infty = 5$ (a-d), 10 (e-h), 20 (i-l) & 30 (m-p) m/s. (a, e, i, m) \bar{u}/U_∞ . (b, f, j, n) u_{rms}/U_∞ . (c, g, k, o) v_{rms}/U_∞ . (d, h, l, p) $-\bar{u}'v'/U_\infty^2$.

The vibrations of the individual hairs of the seal fur are visualised in Figure I.3.

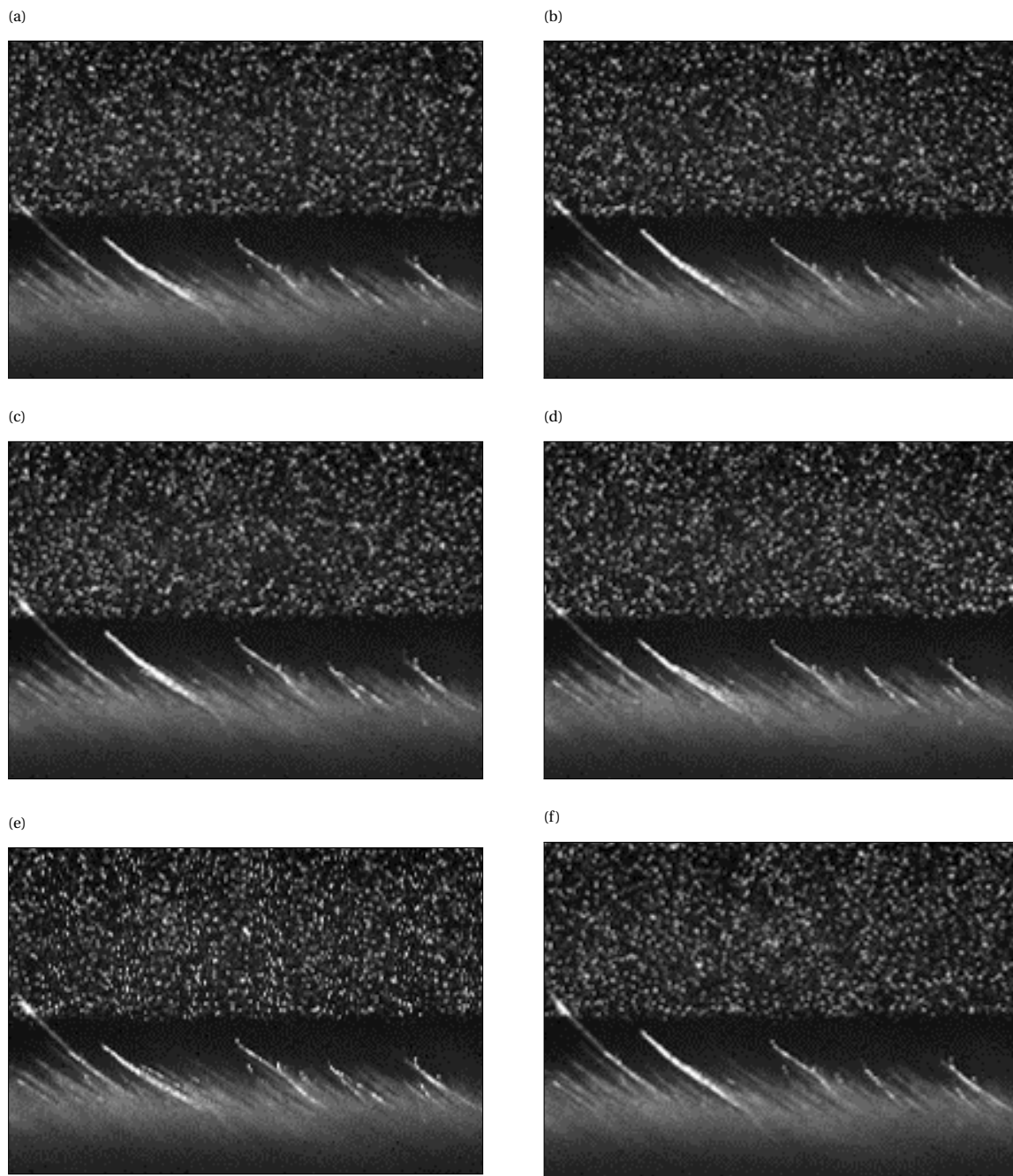


Figure I.3: Visualisation of vibrating hairs of seal fur. Images at six different moments. Flow from right to left.

I.2. 3D-printed surface

Three sets of data are provided here to support the findings as presented in the main body of this report: the BL profiles in Appendix I.2.1, BL fitting parameters in Appendix I.2.2 and the spatial spectra in Appendix I.2.3.

I.2.1. Boundary layer profiles

Figures I.4 to I.8 show the BL profiles (mean velocity and one-point turbulent statistics) for all velocities for stations 1 to 4, and station 4 with zoomed-in view, respectively. They are expressed in normalised outer variables. Note that station 4, zoomed-in view (Figure I.8) does not capture the entire BL. Therefore, the wall-normal distance is not normalised, and the profile variables are normalised with the target velocity.

The main observations are:

- The trends of the two surfaces are similar for most stations and velocities. Differences are best visible for the Reynolds stress, especially at higher velocities.
- Anomalous trends occur for both surfaces near the wall for station 1, especially v_{rms} . Since this was measured just in front of the test plate LE, it could be caused by a small step downstream. It might also have to do with the reflective nature of the tape at the wall at this station.
- The decrease in Reynolds stress at $U_\infty = 5$ & 10 m/s at station 4 when expressed in inner variables (presented in Section 12.3) is visible in outer variables (Figures I.7d and I.7h) as well. This shows that it was not caused by normalisation with u_τ , which is further discussed in Section 12.6.3.
- A decrease in Reynolds stress for the zoomed-in view occurs only at $U_\infty = 5$ m/s (Figure I.8d).
- There is no decrease in Reynolds stress for all other stations.
- Riblets show a clear decrease in Reynolds stress for $U_\infty = 20$ & 30 m/s. Direct force measurements from prior studies under the same measurement conditions have shown that these riblets reduce drag and have not reached their point of maximum DR at 30 m/s yet. Hence, they are more effective at lower viscous length scales, which corresponds to this observation on Reynolds stress.

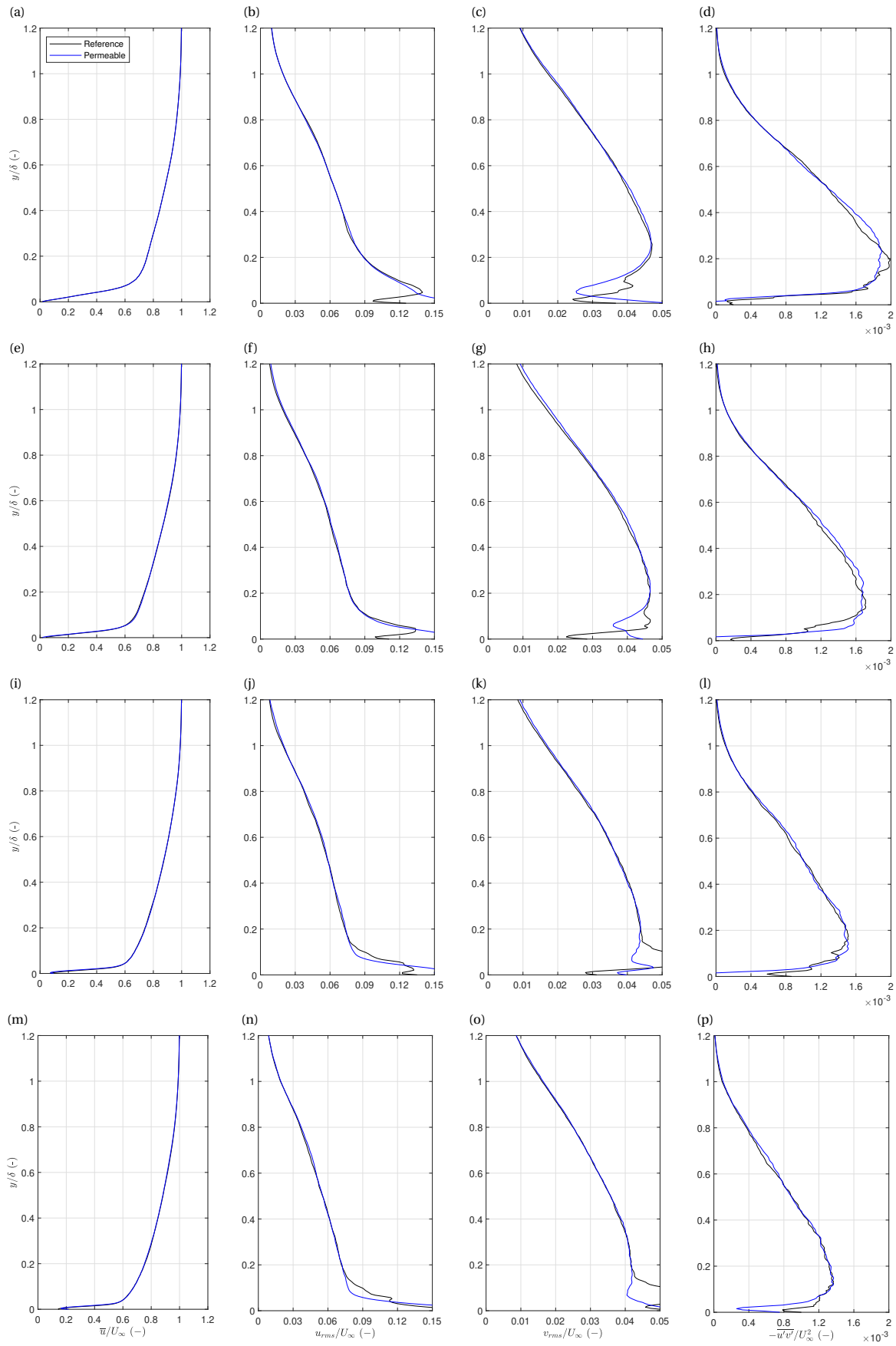


Figure I.4: Boundary layer profiles for Station 1. $U_\infty = 5$ (a-d), 10 (e-h), 20 (i-l) & 30 (m-p) m/s. (a, e, i, m) \bar{u}/U_∞ . (b, f, j, n) u_{rms}/U_∞ . (c, g, k, o) v_{rms}/U_∞ . (d, h, l, p) $-\overline{u'v'}/U_\infty^2$.

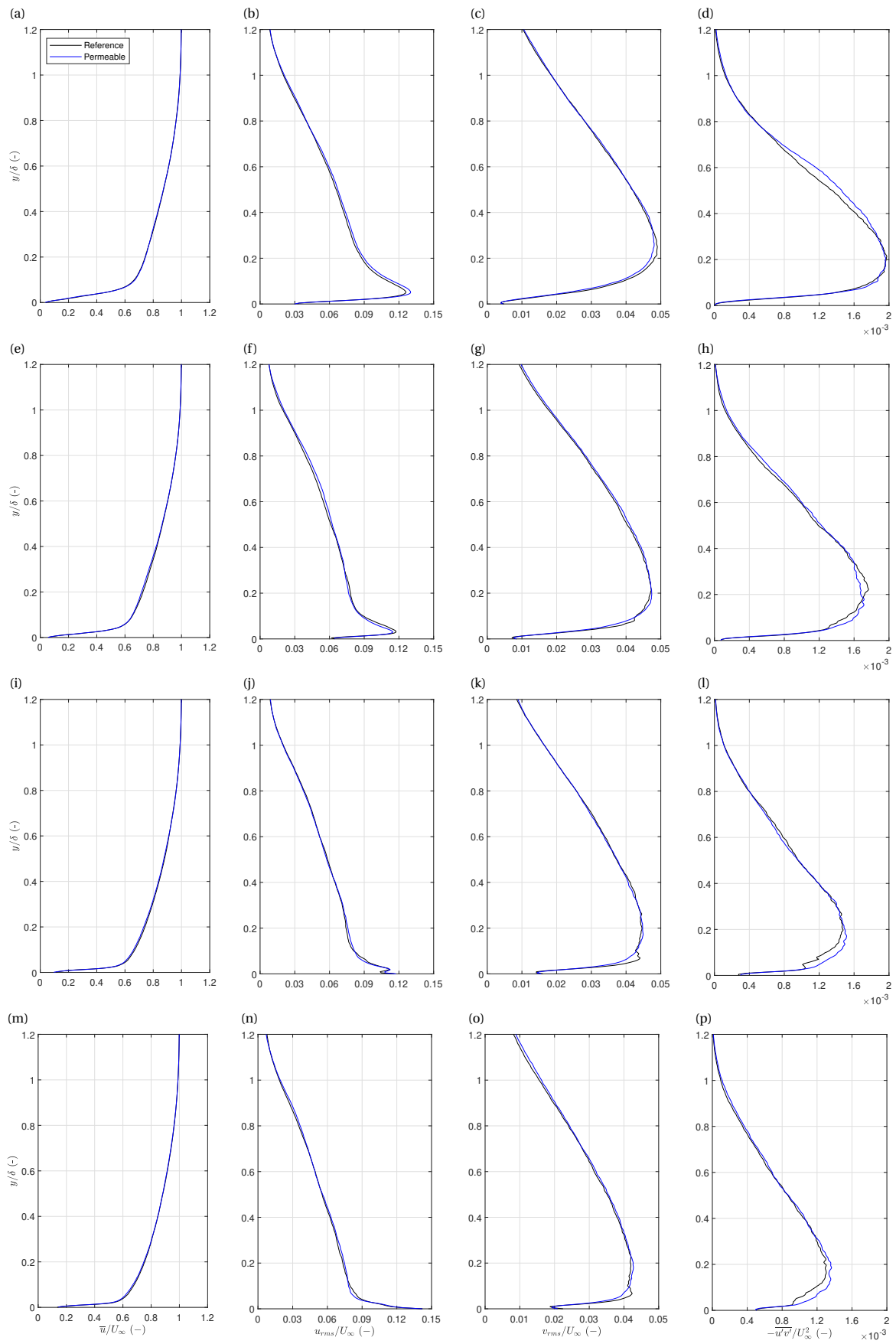


Figure 1.5: Boundary layer profiles for Station 2. $U_\infty = 5$ (a-d), 10 (e-h), 20 (i-l) & 30 (m-p) m/s. (a, e, i, m) \bar{u}/U_∞ . (b, f, j, n) u_{rms}/U_∞ . (c, g, k, o) v_{rms}/U_∞ . (d, h, l, p) $-u'v'/U_\infty^2$.

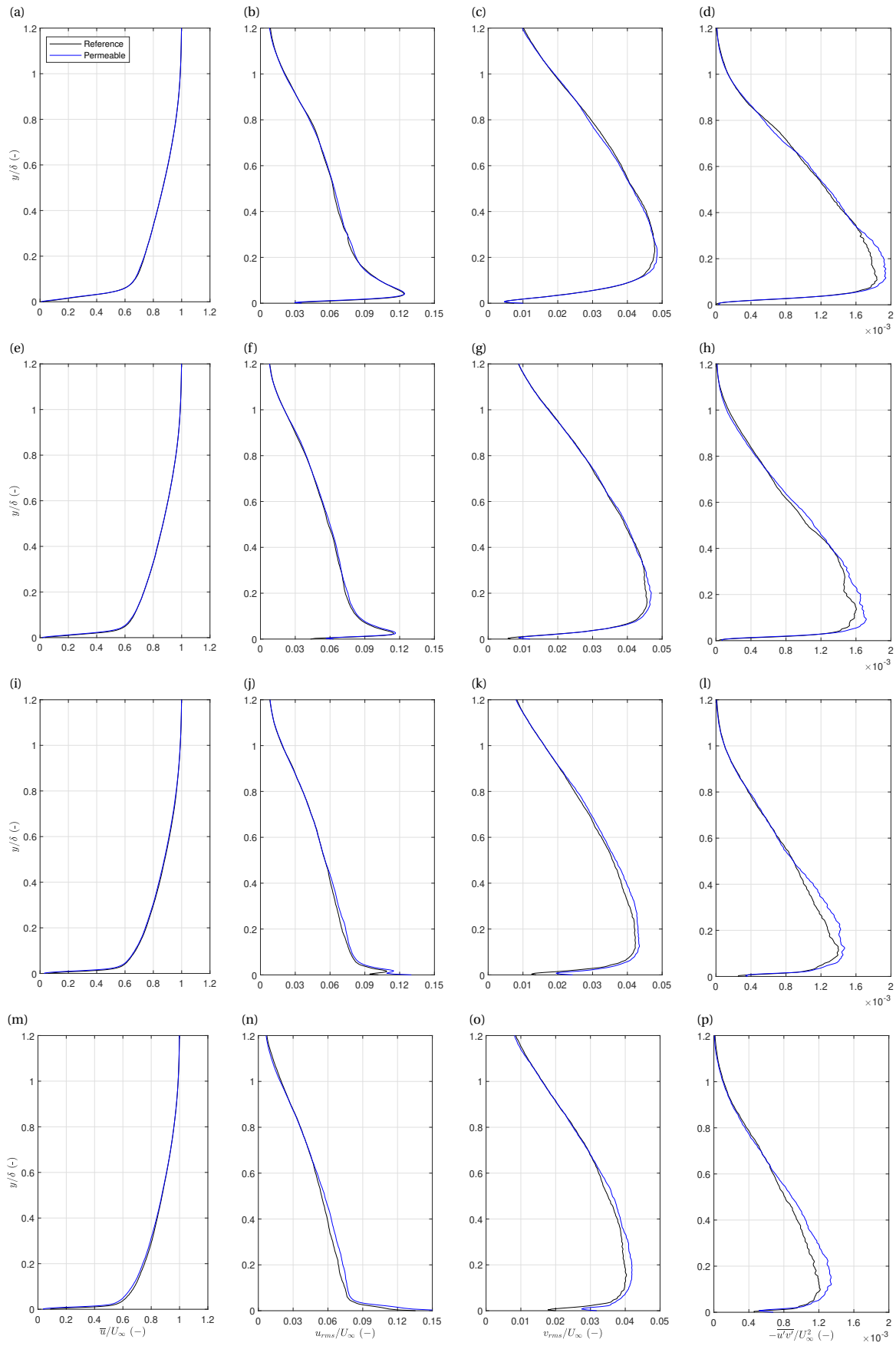


Figure 1.6: Boundary layer profiles for Station 3. $U_\infty = 5$ (a-d), 10 (e-h), 20 (i-l) & 30 (m-p) m/s. (a, e, i, m) \bar{u}/U_∞ . (b, f, j, n) u_{rms}/U_∞ . (c, g, k, o) v_{rms}/U_∞ . (d, h, l, p) $-\overline{u'v'}/U_\infty^2$.

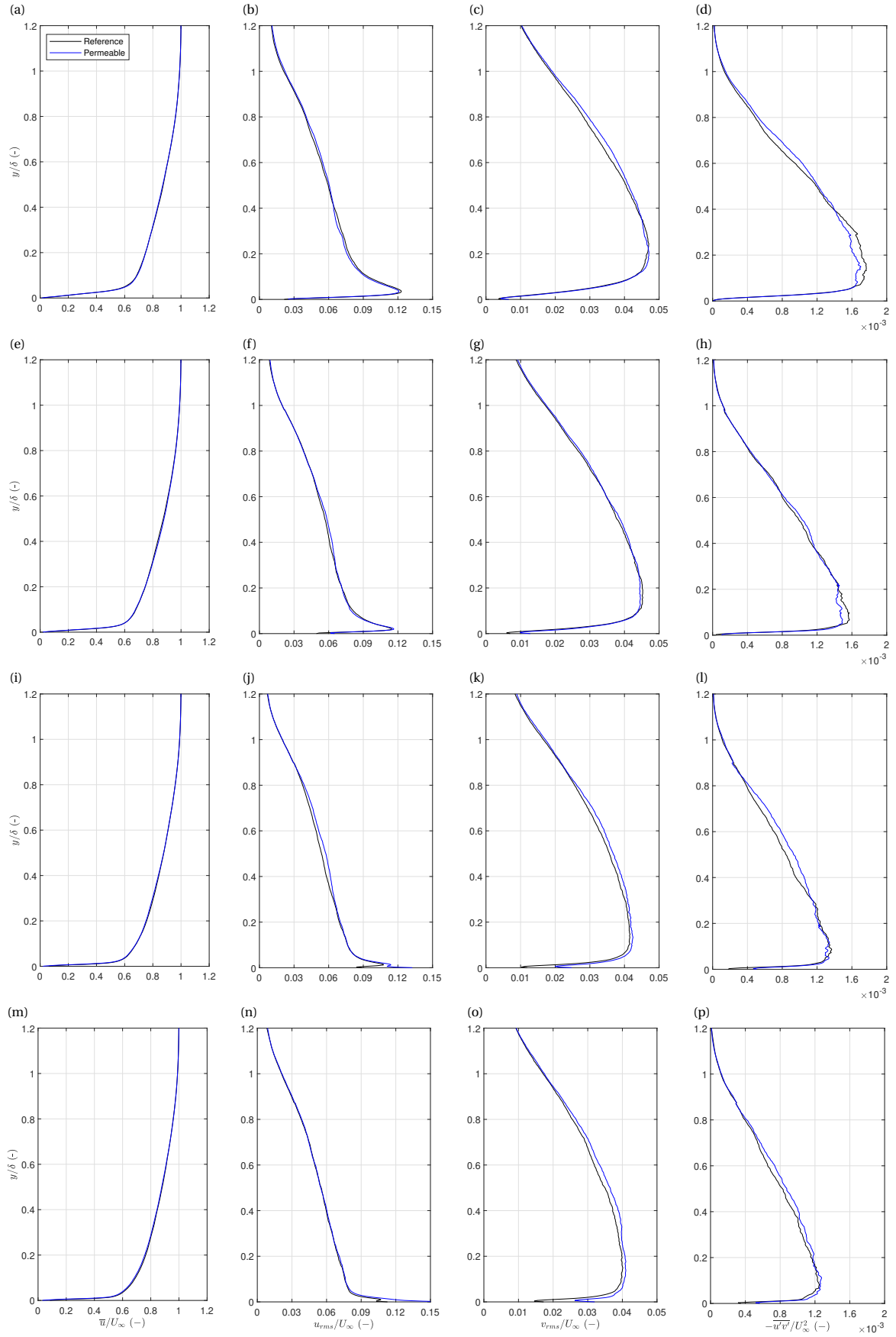


Figure 1.7: Boundary layer profiles for Station 4. $U_\infty = 5$ (a-d), 10 (e-h), 20 (i-l) & 30 (m-p) m/s. (a, e, i, m) \bar{u}/U_∞ . (b, f, j, n) u_{rms}/U_∞ . (c, g, k, o) v_{rms}/U_∞ . (d, h, l, p) $-\overline{u'v'}/U_\infty^2$.

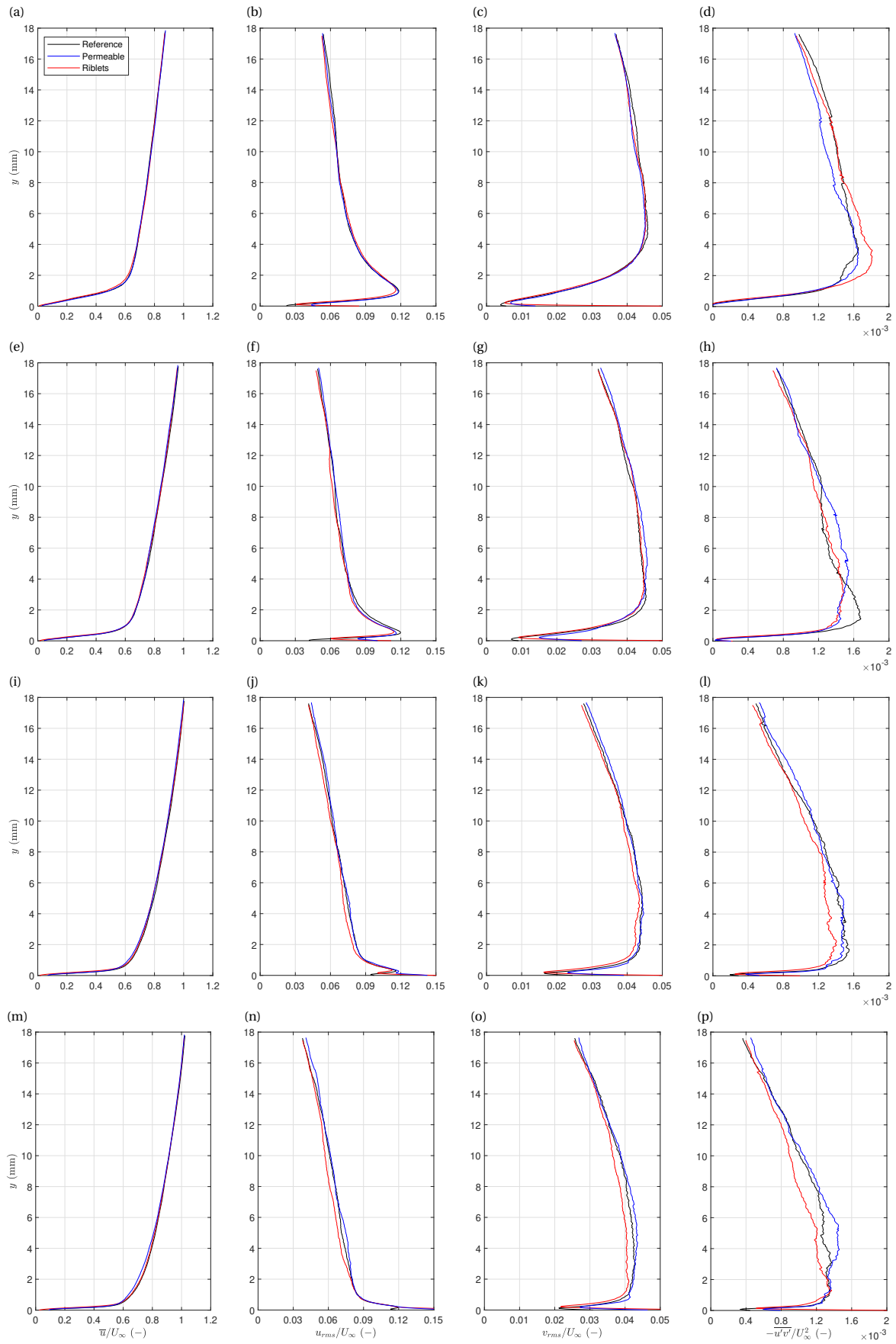


Figure I.8: Boundary layer profiles for Station 4 (zoomed-in view). Velocity normalised w.r.t. target value. $U_\infty = 5$ (a-d), 10 (e-h), 20 (i-l) & 30 (m-p) m/s. (a, e, i, m) \bar{u}/U_∞ . (b, f, j, n) u_{rms}/U_∞ . (c, g, k, o) v_{rms}/U_∞ . (d, h, l, p) $-\overline{u'v'}/U_\infty^2$.

I.2.2. Boundary layer fitting parameters

Table I.1 presents the fitted parameters for the outer layer composite fit optimisation. In several cases, the fitted values for κ and Π are at the set bounds. In these cases, B is also far off from conventional values of $B \approx 5$. It shows that the method might find a local optimum with fitted values that do not reflect the actual BL profile. Nevertheless, u_τ was found to be fairly robust to changes in initial conditions (Appendix H.2.1) and the method was decided to be of sufficient reliability for this study.

Table I.1: Fitted boundary layer parameters of outer layer composite fit optimisation adapted from Rodríguez-López et al. (2015). B is not fitted but results from the other fitting parameters. Initial conditions: $\kappa_0 = 0.4$, $\Pi_0 = 0.3$. Bounds: $0.3 < \kappa < 0.6$, $0.1 < \Pi < 0.6$.

Station	Plate	U_∞ (m/s)	u_τ (m/s)	B	κ	Π
1	Reference	5	0.24	5.1	0.41	0.10
1	Reference	10	0.45	5.7	0.44	0.37
1	Reference	20	0.85	7.0	0.50	0.60
1	Reference	30	1.26	8.9	0.60	0.60
1	Permeable	5	0.24	5.2	0.42	0.11
1	Permeable	10	0.45	5.5	0.43	0.29
1	Permeable	20	0.86	7.3	0.51	0.60
1	Permeable	30	1.26	8.9	0.60	0.60
2	Reference	5	0.23	5.4	0.43	0.23
2	Reference	10	0.44	4.4	0.39	0.28
2	Reference	20	0.85	5.2	0.42	0.38
2	Reference	30	1.24	4.8	0.40	0.29
2	Permeable	5	0.23	4.8	0.40	0.12
2	Permeable	10	0.44	6.0	0.45	0.57
2	Permeable	20	0.84	6.0	0.45	0.58
2	Permeable	30	1.24	4.8	0.40	0.35
3	Reference	5	0.22	5.4	0.42	0.28
3	Reference	10	0.43	4.7	0.40	0.30
3	Reference	20	0.84	4.7	0.40	0.31
3	Reference	30	1.24	5.7	0.44	0.48
3	Permeable	5	0.22	5.4	0.43	0.30
3	Permeable	10	0.43	6.6	0.48	0.60
3	Permeable	20	0.84	7.3	0.51	0.60
3	Permeable	30	1.21	7.2	0.51	0.60
4	Reference	5	0.23	4.7	0.40	0.14
4	Reference	10	0.44	4.3	0.38	0.18
4	Reference	20	0.84	4.7	0.40	0.28
4	Reference	30	1.24	6.4	0.47	0.58
4	Permeable	5	0.23	5.0	0.41	0.17
4	Permeable	10	0.44	6.1	0.46	0.44
4	Permeable	20	0.84	5.1	0.41	0.35
4	Permeable	30	1.23	5.7	0.44	0.53

I.2.3. Spatial spectra

Figure 1.9 shows the premultiplied spatial spectra for the reference smooth wall at station 4. Two main take-aways are:

- The window size is too small to obtain a clear picture of the energetic structures at low velocities, specifically those corresponding to the near-wall cycle ($\lambda_x \approx 1,000$).
- The near-wall data is too unreliable at high velocities and shows up as high-energy noise at $\lambda_x \approx 100$ in both the streamwise and wall-normal spectra.

Given these limitations, the data was not further analysed for the permeable surface or other stations.

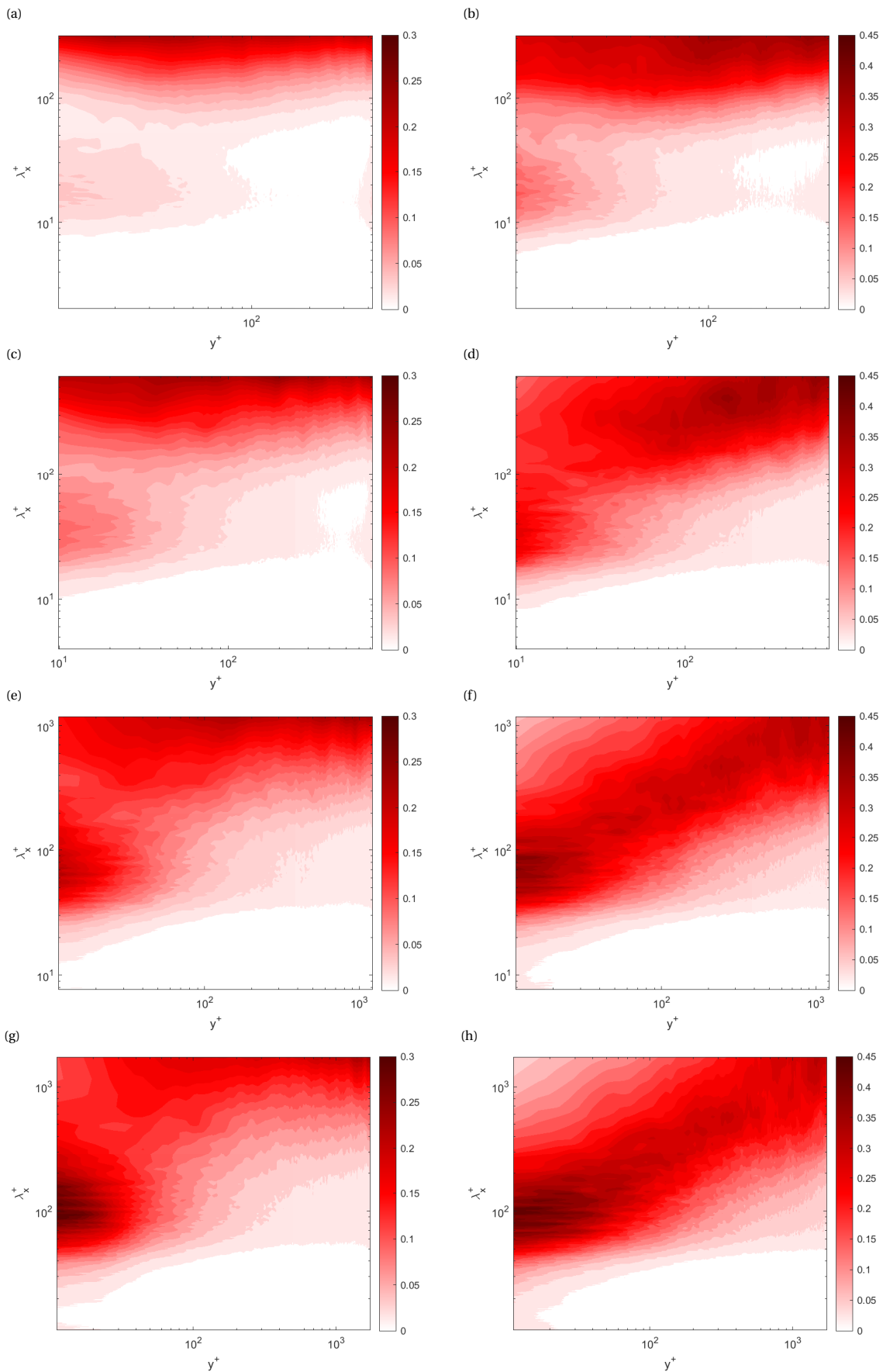


Figure I.9: Premultiplied spatial spectra for reference smooth wall at Station 4. (a, c, e, g) G_{uu}^+ . (b, d, f, h) G_{vv}^+ . $U_\infty = 5$ (a), 10 (b), 20 (c) & 30 (d) m/s.

This page has been intentionally left blank.

This page has been intentionally left blank.

